DISSERTATION

LOCAL STRUCTURE STUDIES IN FUNCTIONAL MATERIALS

AND

SELF-REGULATED LEARNING INTERVENTIONS IN GENERAL CHEMISTRY COURSES

Submitted by

Arnold A. Paecklar

Department of Chemistry

In partial fulfillment of the requirements

For the Degree of Doctor of Philosophy

Colorado State University

Fort Collins, Colorado

Spring 2020

Doctoral Committee:

Advisor: James R. Neilson
Co-Advisor: Melissa M. Reynolds

Matthew G. Rhodes
Richard G. Finke
Carmen S. Menoni

ABSTRACT

LOCAL STRUCTURE STUDIES IN FUNCTIONAL MATERIALS

AND

SELF-REGULATED LEARNING INTERVENTIONS IN GENERAL CHEMISTRY COURSES

The first part of this dissertation is dedicated to understanding how the origin of the chemical and physical properties of functional materials is correlated to their structure. The standard approach to determining the structure of a crystalline material is to measure the average structure of regular, repeating units. However, this approach is not sufficient for more complex compounds including disorder. Hence, to fully understand the structure-property relationships of these advanced materials, identifying the local structure is crucial. This work focuses on designing approaches for optimizing the measurement of local structure data based on X-ray and neutron total scattering techniques as well as computational approaches for analyzing and understanding these data sets. The main focus lies in designing a novel system for collecting neutron total scattering data involving the controlled exposure of gasses to solid samples. Combining this setup with a Steady-State Isotopic Transient Kinetic Analysis system further enables the collection of kinetics data simultaneously with the structural data. This system was successfully used for studying and identifying the adsorption and reaction sites in porous materials such as zeolites and metal-organic frameworks. The disorder in these systems is based on the adsorbate which is a major contributor to the structure. However, there are also materials in which a single solid phase itself contains all the disorder. Some examples for disordered materials, covered in this work, are semiconducting perovskite materials with the general formula A_2BX_6. Computational approaches ranging from single to high-throughput Reverse Monte Carlo modeling were developed to gain more insight into anharmonicity and the interplay of the local structural features.

Understanding how these specific local structural features influence desired physical properties will help guide the design of new materials covering a wide range of applications ranging from photovoltaics to biomedical devices.

While the creation of such new knowledge in material science is important, we must also ensure that this knowledge is understood and transferred effectively. This effort does not only contain educating the general public but also fostering their curiosity and providing them the tools needed to learn that content knowledge. Succeeding in these endeavors is especially important during the first exposure to science courses.

The second part of this dissertation focuses on the aspect of learning by looking at educational interventions in two different introductory general chemistry courses. The effectiveness of these interventions was evaluated based on data collected with paper-based, in-class surveys over the course of the semester. A multitude of self-regulated learning (SRL) measures were assessed and range from extrinsic motivation over self-efficacy to help seeking. Statistical analyses were used to identify differences between entire courses and individual sections exposed to the interventions. Additionally, the students' combined grades were also compared.

Identifying the effective tools for helping students in chemistry courses is expected to have a major impact on changing the rate of failing students in such courses. This is the step needed for students to decide to become the next researchers contributing to the field with new scientific discoveries themselves.

ACKNOWLEDGEMENTS

Completing my PhD program would not have been possible without the help of a lot of people. First of all, I have to acknowledge my advisors. Having had multiple advisors has especially taught me that the more advising one has, the more different approaches, insights and connections one can obtain. I would like to particularly thank my main advisor James Neilson for his patience, encouragement, and thought-provoking inputs. He has pushed me in directions and areas of research that I would never have thought possible. His approach to "just do it" has gotten me into the realm of theoretical chemistry, programming, and high-performance computation. He also allowed me to have a multidisciplinary approach in my Ph.D. program. This allowed me to only spend about half the time on materials chemistry research compared to his traditional students. Furthermore, when I surprised him with a proposal for a collaborative project with a national laboratory and another university, he did not hesitate to help and put time and effort into it.

Additionally, I have to thank my Co-adviser Melissa Reynolds who has allowed me to pursue the chemical education program. Furthermore, she has provided me more insight into the industrial side of chemistry as well as the administrative side of a university. I am particularly thankful for her initiatives for finding positions after my PhD program and her financial support despite not being a full member of her group. Along these lines, I would like to thank the CSU Graduate Student Council and the Department of Chemistry for their financial support through grants but also through salary. The company Revalent, their financial support, and insight gained through the ENERCAT project will not be forgotten!

My research would have not been possible without many collaborators. While this is by no means a comprehensive list, I would like to name just a few here. For the gas adsorption project, I have to particularly thank Daniel Olds, Keith Lawler, Jue Liu, Katharine Page, Peter Peterson, Paul Forster, Gerald Rucker, Mariano Ruiz-Rodriguez, Michael Olsen, Michele Pawel, and Steven Overbury. For my computational science endeavor during my last project, I would like to thank the research computing staff at Colorado State University and University of Colorado Boulder.

Without their support I could not have resolved several issues with SUMMIT. In this context, I have to also particularly mention Elijah Flenner for his solution on how to deal with periodic boundary conditions. Furthermore, I would like to thank Matthew Rhodes for his help and encouragement. Without him, I would have probably given up on my chemistry education projects a long time ago.

Richard Finke and Carmen Menoni, in addition to the already above mentioned committee members, deserve my gratitude for their support. Special thanks to Joseph Zadrozny who was willing to serve as a subsitute committee member for my defense. I would also like to acknowledge my coworkers in the Neilson and Reynolds group who have helped and given me so much additional insight into different fields and projects. Other great support came from the students in my cohort starting with me the adventure of a PhD program at CSU. During my first few years they helped me with a number of things particullarly outside of CSU.

I would like to thank my parents and my siblings for making it possible to come to the USA and for their support during this PhD program. Last but not least, I have to thank my wife for her support in those final weeks and hours (especially for making sure that I never ran out of chocolate).

Finally, there is a countless number of many more who contributed along the way. Despite not naming everybody individually here, none of their support is forgotten nor underappreciated.

TABLE OF CONTENTS

LIST OF TABLES

LIST OF FIGURES

Part 1

The Importance of Studying the Local Structure in Functional Materials

Chapter 1

Introduction

1.1 The current energy crisis

The world's energy consumption has been steadily increasing over the last few years. Based on the fact that most of the energy in the United States is still being generated by the incineration of fossil fuels (Figure 1.1) [1], it is not surprising that this trend has been directly coupled to an elevation in emissions of greenhouse gases such as carbon dioxide (CO_2). These higher emissions are seen as one of the main contributors to global warming and climate change.

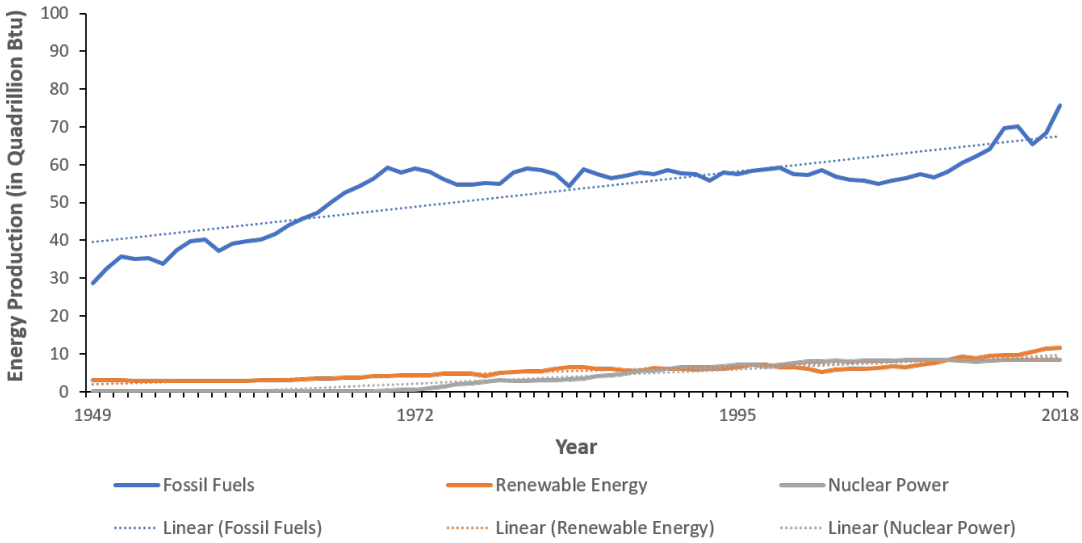

Figure 1.1: Comparison on energy produced in the USA based on fossil fuels, nuclear power, and renewable sources. Data retrieved from the U.S. Energy Information Administration.

The CO_2 concentration in the atmosphere continues to rise due to the increasing amount of power consumption within both the commercial and private sectors. Other factors include, for instance, a growing population leading to more vehicles and also more airplanes powered by combustion engines. To reverse the resulting climate change we have to decrease the level of CO_2 emissions. This can be done in multiple ways by, for example, harnessing different energy sources, and

making industrial processes more efficient. Specifically, the rate of CO_2 emissions will be reduced by replacing fossil fuels as an energy source with carbon neutral sources such as nuclear energy or, ideally, with renewable energy sources like solar power and hydrogen based power. However, to achieve this goal, new materials need to be discovered and developed including photovoltaic absorbers, hydrogen storage materials, and fuel cells.

To find these new functional materials, we cannot follow the original thought and approach of "pure and simple is best". For example, pure metals, such as aluminum, cannot be used for building airplanes due to its ductility, and other elements need to be added to make a durable alloy. The same applies to swords, if they were made out pure iron, they would not withstand any impact. However, structural complexity leads to desirable properties (harness). This can be seen on a micrometer scale in Japanese swords which are everything but simple. [2] However, in the emerging field of complex materials, we must look even further in the nanometer and even atomic scale regime for controlling the desired properties. Complex engineered nanometer structures are used everyday in computer chips. [3] On an atomistic level, it could be shown that high dielectric and thermoelectric properties are controlled by the inhomogeneity in PbTe and $AgSbTe_2$. [4] These materials are not homogeneous, but instead have domains with variations in Ag and Sb concentrations. These extraordinary properties result from competing forces at the atomic scale. The material's structure reflects these conflicting forces resulting in the formation of aperiodic or disordered structures. While most often these distortions are static, they can also move dynamically. These competing forces generate deviation from the perfect structure, but superficially the material may still appear with periodic crystallinity. In order to design and understand materials with these special properties, precise knowledge of this very complex atomic structure is required. The standard techniques to study these functional materials, and the drawbacks of these techniques, are highlighted in the following chapter describing gas adsorption in porous materials. Furthermore, a technique to overcome the obstacles is illustrated and how it can be applied to study other functional materials.

1.2 The importance of studying gas adsorption

Adsorption processes are not only important in separation, but also in catalysis. For example, an intermediate-term solution for decreasing the amount of CO_2 emitted into the atmosphere is to separate it and to safely store it. This can be done by capturing the CO_2 at a power plant, transporting it to an appropriate location, and pumping it into geological formations. This method is known as Carbon Capture and Storage (CCS). [5] There are multiple ways and stages in the process of a power plant where CO_2 can be removed. Traditionally, liquid sorbents, primarily based on amines, are used to extract CO_2 from flue gasses. [6] While this technique is quite efficient, its drawbacks include solvent loss and degradation as well as corrosion of the equipment. One of the most promising alternative methods is called oxy-combustion. With this method, air is separated into its components and oxygen, with a very high purity, is directly injected into the combustion chamber with the fuel. The exhaust from the combustion chamber contains highly concentrated CO_2 and can be directly used for underground storage. There are a number of methods to separate air into its components such as membrane techniques as well as the still most prevalent cryogenic air separation. A promising new technique, based on gas adsorption with solid materials, is called Pressure Swing Adsorption (PSA). [7] This technology uses solid sorbents and has the capability of generating the oxygen in the required purity and amount needed for oxy-combustion.

The implementation of CCS-systems decreases the energy output of a power plant and, therefore, also increases the cost of electricity. In order to influence the process as little as possible the production cost of oxygen needs to be reduced. There are two approaches to do that: improving the process itself (engineering approach) or improving the adsorption step (materials approach). In order to improve the process engineering, methods such as decreasing the adsorption/desorption-cycle time have been applied. [8] However, this approach has limitations and the cycle time can only be decreased to a certain amount due to heat and mass transfer constraints within the material. The more efficient approach to improve the PSA process is to enhance the adsorption step. Improving the adsorption process within the material for oxygen production involves the improvement of the interaction between the gas phase (adsorbate) and the solid phase (adsorbent). In order

to do that, the precise interaction between the gas and solid phase must be understood. Hence, the locations within the structure with the highest probability for adsorbed gases must be determined and how the adsorption process influences the structure. Once this has been achieved, the synthesis and development of new materials can specifically be targeted. Taking this into consideration enables the creation of highly efficient adsorbents. Not only are solid-gas interactions part of gas separation, but also a crucial part of the even more industrially important process of heterogeneous catalysis. For example, out of all processes in the chemical industry, about 85% involve at least one catalytic step and out of this share, about 80% involve heterogeneous catalysis. [9] This contributes over one trillion dollars to the national gross domestic product in the United States alone. [10] Therefore, understanding the underlying fundamental principles of gas adsorption will further increase the specificity and efficiency of catalytic processes, further decrease the amount of energy being used, and consequently the level of carbon emissions.

Adsorption in porous materials

To offer the highest capacity for adsorption, potential materials should offer a high surface area. Porous materials exactly fulfill this criteria and are ideal candidates for adsorption since they do not only have a high outer surface but also excel due to a high degree of inner surface where adsorption can take place. There are several groups of porous materials with different levels of rigidity. [11] The currently most used porous materials range from purely organic substances [12], such as carbon molecular sieves, to purely inorganic materials, such as zeolites [13]. Several groups with constantly growing importance are situated between these two end members, for example, metal organic frameworks (MOFs) [14] and Zeolitic Imidazol Frameworks (ZIFs) [15]. One example, from the group of inorganic materials, used industrially on a large scale, is lithium exchanged zeolite X (LiX). [16] It offers one of the highest capacity and selectivity for nitrogen adsorption over oxygen. In zeolites, the adsorption sites are thought to be mainly the extra-framework cations. Indirect correlations between these cations and adsorption behavior have been assessed by measuring, for instance, isosteric heats of adsorption. [17] For oxygen production from air, the other components, mainly nitrogen, need to be selectively absorbed in zeolite while oxygen does not

interact with the material. The assessment of these direct site interactions of nitrogen with cationic sites, has been also theoretically predicted by density functional theory (DFT) simulations and Grand Canonical Monte Carlo simulations (GCMC). [18] These cation positions are well defined positions within the structure of a zeolite due to the high crystallinity and periodicity of its structure. This makes LiX a well suited system to study the adsorption sites within the crystal.

Analytical Techniques to characterize adsorption sites

To determine adsorption or reaction sites, it is necessary to characterize the binding of adsorbed molecules on the surface and in the pores, as well as how this process leads to modifications of its structural environment. For example, in order to study simple catalysts, surface sensitive techniques are ideal. Characterization techniques can be considered surface sensitive if the detection of the signal comes from the outer layers of the sample. Electrons, ions, and photons travel a relatively short distance in materials which makes them sensitive for studying surfaces. Since most of chemical reactions or adsorption processes occurring on simple catalysts happen on their surfaces, these aforementioned techniques would be very useful. However, the limited mean free path of those particles requires the measurements to be done under vacuum. This hinders the ability to study these materials under real reaction conditions, such as exposure to flowing gases or liquids. [19] Many papers have been published demonstrating techniques to study reactivity and mechanics of reactions. For example, *operando* infrared (IR) studies give information about the chemical change of reactants interacting with catalytic surfaces. [20] However, IR gives limited information about the solid catalyst. This gets even more complicated when adsorption processes or reactions do not just occur on the outer surface of a catalyst, but also inside the material. Therefore, for determining the adsorption sites in a zeolite, crystallographic information has to be acquired through diffraction techniques. Analytical probes, based on diffraction, can also penetrate materials and observe processes on and in the material. To determine the crystal structure of a solid-state material, usually, single crystal diffraction techniques are used. However, very often crystals cannot be grown as a single crystal nor in a size that is sufficient enough for certain measurements. In such cases, powder diffraction is the method of choice. The standard technique to study a crystal is X-ray pow-

der diffraction. To find the gas adsorption sites it is important to find the extraframework cation sites first. To find the lithium positions in the aforementioned sorbent LiX, X-ray scattering faces limitations since lithium, similar to other light elements, has a rather small X-ray scattering cross section. However, when neutrons are used instead of X-rays, scattering experiments can also detect lighter elements such as nitrogen or hydrogen which are not readily accessible with X-rays. While neutron scattering can detect all elements, the most commonly used crystallographic analysis still faces some limitations. For example, a neutron powder diffraction study done by Feuerstein *et al* has shown that, even with neutrons and crystallographic analysis, it is difficult to find all the extraframework cations in the zeolite structure. [21] The number of cations determined by neutron scattering differs from the one found by solid-state NMR and chemical analysis. One reason for the inability to find all lithium atoms and sites is its relative high neutron absorption cross section compared to other elements such as calcium.

After having determined the position of extra-framework cations, the adsorbed species need to be located. Neutron diffraction has also shown success in locating the positions of adsorbed molecules in zeolites such as pyridine in gallosicilate-L [22], xenon in zeolite-rho [23], and benzene in zeolite Y [24]. In the example of NaY, benzene was adsorbed at 4 K as well as room temperature. Crystallographic analysis determined the atomic positions of the benzene molecule. However, this method averages over the entire crystal. Averaging poses a problem since not all extra framework cation sites have an adsorbed benzene molecule. The adsorbed molecules are randomly distributed throughout the crystal and lead to a shift of the sodium positions into the void space of the structure. Therefore, it is not possible to determine the exact positions of the sodium ions in the zeolite with the cyrstallographic method since some of them are shifted due to adsorption while others are still in their initial position. The crystallographic method gives an average sodium position for this scenario since it only finds the long range order of the material. Therefore, crystallography is not the most appropriate technique for determining the atomic positions of irregularly arranged molecules such as adsorbed nitrogen.

1.3 The importance of studying the local structure

To improve and predict the properties of materials, we must fully understand their structure. The way we usually study the structure of crystalline, solid-state materials is through conventional crystallographic diffraction methods and structural refinements as the one developed by Rietveld. [25] The crystallographic method dates back hundred years to the discoveries made by Laue [26] and the Braggs [27] in 1913. Nowadays, crystallography can even solve protein structures with thousands of atoms. [28] A symmetric structure is a prerequisite for this technique. While symmetry is even missing in perfect crystals due to thermal motions, these small variations can be sufficiently corrected for with the Debye-Waller approximation. However, this approach does not work anymore once the sample is not crystalline, the particle size is very small, or when the structural order extends only over a short range. [29] For example, in nanocrystalline materials, the peaks in the diffraction pattern become very broad and diffuse. Peak broadening can be described with the Scherrer approach to study crystallite sizes. [30] This works well for larger crystallites, but once the size is decreased down to a few nanometers, it fails to describe the diffraction line-shape. Hence, as was pointed out in the previous section, crystallography is not an appropriate tool for studying adsorption when the material lacks periodicity or the moiety of interest is not regularly ordered. An analytical technique allowing to obtain information on the short-range and the long-range order is Total Scattering and the Pair Distribution Function (PDF) analysis.

1.4 Total Scattering and PDF analysis

Through total scattering we can access structural information for materials with different levels of order ranging from complete periodicity to completely amorphous. The terminology *Total Scattering* is based on the fact that the collected coherent scattering intensity, measured over a wide range of momentum transfer (Q), includes Bragg peaks (representing the average structure), the elastic diffuse scattering (representing the static local structure), and the inelastic diffuse scattering coming from atomic motions. Hence, it allows the extraction of structural information from liquids, glasses, amorphous materials, nanocrystalline and disordered materials, in addition to crystalline

structures. Total scattering can be done with X-rays, neutrons, as well as electrons. To analyze total scattering data, we use the atomic pair distribution function (PDF) analysis.

While not widespread yet, PDF is not a new analytical technique. Its origins lay in the Debye scattering equation published in 1915. [31] After deriving the Fourier relationship between real-space pair density and the Debye scattering equation, the PDF was born. [32] Shortly after that, this method was introduced for studying liquids and glasses [33–35] but also particularly for studying carbon compounds [36, 37]. For example, Zachariasen used this method to study the short range order of solvent molecules. [38, 39] In the mid 1980s, the first synchrotron PDFs were collected at the Cornell High Energy Synchrotron Source (CHESS) and the National Synchrotron Light Source (NSLS) at Brookhaven National Laboratory. [40, 41] The reason for not being widely harnessed for investigating more crystalline materials up until 70 years later, was based on the instrumental restrictions. The main roadblock was the wavelengths of the radiation. Reactor sources and early generations of synchrotrons did not provide the desired short wavelengths. [42] Additionally, disordered structures require intensive data modeling which is computationally demanding. The access to better computers and the availability of the appropriate software made it more readily available for the scientific community. PDF has since been used in a wide range of disordered and nanocrystalline applications. [43–45] Another milestone was achieved with the currently lowest detection limit achievable with PDF, which was shown to be 0.25 wt%, for organic nanoparticles in aqueous solution in 2015. [46] While 0.2 wt% was previously achieved for CdSe nanoparticles, defining a generic limit is imprecise and other factors such as the type of compounds need to be taken into consideration. [47] Considering that organic substances are weak scatterers, 0.25 wt% is definitely an improvement in sensitivity.

To make inferences about the structure-property relationships, we do not necessarily need the absolute positions of the atoms. What drives the properties are the relative positions of atoms in close proximity where they can interact with each other. To phrase it differently, the local atomic environment and the relative positions of the nearest-neighbor atoms is most important in making inferences about the properties. This is precisely what the PDF does; it presents a one-dimensional

histogram showing the scaled probability of finding pairs of atoms separated by the distance r. The PDF, G(r), is experimentally determined and gets calculated from the corrected and normalized total scattering structure function, S(Q), via a truncated Fourier transform. First, to obtain S(Q), the self-scattering is removed from the coherent scattered intensity per atom, I(Q), followed by dividing it by the average squared atomic scattering factor, $\langle f(Q)^2 \rangle$. [42]

$$S(Q) = \frac{I(Q) - \langle f(Q)^2 \rangle}{\langle f(Q)^2 \rangle} + 1$$

The reduced pair distribution function is attained from the Fourier transform of the reduced total scattering function, F(Q), derived from normalizing the total scattering function by multiplying it by Q. [48]

$$G(r) = \left(\frac{2}{\pi}\right) \int_{Q_{min}}^{Q_{max}} Q[S(Q) - 1] \sin(Qr) dQ \quad = \quad \left(\frac{2}{\pi}\right) \int_{Q_{min}}^{Q_{max}} F(Q) \sin(Qr) dQ$$

Q is the magnitude of the scattering momentum and is dependent on the incident wavelength of the radiation used, λ, and the scattering angle, θ. For elastic scattering it is calculated as follows:

$$Q = \frac{4\pi \sin(\theta)}{\lambda}$$

The experimental setup determines the values of Q_{min} and Q_{max}. The aim is to have the highest possible Q_{max} value. However, the actual value for Q_{max} is usually chosen based on experimental limitations. [49]

After having calculated the experimental PDF, it can be analyzed directly, for instance, by visual inspection, or indirectly by structural modeling. A underappreciated method is to simply visually compare experimentally generated PDFs from different samples or samples under different conditions. [50] This way the length of correlations can give insight on particle size, or help to differentiate between an amorphous or crystalline structure. For example, taking the PDF of Ni powder shows long range order by pair correlations up to high r-values. [51] Contrary, the PDF of a nanoparticle generates only G(r) values to a limited r-range and shows missing long range order. This is based on only well defined intra-particle correlations up to the furthest distances

of its atoms. Atomic inter-particle correlations are too far apart and too diffuse to be visible in the PDF. Further, calculating differences between PDFs and determining the residual signal can provide valuable information.

Another way to analyze the PDF is by structural modeling where parameters such as the lattice parameters, atom positions, and anisotropic atomic displacement parameters can be refined. An alternative way to calculate G(r), particularly used for fitting the G(r) derived from a known structural model to the experimentally determined one, is illustrated below:

$$G(r) = 4\pi r[\rho(r) - \rho_0\gamma_0]$$

$$\rho(r) = \frac{1}{4\pi r^2 N}\sum_i \sum_{j\neq i} \frac{b_i b_j}{\langle b\rangle^2}\delta(r - r_{ij})$$

ρ_0 describes the average number density in they system of N atoms, ρ is called the microscopic pair density or the atomic PDF, and γ_0 is the autocorrelation function of the particle shape. The sums in $\rho(r)$ include all atoms in the sample, b_i is the scattering factor of atom i, b_j is the scattering factor of atom j, $\langle b\rangle$ denotes the average scattering factor, and r_{ij} is the distance between each pair of atoms i and j.

1.5 Harnessing PDF's capabilities for finding new energy materials

PDF has provided valuable insights in different energy materials. One way to tackle the energy problem is by investigating carbon dioxide neutral energy sources such as nuclear power. While current nuclear reactors are based on light water (LW) for energy transfer, the next generation system is proposed to work with molten salts. [52] Using molten salts has been a well established procedure in material synthesis for solvation [53] as well as for heat transfer in concentrated solar power plants [54, 55]. A molten salt reactor would make use of both aforementioned applications which poses several advantages over LW such as higher electrical generation efficiency, no danger of fuel melting, no steam generation in the reactor reducing the risk of steam explosion, and less than 1% of LW reactor long-lived high-level radioactive waste. [56] However, in a similar fash-

ion as with porous materials, to optimize the functionality of the salt mixtures in these reactors, the structure-property relationships need to be understood. This requires a detailed study of the processes occurring in the molten salt. As discussed above, a highly disordered system such as a liquid cannot be studied with standard crystallographic techniques and total scattering needs to be considered. This led to a proposal, titled "*Ab-initio* and Experimental Determination of Solvent & Solute Structure and Property Effects in Molten Salts", in collaboration with Los Alamos National Laboratory and University of Wisconsin to shed more light on the chemistry happening in these disordered mixtures. As an initial structural model served results from *ab initio* molecular dynamics simulations [57] and with the help of the R.I.N.G.S. code, the predicted neutron scattering signal could be computed [58]. While molten salt reactors are a step into the right direction, there is still the problem of radioactive waste.

The preferable solution to our carbon emissions is renewable energy sources. Despite a plethora of options, harnessing the abundance of sun light, and the amount received on the earth's surface per day, indicates the highest potential for alternative energy generation. [59, 60] The direct energy conversion of radiation into electricity can be done through the photovoltaic (PV) effect. There, the incident photons, being absorbed in the photovoltaic material, excite an electron into the conduction band while consequently leaving a hole behind. The time of when the electron-hole pair recombines is a figure of merit when considering the efficiency of a PV material. Another determining factor is whether a PV material has a direct or indirect band gap. Currently, our commercially available photovoltaic devices are based on silicon. While silicon has advantages such as low production cost, it also has drawbacks like an indirect band gap of 1.12 eV. [61] A photovoltaic absorber with an indirect band gap requires larger amounts of material for producing devices. These are just a few examples highlighting the need for the development of new semiconducting materials for PV applications.

A quickly rising-star PV material has been based on the perovskite structure. Perovskite halides have shown promises to be inexpensive and highly-efficient semiconductors that can be used for PV devices. With the benchmark efficiency for perovskite cells currently being at 25.2% [62], this

material is in the same efficiency range as commercial Si based cells. Further, the possibility to produce these materials from solution, instead of the very energy demanding process for Si production [63], has opened multiple doors allowing, for example, easy thin film production. [64–66] The softness and plasticity of this material links it to the previously mentioned framework materials. Based on the type of perovskite structure, and the connectivity of the structural octahedral units, different direct comparisons can be made ranging from zeolites to metal-organic frameworks. Similarly to other complex materials, the unique PV properties of this new group of materials is not based on a highly ordered, periodic structure. Pair distribution function analysis has been providing valuable information on the disordered local structure of these perovskites. [67–70]

While the above mentioned use of PDF has been mainly used for studying neat material, more recently it has also provided information on material under working conditions. For example, PDF analysis has been used for studying fuel cells *in situ* such as particle size changes of the Pt/C and PtCo/C catalyst at the cathode of a proton exchange membrane fuel cell. [71] Similarly, highly complex nanoalloy catalysts for fuel cell applications, such as nanowire shaped platinum-iron alloys, could be characterized with total scattering. [72] Not only the increasing amount of portable devices and higher standards for power density, but also the intermittent nature of energy sources as, for instance, wind and solar requires new materials for energy storage. Hence, the field of battery research has also found the PDF analysis as a valuable tool for elucidating structure-property relationships. [73,74] While there are many more possible applications for total scattering, this introduction has illustrated its potential for describing the structure of even very complicated materials and why its proliferation can have a big impact on our society and the way we live.

1.6 Summary of the Materials Chemistry Part of the Dissertation

The following body of work aims to highlight how the study of the local structure can provide valuable insight to understand and describe the structure-property relationship of solid-state materials. The following five chapters can be broadly broken into two distinct sections covering

a) adsorption and reaction in porous materials, and b) structure-property relationships in hybrid organic-inorganic halide perovskites.

Chapters two and three are focused on the design and commissioning of a new dynamic gas flow cell at the Spallation Neutron Source. Chapter two describes the need for studying adsorption processes and catalytic reactions under industrially relevant, operational conditions and how our approach of combining a Steady-State Transient Isotopic Kinetic Analysis (SSITKA) with neutron total scattering can overcome current limitations faced by analytical techniques in this field. It further illustrates the new sample environment used for our proof of concept system of studying nitrogen adsorption in calcium exchanged zeolite X. With data acquired from neutron scattering and SSITKA, the number of adsorbed nitrogen could be determined. Initial results regarding the adsorption sites and lattice breathing effects were found. Chapter three provides an in depth explanation about the neutron data reduction and the analysis of the dynamically acquired data. To support the results from our neutron scattering experiments, adsorption isotherms were measured and its results were supported by theoretical considerations from Grand Canonical Monte Carlo simulations. This chapter also shows that the lack of sufficient neutron counting statistics limits further detailed studies of adsorption kinetics occurring on individual sites within the porous framework.

Chapters four and five illustrate how a large box approach, such as Reverse Monte Carlo (RMC) modeling, can be a useful tool for describing total scattering data. RMC is helpful, in particular, for materials with a high number of degrees of freedom and where specific structural elements need to be treated as rigid bodies. Chapter four shows how the results from X-ray based RMC modeling were used to determine anharmonic lattice dynamics arising from octahedral tilting and Cs^+ displacements in the end members of the vacancy-ordered double perovskites $Cs_2Sn_{1-x}Te_xI_6$. It is further highlighted how semi-rigid body RMC can improve the fitting results compared to traditional, fully atomistic RMC methods. In chapter four, RMC was used to model the neutron and X-ray total scattering data of the vacancy-ordered double perovskite methyl ammonium thin iodide. This was done to find the tilting of the inorganic octahedral framework and to find the

preferred orientations of the organic methyammonium (MA) cations and their interplay. Since the RMC method does not result in a unique structural solution, a high-throughput approach was generated to confirm the results based on statistics. Furthermore, an *ad hoc* computational code was developed which allows to extract not only the overall orientations of the organic and inorganic species, but also the description of the individual alignment of a single octahedra and the nearest neighbor MAs.

The final chapter outlines possible future work stemming from the above described studies as well as preliminary results. It is drawing from knowledge and experience gained from the experimental and the computational work. The goal of the study is to locate the theoretically predicted active sites of the CysamNO decomposition reaction in the metal-organic framework CuBTTri as well as to confirm them experimentally under working conditions with total scattering. As a first approach, density functional theory (DFT) was used for structural optimization of the MOF. While DFT is a good tool for optimizing the empty MOF, this chapter explains why it fails for our system of choice and what other methods should be used to study the theoretical adsorption sites. Initial experimental data, acquired from in house X-ray total scattering, requires sophisticated modeling methods to describe the empty MOF structure. Experience gained from the previous high-throughput RMC modeling will be important for structural modeling of the disordered MOF.

The appendices for this part of the dissertation contain supplemental information including more details on some experimental procedures, as well as additional tables and figures.

Chapter 2

A high precision gas flow cell for performing in situ neutron studies of local atomic structure in catalytic materials [1]

2.1 Introduction

Catalysts contribute over one trillion dollars to the national gross domestic product in the United States [10], and yet specifics of chemically reactive atomic environments remain almost entirely out of reach by traditional structural probes due to their aperiodic and transient nature. Current studies require either specialized conditions (e.g., high vacuum [75]) or sample preparation (e.g., 4-D electron microscopy [76]). Time-resolved X-ray pair distribution function (PDF) studies have been shown to elicit changes in the local bonding environment of solids during chemical reactions and without a need for crystalline periodicity [77–81]; yet these methods offer limited specificity to the chemical constituents or the interface. The emergence of high flux neutron PDF studies provides opportunities to probe oxide, hydride, and other light atom bearing surface species in functional materials [82–84], with isotopic contrast allowing further precision in chemical specificity through differential PDF analysis [42, 85–87]. At the same time, a powerful technique for revealing kinetic- but not structural- information has evolved with steady-state isotope transient kinetic analysis (SSITKA) [88], involving isotope-exchange experiments. The primary outcome from traditional SSITKA experiments following gas adsorption is the total number of adsorbed molecules in the steady-state, which can be used to derive heats of adsorption and understand the

[1] Substantial portions of this chapter have been reproduced with permission from D. Olds, K. Page, A. A. Paecklar, P. F. Peterson, J. Liu, G. Rucker, M. Ruiz-Rodriguez, M. Olsen, M. Pawel, S. H. Overbury, and J. R. Neilson, *Rev Sci Instrum*, **2017**, 88 (3), 034101. ®2017 the American Institute of Physics

role of chemical composition in reactions and time-dependent gas-specific residencies. More complex kinetic relationships can be elucidated from these methods with the aid of atomistic modeling.

In this contribution, we present a new sample environment tested at the Nanoscale Ordered Materials Diffractometer (NOMAD) beamline [89] at the Spallation Neutron Source (SNS) which allows for precise *in situ* gas flow reaction studies during neutron total scattering measurements. This gas flow cell allows for studies on small volumes of sample (roughly 1 cm^3 of material) which are dosed with a highly-controlled flow of gas at precisely specified rates and partial pressures. A high-speed switching valve in the system allows for fast transitions between dosing gasses. A residual gas analyzer (RGA) continuously monitors exhaust gasses downstream from the sample, and direct encoding of all sample conditions in data streams allows for time-dependent studies of reaction kinetics such as *in situ* SSITKA. We present the design elements and an example study on N_2 adsorption herein, along with a list of anticipated applications.

A residual gas analyzer (RGA) continuously monitors the exhaust gases downstream from the sample and encodes this data in parallel with the event-based diffraction, along with all other pertinent information about the state of the system (valve positions, flow rates, pressures, temperatures, ect). As this information is recorded directly into the metadata of the NeXus files [90] used for powder diffraction data reduction, we can utilize the Mantid data analysis framework [91] to reduce the scattering data via advanced event-based methodologies. Such a comprehensive integration of software and hardware allows for novel uses of the gas flow sample environment, such as pulse probe studies, looping, and SSITKA.

2.2 Experimental and theoretical methods

Note on author contributions: This chapter was published in the *Journal Review of Scientific Instruments*, **2017**, 88 (3), 034101, DOI: 10.1063/1.4978287 by Daniel Olds, Katharine Page, Arnold A. Paecklar, Peter F. Peterson, Jue Liu, Gerald Rucker, Mariano Ruiz-Rodriguez, Michael Olsen, Michelle Pawel, Steven H. Overbury, and James R. Neilson. DO was involved in measuring the neutron scattering data as well as the SSITKA data, assembling the dynamic gas flow rig, and

wrote the initial draft of the manuscript. KP was involved in measuring the neutron scattering data, conceived the project, and supervised the project at ORNL. AAP prepared and analyzed the zeolite material, was involved in the assembling of the dynamic gas flow rig, the measuring the neutron scattering data, initial neutron data analysis, and the collection and analysis of the SSITKA data. PFP developed the software for integration and combination of SSITKA data and neutron total scattering data the MANTID framework. JL did the Rietveld refinements in TOPAS. GR supported the gas flow assembly and integration into the NOMAD instrument. MR implemented the software for controlling the gas flow rig into the instrument computer system. MO did all the glass blowing work and prepared all the pieces for the sample environment. MP helped with the SSITKA measurements at the CNMS. SHO provided valuable information on the SSITKA measurements as well as supervised the work done at the CNMS. JRN supervised the project and all the work done at CSU. All authors contributed to editing and finalization of the manuscript.

2.3 Gas Flow Cell Design

The gas-flow cell is designed to deliver specified pressure and flow rate through small samples, with the ability to very quickly transition between two gas species which differ in either chemical interactivity or neutron scattering power (different isotopes). The change between these two gasses must occur quickly, yet minimize the effect on the physical flow rate and pressure at the sample position. Also critical to the system design is the integration of an RGA following the sample, such that adsorption or reaction processes can be directly measured contemporaneously and in parallel with diffraction data. The data from the RGA must be simultaneously encoded with the diffraction data, such that novel reaction-dependent reduction procedures may be utilized *ex post facto*.

A design schematic for the gas-flow cell is shown in Figure Figure 2.1, with associated images of several components shown in Figure Figure 2.2. NOMAD is a top-loading instrument, and as such, the sample environments are typically designed so that they can be lowered into the standard sample well at the neutron beam position. The high-speed 4-way switching valve (VICI, model ED44UWE) is controlled via a 2-position microelectric valve actuator (VICI, model

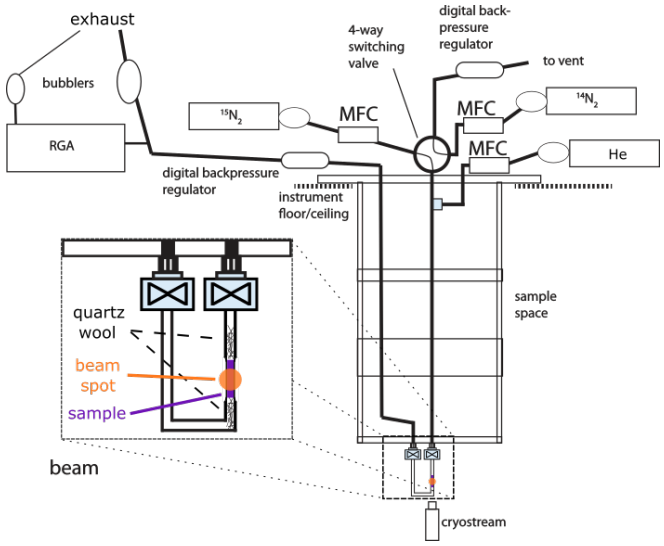

Figure 2.1: Schematic of flow-cell plumbing on NOMAD as it was configured for the presented commissioning experiment. Shown are the 2 dosing gas supplies, $^{14}N_2$ and $^{15}N_2$, as well as the carrier gas, He. Following each supply is a mass flow controller (MFC), with digital back pressure regulators also shown. The 4-way switching valve, RGA, Ar cryostream, and optional bubbler systems leading to the neutron activated gas exhaust lines are also shown. An inset highlights the geometry of the quartz U-tube sample cell, with associated isolation valves, quartz wool, and the sample position relative to the beam.

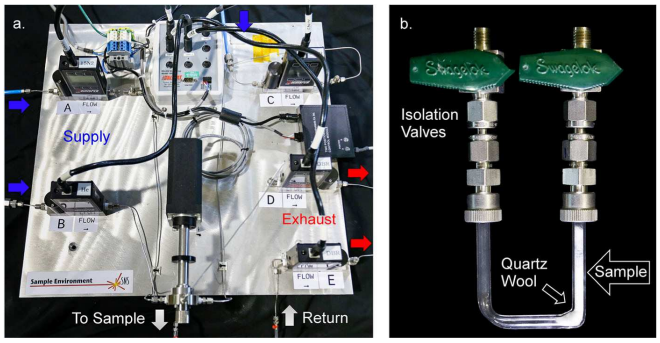

Figure 2.2: (a) Image of the flow controlling apparatus and (b) U-tube style sample cell. Annotated on the apparatus (a) are the gas supply points (blue) which lead directly to mass flowcontrollers. Also shown is the line to the sample, and returning (white), as well as subsequent back pressure regulators and exhaust lines (red). The mass flow controllers are labeled as "A," "B," and "C," while the digital back pressure regulators are labeled "D" and "E." The U-tube style sample cell (b) shows the sample, quartz wool plug below the sample, and sample isolation valves.

E2CA), which can be activated manually or automatically with a desired switching frequency (e.g. switching dosing gasses every 6 minutes). In this way, one dosing gas is always flowing towards the sample, while the other is being vented to system exhaust. This way, the steady-state condition is maintained. The flow of these two dosing gasses is controlled upstream of the switch by a set of low-pressure drop mass flow controllers (Alicat Scientific, MCW-10SCCM-D). Directly downstream of the switch is a carrier gas port, such that an additional (typically inert) gas may flow continuously with the selected dosing gas. The carrier gas flow is controlled via a separate upstream mass flow controller (Alicat Scientific, MCW-50SCCM-D). Downstream of the sample, a digital back pressure regulator (Alicat Scientific, PC-15PSIG-D) controls the net pressure seen at the sample, independent of the specified flow rates. Note that an identical digital back pressure regulator is installed on the exhaust-side of the high-speed switch, such that any fluctuations in pressure due to the action of physically switching between dosing gasses can be minimized. Downstream of both the sample and back pressure regulator, but prior to exhaust vent, an RGA (Stanford Research Systems, UGA200) measures the mass profile of the exhaust gas as it comes off the sample. An optional bubbler system can be installed before exhausting to atmosphere or the neutron activated gas exhaust system at NOMAD. The entire system is plumbed predominately with 1/16" OD, 0.30" ID stainless steel tubing, the lengths of which have been minimized in regards to the NOMAD geometry to facilitate fast transitions between dosing gas species. Swagelok fittings were used to connect the majority of components.

The sample cell itself is a custom made quartz "U-Tube" design utilizing stainless steel-to-quartz adapters (Larson Electronic Glass, model SQ-025-T) directly attached to Swagelok valves, such that a sample may be isolated from atmosphere during the mounting and handling procedures. The NOMAD beam is typically collimated to an area of 1.5 cm $\times$ 1.5 cm at the sample position. The quartz tube in the sample cell narrows directly prior to the beamspot to the dimensions of OD 5.0 mm and ID 4.62 mm (Wilmad 507-PP-7QTZ), minimizing the background contributions to the diffraction data.

An alternative static gas-dosing sample cell is also available, which utilizes the high-precision gas flow instrumentation to dose a sample with a controlled partial pressure of a gas, but does not actively flow the gas through a sample during the diffraction measurement. The sample cell for such a configuration is a sealed quartz tube (Larson Electronic Glass, SQ-018-T) which is connected via a T-section to the flowing gas line between the supplying mass flow controllers and the back pressure regulators. Once a desired dosing gas environment is established, a valve on the sample cell is closed to isolate the sample, thus establishing a static environment.

Under normal operation, the system has a maximum operating pressure at the sample of 15 psig. The two dosing gasses can flow precisely up to 10 mL/min, while the carrier gas flows precisely up to 50 mL/min, in both cases with an accuracy of $\pm 0.4\%$ of reading $\pm 0.2\%$ of full scale. The RGA regularly tracks 4 distinct gas species over approximately 1 second, although more can be tracked with an associated proportional increase in scan-time. The switching time of the high-speed valve is 425 ms. The sample temperature is controlled via an argon cryostream placed directly below the sample position (Oxford Cryosystems, Cobra Plus) which is capable of running at temperatures of 90 K to 500 K.

Samples to be measured must allow for the free flow of gasses at operating pressures, and as such are often pressed and sieved prior to loading to select for the optimal particle size. Due to the relatively small overall volumes associated with the plumbing used, we have found that with a flow rates of 20 mL/min with 1 psig back-pressure, a switch between dosing gasses will be detectable on the RGA within seconds. When a powdered sample is loaded, this response time will increase due to the delay introduced by the gasses physically transporting through the sample. For a 3 cm column of powdered sample, which had been pressed into pellets at 4 metric tons for 5 minutes, broken up and sieved to particle sizes between $100\,\mu\mathrm{m}$ and $500\,\mu\mathrm{m}$, the additional delay time at the above conditions was found to be approximately 50 seconds.

A mechanical flow delay will be introduced by the macroscopic characteristics of the powder composition (sample consistency, sample volume, flow rate, pressure), however this is separate from and in addition to any chemical interactivity or adsorption that may occur between the sample

and the flowing gas. In order to decouple any chemical reactivity in the time-dependent response from the mechanical flow delay, an inert gas may be mixed with one of the two dosing gasses such that a proper hold-up time can be established during data reduction. [92]

2.4 Commissioning Study: Nitrogen Adsorption in Zeolite-X

Commissioning experiments with the flow cell were completed on nitrogen adsorption by calcium exchanged zeolite-X. Zeolitic materials are commonly used for air separation by pressure-swing adsorption (PSA) [92] as well as for heterogeneous catalysis such as catalytic cracking [93] and in NH_3 synthesis as the catalyst [94] or as the support material for the catalyst [95–97]. By simultaneously performing *in situ* neutron total scattering and SSITKA,structure is linked to reactivity during isotope-contrasted adsorption on the Faujasite cage structure of the zeolite X.

2.4.1 Preparation of Sample

The $Na_{78-2x}Ca_xAl_{78}Si_{144}O_{384}$ samples were produced through ion exchange with sodium zeolite X (NaX) powder (Sigma-Aldrich molecular sieve 13X) following a conventional ion exchange technique [98, 99]. 1 g of ground NaX was dispersed in 100 mL of water, into which 1.5 g of calcium chloride dehydrate (supplied by EMD Chemicals Inc.) was added. This mixture was then heated over a boiling water bath for 24 hours followed by a filtration step through a Büchner funnel and a washing step with 100 mL of water. The material was dried on the filter at 90°C overnight. This cation exchange procedure was repeated twice in order to obtain the highest degree of exchange. The sample compositions were characterized using energy dispersive X-ray Spectroscopy (EDS) and optical emission spectroscopy with inductively coupled plasma (ICP-OES), both of which found the degree of cation exchange to be nearly complete for CaX, at 98% in the EDS and 97% in the ICP-OES. Laboratory powder X-ray diffraction revealed the samples to be highly crystalline. The morphology of the exchanged sample examined by scanning electron microscopy (SEM) remained unchanged by comparison with those observed for the parent NaX sample. To make the samples more suitable to gas flow measurements, the powders were pressed at 4 metric

tons for 5 minutes, and then broken up and sieved to form a powder with sizes between 250 μm and 355 μm. Prior to the neutron total scattering measurements, the samples were charged by drying them under vacuum while slowly heating to 400°C at a rate of 0.2°C/min. Samples were stored under vacuum prior to use.

2.4.2 Static Gas Loading Neutron Total Scattering Measurements

Static gas loading neutron total scattering measurements were preformed at room temperature on NOMAD. "Neat samples" under vacuum were measured in the static gas loading configuration for 2 hours. The samples were then dosed with $^{15}N_2$ flowing at 5 mL/min. The back-pressure at the sample was cycled between 1 and 5 psig to ensure complete dosing of the sample and dilution of any present contaminant gas (e.g $^{14}N_2$). The samples were sealed at 1 psig and measured for 2 hours at 300 K. The measured and fit diffraction patterns from these measurements are shown in Figure Figure 2.3.

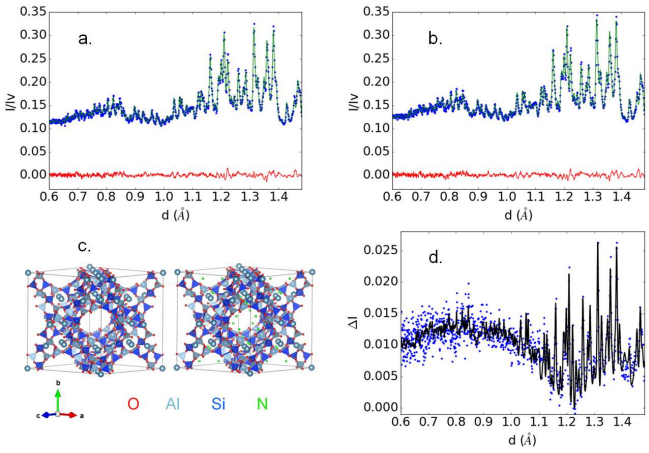

Figure 2.3: Results of Rietveld refinements on the 154° NOMAD detector bank data in the pristine (a.) and pressure dosed with nitrogen (b.) static loading cases. Data are shown in utis of counts normalized by vanadium scattering counts, I/I_0, as a function of d-spacing. The two resultant refined structures are shown, with and without nitrogen (c.), as well as the differences between the data and models (d.). For the Rietveld results, blue corresponds to the data, green lines are the fits, and the red line is the calculated residual. For the dosed minus neat difference curve (d.), blue represents differences between data and black represents differences between the models.

Fits to the data were performed using TOPAS refinement software [100], in which the Ca exchanged zeolite-X structure model was fit to both the neat and nitrogen dosed sample diffraction data. The refined parameters from these fits are summarized in table Table 2.1. Higher quality refinements were found possible in the dosed-sample case through the inclusion of nitrogen atoms, which were not required in fitting the neat data. The presented fits included data from NOMAD banks at 31°, 67°, 122°, and 154° 2θ angles. Limiting refinement to individual banks was found to effect the fit nitrogen occupancy levels, but in all cases was found to vary between 11% and 20%, a factor of 5-10 times greater than would be expected for free flowing (non-adsorbing) nitrogen at 1 psig and 300 K.

Note that the volume of the zeolite unit cell clearly contracts upon exposure to the nitrogen by approximately 2.3%, as would be expected during adsorption. Furthermore, the fit occupancy of nitrogen in the dosed case correlates to approximately 8 N-atoms per unit cell, well above the value expected if only free flowing gas was present (≈ 0.4 N-atoms per unit cell. We note that the occupancy of the nitrogen is strongly correlated to the atomic thermal parameter (b_{iso}). The results of this refinement demonstrate that neutron total scattering techniques are sensitive to the presence of nitrogen adsorption at pressures as low as 1 psig and room temperature, well below those pressures (CD_4 (9 bar) and C_2H_6 (5 bar) [101]) and above temperatures (Xe (210 K) [23], CD_4 (77 K) [102], $CHCl_3$ (20 K) [103] or CO_2 (4 K) [104]) used in previous gas loading measurements. The total scattering and resultant PDF datasets from the static loading measurements of the pristine and pressure dosed samples on NOMAD are shown in Figure Figure 2.4. Clear differences can be observed after the introduction of nitrogen to the system. In particular, the first peak in the difference curve of the PDF (Figure Figure 2.4(b), red) at $\simeq$ 1.1 Å suggests sensitivity to the N_2 pairwise molecular bond. The observed differences require further modeling to interpret.

2.4.3 In Situ SSITKA and Neutron Total Scattering Measurement

One aspect of the flow cell design is to allow for time-dependent kinetic studies of samples under steady-state conditions as well as pump-probe gas flow. To demonstrate this capability, we

Table 2.1: Results of refinements performed as shown in Figure 2.3. The refinements were performed by freeing all parameters with associated uncertainties.

Fit to neat data CSG = $Fd\bar{3}$, a = 25.002(2), $R_{wp} = 2.300\%$					
Atom	x	y	z	occ.	$b_{iso}(Å^2)$
Si(1)	-0.0522(4)	0.1244(5)	0.0345(5)	1.0	0.21(17)
Si(2)	-0.0584(4)	0.0353(5)	0.1215(5)	0.19	0.21(17)
Al(2)	-0.0584(4)	0.0353(5)	0.1215(5)	0.81	0.21(17)
O(1)	-0.1119(3)	0.0025(5)	0.1070(3)	1.0	1.40(18)
O(2)	-0.0043(4)	-0.0033(4)	0.1413(2)	1.0	1.40(18)
O(3)	-0.0349(6)	0.0646(5)	0.0654(5)	1.0	1.40(18)
O(4)	-0.0619(2)	0.0764(5)	0.1735(5)	1.0	1.40(18)
Ca(1)	0.0	0.0	0	0.73(28)	0.77(25)
Ca(2)	0.0620(6)	0.0620(6)	0.0620(6)	0.27(28)	0.77(25)
Ca(3)	0.2228(2)	0.2229(2)	0.2229(2)	0.80(37)	0.77(25)
Fit to dosed data CSG = $Fd\bar{3}$, a = 24.9942(2), $R_{wp} = 2.260\%$					
Atom	x	y	z	occ.	$b_{iso}(Å)^2$
Si(1)	-0.0527(4)	0.1246(4)	0.0356(4)	1.0	0.19(15)
Si(2)	-0.0586(4)	0.0339(4)	0.1206(4)	0.19	0.19(15)
Al(2)	-0.0586(4)	0.0339(4)	0.1206(4)	0.81	0.19(15)
O(1)	-0.1121(3)	0.0027(4)	0.1068(3)	1.0	1.33(16)
O(2)	-0.0043(4)	-0.0033(4)	0.1412(2)	1.0	1.33(16)
O(3)	-0.0351(2)	0.0648(5)	0.0653(4)	1.0	1.33(16)
O(4)	-0.0621(2)	0.0763(4)	0.1736(4)	1.0	1.33(16)
Ca(1)	0.0	0.0	0.0	0.73	0.80(18)
Ca(2)	0.0634(5)	0.0633(5)	0.0633(5)	0.27	0.80(18)
Ca(3)	0.2238(2)	0.2238(2)	0.2238(2)	0.80	0.80(18)
N(1)	0.3030(1)	0.3030(1)	0.3030(1)	0.21	5.30(1.1)

performed *in situ* SSITKA measurements with simultaneous neutron total scattering. Here, the two dosing gasses were $^{14}N_2$ and $^{15}N_2$, where the $^{14}N_2$ was mixed with 3% Ar to act as an inert tracer gas in the SSITKA measurement to determine the gas-phase hold-up time. Helium was used as an inert carrier gas. Approximately 1 cm^3 of the fully charged material, prepared as described above, was loaded into the gas flow cell. Steady-state flow and pulse-probed SSITKA were performed, in each case with 1 mL/min dose gas and 20 mL/min carrier gas with the pressure at the sample held at 1 psig. During the SSITKA measurements, the switch time between dosing gasses was set to 6 minutes and the complete cycle between the two isotopes was performed 12 times for a

total measurement time of ≈ 150 minutes. The averaged results of the SSITKA measurements are shown in Figure Figure 2.5.

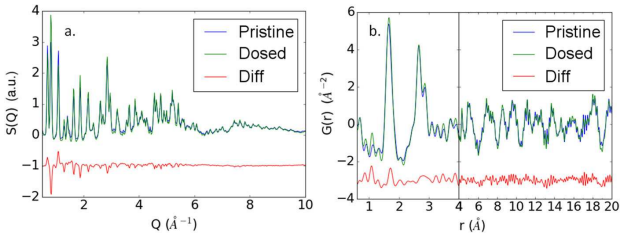

Figure 2.4: (a) The total scattering structure factor, S(Q), presented as a function of momentum transfer, Q= 2d sin α and (b) associated PDF, G(r), from the static loading measurements on NOMAD. Shown in each plot is the pristine (blue), $^{15}N_2$ pressure dosed (green) data, as well as the offset difference between them (red). Below 4 Å, in the PDF (b), the scale of the r-axis is increased to emphasize changes in local structure.

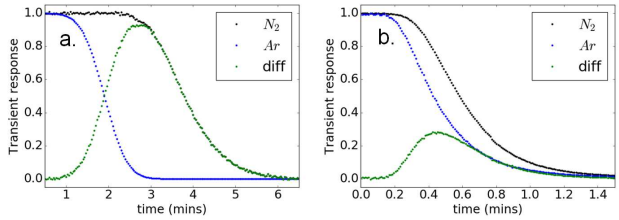

Figure 2.5: A comparison of the developed flow cell SSITKA (a) with the results from commercially available SSITKA measurements (b), showing responses from nitrogen, argon (tracer), and their difference. Nitrogen, argon, and difference gas responses are shown with black square markers, purple triangle markers, and orange circle markers, respectively. The analysis of nitrogen residence times and associated occupancy is shown in Table 2.2 below.

The two most general parameters determined in a SSITKA experiment are the surface concentration of adsorbed nitrogen molecules, N, and the average surface residence time, τ. [105] The latter one was calculated first by integrating the area between the normalized transient response of the $^{14}N_2$ nitrogen isotope and the normalized transient response of the inert tracer argon. The surface concentration of the nitrogen was determined by multiplying the average surface residence time by the total flow rate in the system. To better correlate this value to crystallographic information, the number of nitrogen molecules per unit cell needed to be determined based on the surface concentration. The results of the SSITKA were found to be comparable to the offline commercial

Table 2.2: Results of SSITKA analysis from the curves shown in Figure 2.5 below. Note that differences between the two samples can be attributed to a more thorough charging procedure performed for the *in situ* samples, leading to a more reactive sample.

SSITKA Results	Offline	*in situ*
Total pressure (atm)	1.097	1.055
Total flow rate (mL/min)	34	21
Nitrogen flow rate (mL/min)	5	1
Argon concentration	5.4%	3%
Temperature (K)	303	298
Surface residence time (sec)	8.72	118.46
Adsorbed N_2 (μmol/g)	295.12	394.69
Density of sample (g/cm^3)	1.93	1.93
Nitrogen atoms per unit cell	5.36	7.17

SSITKA measurements performed on the samples. As this information is recorded directly into the metadata of the NeXus files [90] used for powder diffraction data reduction, we utilize the Mantid data analysis framework [91] to reduce and analyze the scattering data via advanced event-based methodologies. Such a comprehensive integration of software and hardware allows for novel uses of the gas flow sample environment, such as pulse probe studies, looping, and SSITKA.

The results of the neutron total scattering measurements during the *in situ* SSITKA measurements are also shown in Figure Figure 2.5. With this limited data set, the measured results from the flow cell are consistent with the corresponding static gas-loading data.

2.5 Conclusions

A high-precision gas flow cell sample environment has been developed for neutron total scattering measurements at the SNS. Combined with the intense neutron flux available at the NOMAD instrument, novel opportunities to directly address the interactions between gas-solid interfaces are now possible. A commissioning experiment on N_2 adsorption in zeolite-X combined *in situ* neutron diffraction and SSITKA measurements. Of important significance, the effect on the overall lattice structure and the adsorption location of N_2 were identified at 300 K and 1 atm, in line with operational conditions of the material, and in striking contrast to the conditions of previous studies. The gas flow cell with in-line RGA, neutron diffraction, and neutron PDF capabilities

is a versatile sample environment that will aid in identifying structural responses, characterizing nanoscale interfaces, and following structure transformations in chemical, biological, and geological gas-solid processes alike. Steady-state and time-dependent phenomena can be explored as a function of temperature, pressure, or flowing gas species. A wide range of fundamental and applied science uses are anticipated, including the identification and evolution of chemical compositions and unique atomic structure environments involved in heterogeneous catalysis, gas storage, oxidation/reduction processes, solid-oxide fuel cell cycles, sensor technology, capture of atmospheric pollutants, ion exchange processes, and more.

In the future, the flow cell's capability to deliver time-dependent isotope contrast to reacting/growing material interfaces in the neutron beam can be developed, together with stroboscopic data binning, to probe the kinetics of detailed surface structure species in steady-state processes (for example, utilizing the contrast of ^{14}N verses ^{15}N for improved sensitivity to N_2 adsorption/fixation, NH_3 synthesis, or NO reduction processes, or utilizing the contrast of ^{12}C verses ^{13}C for improved sensitivity to CH_4 oxidation, CO oxidation, propene epoxidation, or CO_2 reduction/fixation). Extensions to liquid flow in this set-up can enable studies on liquid-solid materials processes, including studies of environmental effects on medical implants and cycling behavior in electrochemical insertion electrodes and batteries. Overall, this new sample environment will provide new opportunities to validate theory and simulation, demonstrate synthesis and operation, and elucidate structural underpinnings of behavior in a host of gas-solid materials phenomena.

Chapter 3

Capturing the Details of N_2 Adsorption in Zeolite X Using Stroboscopic Isotope Contrasted Neutron Total Scattering [2]

3.1 Introduction

Porous materials, such as zeolites and metal organic frameworks (MOFs), have enabled significant industrial processes and continue to be developed for new trans-formative technologies. [106] For example, zeolites are widely used industrially for petroleum refining [93, 107, 108] and large-scale gas separations. [109–111] Despite their widespread adoption, the precise nature of adsorbent/sorbate interactions in the framework structure, and thus clear design principles for specific gas-solid interactions, are not widely available in the literature. A lacking atomistic understanding regarding the binding of substrate gas molecules in porous materials under operational conditions, owing primarily to the lability and heterogeneous dispersion of the gas molecules, is a particular challenge. Conventional approaches, often employing neutron scattering or NMR to gain sensitivity to light elements, locate adsorbed molecules in porous materials either under high pressure (CD_4 (9 bar) and C_2H_6 (5 bar) [112]) or at low temperatures (Xe (210 K) [23], CD_4 (77 K) [102], $CHCl_3$ (20 K) [103], N_2 (10 K) [104], or CO_2 (4 K) [104], p-xylene (1.5 K) [113], and many others in MOFs [114]) in order to freeze the guest molecules at high occupancy to their most stable binding sites. However, it is important to understand the heterogeneity and lability of gas molecules in these materials under operational conditions to facilitate real-world applications and development. There are many techniques that can study the functional behavior of porous mate-

[2] Substantial portions of this chapter have been reproduced with permission from D. Olds, K. V. Lawler, A. A. Paecklar, J. Liu, K. Page, P. F. Peterson, P. M. Forster, and J. R. Neilson, *Chem. Mater.*, **2018**, 30, 296-302. ®2018 the American Chemical Society

rials under operational conditions. For example, Steady-State Isotopic Transient Kinetic Analysis (SSITKA) [88, 105] provides insight into the steady-state kinetics of gas-solid interactions, which can be readily combined with DRIFT (Diffuse Reflectance Infrared Transform) Spectroscopy [115] to yield information about the chemical change of reactants interacting at surface inter-faces. While these approaches are deeply insightful, they are not amenable to describing the nature of the range of sites occupied by guests or the framework's structural response to guest uptake. Several X-ray scattering and spectroscopic methods have been developed to study porous framework materials. Single crystal X-ray diffraction was used to study nitrogen in metal-organic zeolites [116]. More advanced techniques such as Extended X-ray Absorption Fine Structure (EXAFS) [117, 118] and quick-scanning-EXAFS ((Q)EXAFS) [119] can provide element-specific local structure information about atomic sites that may change upon gas absorption or desorption. Total scattering methods, including pair distribution function analysis, have found utility in this area owing to the fact that they can yield useful structural information even when the guest molecules do not pack into the host pores with regular periodicity. Total scatter-ing has successfully identified the presence of guest mol-ecules and host-guest interactions such as hydrogen and nitrogen in the Prussian blue system $Mn_3[Co(CN)_6]_2$ [77,120], ammonia borane in mesoporous silica [121] and the formation of AgI in a zeolite. [122] To gain sensitivity to light elements while also providing chemical selectivity, isotope substitution ($^{(Nat}$Ni/$_6$2Ni) experiments with neutron total scattering have yielded insight into the interaction between acetylene and NiNa-zeolite Y [123]. However, these approaches do not readily permit study of the material under steady-state, operational conditions. Here, we report the main results of steady-state isotope-contrasted neutron total scattering experiments that study the nature of N_2 absorption in Ca-substituted zeolite X. Nitrogen adsorption in zeolite X was studied previously using inelastic neutron scattering [124]. We previously described the gas-handling instrumentation commissioned on the "Nanoscale Ordered MAterials Diffractometer" (NOMAD) at the Spallation Neutron Source at Oak Ridge National Laboratory [89]. This instrumentation permits the delivery of multiple gas streams to a solid sample immobilized in the primary neutron beam; a high-speed switching valve rapidly alternates between two different gas streams (e.g.,

$^{14}N_2$ and $^{15}N_2$) with negligible change in flow rate and pressure. This precision gas handling environment permits cross-correlation of the isotope compo-sition with the event-based time-of-flight neutron scattering data. Additionally, a computation approach, common-ly used to understand gas adsorption studies based on diffraction, [125] was used. Grand Canonical Monte Carlo (GCMC) simulations and isothermal gas adsorption experiments performed on the same N_2/zeolite system are found to be consistent with the results of isotope-contrasted total scattering studies. The simulations sup-port our crystallographic determination of Ca positions and reveal a distribution of N_2 molecules clustered near one of these sites. Calculation of the isotope-contrasted neutron total scattering from the theory-derived simulation reproduces the experimental observation after complex data reduction procedures. These methods provide a unique opportunity to gain insight into chemically dynamic and heterogeneous systems in operando.

3.2 Experimental and theoretical methods

Note on author contributions: This chapter was published in *Chemistry of Materials*, **2018**, 30 (1), 296-302, DOI: 10.1021/acs.chemmater.7b04594 by Daniel Olds, Keith V. Lawler, Arnold A. Paecklar, Jue Liu, Katharine Page, Peter F. Peterson, Paul M. Forster, and James R. Neilson. DO was involved in measuring the neutron scattering data, assembling the dynamic gas flow rig, and wrote the code for analyzing the stroboscopic neutron scattering data. KVL measured the adsorption isotherms, performed and analyzed the GCMC simulations. AAP prepared the material, was involved in measuring the neutron scattering data, and writing the manuscript. JL did the Rietveld refinements with TOPAS. PFP developed the software for integration and combination of SSITKA data and neutron total scattering data the MANTID framework. KP conceived the project, was involved in measuring and analysing the neutron scattering data, and supervising the project at ORNL. PMF supervised the work done at ULVN. JRN conceived the project, supervised it and all the work done at CSU. All authors contributed to editing and finalization of the manuscript.

Sample Preparation

The material preparation and characterization has been described previously [126] and is summarized here. The zeolite used for gas adsorption was produced through ion exchange of sodium zeolite X (NaX) powder with aqueous calcium chloride. X-ray powder diffraction showed retained crystallinity and scanning electron microscopy showed retained morphology after the exchange step. Energy dispersive X-ray spectroscopy (EDS) and optical emission spectroscopy with inductively coupled plasma (ICP-OES) were used to determine the cation exchange level (EDS (98%) and ICP-OES (97%)) suggesting a final sample composition of $Na_{86-2x}Ca_xAl_{86}Si_{106}O_{384}$ with x ≈ 42. In preparation for the neutron scattering experiments, the powders were pressed into a pellet at 4 metric tons, crushed into large chunks, sieved to sizes between $100\,\mu m$ and $500\,\mu m$ and dried in vacuum at 673 K.

Neutron Total Scattering Measurements

Initial neutron total scattering measurements were per-formed in static gas loading configurations, consisting of a quartz glass tube sealed with a plug valve, at room temperature on NOMAD. Samples were first measured under vacuum for 2 hours at 300 K followed by a pressure dosed condition with $^{15}N_2$. The samples were then sealed at 1 psig and measured for 2 hours at 300 K. Data reduction and PDFs were generated using standard data reduction protocols on NOMAD, but found to have insufficient statistics for quantitative real-space analysis. Structural refinements from the diffraction data were obtained with the program TOPAS and Fourier difference maps were created with the program JANA. [127] Details of the refinements and tabulated results are provided in the Appendix A. Stroboscopic neutron total scattering data were collected using the high-precision gas flow cell sample environment designed for SSITKA measurements. [128] In situ SSITKA measurements with simultaneous neutron total scattering were performed by flowing alternately $^{15}N_2$ and $^{14}N_2$, where the $^{14}N_2$ was mixed with 3% Ar to function as an inert trace, with helium as an inert carrier gas through the sample. The switching time between the two gases was set to 6 min with an overall number of 12 switching cycles between the two isotopes, resulting in a total measurement time of 150 min. An advanced data reduction procedure was developed to stroboscopically reduce the data using the Mantid data analysis framework. [91] An unexpected

time-dependent uptake of water by the sample during the stroboscopic measurement was observed, which was attributed to the presence of some humidity in the lines and gasses. The details of the data-informed reduction procedure can be found in the Appendix A. The resultant stroboscopically reduced scattering data is presented and described in the Results and Discussion.

Gas Adsorption Measurements

The Ca-exchanged zeolite X sample was activated under dynamic vacuum at 673 K for 24 hours followed by a N_2 surface area measurement at 77 K. Adsorption isotherms were measured using a Micromeritics ASAP 2020 adsorption analyzer. Desorption measurements were taken at the end of each isotherm to monitor that no hysteresis occurred. Prior to each measurement, the sample was reactivated at 473 K under dynamic vacuum for an hour followed by an hour of equilibration in the cryostat at the target temperature. N_2 isotherms were measured at 77 K and then every 10 K from 140 K to 300 K. The BET surface area was evaluated over the nanoporous regime, 0.01 $\leq P/P_0 \leq$ 0.10, of the 77 K N_2 adsorption isotherm following the recommendation of Walton and Snurr. [129]

Theoretical Evaluation of Adsorption Behavior Gas adsorption was simulated with Monte Carlo in the grand canonical ensemble (GCMC) with a modified version of the MuSiC package (full details in the SI). [130] A rigid $2 \times 2 \times 2$ super cell of the experimentally determined crystal structure was used to represent the zeolite framework with the ideal Ca-86X stoichiometry: $Ca_{43}Si_{106}Al_{86}O_{384}$ $^{14}N_2$. Ca and N_2 were allowed to fluctuate.

The volumes in the zeolite framework inaccessible to N_2 were blocked using our energy based pore mapping pro-gram. [131] The guest (cation and adsorbate)-framework Coulomb interactions were computed using electrostatic and dispersion-repulsion interactions. The T-atom framework and cation models of Boutin et al. were used for the zeolite. [132, 133] N_2 was represented by the TraPPe-small force field. [130]

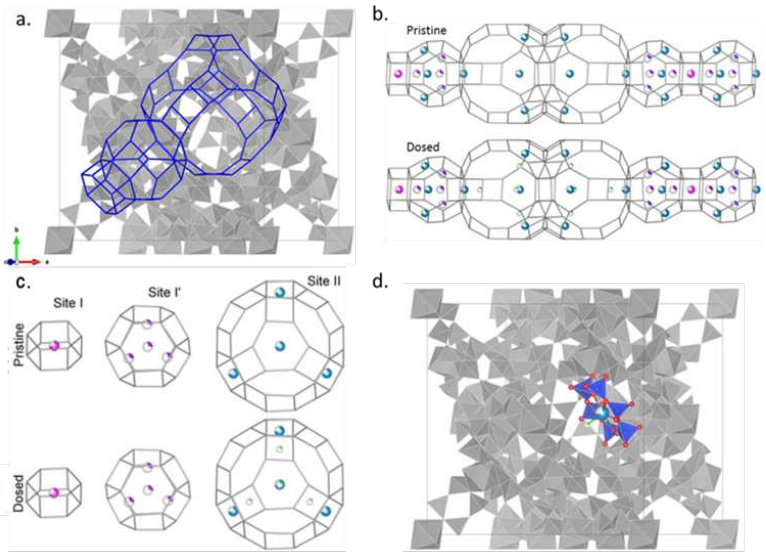

Figure 3.1: (a.) The zeolite cage structure, viewed down the (130) axis, with the subunit ensemble overlaid in blue. (b.) The subunit ensemble as determined from crystallographic refinements plotted normal to the (111) axis, pristine (top) and dosed with nitrogen (bottom), where nitrogen positions are in green, and calcium positions are in pink (site I), purple (site I'), and cyan (site II). (c.) The individual cage subunits from the pristine (top) and dosed (bottom) refinements, us-ing the same color scheme. (d.) A view down the (130) axis, where the 6-member ring of the site II position, with associat-ed crystallographic fit nitrogen position, has been colored. The (Si/Al)O_4 tetrahedral units forming the ring are shaded blue, with oxygen atoms depicted in red.

3.3 Results and discussion

Ca positions and occupancy Ca is known to occupy three distinct sites in the zeolite X structure, [134] where each position is associated with a different component cage subunit. Here, we refer to these positions as site I (in the hexagonal prism cage), site I' (in the beta or sodalite cage), and site II (in the alpha or su-per cage). These cages, as well as their relative connectivity, are shown in Figure 3.1. Neutron total scattering is a well-suited method to determine the positions and occupancies of Ca at these three sites. The refined structure for the static pristine compared to $^{1}5N_2$-loaded cases can be seen in Figure 3.1 (b–c), with details of the refinement found in the Appendix A. The Ca at site II sits 0.213 Å above the plane of the 6-member ring (towards the subunit cavity). This Ca is seen to be drawn further into the subunit cage upon gas loading to a position 0.257 Å above the plane of the 6-member ring. Note that occupancy and atomic displacement parameters can be correlated, so the atomic displacement parameter of Ca was fixed

to 0.58 $Å^2$ for these refinements. Initially refined populations of Ca in the pristine material were found to be 11.63(94) atoms at site I (out of a possible site multiplicity of 16), 8.00(74) atoms at site I' (out of a site multiplicity of 32), and 23.36(58) (out of a site multiplicity of 32) atoms at site II which are in agreement with previous investigations. [135, 136] We find that upon exposure to nitrogen, there is a migration of the Ca to the site II (now 23.42(.90)) and site I' (now 8.54(70)), presumably from the site I (now 11.04(58)). Migration behavior of extra framework cations was also observed in zeolite Y (faujasite structure) upon N_2 adsorption [137] as well as benzene adsorption. [138] The migration of the cations can be attributed to the strong interaction of the cation's positive charge and the high electric quadrupole moment of N_2 and CO_2 (4.7×10^{-40} C/m^2 and 13.4×10^{-40} C/m^2) [139] as well as the interaction with the π-electron system of the benzene molecule. This migration likely occurs via Ca passing through the shared faces of the cages. Grand Canonical Monte Carlo simulations that permitted Ca ion site hopping found 16 Ca ions/cell at site I and 27 Ca ions/cell at site II. A full occupation of site I should be viewed as the most idealized cation arrangement of a low silica evacuated zeolite X. [135, 136] The presence of water or residual monocations will tend to shift Ca from the most energetically favorable site I into site I', and this will likely be coupled with a migration of ions from site II to the more favorable site I' since the strong electrostatic repulsion at site I' from site I is no longer present. [136] Thus, deviations between the Ca occupancies in the idealized simulation and the experimental findings may be explained by water-uptake of the sample. In fact, it has been hypothesized that all of the water cannot be removed or prevent-ed from co-adsorbing during experimental uptake measurements, and the presence of water was shown to in general reduce the adsorptive capacity for N_2 and Ar into Ca containing zeolites (although at very low pressures they did observe an increase in Ar adsorption with water present). [140]

N positions and occupancy

The location and adsorption site of nitrogen was also experimentally determined using neutron diffraction. The structure was refined without the presence of nitrogen, and then compared to the data to generate a Fourier difference map, shown in Figure 3.2a. This Fourier difference map

indicated likely N_2 positions and occupancy. The clear preference for nitrogen to adsorb at site II can be seen as an irregular pocket of residual just outside the refined Ca position. The density map, attained from GCMC simulations for nitrogen at 300 K and 1 atm (Figure 3.2 b), also suggests that the Ca ions at site II are the primary binding sites for nitrogen under ambient conditions. There is no N_2 loading at site I and site I' as those cations are within the sodalite cage and the hexagonal prism which are well known to be inaccessible to ad-sorbed guest molecules in faujasite zeolites and were blocked by the pore mapping program in the GCMC simulations. [93, 105, 117, 141–147] This preference suggests that nitro-gen molecules cannot easily access the hexagonal prism site I', nor the sodalite site I.

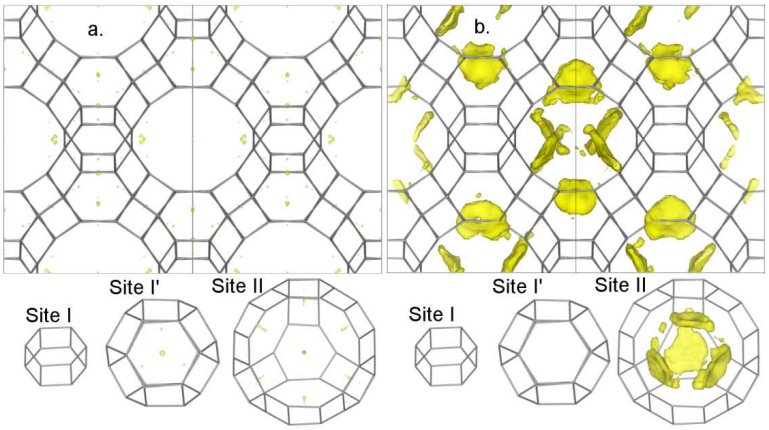

Figure 3.2: (a.) The resultant Fourier difference map from fits to the statically dosed zeolite sample with a model lacking N_2, (b.) compared to the nitrogen positions found through GCMC simulations. To avoid any confusion by the projection of the structure, we have shown isolated views of each cage set below the figures with corresponding residual (from refinements) or simulated nitrogen density (from simulation).

Subsequent Rietveld refinements with a nitrogen atom, representing the center of mass for the molecule in these locations provided the occupancy for the N_2 molecules. Only about 8 N_2 molecules could be found based on diffraction data. However, under ambient conditions, GCMC predicts a loading of 17.9 N_2 molecules/unit cell which agrees well with the adsorption isotherm measurements indicating 15 N_2 molecules per unit cell. A possible explanation for the discrepancy between the number of nitrogen molecules found from neutron scattering data analysis compared to the GCMC calculations and adsorption isotherm measurements could be the diffuse nature of

the nitrogen density, as the crystallographic chemical occupancies reflect only those N_2 molecules that appear with some long-range order (on average). However, we cannot rule out the occlusion of some binding sites from the presence of water.

Nitrogen adsorption in operando

The absorption of N_2 molecules modifies the structural framework of the zeolite. As previously reported, [127] neutron diffraction data indicates that the zeolite structure responds to the presence of nitrogen by shrinking the unit cell volume upon gas loading. Since these contractions are reversible upon desorption, they are often referred to as "lattice breathing". [114] Shrinking of lattice parameters has been observed for zeolite Y upon CO_2 adsorption [137] whereas nitrogen adsorption led to an expan-sion of the unit cell in the Co(BDP) MOF [148] as well as in the Prussian blue system $Mn_3[Co(CN)_6]_2$. [120] GCMC simulations confirm an experimentally observed shift of the Ca ions at the site II further into the subunit cage upon gas loading based on the interaction with nitrogen.

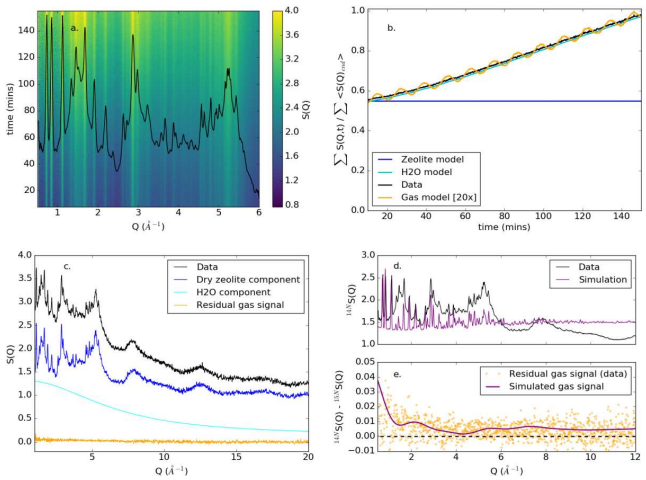

Figure 3.3: (a.) A time-dependent top-down view of the measured scattering, S(Q), binned into 10-second slices which demonstrates little change in the measured Bragg peaks, but a steady increase in the diffuse scattering attributed to water. The average S(Q) has been overlaid in black for comparison. (b.) The time-dependent weighting of the model contributions to the total pattern. (c.) The isolated components which are weighted by the time-dependent model to recover the data. (d.) The stroboscopically binned $^{14}N_2$ data, compared to the pattern from the GCMC simulated structure. (e.) The recovered residual gas signal in the data compared to the simulated GCMC nitrogen signature.

To isolate the signal of adsorbing nitrogen separate from any lattice breathing behavior, it is necessary to measure the system under steady-state conditions. Under steady state conditions, the lattice parameters will not change upon adsorption and desorption of different nitrogen isotopes. In conventional techniques, where a gas filled system is compared to an evacuated condition, the lattice parameters tend to change, convolving analysis of gas adsorption with changing lattice behaviors. We have avoided this complication by performing steady-state isotope varied stroboscopic neutron diffraction. The data was collected under constant flow and pressure, but with symmetrically varying isotope composition of $^{14}N_2$ and $^{15}N_2$, measured over 12 cycles of switching feed gas. While the aforementioned neutron density maps describe only the crystallographically ordered nitrogen site probability densities, the neutron total scattering function, S(Q), (the inverse Fourier transform of the pair distribution function) describes the scattering from all nitrogen molecules (e.g., those that are ordered and disordered). However, the diffuse scattering signature requires additional counting time to build up the needed signal to noise ratio. Therefore, the attained neutron total scattering data from the different isotope adsorption and desorption steps (in the steady state) was re-binned stroboscopically over all cycles to have better signal statistics. To obtain the neutron isotope-difference total scattering function, a data-informed stroboscopic reduction procedure was developed. The reduction was complicated by trace amounts of water, which was found to have infiltrated the sample during data collection, as can be seen in Figure 3.3a. Neutron scattering is inherently very sensitive to the presence of hydrogen due to its' large incoherent cross section. Previous work has shown sensitivity of neutron diffraction to changes in hydration levels as little as 0.02% [149] via changes in the incoherent scattering signal. This is well below the levels that would contribute structural features in the analysis of the refined Bragg reflections in the diffraction data. Models were developed for the dry zeolite structure and the slowly varying incoherent contributions of water (Figure 3.3b. and Figure 3.3c.), which were then removed from the data. The integrated intensity of the remaining signal, attributed to the adsorbed nitrogen, was found to oscillate with a frequency matching the prescribed gas-dosing rates. Notably, the total intensity of this nitrogen signal is $\sim$0.5% of the total integrated intensity. Further details of this reduction

procedure can be found in the Appendix A. The stroboscopically reduced neutron total scattering data is consistent with a heterogeneous distribution of N_2 sites localized near site II predicted by GCMC. Rietveld refinements of this data reveals sensitivity to the isotope of adsorbing nitrogen through fit occupancy values, which vary by a ratio of 1.45 between the sample exposed to $^{14}N_2$ compared to $^{15}N_2$, which compares remarkably well with the ratio of scattering power between the two isotopes ($b^{14}N/b^{15}N$ = 1.46). Details of this refinement are found in the Appendix A. The static nitrogen-loaded data, as well as the differential signal from the data reduction process, are illustrated in Figure 3.3d. The isotope difference signal, represented as the total scattering function, is very weak and is therefore not analyzed as its Fourier transform, the pair distribution function. Instead, the isotope contrasted total scattering is consistent with the equivalent scattering function calculated from the GCMC simulation (Figure 3.2). GCMC also gives information about the orientation of the diatomic nitrogen molecule in the structure. The simulations demonstrated that nitrogen prefers a co-linear binding with the calcium ions along the N_2 molecular axis. To summarize, it becomes interesting to compare the stroboscopic and isotope-contrasted results to more traditional gas-adsorption experiments performed under cryogenic conditions. Single-crystal X-ray diffraction is not able to achieve sufficient residual electron density to study the adsorption of nitrogen at room temperature in a metal organic framework. [116] In another study, single crystal neutron diffraction also lacked the ability to detect adsorbed hydrogen at RT, likely due to the molecular dynamics. [150] Here, we show a distribution of nitrogen molecule positions at room temperature, which provides a structural basis for such types of molecular motion. Adsorption studies in NaY could locate CO_2 [137] at 4 K as well as RT with an U_{iso} for CO_2 of 0.145 $Å^2$ and 0.504 $Å^2$ respectively. Due to the large displacement coefficients of NaY and CO_2 at RT, not all sodium atoms could be located com-pared to the measurement at 4 K, likely due to atomistic dynamics. Similarly, the high temperature-factors describing the adsorption of benzene in NaY at RT is, according to the authors, not very meaningful either. [140] Adsorption studies of nitrogen in the zeolite SSZ-13 located N_2 at 10 K with U_{iso} values of 0.033 $Å^2$ and 0.04 $Å^2$ for N1 and N_2, respectively. [104] In the study of nitrogen adsorption here, at room temperature, a U_{iso} value of

0.067(14) $Å^2$ is found, in good agreement with increased thermal motion expected at higher temperatures. However, it should be noted that the occupancy and atomic displacement parameters for N are found to be correlated in refinement, and the value of U_{iso} (fixed in final analyses) was initially determined while holding the occupancy fixed to the value derived from SSITKA analysis (further details are provided in the Appendix A). Total scattering can also provide crucial information to address questions that cannot be answered with traditional crystallographic refinements alone. For example, the binding angles in CO_2 adsorbed in NaY were determined to be 149.3$\circ$ with Rietveld refinement, which leaves the question if the result is physically relevant or is the result of occupational or dynamical disorder. Total scattering with pair distribution function analysis could help determine whether the distortion of the CO_2 molecule is based on disorder. [116] This isotope-contrasted stroboscopic neutron scattering method shows promise for the study of these and other gas/adsorbent interactions.

3.4 Conclusion

Through a combination of isotope-contrasted stroboscopic neutron diffraction, steady-state isotope transient kinetic analysis, gas isotherm measurements, and Grand Canonical Monte Carlo simulation techniques, the heterogeneous distribution of nitrogen molecules in the faujasite structure of a zeolite X was determined under ambient operational conditions (300 K, 1 atm). The approach taken here shows an increased ability to locate the absorption sites (or distributions thereof) of gas molcules in porous structures, in contrast to traditional crystallography or cryogenic experiments. These results high-light the predictive power of the relatively simple force fields employed in the GCMC simulations, which are able to reproduce both macroscopic and microscopic observables. However, the microscopic, crystal chemical observables required isotope-contrasted stroboscopic neutron scattering with advanced data treatment to provide a unique experimental structural probe for gas-solid phase interactions. Unlike in the static case, where the lattice responds to adsorbed nitrogen relative to the neat and vacuum condition, the stroboscopic method can look at the structural correlations involved in adsorption alone under steady-state conditions. The powerful combination

of neutron total scattering, gas isotherm measurements, and theoretical calculations each independently informs and supports the other and builds a consistent, predictive picture. This demonstrates a fertile framework for future investigation of industrially relevant gas sorption, separation, and catalysis processes also *in operando* conditions.

Chapter 4

Bond valences and anharmonicity in vacancy-ordered double perovskite halides [3]

4.1 Introduction

Lattice dynamics play a crucial role in dictatingmaterials properties, including thermal conductivity, [151] ionic and electronic transport, [152, 153] optical emission, [154, 155] piezoelectricity and ferroelectricity, [156, 157] and superconductivity, [158] to name a few. Divergence from a purely harmonic vibrational landscape further manifests interesting physical behavior. High amplitude anharmonic vibrations in systems such as the tin and lead chalcogenides introduce vibrational disorder to which their low thermal conductivities and advantageous performance in thermoelectric devices are attributed. [159–161] Anharmonic rattling of guest atoms within host structures has been exploited as a mechanism to disrupt thermal conductivity in other candidate thermoelectric materials such as skutterudites. [162] Additionally, ionic conductivity may be enhanced in materials in which the mobile ion occupies a flat and broad anharmonic potential well, [163, 164] while lower-energy anharmonic vibrational modes can couple to mobile electrons to reduce electron mobilities. [152, 165] Despite the extensive influence of anharmonicity upon functional properties in crystalline materials, a unified understanding of the structural and bonding motifs necessary to leverage anharmonic behavior to target particular materials properties is fundamentally lacking. Halide-based perovskite materials are redefining the paradigm of semiconductor materials design principles, in that they appear to follow a set of structure–dynamics–property relationships that are distinct from conventional semiconductors. The perovskite structure adopts the general formula ABX_3, and the structure is composed of corner sharing BX_6 octahedra with A-site cations in the 12-coordinate void. Anharmonic lattice dynamics in perovskite halides have been shown

[3] Substantial portions of this chapter have been reproduced with permission from A. E. Maughan, A. A. Paecklar and J. R. Neilson, *J. Mater. Chem. C*, **2018**, DOI: 10.1039/c8tc03527j. ®2018 The Royal Society of Chemistry

to arise from rotational instabilities of the soft, deformable BX_6 octahedral framework coupled with motions of the A-site cation. [166–168] These dynamic instabilities yield an anharmonic double potential well, resulting in an instantaneous local structure characterized by cooperative octahedral tilting that averages to a higher-symmetry, untilted structure. [166–169] Anharmonicity has been further correlated with the remarkable photoconversion efficiencies of halide perovskite materials in photovoltaic devices. [170, 171] Of particular note is the observation of long carrier excited-state lifetimes, [172–174] which are hypothesized to arise from the formation of polarons that protect photogenerated charge carriers and prevent recombination. [165, 174–180] The intimate link between anharmonic lattice dynamics and functional properties motivates a fundamental understanding of the structural and compositional origins of anharmonicity in perovskite halides.

Vacancy-ordered double perovskites present a materials family to study anharmonicity in a lattice with additional dynamic degrees of freedom. The vacancy-ordered double perovskite structure is formed by doubling the conventional ABX_3 perovskite unit cell and removing every other B-site cation to form a face-centered lattice of isolated BX_6 octahedral units bridged by A-site cations in the void. Alternatively, the structure can be thought of as an ordered double perovskite of the formula $A_2B\,\square\,X_6$, with rock salt ordering of BX_6 and $\square\,X_6$ octahedra, where $\square$ denotes a vacancy, as shown in Figure 4.1. Anharmonicity in the vacancy-ordered double perovskites Cs_2SnI_6, $(CH_3NH_3)_2SnI_6$, and $(CH(NH_2)_2)_2SnI_6$ has been correlated with reduced carrier mobilities. [70] Replacing the inorganic Cs^+ with the molecular methylammonium ($CH_3NH_3{}^+$) and formamidinium ($CH(NH_2)_2{}^+$) cations is accompanied by a significant reduction in electron mobilities due to softer, more anharmonic lattice dynamics that result in stronger electron–phonon coupling interactions. In order to leverage anharmonicity as a design principle for perovskite halide semiconductors, a fundamental understanding of the structural and compositional origins of anharmonic lattice dynamics are required.

In this contribution, we assess the structural origins of anharmonicity in the series of inorganic vacancy-ordered double perovskites $Cs_2Sn_{1-x}Te_xI_6$. X-ray pair distribution function analysis reveals asymmetry in the local coordination environment of Cs_2SnI_6, which systematically decreases

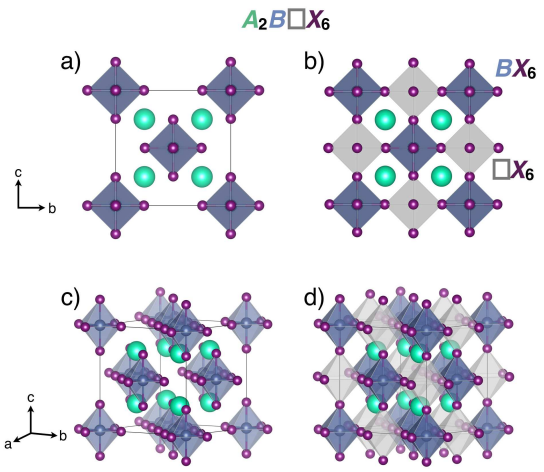

Figure 4.1: Unit cell representation of the cubic vacancy-ordered double perovskite structure. A-site cations are shown in teal, B-site cations are shown in blue, and X-site anions are shown in purple. Panels (a) and (c) highlight the isolated BX_6 octahedral units. In (b) and (d), the grey, transparent octahedra represent the ordered vacancies, denoted as $\square X_6$.

and vanishes with increasing tellurium content. Neutron total scattering of Cs_2SnI_6 reveals that the peak asymmetry becomes increasingly pronounced at higher temperatures, indicating that this feature is likely due to a dynamic effect rather than a static structural distortion. We attribute the subtle deviations in the local coordination environment of the $Cs_2Sn_{1-x}Te_xI_6$ series to anharmonic lattice dynamics brought about by octahedral rotations and Cs^+ displacements, consistent with the concave-down of the atomic displacement parameter vs. temperature curves for cesium and iodine. This assertion is supported by pseudo-rigid-body Reverse Monte Carlo simulations of Cs_2SnI_6 and Cs_2TeI_6. From the RMC-optimized structures, we find that the Cs–I and I–I_{inter} partial pair correlations exhibit a broad, asymmetric distribution, indicating that the anharmonicity arises from these atom pairs. We further quantified the trend in anharmonicity in the XPDFs of $Cs_2Sn_{1-x}Te_xI_6$ using a modified anharmonic Toda potential and find a strong correlation of the peak asymmetry with the calculated bond valence of the Cs^+ cation, suggesting that the anharmonicity arises due to dissatisfied bonding preferences of the Cs^+ cation within the cuboctahedral void, giving rise to dynamic octahedral rotations coupled to displacements of the Cs^+ ions. The relationship between bonding and anharmonicity provides a hand-hold for tuning the vibrational properties in vacancy-ordered double perovskite semiconductors.

4.2 Methods and materials

Note on author contributions: This chapter was published in *Journal of Materials Chemistry C*, **2018**, 6 (44), 12095-12104, DOI: 10.1039/c8tc03527j by Annalise E. Maughan, Arnold A. Paecklar, and James R. Neilson. AEM performed the experiments, wrote the initial draft, and collected and analyzed data. AAP performed the RMC simulations, wrote the initial draft for the RMC section of the manuscript, calculated bond valence sums and Toda potentials. JRN conceived the project, supervised it, and assisted with data analysis. All authors contributed to editing and finalization of the manuscript.

Synthesis of $Cs_2Sn_{1-x}Te_xI_6$

The solid solution series $Cs_2Sn_{1-x}Te_xI_6$ was prepared by previously reported methods. [181]

Structural characterization

Synchrotron X-ray scattering data suitable for pair distribution function (PDF) analysis were collected at beamline 11-ID-B at the Advanced Photon Source, Argonne National Laboratory, using 86 keV photons and sample-detector distance of 19 cm. Powdered samples of $Cs_2Sn_{1-x}Te_xI_6$ were loaded into polyimide capillaries and measured in transmission mode at room temperature using a PerkinElmer amorphous silicon image plate detector. [182] Experimental PDFs were extracted using PDFgetX3 [183] and analyzed using PDFgui. [184] The program Fit2D [185] was used to calibrate the sample to detector distance and detector alignment with data from a CeO_2 powder standard. Raw scattering data were integrated into Q-space spectra, applying a mask and polarization correction during integration. The normalized total scattering pattern, S(Q), was produced in PDFgetX3 by subtracting polyimide container scattering, utilizing the appropriate sample composition, and applying standard corrections for the area detector setup. [182] The pair distribution function pattern, G(r), was calculated via Fourier transformation of the total scattering data utilizing a maximum Q = 30 Å. G(r) for each member of the series was extracted for several values of Q_{max} to infer the influence of Fourier termination ripples in our subsequent analyses. Values of Q_{damp} = 0.0538 Å and Q_{broad} = 0.003 Å were extracted from refinement of a Ni standard in PDFgui and used for further refinement. Neutron total scattering measurements of Cs_2SnI_6 were

performed on the nanoscale ordered materials diffractometer (NOMAD) at the Spallation Neutron Source, Oak Ridge National Laboratory. For measurements collected at T = 90, 300, and 500 K, a powdered sample of Cs_2SnI_6 was loaded and sealed in a quartz capillary (capillary diameter = 3.0 mm) in the multisample changer. Data were normalized against scattering data collected for an empty quartz capillary, and background scattering from the quartz capillary was subtracted. For measurements at T = 10 K, a powdered sample of Cs_2SnI_6 was loaded into a 6 mm vanadium canister under He atmosphere. Data were normalized against scattering collected for a vanadium rod, and background scattering from the vanadium can was subtracted. Temperature-dependent neutron total scattering data were merged to the total scattering structure function using the IDL codes developed for the NOMAD instrument. [186] The pair distribution function was then produced through the sine Fourier transform of the total scattering structure function using Q_{max} = 31.4 Å. For Cs_2SnI_6 at T = 90, 300, and 500 K, values of Q_{damp} = 0.0201 Å and Q_{broad} = 0.0196 Å were extracted from refinement of a diamond standard in PDFgui. For Cs_2SnI_6 at T = 10 K, values of Q_{damp} = 0.01766 Å and Q_{broad} = 0.01918 Å were extracted from refinement of a silicon standard. Analysis of the nPDFs was performed using PDFgui.

Reverse Monte Carlo simulations

Reverse Monte Carlo (RMC) simulations were performed with 6 × 6 × 6 supercells of the cubic structures of Cs_2SnI_6 (a = 69.830 Å) and Cs_2TeI_6 (a = 70.212 Å), each containing 7776 atoms. The simulations were constrained in reciprocal-space by S(Q)-1 data, and in real-space by the X-ray pair distribution function, G(r). S(Q)-1 was convolved with a Gaussian function with a full-width-half-maximum of 1/2 the length of the supercell edge prior to use in simulations in order to capture appropriate peak broadening due to finite size of the box. [187] The experimental data were simulated using two independent RMC approaches within the fullrmc package. [188] Both RMC simulations were run for 89 882 085 steps. Traditional free-motion RMC simulations were performed in which all atoms were independently allowed to displace randomly within the Cartesian reference. The Sn–I/Te–I bond lengths were constrained between 2.65–3.05 Åand the I–Sn–I and I–Te–I bond angles were constrained to 80–100 ° and 170–180°. The simulations were optimized

against the experimental data from 0.9–17.45 Å for G(r) and 0.5–25 Åfor S(Q)-1. Pseudo-rigid-body RMC simulations were also implemented, in which the [SnI_6] and [TeI_6] octahedra were randomly rotated and tilted as rigid units, prior to and after their free relaxation. Similarly to the free-motion RMC simulations, the Sn–I/Te–I bond lengths were constrained between 2.65–3.05 Å and the I–Sn–I and I–Te–I bond angles were constrained to 80–100° and 170–180°. After initiating the refinements with only the intraoctahedron bonds, the refinement range was increased step-wise to include longer-range pair correlations while all atoms were permitted to displace in the Cartesian reference. After the fitting range reached r = 17.45 Å and after a finite number of atomic displacements, the octahedra were constrained as rigid bodies (Sn/Te–I bond lengths and angles were frozen) and allowed to tilt about the center of the octahedra around all three Euler angles up to a maximum tilt angle of 10°. The entire fitting process was reiterated twice from the start to achieve the final configuration. VESTA was used to visualize and render all crystal structures presented in this publication. [189]

4.3 Results

All members of the $Cs_2Sn_{1-x}Te_xI_6$ series crystallize in the cubic vacancy-ordered double perovskite structure shown in Figure 4.1. [181] The Sn(IV) and Te(IV) ions randomly occupy the B-site coordinated to six I^- ions at the X-site, and the Cs^+ cations occupy the cuboctahedral A-site void. The local coordination environment probed by XPDF analysis is consistent with solid solution behavior between Cs_2SnI_6 and Cs_2TeI_6. In Figure 4.2a, the X-ray pair distribution function (XPDF) of each member of the $Cs_2Sn_{1-x}Te_xI_6$ series are modeled with the cubic structural model with appropriate fractional occupancies of tin and tellurium. Over medium and long length scales ($r > 6$ Å), the XPDFs are fairly well described by the cubic structural model, consistent with each member of the series adopting the cubic vacancy-ordered double perovskite structure; however, the fit quality is worse closer to Cs_2SnI_6 (Figure 4.2b). As shown in Fig. 4.3a, tellurium substitution is accommodated by a linear increase in the lattice parameter, consistent with Vegard's law. Further, the larger tellurium ion results in an increase in the average B–I bond length (Figure 4.3b) at

the expense of the interoctahedral I–I contact distances along the $\langle 110 \rangle$ directions (Fig. 3c). This also results in a slight increase in the average Cs–I bond lengths across the series (Figure 4.3d). The structural parameters extracted from the XPDF fits in Figure 4.3 are plotted with the previously reported parameters from analysis of high-resolution synchrotron powder X-ray diffraction data. [181] Although all members of the series appear to adopt nearly identical crystalline structures by both SXRD and XPDF, the local coordination environment over short length scales reveals subtle differences across the series. The first nearest-neighbor pair correlation at r $\approx$ 2.85–2.9 Å due to Sn–I/Te–I bonds moves to higher r due to an increase in the average B–I bond length with substitution of the larger tellurium ion. Despite mixed Sn–I and Te–I bond lengths, this peak remains symmetric across the series and is well-described by the cubic structural model, consistent with regular, undistorted BX_6 octahedral units. In contrast, deviations in the next-nearest-neighbor (nnn) pair correlation at r $\approx$ 4.1 Å, due to I–I and Cs–I pairs, are observed across the series, manifesting as a slight asymmetry of the high-r side of the peak present in the difference curves in Figure 4.2. The apparent asymmetry is most pronounced in Cs_2SnI_6 and gradually decreases with increasing tellurium content, consistent with the nearly monotonic decrease in R_{wp} with x shown in Figure 4.2b. Our previous work found that the XPDFs of the intermediate members could be obtained by a linear combination of the XPDFs of the Cs_2SnI_6 and Cs_2TeI_6 end members, [181] indicating that this apparent asymmetry evolves smoothly as a function of tellurium content. As the BI_6 octahedra remain relatively undistorted and all members of the solid solution adopt nearly identical crystal structures by X-ray diffraction, we propose that this asymmetry may be due to anharmonic lattice dynamics rather than a static structural distortion.

Neutron total scattering experiments of Cs_2SnI_6 reveal a temperature-dependence of the asymmetry observed in the local coordination environment. Neutron diffraction data of Cs_2SnI_6 collected from the 31° bank (bank 2) of NOMAD at T = 10, 90, 300, and 500 K reveal that Cs_2SnI_6 adopts the cubic vacancy-ordered double perovskite structure at all measured temperatures, as shown in the Rietveld refinements in Figure 4.4. The neutron pair distribution functions (nPDF) extracted from total scattering data are shown in Figure 4.5. At all temperatures the nPDFs were

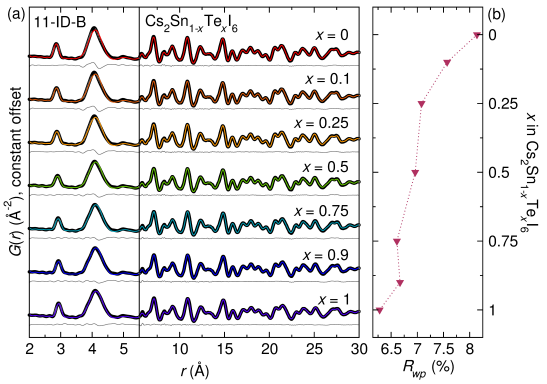

Figure 4.2: (a) X-ray pair distribution functions of the solid solution $Cs_2Sn_{1-x}Te_xI_6$ modeled with the cubic vacancy-ordered double perovskite structure with isotropic, harmonic atomic displacement parameters. The data are shown as black circles, the fits are colored lines, and the difference is shown in grey. The x-axis is split to highlight the low-r pair correlations, particularly the asymmetry of the next-nearest neighbor pair correlation at r $\sim$ 4.1 Å. The R_{wp} for each fit is shown in (b).

modeled with the cubic vacancy-ordered double perovskite structure of Cs_2SnI_6, consistent with previous reports [181,190] and with the corresponding diffraction data that indicate Cs_2SnI_6 adopts the cubic structure at all temperatures (Figure 4.4). At T = 10 K, the pair correlations are sharp, narrow, and symmetric, consistent with low-amplitude harmonic thermal vibrations at this temperature. Increasing temperature to T = 90 K and T = 300 K is accompanied by broadening of all pair correlations. The nnn pair correlation becomes visibly asymmetric with increasing temperature, with a slight tailing on the high-r side of the peak revealed in the difference curves. At T = 500 K, the peaks in the nPDF are significantly broadened and dampened, and we observe significant asymmetry of the nnn pair correlation that is not captured by the cubic structural model. The nPDFs for Cs2SnI6 at T = 10, 90, and T = 300 K are taken from our previous study and re-fit here for comparison with the T = 500 K data. [190]

Temperature-dependent peak asymmetries have been observed in the XPDF of the related perovskite $CsSnBr_3$. [67,69] At T = 300 K, the nearest-neighbor pair correlation due to Sn–Br bonds is symmetric, but becomes noticeably asymmetric on the high-r side of the peak at higher temperatures. The emergence of this asymmetry with temperature, termed "emphanisis", has been attributed to dynamic off-centering of the Sn^{2+} ion within the $SnBr_6$ octahedra, which arises from stereochemically-active $5s^2$ electrons. While the formal $[Kr]4d^{10}5s^0$ electron configuration of

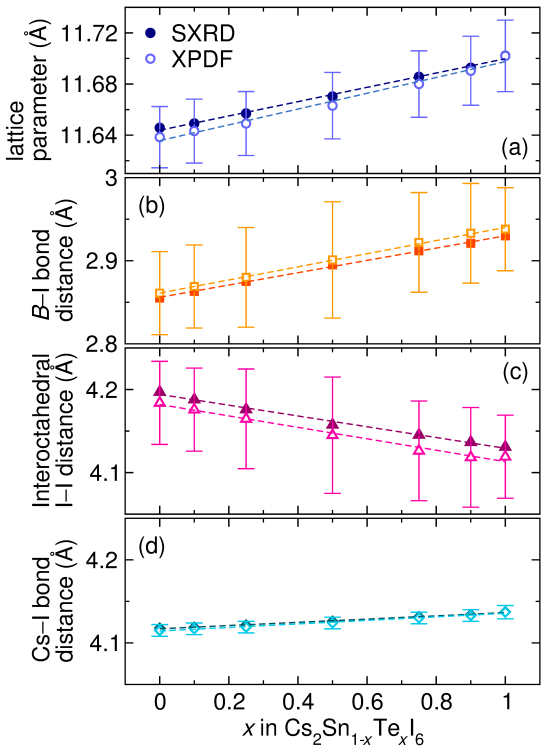

Figure 4.3: Structural parameters for the $Cs_2Sn_{1-x}Te_xI_6$ solid solution from refinement of the cubic structural models against high-resolution synchrotron powder X-ray diffraction (SXRD) data (filled symbols) and X-ray pair distribution function analysis (open symbols). In (a), the lattice parameters for each member of the solid solution follow Vegard's law. In (b), the average B–I bond lengths increase linearly with substitution of the larger tellurium ion at the expense of the interoctahedral I–I contact distance along the $\langle 110 \rangle$ direction shown in (c). In (d), the average Cs–I bond length increases. The dashed lines represent linear regressions performed for each data set. Error bars are shown for the parameters extracted from the XPDF fits. The error bars for the SXRD parameters are within the size of the symbol and are therefore omitted for clarity. The structural parameters from the SXRD data are taken from ref. [244].

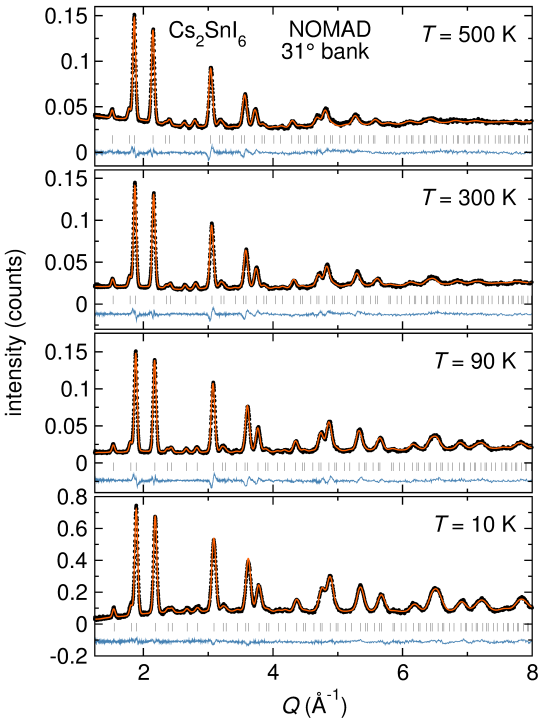

Figure 4.4: Rietveld refinements of temperature-dependent neutron diffraction of Cs_2SnI_6 at T = 10, 90, 300, and T = 500 K from the 31° bank (bank 2) of the NOMAD instrument at the Spallation Neutron Source, Oak Ridge National Laboratory. The data are modeled with the cubic vacancy-ordered double perovskite structure at all temperatures. Black circles are the data, the orange line is the fit, the blue line is the difference, and the grey tickmarks represent positions of anticipated reflections for the $Fm\bar{3}m$ vacancy-ordered double perovskite structure. The data at T = 10, 90, and T = 300 K have been previously reported.[243]

Sn^{4+} in Cs_2SnI_6 precludes the presence of stereochemically-driven structural distortions, the temperature dependence of the peak asymmetry suggests that this effect arises from high-amplitude anharmonic lattice vibrations rather than a static structural distortion. To gain insight into the atomistic contributions to the anharmonicity and peak asymmetry in Cs_2SnI_6, we extracted values for the atomic displacement parameters (ADPs) from the Rietveld refinements of the neutron diffraction data shown in Figure 4.4.

The iodine ADPs were refined anisotropically; U_{11} corresponds to displacements along the Sn–I bond, while $U_{22} = U_{33}$ corresponds to displacements perpendicular to the Sn–I bond. As shown in Figure 4.6, the ADPs for Cs and I ($U_{22} = U_{33}$) increase monotonically (though not linearly) with increasing temperature, while the ADPs for Sn and I (U_{11}) increase only slightly from T = 10 K to T = 500 K. In systems with harmonic interactions, the relationship between

the atomic displacement parameter (U_{iso}) and temperature is well-described by a Debye–Waller model. [191, 192] In Cs_2SnI_6, however, the ADPs for Cs and I U_{22} = U_{33} follow a concave-down shape with increasing temperature, a trend which has previously been attributed to anharmonic dynamics in the $VAl_{10+\delta}$ system due to rattling of the Al atoms within the structural voids. [192] Similarly, neutron diffraction studies of $CsPbX_3$ halide perovskites reveal anomalously large atomic displacement parameters of the Cs and X ions that diverge from the harmonic Debye–Waller model, indicating the presence of anharmonic effects due to coupled displacements of the Cs^+ and X^- ions. [193] The similarities observed between the $VAl_{10+\delta}$ and $CsPbX_3$ systems and Cs_2SnI_6 suggests that the trends in ADP vs. temperature arises from anharmonic dynamics of the Cs and I atoms in Cs_2SnI_6. Furthermore, the observation that iodine displacements perpendicular to the Sn–I bond (U_{22} = U_{33}) follow the same trend as the atomic displacement parameter for cesium and are significantly larger than iodine displacements along the Sn–I bond (U_{11}) may suggest the presence of [SnI_6] octahedral rotations coupled to Cs^+ displacements as the source of anharmonicity. Prior nuclear quadrupole resonance studies of the vacancy-ordered double perovskite family support this assertion, as dynamics in these materials originate predominantly from rotations of the rigid octahedral units. [194–197]

Reverse Monte Carlo (RMC) simulations of Cs_2SnI_6 and Cs_2TeI_6 were performed to provide atomistic insights into the asymmetry observed in the XPDFs. As the dominant lattice dynamics in vacancy-ordered double perovskites arise from octahedral rotations rather than deformations of the octahedra, [194–197] we elected to use a pseudo-rigid-body RMC approach, in which the isolated [SnI_6] and [TeI_6] octahedra were allowed to tilt as rigid bodies, to encourage chemically reasonable descriptions of the anharmonicity. The constraint of rigid-bodies has been shown to improve RMC simulation results, especially in cases with dynamics such as rigid-unit modes. [198] From this approach, we find that the XPDFs are best described by structures with random rotations of the SnI_6 and TeI_6 octahedra and displacements of the Cs^+ ions away from their crystallographic positions, as shown in the optimized supercells in Figure 4.7 and in the fits to the XPDF shown in Figure 4.8a and b. We have also performed traditional free-motion RMC simulations to ensure

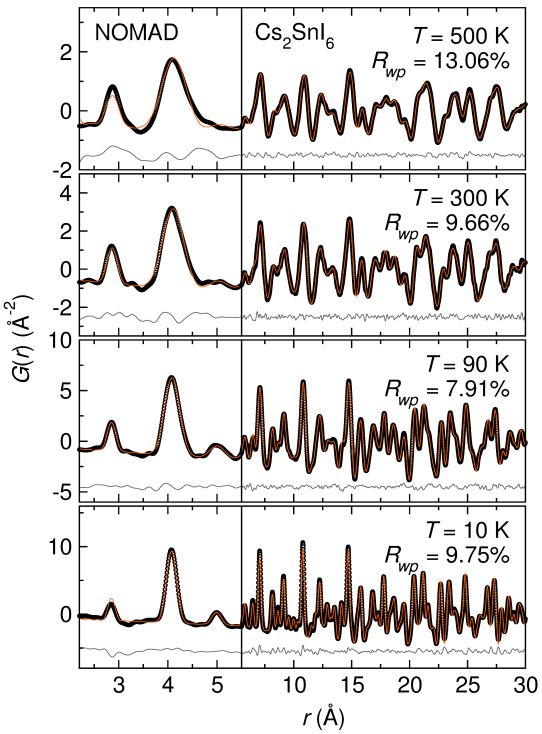

Figure 4.5: Temperature-dependent neutron pair distribution function analysis of Cs_2SnI_6 at T = 10, 90, 300, and T = 500 K. The data are modeled with the cubic vacancy-ordered double perovskite structure at all temperatures. Black circles are the data, orange lines are the fits, and grey lines are the difference curves. The x-axis is split to highlight the low-r pair correlations and the increasing asymmetry of the next-nearest-neighbor pair correlation at r $\sim$ 4 Å with increasing temperature. The nPDFs at T = 10, 90, and T = 300 K have been previously reported and are re-fit here for comparison with the T = 500 K data.[243]

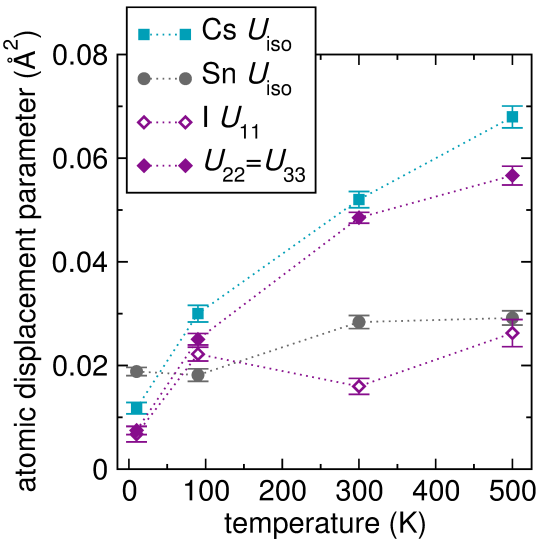

Figure 4.6: Atomic displacement parameters (ADPs) extracted from the temperature-dependent neutron diffraction data for Cs2SnI6 using Rietveld analysis. Isotropic atomic displacement parameters were refined for cesium and tin. The ADPs for iodine were refined anisotropically, such that U_{11} corresponds to iodine displacements along the Sn–I bond and U_{11} = U_{22} corresponds to displacements perpendicular to the Sn–I bond. The dotted lines are a guide to the eye to highlight the trends in ADP for each atom.

that the outcome is consistent with our pseudo-rigid-body RMC approach. These calculations are independently consistent with those of our pseudo-rigid-body approach, though the quality of fit is not as good for the same number of moves. These results are shown in the Appendix B. To determine the atom pair contributions to the asymmetry observed in the next-nearest-neighbor pair correlation at r $\approx$ 4 Å, the partial radial distribution functions (RDF) for the intraoctahedral I–I (I–I$_{intra}$), interoctahedral I–I (I–I$_{inter}$), and Cs–I pairs were extracted from the RMC-optimized supercells. As shown in Figure 4.9, the partial RDFs are relatively consistent between both Cs_2SnI_6 and Cs_2TeI_6 and show only subtle variations between the two compounds. In both compounds, the I–I$_{intra}$ RDFs for Cs_2SnI_6 and Cs_2TeI_6 are fairly welldescribed by a Gaussian function. In contrast, both the I–I$_{inter}$ and Cs–I partials exhibit an asymmetric peak shape evidenced by the deviations from a Gaussian function shown in Figure 4.9, indicating that the overall peak asymmetry arises due to these atom pairs. It is important to note that the I–I$_{inter}$ and Cs–I pairs in both Cs_2SnI_6 and Cs_2TeI_6 exhibit slightly asymmetric peak shapes, and therefore we cannot unambiguously assign one compound as being more anharmonic than the other from these simulations. Instead,

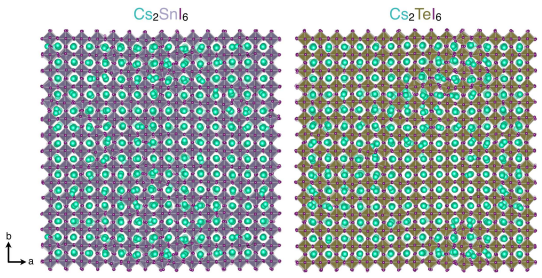

Figure 4.7: Supercell structures of Cs_2SnI_6 and Cs_2TeI_6 optimized from pseudo-rigid-body RMC simulations.

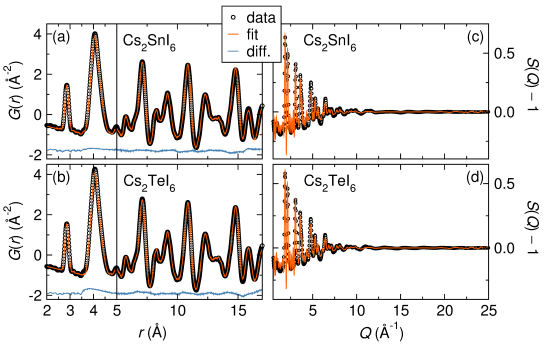

Figure 4.8: Calculated G(r) and S(Q)-1 from pseudo-rigid-body RMC-optimized supercells of Cs_2SnI_6 and Cs_2TeI_6 compared against the experimental G(r) and S(Q)-1 from X-ray total scattering data. Experimental data are shown as open circles, the fits from the RMC optimizations are shown as orange lines, and the difference curves are shown as blue lines. The x-axes in (a) and (b) are split to highlight the low-r pair correlations.

these simulations are consistent with the notion that anharmonicity in these compounds arises from octahedral rotations coupled with displacements of the Cs^+ cations.

In order to quantify the trends in anharmonicity across the intermediate members of the $Cs_2Sn_{1-x}Te_xI_6$ series, the asymmetry of the nnn pair correlation was modeled with a modified Toda potential, which has been previously used to describe anharmonic interactions between nearest-neighbors in a linear atomic chain. [199, 200] This modified Toda potential, U(r), takes the form

$$U(r) = \frac{\mu}{\beta^2} e^{-\beta(r-b)} + \frac{\mu}{\beta}(r-b) - \frac{\mu}{\beta^2}$$

where m is the elastic constant, b is the degree of anharmonicity, and b is the interatomic distance. Harmonic interactions are described in the limit as $b \to 0$. The potential, U(r), was approximated as the potential of mean force and then transformed to the reduced pair distribution

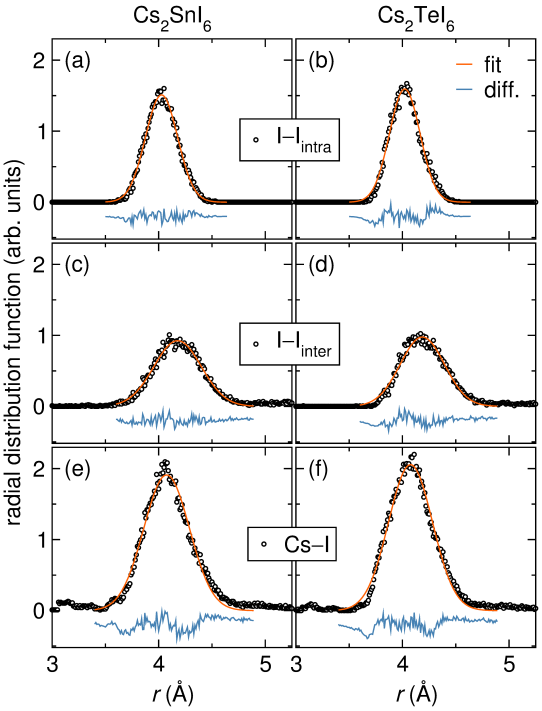

Figure 4.9: Partial radial distribution functions for I–I$_{intra}$ (a,b), I–I$_{inter}$ (c,d), and Cs–I (e,f) pair correlations in Cs_2SnI_6 and Cs_2TeI_6 obtained from pseudo-rigid-body Reverse Monte Carlo simulations (circles). The distributions are fit with Gaussian functions, shown by the orange line. The difference curves are shown in blue and reveal asymmetries in the I–I$_{inter}$ and Cs–I RDFs.

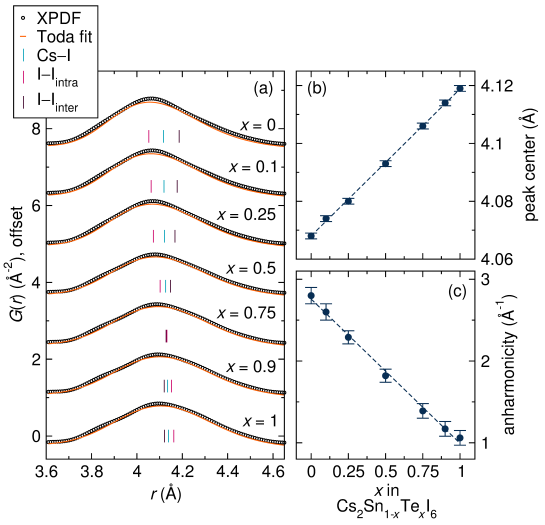

Figure 4.10: (a) Toda potential fits to next-nearest-neighbor pair correlation in the X-ray pair distribution function analysis for $Cs_2Sn_{1-x}Te_xI_6$. The data are shown as black circles and the fit is the orange line. The PDF data are fit with one Toda potential peak, and are offset vertically for comparison and clarity. In (b) and (c), the interatomic distance (b) and degree of anharmonicity (β) are plotted as a function of x in $Cs_2Sn_{1-x}Te_xI_6$, respectively. The colored tick marks in (a) represent the contact distances for Cs–I (teal), intraoctahedral I–I (pink), and interoctahedral I–I (purple) atom pairs taken from the refinements of the cubic model against the XPDF data from Figure 4.2. Dashed lines in (b) and (c) represent linear regressions.

function, G(r), via $G(r) = [(k_B T e^{-U(r)})/r] - 4r\pi\,\rho_0$, where ρ_0 is the average number density, N/V, of each member of the series. The transformed Toda potential was fit to the asymmetric pair correlation at approximately 4.1 Åin the XPDF for each member of the $Cs_2Sn_{1-x}Te_xI_6$ series (Figure 4.10a) using a non-linear least squares optimizer implemented in Python. In Figure 4.10b and c, the fitted parameters for the interatomic distance (b) and the degree of anharmonicity (β) are plotted as a function of x in $Cs_2Sn_{1-x}Te_xI_6$. From this analysis, we find that the interatomic distance (b) increases linearly with increasing tellurium content, consistent with the increase in Cs–I bond length extracted from fits to the XPDF data shown in Figure 4.3d. Of particular significance is the trend in the degree of anharmonicity (Figure 4.10b), which decreases linearly with increasing tellurium content, consistent with qualitative inspection of the fits to the XPDFs shown in Figure 4.2. We note that the Toda potential is conventionally used to describe anharmonic interactions in a linear atomic chain, and thus our use of the Toda potential to describe the more complex interactions in this system serves as a comparative analysis of the trends in anharmonicity between members of the $Cs_2Sn_{1-x}Te_xI_6$ series.

4.4 Discussion

Previous studies of anharmonicity in perovskite halides provide further insight into the atomistic origins of anharmonicity in the inorganic vacancy-ordered double perovskites presented here. In our previous study of the vacancy-ordered double perovskites $(CH_3NH_3)_2SnI_6$ and $(CH(NH_2)_2)_2SnI_6$, we observed significant tailing of the A–I/I–I pair correlation of the XPDFs of the hybrid compounds. In the hybrid compounds, the extensive tailing observed in the XPDF was attributed to coupled organic–inorganic dynamics via hydrogen bonding interactions resulting in a distinctly anharmonic potential. [70] However, the lack of hydrogen bonding interactions available in Cs_2SnI_6, yet asymmetry in he local coordination environment, indicates that the anharmonicity originates from a different source. We propose that the subtle deviations in the Cs–I/I–I pair correlations of the $Cs_2Sn_{1-x}Te_xI_6$ series arise from anharmonic lattice dynamics originating from $[BI_6]$ octahedral rotations coupled with displacements of the Cs^+ ions. Octahedral rotations in vacancyordered double perovskites have been studied at length by nuclear quadrupole resonance, which reveals that these modes are the dominant source of dynamics in these materials. [194–197] Furthermore, prior studies of inorganic perovskite halides $CsPbX_3$ and $CsSnX_3$ have shown that anharmonic lattice dynamics originate from coopetive tilting of the BX_6 octahedral units coupled with small displacements of the A-site cations within the cuboctahedral void. [167, 168, 201]

In the present study, the presence of octahedral rotations coupled with Cs^+ displacements is supported by analysis of the neutron total scattering experiments of Cs_2SnI_6; the concave-down shape of the curves for the Cs atoms and the I U_{22} = U_{33} atomic displacement parameters with increasing temperature follow a similar trend observed for localized vibrations associated with an ion rattling in a cage.45 Notably, the iodine atomic displacement parameter parallel to the Sn–I bond (U_{11}) remains relatively constant while the perpendicular displacements (U_{22} = U_{33}) increase significantly with temperature. This observation indicates that iodine displacements perpendicular to the Sn–I bond dominate over those parallel to the Sn–I bond, lending further support to the notion of octahedral tilting as the primary source of dynamics and anharmonicity in Cs_2SnI_6 (Table 1).

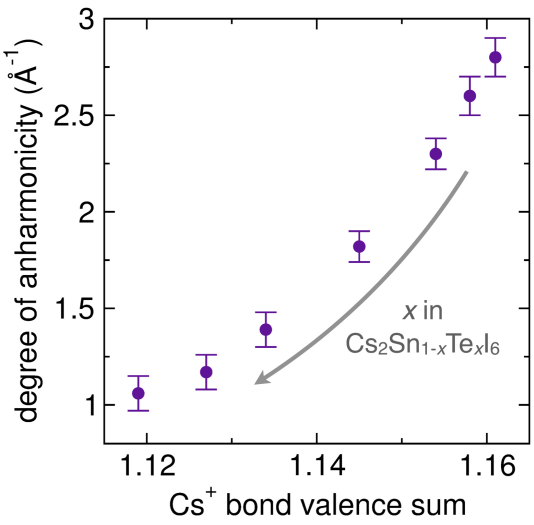

Figure 4.11: The degree of anharmonicity from the Toda potential fits plotted as a function of the Cs^+ bond valence sum.

Table 4.1: Bond valence sum analysis for Cs–I bonds in $Cs_2Sn_{1-x}Te_xI_6$. Cs–I bond lengths were taken from the XPDF and SXRD analyses. Values of B = 0.609 and R_0 = 2.6926 Å were used in calculation of the bond valence sum.

	XPDF		SXRD	
x	Cs-I length (Å)	BVS	Cs-I length (Å)	BVS
0	4.115	1.161	4.118	1.156
0.1	4.117	1.158	4.119	1.154
0.25	4.119	1.154	4.122	1.149
0.5	4.124	1.145	4.126	1.140
0.75	4.130	1.134	4.132	1.130
0.9	4.133	1.127	4.134	1.125
1	4.137	1.119	4.137	1.119

Anharmonicity in the vacancy-ordered double perovskites $Cs_2Sn_{1-x}Te_xI_6$ can be correlated with the bonding preferences of the cesium cation within the cuboctahedral void. In Figure 4.11, the degree of anharmonicity extracted from the Toda potential fits are plotted as a function of the Cs^+ bond valence sum. [202] For x = 1 (Cs_2TeI_6), the degree of anharmonicity is the lowest and corresponds with a bond valence sum of $\sim$ 1.12, suggesting that the Cs^+ is most optimally bonded in Cs_2TeI_6. As tellurium is replaced with tin, the bond valence sum of Cs^+ increases concomitantly with an increase in the degree of anharmonicity, reaching a maximum bond valence of $\sim$ 1.16 for Cs_2SnI_6. This analysis suggests that the anharmonicity is minimized when the size

of the cuboctahedral void satisfies the bonding preferences of the Cs^+ cation. Conversely, increasingly anharmonic lattice dynamics are therefore expected as the bond valence of the Cs^+ ion diverges from ideal coordination. The bond valence sum has previously been applied to other perovskite halide systems to predict the presence of dynamic and cooperative octahedral tilting distortions. [190,201,203,204] Bond valence sum calculations of the vacancy-ordered double perovskite Rb_2SnI_6 indicate that the coordination to the smaller Rb^+ ion is optimized by symmetry-lowering cooperative octahedral tilting distortions, [190] as is also observed in the $Cs_{1-x}Rb_xPbX_3$ (X = Cl^-, Br^-) series. [204] In the $Cs_2Sn_{1-x}Te_xI_6$ series, the Cs^+ coordination is nearly optimal in the cubic structural models, consistent with the observation that neither Cs_2SnI_6 nor Cs_2TeI_6 undergo structural phase transitions down to T = 10 K. [181] Rather, the slight deviations in bond valence sum in this system manifest as a small degree of anharmonicity. Therefore, anharmonic effects in vacancy-ordered double perovskites may be expected when the bond valence sum of the A-site cation deviates slightly from ideal, while more significant structural changes due to cooperative octahedral tilting may be expected if the A-site is significantly underbonded. As the properties of halide perovskites are intimately linked to (anharmonic) lattice dynamics, the bond valence sum provides a simple tool for predicting the presence and extent of anharmonic behavior and may further be leveraged as a design principle for materials with desired structure–dynamic–property relationships.

4.5 Conclusion

The series of vacancy-ordered double perovskites $Cs_2Sn_{1-x}Te_xI_6$ presents an interesting test case for anharmonic lattice dynamics. While each member of the series adopts the cubic vacancy-ordered double perovskite structure by high-resolution powder X-ray diffraction, the local coordination environment probed by X-ray pair distribution function analysis reveals subtle deviations. These deviations manifest as an emergent asymmetry of the next-nearest-neighbor pair correlation due to Cs–I and I–I atom pairs in Cs2SnI6, which gradually disappears with increasing telluriumcontent. Through analysis of temperature dependent neutron pair distribution function analysis

for Cs_2SnI_6, we propose that this asymmetry arises due to anharmonic lattice dynamics associated with coupled motions between the isolated SnI_6 octahedra and the Cs+ ions within the cuboctahedral void, supported by RMC simulations and the trends in atomic displacement parameters for the Cs and I atoms extracted from neutron diffraction data. Using bond valence sum analysis, we find that the valence for Cs^+ is optimized when tellurium occupies the B-site rather than tin. This observation is consistent with the trends in anharmonicity extracted from Toda potential fits, and suggests that the asymmetry observed in the Cs–I/I–I pair correlation in the XPDFs of Sn-rich samples originates from dissatisfied bonding preferences of the Cs^+ cation with the surrounding iodide cage. We further demonstrate that bond valence sum analysis can be correlated with anharmonic behavior in halide perovskites and used as a simple tool for predicting anharmonicity in perovskite halide systems.

Chapter 5

Finding order within the disorder of methylammonium tin iodide

5.1 Introduction

The proliferation of photovoltaics as a source of renewable energy has been slow due to this technology's relatively high construction cost compared to other renewable energy sources. [205] However, the entire sector has seen an overhaul with the introduction of low-cost, solution-processed perovskite materials with conversion efficiencies already reaching 24.2% which outperform that of other conventional photovoltaic materials such as Cu(In,Ga)(Se,S)$_2$, CdTe, and Si [62, 206] and even leads to an absorption coefficient higher than GaAs. [207] The unique properties of perovskite materials as photovoltaic absorbers and their versatility has been recently highlighted in a collection of reviews. [208] The most studied material in this family of 3D hybrid organic-inorganic perovskite (HOIP) is methylammonium (further denoted to as MA) lead iodide. [209] Due to the high toxicity of lead other alternatives, such as the germanium or the tin analog, have been the focus of attention. [206, 210] Large scale electronic property calculations of stable AMX_3 perovskites have shown that the optoelectronic properties of tin compounds are surpassing the ones of other non-toxic B-site cations. [211] In this work, we particularly focus on the vacancy-ordered double perovskite methylammonium tin iodide $(MA)_2SnI_6$. The archetypal structural building block of a vacancy-ordered double perovskite are the octahedral building block units composed of B-site cations (Sn^{4+}), residing in the center of the octahedron, surrounded by six X-site anions (I^-). These octahedra are isolated from each other with A-site cations (MA^+) between them (Figure 5.1).

These unique structural features of non-connected octahedra, generate a very soft lattice with an increased level of degrees of freedom which is one noticeable difference to conventional materials.

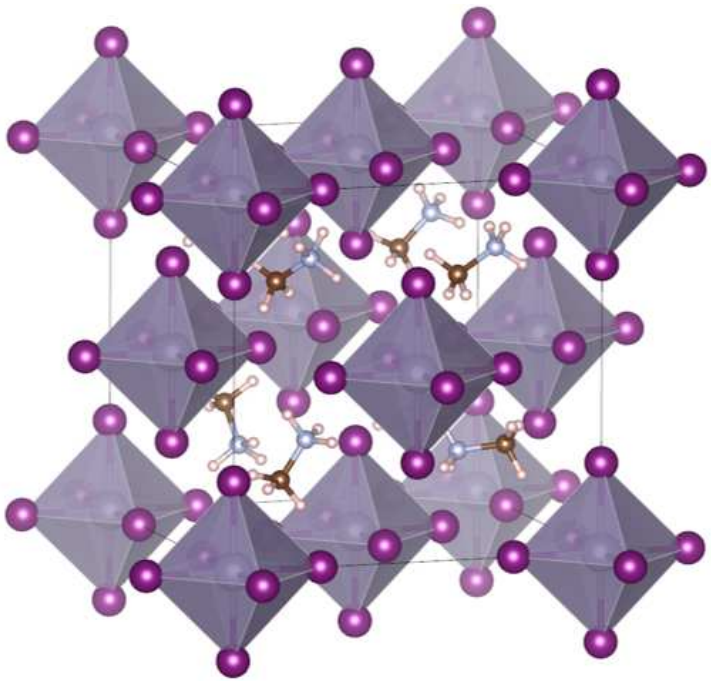

Figure 5.1: The schematic crystal structure of the vacancy-ordered double perovskite $(CH_3NH_3)_2SnI_6$ with an arbitrary depicted orientation of the $CH_3NH_3^+$ molecules.

Lattice softness in hybrid organic-inorganic perovskites has already shown to lead to improved physical properties such as polaron formation enabling extended lifetimes of excited states [212] or reduced carrier mobilities [178]. Despite the lack of octahedral connectivity in $(MA)_2SnI_6$, it is an n-type semiconductor with an optical band gap of about 1.35 eV and Hellwarth electron mobility of 52 cm^2/Vs. [70]

The valence and conduction band edges of halide perovskites are mainly determined by the inorganic octahedral framework, composed of the metal and halogen atoms, governing the light absorption and charge transport processes. [181, 213–217] For example, substitution of X-site anions has shown to change band dispersion [217, 218], while B-site substitution influences the magnitude of the band gap. [181, 219] Furthermore, it was shown that the band gaps of the A_2SnI_6 series are mainly determined by the dispersion of the conduction band influenced by the iodine sublattice. [70] While the organic A-site cation does not directly affect the electronic structure, it can indirectly influence the electronic band structure by changing the spacing between the octahedra which further changes the inorganic lattice and the unit cell size. [181, 219, 220] This can also lead to co-

operative tilting of the octahedra based on the size of A-site cations. [217, 221, 222] Furthermore, A-site cations such as NH_4^+ can strongly interact through hydrogen-bonding with the X-sites inducing distortions of the octahedral network influencing, for example, phase-transitions [223, 224] or low-temperature structural behavior [225].

Hence, it is important to understand the interplay between the organic cations and the inorganic orctahedral framework. Due to the lack of octahedra connectivity, the vacancy-ordered double perovskites are ideal for studying the coupling between the organic and inorganic lattice. A previous study done in the Neilson group showed that organic A-site cations strongly influence physical properties by inducing octahedral tilting. [70] There, the relationship between the experimentally measured carrier mobility, the calculated electron band effective mass and the carrier scattering mechanisms could not be explained by the standard mathematical models for carrier scattering mechanisms [226–228]. This suggested that there might be further contributions to the charge transport in the A_2SnI_6 series. The anomaly was explained with structural distortions arising from anharmonic atomic displacements of the I-I distances between octahedra in the local coordination range of 3.5 to 5 Å. The local structure of the iodine sublattice could not be modeled using the cubic structure with harmonic atomic displacements, suggesting a strong anharmonic influence, which also manifest in the all-inorganic vacancy-ordered double perovskites [229].

This anharmonicity of dynamic octahedral rotations appears in other vacancy-ordered double perovskite compounds [195, 196], as determined by nuclear quadrupole resonance spectroscopy. Further studies, using nuclear quadrupole resonance and proton magnetic resonance spectroscopy, showed simultaneous reorientation of octahedra and methylammonium cations. [230–232] In our previous PDF study, we showed that the degree of anharmonicity increases in the presence of dynamic organic molecules. [70] It was therefore assumed that the coupling between the organic and inorganic units has a big influence on the anharmonicity and thus electronic properties.

To further understand the nature of this coupling, the orientations of the MA molecules need to be determined, and described with respect to the inorganic lattice. Neutron scattering was used to investing MA orientations within $CH_3ND_3PbBr_3$ at 11 K [233] and on $CH_3NH_3PbI_3$ at 180

K [234]. Their results found preferred orientations and showed that the NH_4^+ group can form hydrogen bonds to the halogen atoms. However, it was argued that even at low temperatures the refinements of pure hybrid organic perovskites are difficult based on remaining lattice disorder. [235] Once heated above the temperature of 180 K, Weller *et al.* found that the MA cation becomes orientationally disordered along the three unit cell directions with weak NH-I interactions. This is similar to what was seen at higher temperatures for $CH_3NH_3PbX_3$ (X = I, Br and Cl) using single crystal X-ray diffraction as well as single crystal Laue neutron diffraction confirming the disordered nature of the MA. [236] The tumbling motion of the MA molecules was also experimentally observed by other techniques such as millimeter wave spectroscopy, NMR spectroscopy, and dielectric measurements. [237–240] For example, ^{1}H and ^{13}C NMR spectroscopy indicated that methylammonium does not have a fixed position. However, the unusually long carbon relaxation times suggest that only the NH_4^+ group of the MA interacts with the inorganic framework. Similar to these previous studies, due to dynamic disorder of the MA cation, unique positions could not be identified with XRD by Maughan *et al.* [70]. Therefore, at elevated temperatures the general assumption is that the positions of the organic cations are dynamically averaged in 3D HOIPs, but still interacting with the inorganic sublattice.

Theory-based techniques can provide further insight into the correlated nature of octahedral tilting and molecular reorientations, but they are not easy. Since the materials proposed applications of semiconducting nature, quantum mechanical descriptions of the systems are desired using approches such as Density Functional Theory (DFT) calculations. This was used to examine hydrogen-bonding and its influence on octahedral rotations in $CH_3NH_3PbI_3$. [241] Their structure optimization yielded comparable results to the experimental data acquired by Weller *et al.* at 100 K. [234] The theoretical studies for C-N bonds in the MA cations indicated preferred alignment about the [101] and [10$\bar{1}$] directions with a head-to-tail configuration with the most stable configuration being staggered. Their calculations also showed that a non-titled octahedra structure leads to reduced hydrogen-bonding indicating that the octahedra tilting is highly correlated with hydrogen-bonding interactions. While these quantum mechanical calculations deliver a precise picture, they

are computationally very expensive. On the other side, molecular dynamics simulations need long simulation times due to the rotational degrees of freedom of the organics and the anisotropy in the dynamics of the halide anions. A well-established compromise in the field, between these two aforementioned techniques, are Ab Initio Molecular Dynamics (AIMD) simulations. AIMD was used to highlight the interplay of the inorganic and organic components. This technique showed that the orientations of the MA molecules in $MAPbI_3$ are not completely random and the order is mediated by cage stress and strain effects in addition to deformation and rotations of the octahedra. [242] In the cubic phase, which is the high-temperature phase, the octahedra are almost not rotated and all molecules are aligned in a ferro-electric ordering pattern. However, at that temperature it is dynamically unstable leading to rotating MA cations. Overall, it was observed that the nitrogen side of the molecule is closest to the X-side anions I^-. These results presented by Lahnsteiner *et al.* are in good agreement with previous AIMD and classical MD calculation for 300 K. [243, 244] The results from an AIMD simulation at 400 K for MA orientations in $MAPbI_3$ showed a mixing between the directions toward a cubic cell facet, a halogen atom, and the center of an octahedron, with preference for the halogen atoms and less preference for the center of the octahedron. [245]

While computer simulations are not always straightforward when it comes to disorder [243, 246, 247], introducing additional tools, such as the concept of pseudo spins, [248] has further advanced the possibility for rigorous group symmetry analysis in the hybrid organic-inorganic $CH_3NH_3PbI_3$ perovskites. This approach has already supported analyzing orientations of the organic A-site cations MA and FA in AIMD siulations. [245, 249]

Theoretical studies are good as initial trials, but there is the need to confirm these results experimentally. However, direct measurement of these interactions is difficult and there are not many analytical techniques capable of determining the interplay between the organic and the inorganic species. One analytical technique capable of directly measuring coupling between organic and inorganic lattice is two-dimensional terahertz-infrared-visible spectroscopy. [250] Grechko *et al.* were able to correlate the high-frequency N-H stretch modes of the methylammonium and the low-

frequency Pb-I phonon modes of the inorganic lattice in $MAPbI_3$ with this technique. [251] While this method can identify coupling at room temperature, it is challenging to extract geometrical data allowing identification of the alignment of the MA in correlation to the inorganic octahedral units.

In this current study we use room temperature total scattering data as an input for large-box structural modeling to get a detailed view into the structure of the hybrid organic-inorganic halide perovkiste $(MA)_2SnI_6$. The combination of X-ray total scattering and neutron total scattering provides sensitivity to the light and heavy elements within the structure and to evaluate the interplay of each methylammonium cation with its nearest neighbor [SnI_6] octahedron. We were able to show that the MA cations are mainly preferentially orientated along the $\langle 111 \rangle$ and the $\langle 110 \rangle$ directions. Additionally, we could confirm previously published results indicating that the [SnI_6] octahedra are randomly tilted up to 11° in any direction. [70]

5.2 Experimental Methods and Materials

Note on author contributions: This chapter will be submitted for publication in the journal Physical Review Materials by Arnold A. Paecklar, Annalise E. Maughan, Daniel Olds, Katharine Page, and James R. Neilson. AAP designed and performed the RMC modeling approach, wrote the code for analyzing the results, and wrote the initial draft. AEM was responsible for synthesizing the material and for collecting the neutron and X-ray data. DO wrote the initial code for subtracting of the hydrogen background and rebinning the neutron data. KP helped with collecting the total scattering data. JRN supervised the project, helped with data analysis and the neutron experiment. All authors are contributing to editing and finalization of the manuscript.

5.2.1 Synthesis of Material

The synthesis of the $(MA)_2SnI_6$ was reported previously [70], but is briefly outlined again here:

Preparation of Methylamine Hydroiodide ($CH_3NH_2 \cdot$ HI): Methylamine hydrochloride (0.5 g) was added to 2.0 mL of hydriodic acid (57%, aqueous, 1.5% H_3PO_2) and 3.0 mL of absolute ethanol and stirred until dissolved. Afterwards, the solution was cooled in an ice bath while stir-

ring. The product, a sparkly white precipitate, was attained by adding diethyl ether to the solution. The precipitate was washed thoroughly with diethyl ether until no yellow color was visible and separated by centrifugation. After drying the product overnight, energy dispersive X-ray spectroscopy was used to measure the impurities by determining the molar ratio of 0.04 for [Cl]:[I].

Preparation of Tin(IV) Iodide (SnI_4): Tin metal (0.3108 g) and iodine (1.3347 g) were reacted in an evacuated, fused silica ampule (1.3 kPa). The ampule was heated in a furnace at 200 °C for 60 h until the purple vapor had subsided. Then the sample was quenched in air to yield bright orange-yellow SnI_4 powder.

5.2.2 Characterization

Energy-Dispersive X-ray Spectroscopy (EDS): EDS measurements were performed with a JEOL JSM-6500F field emission scanning electron microscope equipped with an Oxford 80 X-MAX (80 mm) SDD detector using a 15 kV beam. Polycrystalline powders of CH_3NH_2·HI and $(CH_3NH_3)_2SnI_6$ were measured on Cu-tape. The average molar [Cl]:[I] ratios were determined from the average of 6 scans taken at 1000x magnification in macroscopically separated locations of the samples.

X-ray Total Scattering:

Synchrotron X-ray total scattering data, suitable for Pair Distribution Function (PDF) analysis, were collected on beamline 11-ID-B at the Advanced Photon Source, Argonne National Laboratory, using 86 keV photons and a sample to detector distance of 25 cm. Powdered samples were loaded into polyimide capillaries and measured in transmission mode at room temperature using a PerkinElmer amorphous silicon image plate detector. [182] Experimental PDFs were extracted using PDFgetX2. [252] The program Fit2D was used to calibrate the sample to detector distance and detector alignment with data from a CeO_2 powder standard. Raw scattering data were integrated in Q-space, applying a mask and polarization correction during integration. The total scattering structure functions, S(Q), were calculated in PDFgetX2 by subtracting the background scattering arising from the polyimide container, utilizing the appropriate sample composition, and applying

standard corrections for the area detector setup. [253] Pair distribution function patterns, G(r), were calculated via Fourier transformation of the S(Q) data utilizing a maximum momentum transfer, Q, of 20 $Å^{-1}$ for $(CH_3NH_3)_2SnI_6$.

Neutron Total Scattering:

Temperature-dependent neutron total scattering data were collected on the Nanoscale Ordered MAterials Diffractometer (NOMAD) at the Spallation Neutron Source. [186] The MA_2SnI_6 powder sample were measured in a vanadium container. Samples containing hydrogen are usually deuterated due to the high incoherent scattering cross section of hydrogen. Additionally, hydrogen's negative scattering cross section can cancel out postive scatterering. However, it was also shown that deuterium substitution strongly influenced phase transition in the $CD_3ND_3GeCl_3$ perovskite material [254] as well as in the vacancy-ordered ammonium and alkylammonium perovskites [255]. Additionally, since it was previously shown that sufficient data collection could be achieved without deuteration in $CH_3NH_3PbBr_3$ [256] and $CH_3NH_3PbI_3$ [257], the MA_2SnI_6 sample was not deuterated. This led to the collected total scattering data containing a high background signal from the incoherent scattering of hydrogen. It is generally possible to collect neutron data with sufficient quality from undeuterated samples and appropriate treatment of the background. [258–260] Here, the hydrogen signal was manually subtracted from the raw Time-Of-Flight (TOF) data by fitting the background signal in each constant-angle detector bank with a pseudo-voigt function. The corrected signal for each detector bank was evaluated and truncated based on subjective evaluation of the data quality. Then, the total scattering structure functions and the PDFs were calculated for each detector bank and rebinned in one data set. Since it was difficult to objectively determine the optimal TOF-data range for each corrected bank, three different neutron total scattering data sets were generated. The first set containing data from the detector banks 1 to 5 (Table 5.1), the second set had the TOF-data range from these banks decreased by about 5%, and the third data set had the same data range as set two, but without the data from detector bank 1 (Table 5.1). The data from Bank 6 was altogether removed due to the low signal-to-noise ratio.

Reverse Monte Carlo modeling:

Table 5.1: The NOMAD detector bank ranges that were used for generating the neutron total scattering data sets.

	Original Range		
Detector	TOF-range (μs)	d-range (Å)	Q-range (Å^{-1})
Bank 1	50 - 2500	0.58 - 7.17	0.88 - 10.69
Bank 2	1600 - 2500	1.46 - 3.92	1.60 - 4.30
Bank 3	700 - 2600	0.28 - 2.48	2.53 - 22.24
Bank 4	0 - 2800	0.24 - 1.44	3.62 - 49.81
Bank 5	20 - 2900	0.23 - 1.12	4.35 - 49.12

	Reduced Range		
Detector	TOF-range (μs)	d-range (Å)	Q-range (Å^{-1})
Bank 1	550 - 2450	0.63 - 6.75	0.93 - 10.03
Bank 2	1622 - 2477	1.50 - 3.82	1.64 - 4.20
Bank 3	747 - 2552	0.30 - 2.35	2.67 - 21.09
Bank 4	70 - 2730	0.25 - 1.38	3.86 - 46.66
Bank 5	92 - 2828	0.24 - 1.08	4.62 - 46.23

Reverse Monte Carlo (RMC) modeling was performed with 6 x 6 x 6 supercells of the cubic structure of $(MA)_2SnI_6$ (a = 72.097 Å) containing 19,872 atoms. The starting structures were based on the previously published refinement results with octahedral units randomly tilted up to 11.2° and the MA molecules randomly rotated. [70] The orientations of the MA molecules are illustrated in the Appendix C. Three sets of simulations, each containing 240 individual simulations with the same input data and starting structure, were run in parallel using GNUparallel [261] on 10 nodes with 24 cores each on the High-Performance Computing (HPC) system called SUMMIT. [262] Due to the runtime restrictions, one full simulation was split into 10 segments and run in serial using the workload manager SLURM. [263] Each individual segment generated an optimized output structure which served as the starting configuration for the next run. This set-up also enabled the option of easy restarts in case of any error or system failures.

Each distinct simulation was constrained in reciprocal-space by neutron scattering data as S(Q)-1 (0.8 - 40 Å^{-1}) and X-ray scattering data s S(Q)-1 (0.7 to 24 Å^{-1}), and in real-space by the neutron pair distribution function (0.9 to 19.99 Å) and the X-ray pair distribution function (0.9 to 18 Å), G(r). Both S(Q)-1 data sets were convolved with a Gaussian function with a full-

width-half-maximum of 1/2 the length of the supercell edge prior to use in simulations in order to capture appropriate peak broadening due to finite size of the box. [187] Additional constraints were set for coordination number as well as inter molecular distances (1 Å) and intra molecular distances (1 Å). The experimental data were modeled using a RMC approach within the fullrmc package (version 3.3.0). [188] Pseudo-rigid-body RMC modeling was performed, in which the MA molecules and [SnI_6] octahedra were randomly rotated and tilted as rigid units, prior to and after their free relaxation. This included first the relaxation of the individual atoms starting with the $CH_3NH_3^+$ molecule. C–N, C-H and N-H bond lengths were constrained between 1.2–1.7 Å 1.0–1.2 Å and 1.0–1.2 Å respectively. The bond angles for H-C-H, H-C-N, H-N-H and H-N-C were all constrained to 100–120°. This was done step wise first between 0.9 Å and 2.5 Å. After initiating the refinements with only the intramolecular MA bonds, the bond lengths were frozen and the intraoctahedron bonds were allowed to be refined. The Sn–I bond lengths were constrained between 2.6 to 3.05 Å and the orthogonal I–Sn–I bond angles were constrained to 80 – 100°. After initiating the refinements with only the intraoctahedron bonds, the refinement range was increased step wise to include longer-range pair correlations while all atoms were permitted to displace in the Cartesian reference. After the full G(r) fitting range was reached, and after a finite number of atomic displacements, the octahedra were constrained as rigid bodies (Sn–I bond lengths and angles were frozen). As so, they were allowed to tilt about the center of the octahedra around each crystallographic axis up to a maximum tilt angle of 10° followed by moves along the three crystallographic axes up to a maximum of 0.2 Å. Afterwards, the methylammonium were constrained as rigid bodies (all bond lengths and angles were frozen) and allowed to move. Similarly, they could rotate about the center of mass around each crystallographic axis up to a maximum rotation angle of 180° followed by movements along the three crystallographic axes up to a maximum of 0.2 Å. Finally, the MA molecules were allowed to randomly move and rotate up to 0.2 Å and 10°, respectively. The entire fitting process was reiterated three times from the start to achieve the final configurations.

5.3 Results and Discussion

As was pointed out above, some of the desired physical properties in materials originate from structural disorder. However, disorder in crystalline materials arises from non-periodic defects which are difficult to analyze and use to control structure-property relationships. The standard tools, using only Bragg diffraction data, provide only the average atomic positions and cannot elucidate non-periodicity. In order to gain further insight into the local atomic arrangement within a material, Pair Distribution Function (PDF) analysis can be used. [42] The most common way to model the PDF data is by refining atomic positions within their unit cell using programs such as PDFgui. [264] However, very often these "small box" approaches cannot fully describe complex disorder and, for example, describing antiferrodistortive local order, such as tilting, cannot be done with the use of only one cell. [265]

Hence, to better describe aperiodic structures, large unit cells without explicit symmetry operations can be combined with both local as well as average structure information into the modeling process. This can be done with the Reverse Monte Carlo (RMC) method. RMC was developed for very disordered structures such as liquids and glasses but has also been advanced for analyzing crystalline materials. [266–269] While there are a number of different programs and codes available allowing the integration and treatment of different structural information and even considering force fields, [270–272] we specifically selected the package fullrmc based on its capabilities of individually defining and refining rigid bodies. [188] Despite RMC's previous use in structural refinements for orientations of CN molecules [273, 274] as well as perovskite structures [229, 275–281] it has not been used for describing HOIPs.

One RMC run can be seen as a single simulation and yields only one possible snapshot of the system in dynamic disorder. While there are multiple constraints in place during the modeling process, a modeling result is not a unique solution and many different structures can fulfill the same given constraints. To improve the likelihood of getting a better representation of the real, dynamic structure, multiple snapshots were collected. To build a statistical description of the disorder, many simulation runs are analyzed in ensemble.

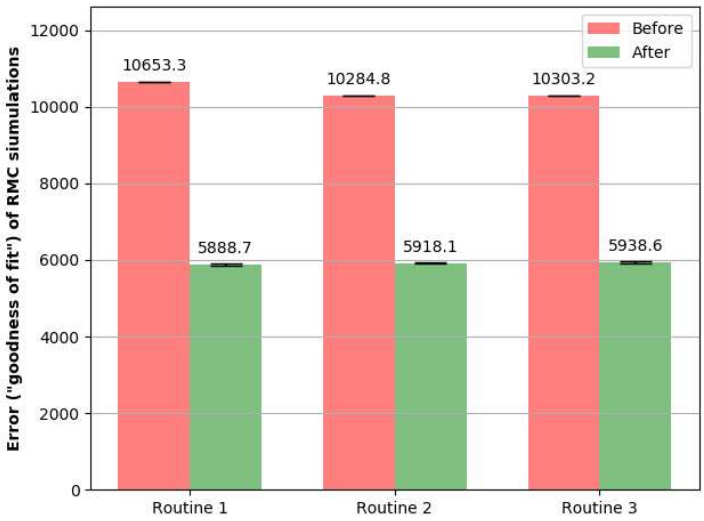

Figure 5.2: Bar graph highlighting the average error before and after the outlined RMC modeling procedure for each of the three input neutron scattering data. Error bars are shown in black.

For our system we chose to use 240 modeling approaches for each of the three slightly modified neutron data set. Each of the 720 structural models was optimized by decreasing the difference between the calculated and the experimental S(Q)-1 and G(r) pattern determining the error representing a Goodness-of-Fit variable. Despite the same starting structures for all simulations, the final errors and structures differed from each other confirming the randomized selection and optimization process during the fitting processes. The final error values were extracted and averaged after the above described modeling procedure was concluded. In Figure 5.2, the error values for each of the three batches of 240 runs is shown for before and after the refinement. It can be seen that the modeling with the slight variations in neutron data sets did not result in a statistically significant difference in the error values.

Similarly, the calculated neutron PDF (nPDF) (Figure 5.3) and S(Q) function (Figure 5.4) were averaged over each simulation batch containing 240 individual simulations and compared to the experimental data. Since the small changes in the input neutron data did not result in significant changes in either the error or the nPDF fits, the optimized structures from the three data sets were combined and analyzed as one data set.

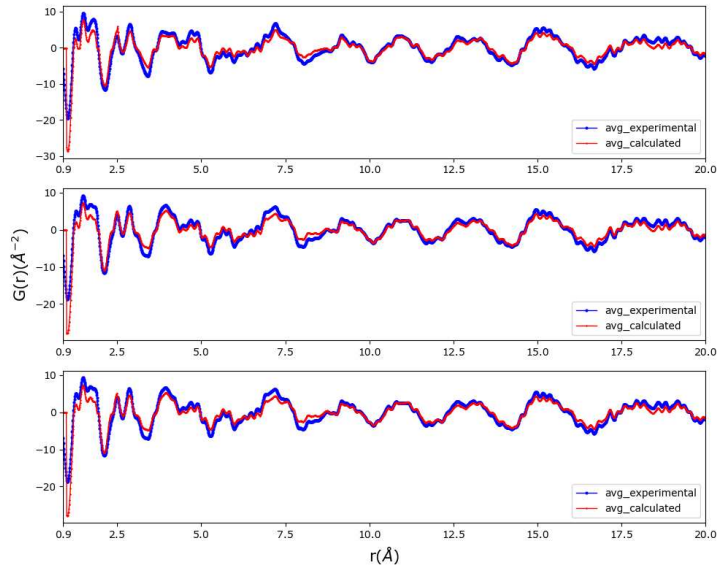

Figure 5.3: Averaged experimental and calculated neutron PDFs for each neutron scattering data based on the a.) original range, b.) area decrease by about 5%, and c.) area decreased by about 5% and also bank 1 omitted.

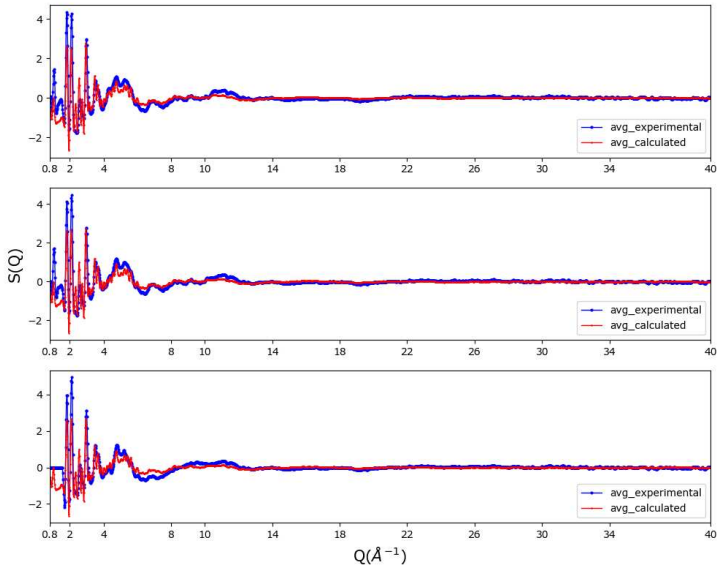

Figure 5.4: Averaged experimental and calculated neutron S(Q) for each neutron scattering data based on the a.) original range, b.) area decrease by about 5%, and c.) area decreased by about 5% and also bank 1 omitted.

While initial, visual inspection of the refined structures can easily be done with crystal structure visualization programs [189, 282], when it comes to larger structures limitations are quickly faced. Therefore, we developed our computational analysis routine for the vacancy-ordered double perovskite $(MA)_2SnI_6$ as described in the following sections. The code for this computational analysis is publicly available on github. [283]

5.3.1 Qualitative Observations

Due to the dynamic nature of the methylammonium, their corresponding pair correlations result in rather broad peaks. Therefore, paired with the high weighting of its atoms comprised in the nPDF, it is difficult to interpret the nPDF data visually. One particular distinguishing feature in the nPDF from the X-ray PDF (XPDF), are negative pair correlations which are based on the negative coherent scattering length of hydrogen. The XPDF data (Figure 5.5) is mainly sensitive to the heavier atoms iodide and tin representing the inorganic framework; the first sharp peak can thus be attributed to the Sn-I distances. The second peak in the XPDF comprises the I-I distances along the edges of the $[SnI_6]$ units. The broad peak suggests some plasticity and that the octahedra are not completely rigid. An additional noteworthy feature is the tailing on the higher r-side which was previously attributed to anharmonicity. [70] The lack of rigidity can also be described by the off-centering of the Sn^{4+} atoms (B-sites) within the $[SnI_6]$ octahedra (Figure 5.6). This was determined by calculating the theoretical centroid position of the octahedra, based on the six I-atom positions, and compared to the actual Sn positions in each octahedra. Figure 5.6 shows that the maximum of the off-centering is located at 0.116 Å. Similarly, previous local structure studies on $CsSnBr_3$ [67], $FASnI_3$ and $MASnI_3$ [69] have found dynamic, temperature activated B-site cation off-centering. However, the authors showed much higher levels of displacement for the Sn^{2+} (0.2 Å($CsSnBr_3$), 0.24 Å($FASnI_3$), and 0.22 Å($MASnI_3$)) compared to what we observed for the Sn^{4+}. These displacements found for Sn^{2+} compounds are attributed to the stereochemical active s^2 lone pair and are suggested to be responsible for their remarkable defect tolerant electronic properties. [69] Indeed, the lack of a lone pair did not result in an off-centering for another perovskite with

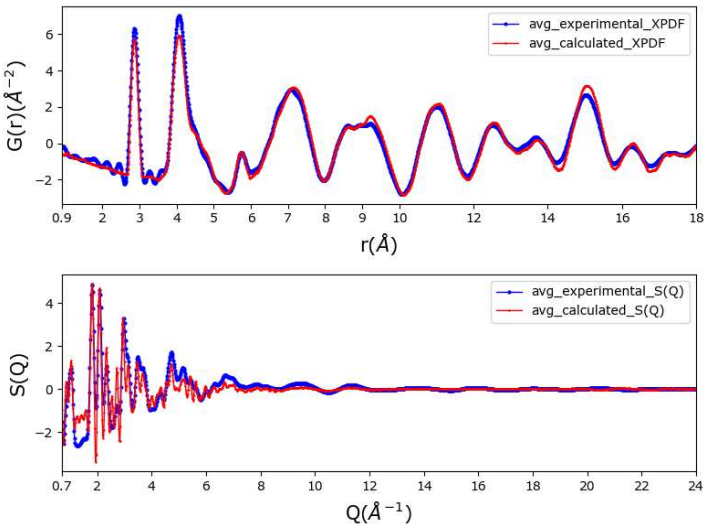

Figure 5.5: Averaged experimental and calculated X-ray PDF (top) and S(Q) data (bottom) for all 720 RMC modeling runs.

a divalent cation such as $CsCaBr_3$. [67] Contrary to these literature reports, our observation of a decreased level of off-centering for the Sn^{4+} cannot be purely based on atomic displacements based on thermally induced motions and other mechanism might play a role here.

The partial X-ray pair correlations for Sn-Sn are shown in Figure 5.7. The first peak at about 8.5 Å represents the Sn-Sn correlations across neighboring octahedra. The succession of the peaks in a fashion of a, $\sqrt{2}$a, $\sqrt{3}$a, and 2a, shows that, despite high degrees of freedom and disorder, the cubic order is still maintained on average within the inorganic structure. Figure 5.7 also illustrates the partial neutron and X-ray C-I and N-I pair correlations. The higher amount of pair correlations for the N-I between 3 and 5 Å provides indirect support that the methylammonium preferentially aligns closer to the octahedra with the nitrogen side. This could further suggest hydrogen bonding between the organic and inorganic framework as previously observed. [241]

5.3.2 Orientation of the methylammonium cations

To understand the coupling between the inorganic and organic sublattice, knowledge about MA cations orientation preferences is needed. For example, theoretical studies showed that a random disorder of MA cations alone can lead to an increase in charge carrier lifetimes. [284] Leguy *et*

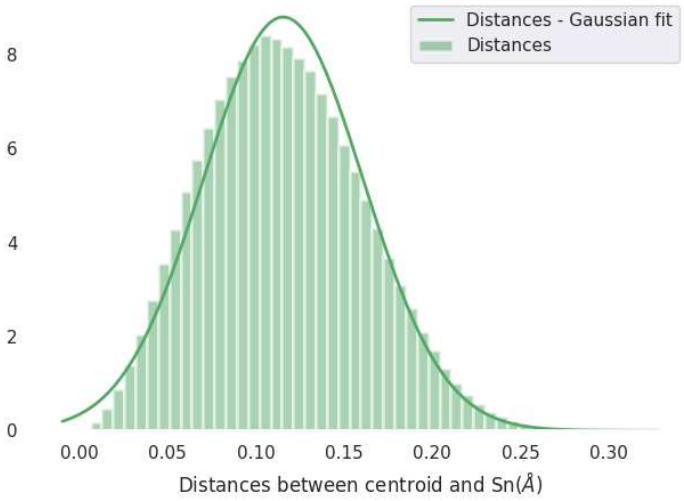

Figure 5.6: Histogram showing the displacement of the Sn atoms from the centroids of the octahedra. A fit to the data based on a Gaussian function is depicted in green.

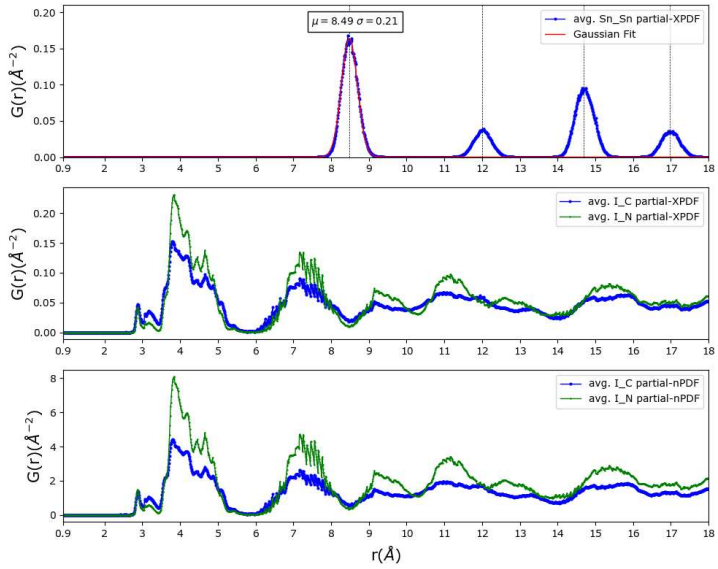

Figure 5.7: Averaged partial X-ray pair correlation function for Sn-Sn (top), I-C and I-N (middle), and partial neutron pair correlation function for I-C and I-N (bottom).

al. [285] hypothesized that localization of the MA cations could increase carrier lifetimes even further enabling observed long-carrier collection lengths [286].

To shed more light on this, we tried to address the question about whether the methylammonium has a preferred crystallographic orientation by plotting the combined MA molecule orientations. To gain access to the average orientation, the coordinate system was changed from Cartesian to spherical coordinates. First, the absolute coordinates of the C and N atoms were used to create vectors, $\vec{r}_{CN}$=($\vec{r}_N$ - $\vec{r}_C$), representing only the axes in the MA molecules, followed by transformation of their x,y,z coordinates into local spherical coordinates (ϕ, θ). The polar angle, ϕ, is measured with respect to the positive direction of the z-axis, and the azimuthal angle, θ, is measured on the xy-plane from the positive direction of the x-axis. This approach is similar to what was done for published results from AIMD simulations. [242, 249]

In order to understand the molecular order at 300 K, the C-N vector orientations were plotted as a 2D histogram, first over the entire ϕ and θ (0 to 180° and 0 to 360°) range, followed, due to the cubic symmetry, by down folding into the representations projected on the unit sphere (0 to 90° and 0 to 90°) (Figure 5.8). Each plot summarizes the behavior of 1,244,160 MA molecules from all the 720 simulations with 1728 MA molecules each. While plotting the entire range shows a very diffuse picture, the folded plot clearly highlights two preferred MA orientations with the highest density for the center of the bin at $\langle\theta\rangle$= 59.52° ± 1.45° and $\langle\phi\rangle$= 45° ± 1.45° and the center of the bin at $\langle\theta\rangle$= 88.55° ± 1.45° and $\langle\phi\rangle$= 50.81° ± 1.45°. These angles correspond closest to the crystallographic $\langle 111\rangle$ direction (θ=54.736°, ϕ=45°) and the $\langle 110\rangle$ direction (θ=90°, ϕ=45°). Since the intensities of $\vec{r}_{CN}$ vectors distributions do not drop to zero outside the two high density areas, it is suggested that the molecules are indeed quite disordered which confirms the experimentally observed macroscopic picture of a disordered MA system. [236] As controls, reference structures were also generated for specific set crystallographic orientations ($\langle 111\rangle$, $\langle 110\rangle$, $\langle 100\rangle$) of the MA cations (Figure 5.8). In addition, the MA molecules from the starting structure (aligned in $\langle 111\rangle$) were also randomly rotated about the three Euler angles to create a uniform spherical distribution. All these data were also created by combining the results from 720 individual 6×6×6 supercells.

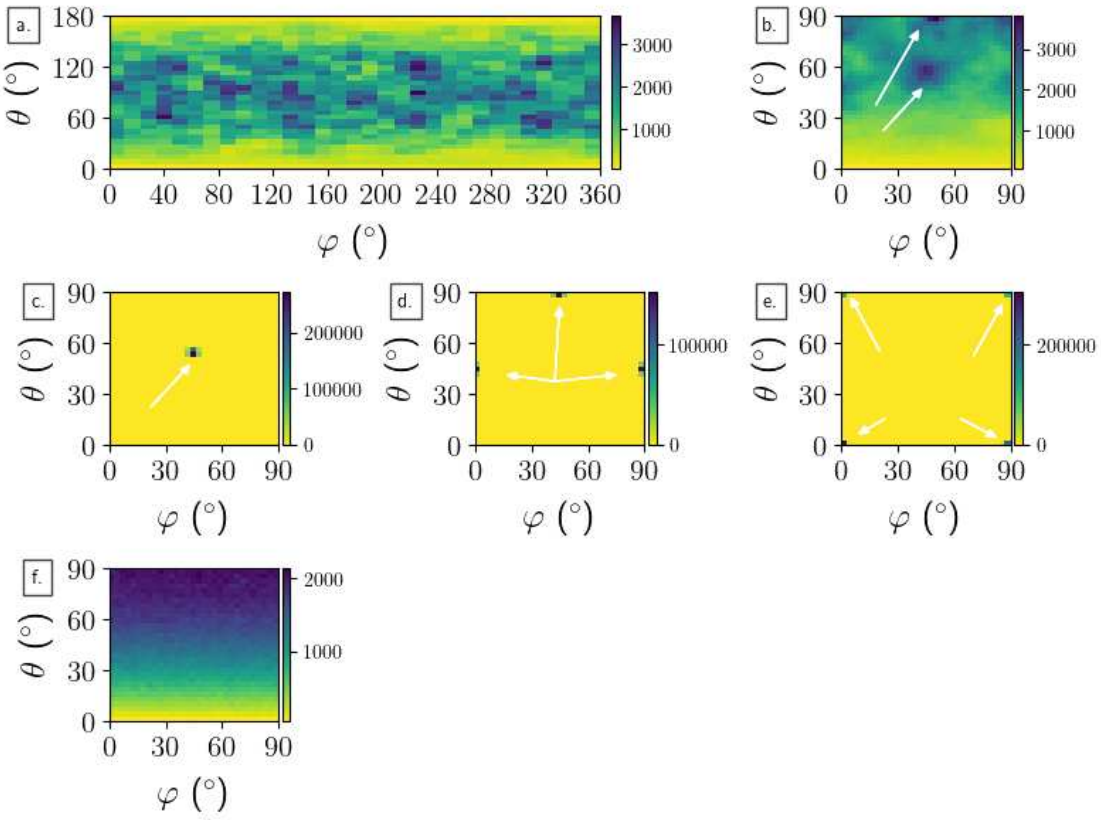

Figure 5.8: Histogram of the C-N-vector in spherical coordinates folded to 0 to 90° for a.) the combined data from RMC modeling b.) the ⟨111⟩ direction with up to 2° noise, c.) the ⟨110⟩ direction with up to 2° noise, d.) the ⟨100⟩ direction with up to 2° noise, and e.) the random rotation of MA.

In addition to the two-dimensional analysis of the MA cations (Figure 5.8), we also illustrated the orientations of the MA by generating a three-dimensional kernel density estimate plot of the nitrogen positions. First, the supercells were tiled into the unit cell followed by tiling it further into a quarter of its volume. This way the 8 different MA sites in the unit cell can be overlayed in one position. Further, to depict the MA orientations, only the nitrogen positions are plotted (Figure 5.9). Since the data from the RMC modeling is noisy, only the positions corresponding to the 1% with the highest density were highlighted. There, higher levels of density can be found for the crystallographic directions of ⟨111⟩, ⟨110⟩, as well as ⟨100⟩. Despite ⟨100⟩ appearing in the plot of the highest 1% density, it does not have as high of a density in in the 2D plot compared to ⟨111⟩ and ⟨110⟩. This might be explained by taking the entire density range in to account and combining the density sums of all four quadrants of the sphere.

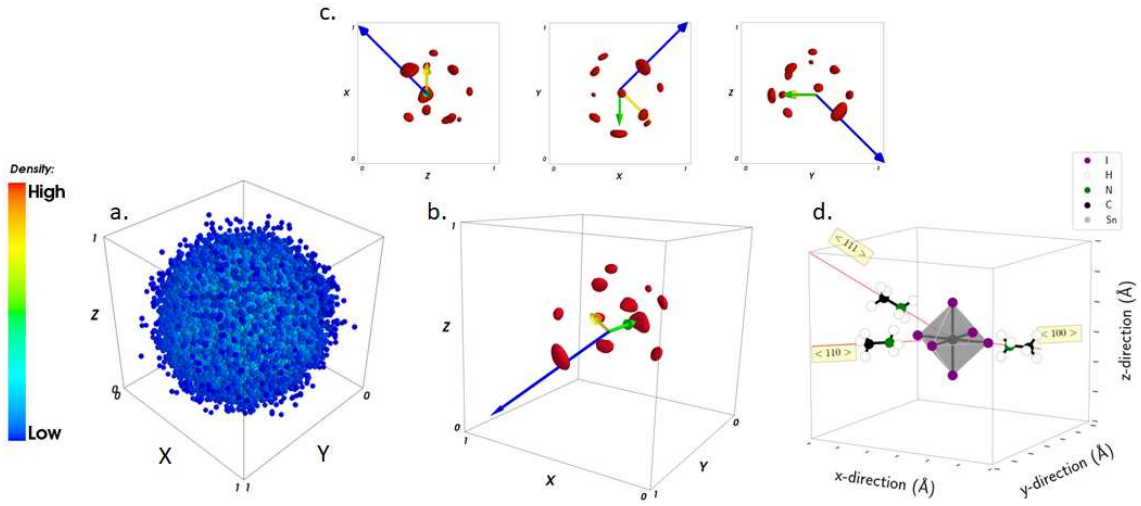

Figure 5.9: Three-dimensional kernel density estimate (KDE) of the nitrogen positions within the folded unit cell (a.) and only the highest 1% KDE (b.) highlighting the $\langle 111 \rangle$ (blue arrow), the $\langle 110 \rangle$ (yellow arrow), and the $\langle 100 \rangle$ (green arrow) reference directions. Above the middle (c.) specific orientations of the highest density plot are shown. The illustration on the right (d.) depicts the $\langle 111 \rangle$, the $\langle 110 \rangle$ directions.

There is no clear consensus in the literature on the preferred orientations of MA in HOIPs. Our results are comparable to what was deducted from milimeterwave spectroscopy data indicating for the $MAPbI_3$, with octahedral connectivity, that the MA alignment towards the cage corners is most likely. [237] However, this is contrary to what was calculated with ab initio molecular dynamics for the $MAPbI_3$ where the room-diagonal orientation is systematically avoided by the MA molecules and the preferred direction is close to the body or face diagonal. [242] Additionally, Lahnsteiner *et al.* showed that all directions but the room-diagonal exhibit a high probability for the MA molecules. Their simulated results agree well with the picture drawn from NMR measurements indicating free rotation within a potential energy landscape with several high-symmetry directions. [236] Having the cage edges as the directions of preferred alignment was also estimated for $MAPbCl_3$ based on single crystal X-ray diffraction and single crystal neutron diffraction for $MAPbBr_3$. [256, 287] Quasielastic neutron scattering (QENS) data demonstrated that the dipolar MA ions jump between preferential orientations within the inorganic lattice and do not undergo free rotation (below 370 K). [285] It was found that the preferred alignments for MA cations are

corners, edges and faces, however, an unambiguous distinction between these directions could not be made.

Another explanation for the combination of preferred orientations and disorder could be that only a small fraction of MA cations stay in one position long enough to register any diffuse scattering. This notion is based on previous results from MD simulations [245] where about 30% of the MA cations in $MAPbI_3$ remained almost frozen. Similar ideas were based on QENS data showing 60-77% of cations having a residence times above 200 ps. [285]

While not investigated in this study, it might be interesting to perform further analysis of the MA molecules looking at long range correlations to determine the presence of interactions between MA molecules or even domains. While there is precedence in the literature for this, it still might be difficult to find this in scattering data based on what was seen with Monte Carlo simulations done on $MAPbI_3$ at 300 K. [285] Their results showed significant thermal noise being superimposed on the antiferroelectric ordering.

5.3.3 Orientation of the [SnI_6] octahedra

Our analysis confirmed octahedral tilting of up to 11° as was seen previously. [70] To visualize the cooperative tilting of the octahedra, a similar approach to analyzing the results from AIMD simulations was used for our [SnI_6]. [249] A 2D histogram shows the tilting of 622,080 octahedra comprising 720 simulations with 864 octahedra each in respect to their spherical coordinates (Figure 5.11). The absolute displacement of the three octahedral axes with respect to the fixed reference coordinate system in all directions (x-axis, y-axis and z-axis) creates a distribution of the three pairs of angles. An example highlighting the angles in spherical coordinates for an ideal octahedron, with respect to the y-axis, is shown in Figure 5.10. The figure shows also the distributions for three reference structures with different octahedral tilting angles. The data for the reference structures was generated by creating 720 of the 6x6x6 supercells and combining the data. Despite the narrower distribution, the RMC modeling results resemble most closely the reference structure

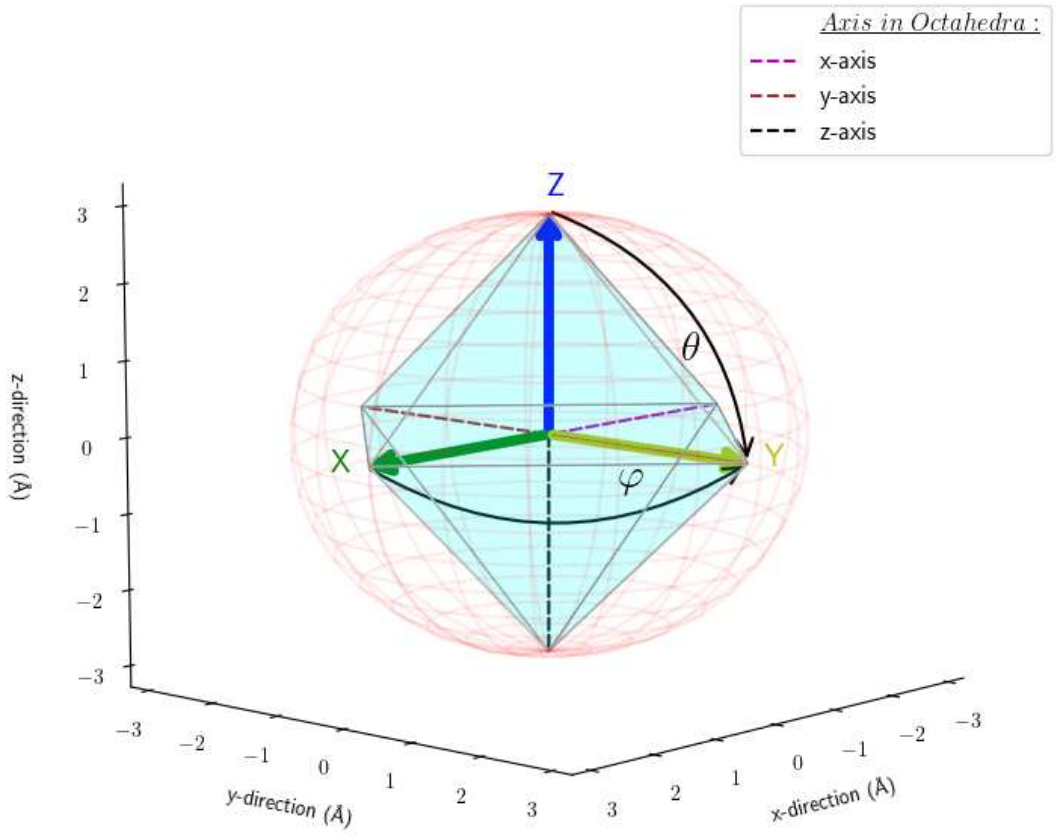

Figure 5.10: Ideal SnI_6 octahedron illustrated in a combination of a spherical and Carthesian coordinates. The here highlighted spherical angles θ and ϕ describe the y-axis.

with the octahedra randomly tilted up to 11° in any direction. This initial few confirms the results previously found by Maughan *et al.* [181] with only a 2×2×2 cell and a different fitting algorithm.

However, to gain more detailed insight into the titling of the octahedra, we must evaluate the observed shifts of each axis individually. This can be done by analyzing the distributions of the densities for each axis shown in Figure 5.11. There, it can be seen that along the x-axis and y-axis the highest intensity are centered in the center of the bins at θ = 88.55° ± 1.45° and ϕ = 1.45° ± 1.45° as well as θ = 88.55° ± 1.45° and ϕ = 88.55° ± 1.45°, respectively. These highest intensities very quickly decreases at around θ = 78° and ϕ = 78° as well as θ = 78° and ϕ = 15° for the x-axis and y-axis, respectively. This indicates that the movement of the octahedra around the x-axis and y-axis is very restricted. Furthermore, it can be said that the axes have a very narrow

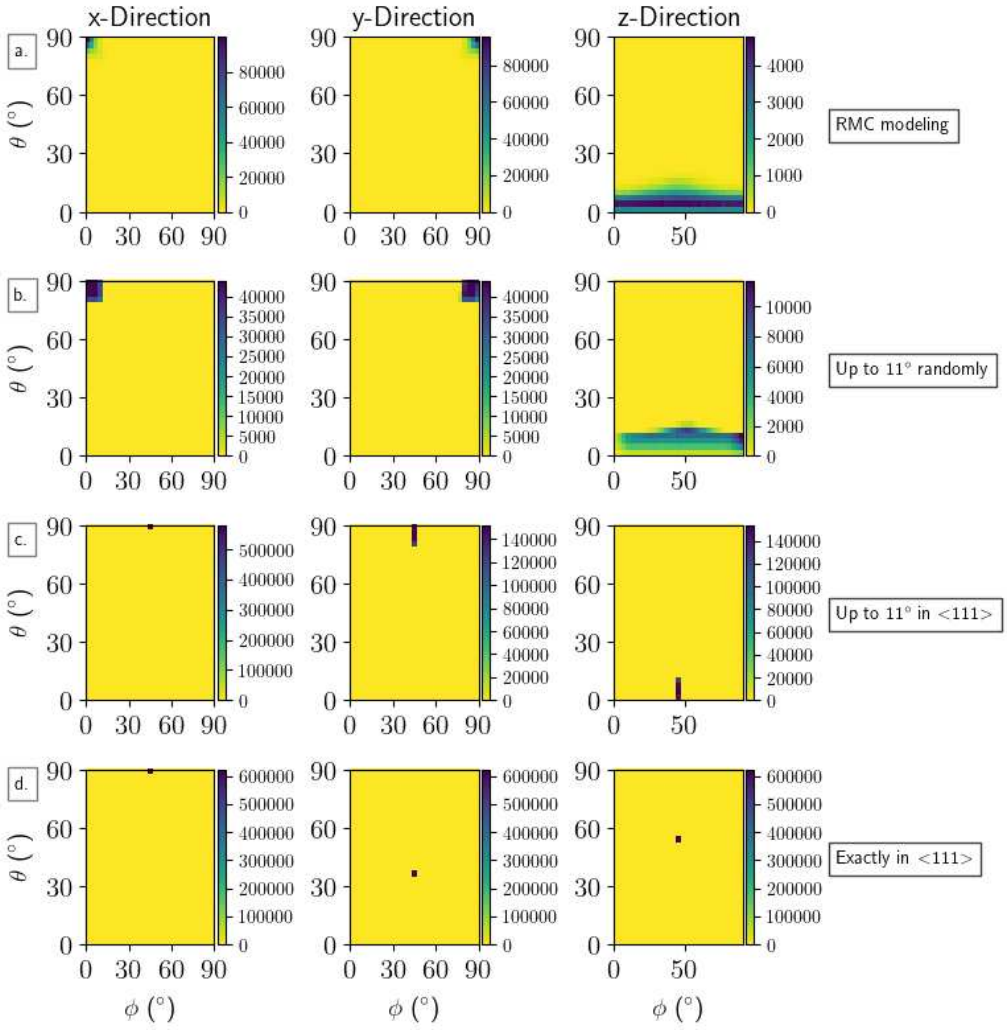

Figure 5.11: Folded histogram depicting octahedra tilting in reference to the x-axis (left), the y-axis (middle), and the z-axis for a.) 720 RMC modeling runs, b.) up to 11° titling in any direction, c.) up to 11° tilting in $\langle 111 \rangle$ direction, and d.) tilting in the $\langle 111 \rangle$ direction. This bin size is $2.9° \times 2.9°$.

rotation probability of about 10° along these axes. The picture for the z-axis indicates that the highest intensity is in the bins between θ = 4.36° ± 1.45° and ϕ = 0-90°. The intensity quickly decreases at around θ = 18°. This indicates a higher degree of freedom around the z-axis. Since the MA_2SnI_6 consists of isolated octahedra, more degrees of freedom are present and, further, no collective tilting is expected compared to the group of ABX_3 perovskites.

5.3.4 Alignment of methylammonium in relation to the octahedra

A significant difference between the all inorganic halide perovskite and the HOIPs is the charge distribution in the A-site cation. The charge of a single atom is confined in a spatially symmetric, mostly spherical, position. Having a molecular cation in the A-site position can change the symmetry of the charge distribution which also entails unequale charge distribution within the voids between the [SnI_6] octahedra. This effect is particularly pronounced in the methylammonium which has an permanent electrical dipole of 2.29 D. [220] While many inorganic perovskites display spontaneous electric polarization based either on temporal spatial displacement of the B-site cations [288] or lone pairs of electrons [289, 290], this can also be induced by external electrical fields, including by light. Polarized organic cations can influence the surrounding inorganic framework, a polarizable medium, leading to deformations but also to strong interactions and coupling which could explain the observed properties and behavior of perovskite solar cells. [285]

In order to further analyze the interplay between the organic and inorganic framework, the relative orientations of the octahedral [SnI_6] units with respect to MA cations were considered. This was done by sequentially selecting each MA molecule individually and searching for the nearest neighbor face centroid on an octahedra to the MA nitrogen atom. To better describe the alignment of the MA cations in regard to the faces of the octahedra, the normal vectors on the face were calculated. With this information, the angles between these vectors and the $\vec{r}_{CN}$ vector were calculated and paired with the angles between the $\vec{r}_{CN}$ vector and the vertical axes of the octahedra. Figure 5.12 shows histograms of the aforementioned parameters for the combined RMC fits, but also the expected values for model reference structures. Seven different reference structures were

generated where the MA cations were rotated randomly, but also along the special crystallographic orientations $\langle 111 \rangle$, $\langle 110 \rangle$, and $\langle 100 \rangle$ allowing the addition of noise up to 2° in respect to the used polar and azimuthal angles.

Initial visual inspections suggested that the best match for the distances between the nitrogen atoms seem to be random MA orientations. However, when taking a closer look at the angle distribution between CN and the normal vector on the faces, it seems to be three overlapping, broad distributions. The peak maxima of these distributions as well as the above shown preferred MA orientations suggest, that the configuration with MA along $\langle 111 \rangle$ and octahedra tilted up to 11° best describe the modeling results. However, the aforementioned observed preferred $\langle 110 \rangle$ directionality of the MA cations (Figure 5.8) also needs to be taken into consideration. Therefore, multiple different supercells for each reference structure were created and combined in several different ways to explore possibilities of how these combinations might resemble the observed RMC results (Figure 5.12 e-g). Based on the illustrated data, it is suggested that when combining the three scenarios (MA randomly oriented with octahedra randomly tilted up to 11° in any direction, MA oriented about $\langle 111 \rangle$ with octahedra randomly tilted up to 11° in any direction, and MA oriented about $\langle 110 \rangle$ with octahedra randomly tilted up to 11° in any direction) the amount of randomly oriented MA must be above $\approx 90\%$ for it to show similarities to the data from the RMC modeling. However, even with the mixture containing 91% randomness, the distribution profile of the RMC modeling results cannot fully be covered. One explanation could be that the reference structures were created with noise only up to 2° and higher levels are needed to capture the observed distribution. Also, the octahedra are all ideal and only rotated. This means that no atomic displacement parameters are included or used to describe these structural units. Additional contributions from other preferred orientations such as $\langle 100 \rangle$ directions can also not be excluded. The presence of slightly elevated densities in the 2D CN-orientation plot corresponding to $\langle 100 \rangle$, as well as more clearly in the 3D plot provide, evidence for that. Therefore, a mixing of the different reference structures involving MA oriented about $\langle 111 \rangle$ with octahedra randomly tilted up to 11° in any direction, MA oriented about $\langle 110 \rangle$ with octahedra randomly tilted up to 11° in any direction, as

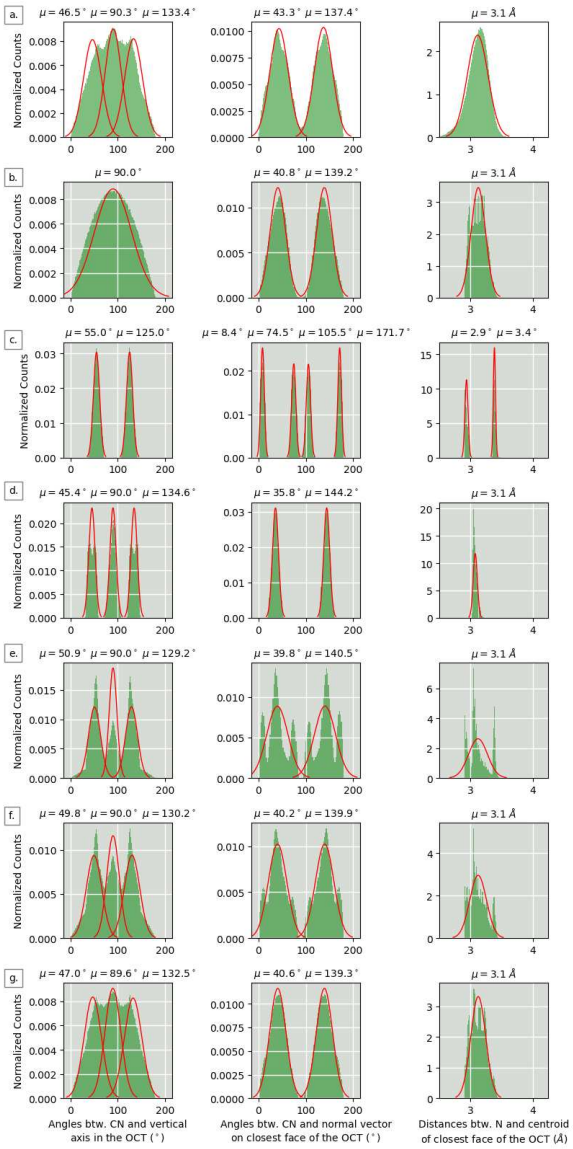

Figure 5.12: Histograms illustrating the distances between N and centroid on the faces of the octahedra (left), angles between the C-N vector and the normal vector on the faces of the octahedra (middle), and the vertical axis of the octahedra (right). Gaussian fits are overlaid to the extracted data (red). Data for a.) Data from the 720 RMC simulations, b.) MA randomly oriented with octahedra randomly tilted up to 11° in any direction, c.) MA oriented about ⟨111⟩ with octahedra randomly tilted up to 11° in any direction, d.) MA oriented about ⟨110⟩ with octahedra randomly tilted up to 11° in any direction. e.) to g.) contain mixtures of b.),c.) and d.), with 33.3%/33.3%/33.3%, 66.7%/16.7%/16.7%, 91.2%/4.2%/4.2%, respectively.

well as the MA oriented about ⟨100⟩ with octahedra randomly tilted up to 11° in any direction can be found in the Appendix C. However, with so many degrees of freedoms, it is unlikely to find a unique solution for the matching mixing ratio.

As was briefly addressed above, previous local structure studies on $MASnI_3$ [69] have found dynamic, temperature activated B-site cation off-centering. This induces unequal distributions of the positive and negative charges in the octahedra which could further influence, or be influenced by, the charged MA cation. This could indicate coupling between the inorganic and the organic sublattice. To further elaborate on the question of coupling, it was evaluated whether there is a correlation between the directionality of the tin off-centering in the octahedra and the preferred orientations of the MA. In case the off-centering influences the MA, the spatial orientation should be similar. Unfortunately, no correlated, preferred directionality was observed and the distribution is completely random. (see Figure C.3 in the Appendix C) The lack of congruent alignment could be explained by the lack of a stereochemical active s^2 lone pair on Sn atom.

5.4 Conclusion

High-throughput Reverse Monte Carlo modeling of the vacancy-order halide perovskite has been performed to better understand the nature of organic-inorganic coupling in this dynamically-disordered semiconductor. Using the local structure to correlate the interaction between the octahedral [SnI_6] units and the highly dynamic organic A-site cations is key in understanding the structure-property relationships. While other analytical techniques are limited in doing so, we were able to determine from room temperature total scattering data that, while the MA is highly dynamically disordered, the highest probability for finding the MA cations is along the ⟨110⟩ and ⟨111⟩ crystallographic directions. Additionally, while less pronounced, there also seems to be some preference for the ⟨100⟩ direction. Our analysis of octahedral tilting showed similar results to what was previously presented in the literature; the octahedra tilt up to about 11°. However, we found that the highest density for the distribution of the octahedra tilt angles is very narrow with about 5°. Our analysis of MA cations in correlation to the octahedra showed that their alignment

to each other is not completely random. While very broad due to thermal motions, the found distributions for distances and angles closest resemble those found for a 91.2%/4.2%/4.2% mixture of the reference structures containing MA randomly oriented with octahedra randomly tilted up to 11° in any direction, MA oriented about ⟨111⟩ with octahedra randomly tilted up to 11° in any direction, and MA oriented about ⟨110⟩ with octahedra randomly tilted up to 11° in any direction. To summarize, we have shown that Reverse Monte Carlo modeling provides a good approach to gain additional structural insights into a disordered materials such as hybrid organic-inorganic perovskites at room temperature. This analysis represents a good foundation for further understanding the unique opto-electronic properties of vacancy-ordered double perovskite semiconductors. Furthermore, our approach to highlighting the short-range interplay between individual structural units can easily be transferred and used for other complex, disordered functional materials.

Chapter 6

Locating the active sites within CuBTTri enabling the S-nitrosocysteamin decomposition

6.1 Introduction

The radical nitric oxide (NO) [291, 292] has commonly been known to be a toxic gas [293]. With a concentration of 800 ppm [294], NO has also been perceived as one of the major toxins in tobacco smoke. However, as was discovered around 1990, it also has some very important biological functions. [295,296] It is naturally produced in biological systems through NO synthase (NOS) which oxidizes L-arginine eventually to L-citrulline while releasing NO. [297] In 1992, NO was declared to be the molecule of the year and in 1998 research involving NO was significant enough to be worthy of the Nobel Prize. [298] NO plays an important role in natural areas such as cardiovascular, respiratory, and nervous and immune systems. [299–302] For example, NO is a vasodilator, which induces relaxation of blood vessels. [303,304] It also helps with the relaxation in the corpus cavernosum which is responsible for penile errections. [305] Furthermore, it functions as a platelet aggregation inhibitor, a neurotransmitter, an antimicrobial and antitumor agent. [306] Another use of NO is to enhance wound healing. [307–311]

For mediating the NO activity and concentration in these physiological processes either the endogenic production of NO can be influenced or it can be delivered from exogenic sources. There are several possibilities to have NO delivered from exogenic sources, but in many instances they need to be located in proximity to the desired biological site. Depending on the biological environment, NO is only stable for an average time of 5 seconds resulting in an influence sphere from its source of about $200\,\mu\mathrm{m}$. [312] This indicates, that systemic application of nitric oxide is not feasible. Hence, the molecule needs to be released locally in the affected area. This can be done with materials that either have NO chemically bound or physically adsorbed which can then be

released upon a trigger (UV-light, temperature, moisture) with the desired rate and concentration. Materials that have been used for this application are polymers [313], hydrogel [303], nanoparticles [314], silica, zeolites [315] and metal organic frameworks (MOFs) [316–318]. The materials choice depends on the required NO concentration and release rate for its biomedical application. NO concentrations that are too high can lead to rheumatoid arthritis whereas concentration that are too low induce respiratory distress. [319] Different NO concentrations are necessary to impact physiological cell signaling processes. For example, the relaxation of vascular smooth muscle cells requires levels of 10-30 nmol/L of NO to facilitate vasodilation. However, the NO concentration that mediates physiological responses has been determined to already occur at the sub nmol/L levels. In addition to the concentration, the exposure time to NO is of similar importance. For example, the activation time for certain proteins ranges from less than a second to hours or even day. [320]

Zeolites and MOFs are some of the most promising materials for NO release since they show the highest NO storage capacities reported in the literature and they have well defined structural features that can be modified easily to change properties such as the release rate or the chemical stability. For instance, NO can be chemically stored in a MOF by attaching specific groups onto the framework forming linkers. This can either be done during the synthesis of the MOF or photosynthetically. [321–323] Another way to store NO is through physisorption within the porous structures of MOFs and zeolites. The adsorption sites are easily accessible due to the porous structure of MOFs and zeolites resulting in a very high surface area.

Several different analytical techniques have been used for determining the adsorption interaction of NO with these structures. For example, Infrared spectroscopy (IR, HKUST-1 [317, 324], MIL-88(Fe) [325], Cu-ZSM-5 [326]), UV-VIS-NIR (Ni-CPO [327]), solid-state NMR (amino-modified HKUST-1 [328], MIL-100 [329]) and electron paramagnetic resonance (EPR, Cu-ZSM-5 [326], MIL-100 and CPO-27 [330, 331], and DUT-8 [332]) are methods that have been used to determine the adsorption sites of NO. However, these methods are considered to be indirect methods. Direct methods for considering the position of NO within the material are neutron

diffraction (Fe2(NO)2(dobdc) [333]), powder X-ray diffraction(PXRD, Co-CPO-27 [334]), single crystal X-ray diffraction (Co-CPO-27), and X-ray absorption spectroscopy (Ni-CPO [327], Cu-ZSM-5 [326]). The summarized consensus of these studies is to have, as the main adsorption site, NO bind on uncoordinated metal centers within their framework structure.

Despite their high storage capacity, zeolites and MOFs based on NO desorption are constrained to only certain topological biomedical applications. All of the materials desorbing NO have a restricted time frame where they can be used for releasing NO due to the limited amount of NO that can be stored within the material. Materials relying on gas adsorption can only deliver NO for several hours. This is not a problem for wounds that heal quickly or other external applications where the NO delivering device can easily be replaced. However, once a longer release time is required materials with sole adsorption/desorption behavior reach their limit. This is especially critical when trying to prevent biofilm formation on medical devices that are inserted or implanted in a physiological system. Some examples of devices that are susceptible to biofilm growth are contact lenses, mechanical heart valves, pacemakers, prosthetic joints or central venous catheters. Problems that can arise from biofilm formation range from tissue damage near prosthetic heart valves, which can cause leakage as well as destruction of the material, to artificial hip and knee prostheses being loosened. While some of these infections cause minor problems, others can have serious consequences. This way microorganisms such as coagulase-negative staphylococci, that usually life on the skin where they do not cause infections, can cause diseases or even death. [335] For example, contraction of endocarditis during initial hospitalization led to the death of 40 - 50% of patients with prosthetic heart valves. [336] Long NO release rates are required for implants such as hip replacements which introduces a foreign body into a biological system. Situations like that can lead to biofouling [337–339] resulting in a destruction of the material and the need to replace it sooner than anticipated. Some consequences of biofilm proliferation on prosthetic joints are acute septic arthritis leading to joint pain or, in more severe cases, even to swelling and fever and further to loose joints and chronic pain. [340] Another problem for catheters can arise from encrustations being formed by mineral deposition within the device. This is caused by biofilm

induced hydrolysis of urea in urine which leads to the formation of free ammonia leading to a lower pH which is responsible for precipitation of calcium phosphate or magnesium ammonium phosphate. [341]

Besides the above mentioned negative impacts, biofilms can affect biological systems in multiple other ways by, for instance, detachment of cells or cell aggregates from the films, endotoxin production, or providing an environment that leads to the generation of resistant organisms. The latter point is especially a problem when biofilm treatment is necessary. Once a biofilm is formed, the microorganisms are 10 – 1000 times less susceptible to the same type of antibiotics than when dispersed as individual cells in the blood stream. [342] Resistance is achieve with extracellular polymeric matrices and physico-chemical gradients within the films. The extracellular polysaccharide production is especially enhanced in proximity of surfaces. While there has been some success in biofilm treatment with low-frequency ultrasound in combination with aminoglycoside, the prevention of formations of biofilms is desired in the first place. This can be done with antimicrobial polymers and surface coatings. However, so far these approaches have only been successful for category 2 and 3 implants which are considered medical implants for short-term use. Another example of short-lived biocompatible coatings, for artificial material being exposed to blood, is based on NO desorption and has been used for biosensor electrodes. The incorporation of NO releasing diazeniumdiolate stopped blood platelets from covering the surface. [343] However, for category 1 implants, which are meant to stay in a body forever, a more long-lasting alternative needs to be found. [337]

One option for long-term prevention of biofilm formation *in vivo* is to have the surface of biomedical devices release NO for as long as the device is in contact with a biological organism. As described above, unlike in external applications, NO desorption needs to continue as long as the device is in place which can be multiple years. An approach to solve this problem is by using the metal centers in MOFs as catalysts, instead of only a storage site, to produce the NO *in situ* from endogenous biomolecules on the surface of the implant. This can be done in analogy to processes naturally occurring in a human body where NO, stored within S-nitrosothiols (RSNO)

and nitrates, gets released in the desired places. RSNOs were the first known biologically active NO donor in 1980 [294], are the most prevalent form of NO donor in the blood and several mechanisms have been identified how these molecules decompose [344]. RSNO is also not pertinent to the development of tolerance which is commonly observed during clinical therapy with organic nitrates. [345] Similar to the above mentioned method of releasing NO with light, it has also been reported that visible light can cause GSNO to split off NO. [346] The biological process uses NO synthase which possibly interacts with zinc ions to split the RSNO. [294] The first study that has shown that the exposure of RNSOs to metal cations in solution accelerates these reactions was published 1995. [347] While catalytic activity could be shown for the ion Cu^{2+}, Fe^{2+} only showed minimal activity. Zn^{2+}, Ca^{2+}, Mg^{2+}, Ni^{2+}, Co^{2+}, Mn^{2+}, Cr^{3+}, and Fe^{3+} did not show any activity. It was reported that a copper ion concentration of 10^{-6} mol/L is already sufficient enough to split off NO from RSNOs. [345] Further studies investigated the RSNO decomposition with polymers that have Cu^{2+} ions embedded and the decomposition of smaller molecules that have copper incorporated within zeolites. [348–350] The first reported use of a MOF as a catalyst for nitric oxide release was published by Harding *et al.* [351] in 2012. They used a copper based MOF (HKUST-1 [352]) to split S-nitrosocysteine (CysNO). CysNO was the molecule of choice based on its high bioavailability. [345] Literature reports the concentration of CysNO in plasma to be $0.3\,\mu\mathrm{mol/L}$ which is comparable to bigger molecules such as S-nitrosohaemoglobin in arteries $(0.3\,\mu\mathrm{mol/L})$ or S-nitrosoalbumin in plasma (0.25-1 $\mu\mathrm{mol/L}$). [294]

Other smaller molecules, for example S-nitrosoglutathione (GSNO), have a considerable lower availability which is in the range of 120 – 180 nmol/L. While these concentrations have been measured in blood, the intracellular concentrations might be different. [345] This is especially anticipated since glutathione has intercellular concentrations above 1 mmol/L and NO has been shown to react freely with thiols to form RSNOs. [294] Despite the initial success with HKUST-1 and its widespread use, other MOFs need to be considered for *in vivo* applications due to the lack of chemical long-term stability. While the copper ion in HKUST-1, responsible for the RS-NO bond cleavage process, is bound in the MOF framework, small amounts leaked during the reaction with

CysNO. [351] Copper ions can be toxic and longer exposure times of HKUST-1 to physiological conditions could lead to a copper ion level that cannot be considered non-hazardous anymore. Therefore, a follow up study used CuBTTri, a MOF with higher stability regarding its solubility, as a catalyst. [353] Several different tests were reported showing CuBTTri's higher stability. The initial tests of stability are very promising and showed that neither boiling the material for three days in water nor the exposure to hydrochloric acid for one day changed its structure which was confirmed by collecting powder X-ray diffraction pattern. [354] Additional tests with phosphate buffered saline (PBS), cell media and whole blood could also indicate a high stability by non-altered XRD patterns. Furthermore, no differences could be observed after the reaction with S -nitrosocysteamine (CysamNO). [353] However, no long-term exposures of the CuBTTri to continuous flow of fluids have been reported yet. This scenario would be a more accurate representation of an *in vivo* environment.

CuBTTri has already shown promising results as catalytic material for NO release by itself, but to prevent biofilm formation *in vivo*, it needs to be incorporated into biomedical devices. As was mentioned above, category 1 implants basically need to have an unlimited NO release properties. This can be done by incorporating the MOF into, for example, polymeric matrices used in biomedical devices. Its feasibility has been shown for CuBTTri in biomedical grade polyurethane [353], poly(vinyl chloride) [355] and a biodegradable, nontoxic polymer such as chitosan [356]. Results like that can be considered big milestones towards *in vivo* biofilm prevention and with the help of companies such as MOFgen [357], focusing on the commercial proliferation of MOFs for biomedical applications, MOFs could soon be found readily in medical facilities.

Materials for biofilm prevention:

To design new materials with higher catalytic efficiency, the adsorption and reaction sites within the porous structures of the catalysts need to be determined. In a similar manner, to understand the formation of the NO molecule in MOFs, it is important to find the sites where the RS-NO cleavage process occurs. Once these sites have been identified, the design and synthesis of new MOFs can specifically target availability and accessibility of these sites within the desired

structures. The first step in this process is to determine the theoretical reaction sites by performing calculations. Previous computational studies used molecular dynamics simulations (MD) to determine the interaction of a variety of RSNOs with the copper metal center in HKUST-1 [358] and a derivative of it, MOF-143 [359]. The simulations for HKUST-1 were done for methyl nitrosothiol and CysNO in a solution of ethanol. It was hypothesized that the thiol reduces the Cu^{2+} to Cu^{+}. [358] The lowest energy was reached where the sulfur atom of the R-S-NO is coordinated to the Cu^{+} ion at a S-Cu bond distance of 2 Å. The next step is the release of the NO molecule. Upon RSNO approaching the Cu^{+} centers, the ethanol in the copper coordination shell gets replaced with RSNO. The second RSNO molecule does the same upon approaching the copper ion and forms a disulfide bond with the remains of the first RSNO molecule. The reaction of RSNOs within HKUST-1 also influences the atom positions within the framework. This can be seen with the presence of two CH_3SNO molecules on adjacent copper ions which increases the Cu-Cu distance from 2.5 Å to 3.5 Å. Hence, it is very important to have flexible MOF frameworks to accommodate these interactions. [358] The follow up study illustrated multiple possible reaction pathways resulting in a range of NO release rates. [359] Further, it was shown that not only the size of the MOF or the RSNO influences the reaction rate, but also its chemical composition.

Despite the theoretical insight into the interaction processes of the RSNO molecules with the metal centers, these findings have not yet been confirmed experimentally. Therefore, this proposed study tries to give more information on the location and interaction sites of RSNO molecules in MOFs based on experimental techniques. Due to the higher chemical stability [353] and the less complex framework structure, compared to HKUST-1, the reported MOF CuBTTri – CysamNO system was chosen for a proof of concept study. While CysamNO has a lower physical relevance compared to other RSNOs such as GSNO and CysNO, its structure is simpler and therefore better situated for a proof of concept study. The reaction occurring with two CysNO molecules resulting in NO and a Cys-dimer is illustrated in Figure 6.1.

For locating the CysamNO in the CuBTTri a scattering method was selected. While neutron scattering would be more sensitive to the light elements, contained within the MOF and RNSO

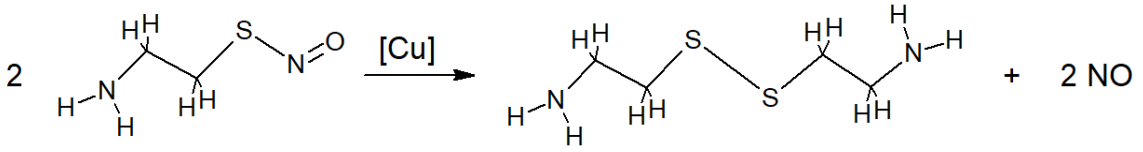

Figure 6.1: Decomposition reaction of cysamNO occuring in the presence of a copper catalyst.

systems, the large amount of hydrogen (found in the host, guest and the solvent) would result in a very high background signal making the data difficult to analyze. Therefore, the method of choice was powder X-ray diffraction.

Having a very disordered system, crystallographic analysis using Rietveld refinements is not sufficient for determining the reaction sites. Total scattering and Pair Distribution Function (PDF) analysis can overcome this restriction. While originally developed for liquids and glasses, due to its ability to acquire structural information on both the short- and the long-range order, it has been used for amorphous, nanosized structures as well as crystalline structures. [42]

Furthermore, in addition to determining the long-range order with full pattern refinements, the local structure will be identified by calculating the local coordination environment around the copper metal centers. This will be done by calculating the pair correlation functions. While the atoms of RSNO have rather low scattering cross sections for X-ray diffraction studies, the pair correlation takes the cross section of both atoms into consideration. Since copper has a higher cross section, the pair correlations are easily detectable as was demonstrated with the adsorption of another physiological relevant gas, H_2S, in the MOF Ni-CPO-27. [360] To only determine the pair correlations between copper and the adsorbed species, the differential pair distribution function needs to be calculated by subtracting from the MOF/RSNO signal the empty MOF signal as well as the background signal from the solvent. Previous studies have used PDF to characterize small molecules within porous structures such as NH_3BH_3 in MCM-41 [361], however, the higher level of rigidity simplifies systems like this. Contrary to these stiffer frameworks, MOFs show a high level of structural flexibility. This is a very important property in chemical reactions, facilitating attaching and detaching of molecules and levitating framework stress, but it can also lead to higher levels of static disorder in the neat structure itself. How total scattering can be used to study dis-

order in framework structures such as MOF is discussed in the literature. [362] For example, PDF and Reverse Monte Carlo modelling were used to describe the static disorder in zinc (III) isonicotinate [363]. Total scattering has also been applied to local study structural features in amorphous MOFs. [364–366] While most of the published PDF studies are focused on inorganic materials, the study of organic and molecular compounds are gaining momentum. Studying organic materials is more difficult due to the complexity of the atomic bonding possibility, but small box approaches have shown success in describing intra- and intermolecular interactions [367] as well as large box approaches [368]. PDF has also been introduced to particularly study pharmaceutical compounds and substances used in medicine. [50, 367, 369–374]

The aforementioned reports on applying PDF analysis are generally limited to a two-phase system including only a sorbent and sorbate. Since CysamNO in our proof of concept system needs to be dissolved, this adds another phase or signal during the total scattering experiments. While still difficult, the feasibility of this approach is based on previous literature examples using PDF analysis to study materials in solutions and even under reaction conditions. [375] For example, the structure of gold nanoparticles with size ranging from 3 to 30 nm in water was studied with total scattering. [376] The water content (about 85%) in the sample volume was substantial, contributing most of the signal to the experimental diffraction patterns. PDF analysis provided also information on the ordering of organic polar and non-polar solvent molecules on the surface of metal and metal-oxide nanoparticles. [377] Insight on the growth mechanism and kinetics during solvothermal nanoparticle formation under 250 bar hydrostatic pressure with supercritical solvents could also be achieved with PDF for, for example, TiO_2 with a water/isopropanol mixture at 250 °C [378], 4% YSZ with methanol at 270 °C [379], intermetallic PtPb with ethanol at 300 °C [380], and SnO_2 with water at 350 °C. [81]

To determine the feasibility of the project and see whether differences in the loaded and the empty CuBTTri structure exist, the PDFs for the empty and the CysamNO CuBTTri were calculated. A weak PDF difference signal indicates the possibility of being able to answer the question: Can we experimentally determine if Cu in CuBTTri controls the RSNO decomposition?

6.2 Experimental Procedure

The synthesis of the DMF form of the MOF CuBTTri was done by Alec Lutzke. All the other work stated below was done by Arnold A. Paecklar.

6.2.1 Prediction of the initial structures

CysamNO: To calculate theoretical PDFs, structural models needed to be generated. First, the structure of CysamNO was created and optimized, using the universal force field (UFF) [381], with the program Avogadro. [382]

CuBTTri: We began from the published data for the experimentally determined structure of CuBTT [383] (determined by neutron scattering) which is isotypic with the cubic sodalite-type structure of CuBTTri. The difference is a N atom in the ligand 1,3,5-benzenetristetrazolate versus the 1,3,5-Benzene-Tris-Triazole ligand. Isodistort [384] was used to transform the symmetry group from Pm3-m to P432 to allow the change of the ligand. This structure was then optimized with Density Functional Theory (DFT) using the Vienna Ab initio Simulation Package (VASP) [385–388] with a planewave basis set and projector-augmented-wave [389] pseudopotentials.

The exchange-correlation functional used was within the Generalized Gradient Approximation (GGA) of Perdew–Burke-Ernzerhof (PBE). [390] First the structure of the CuBTTri framework was optimized using a planewave cutoff energy of 1000 eV for the basis set and Γ-point sampling for the Brillouin zone integration allowing the optimization of forces, stress tensor, atomic positions, the cell shape, and the cell volume until the electronic structure converged to an energy difference of 10^{-3} eV and a force difference of 10^{-2} eV/Å. The calculations were performed with spin polarization. To correct for valence d electrons in Cu, a Hubbard U correction was applied with 10.4 eV based on what used Cu in a similar MOF (CuBTT) and determined by *ab initio* approaches. [391] To account for Van der Waals (vdW) interactions, Rev-vdW-D2 was used as a correction. [392] These calculations were run on an HPC system with one core per atom.

CuBBTri with CysamNO: The insertion of CysamNO molecules into the optimized, empty CuBTTri structure was done quasi-stochastically. The used positions were based on MD calcula-

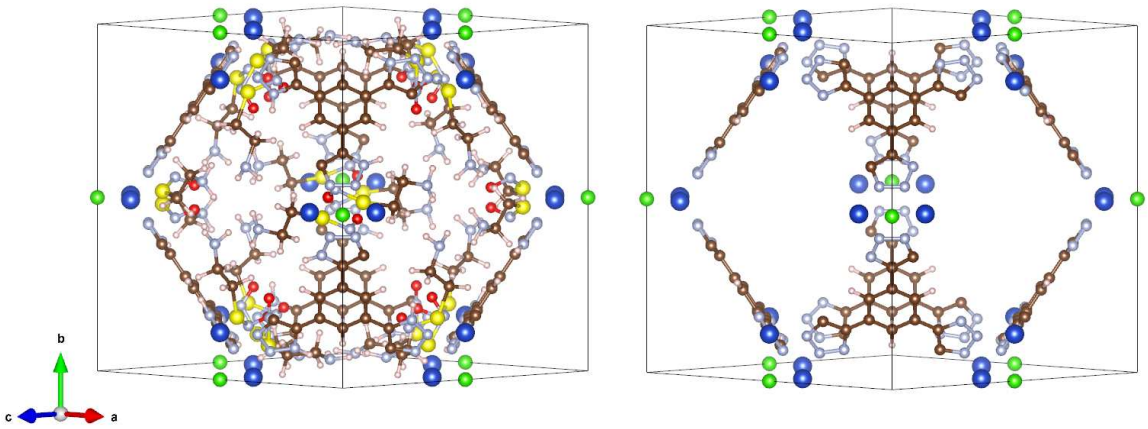

Figure 6.2: (left) CuBTTri with cysamNO coordinated to the copper atoms (blue) and (right) the empty CuBTTri structure.

tions in other Cu MOFs [358] placing the S atom approximately 2 Å away from the Cu positions. Initially, this was done with 24 molecules with each containing 12 atoms. During the second approach only one CysamNO molecule per sodalite (SOD) cage was used. This was based on another study locating CO_2 in CuBTT with DFT and GCMC. [393] The framework atoms were frozen while the atoms of the CysamNO molecule were allowed to move. The same parameter settings were used as for only calculating the empty CuBTTri structure.

Figure 6.2 shows CysamNO molecules coordinated with their S-atoms to all the Cu^{2+} ions within a unit cell of CuBTTri. CuBTTri crystallizes in the space group P432 and the SOD structure which is characterized by structure type derived from zeolites. With the current location of the CysamNO atoms, it was possible to use the P432 space group symmetry operations to place a CysamNO molecule at a distance of 2 Å next to all Cu^{2+} atoms. This distance is based on the calculations for RSNO – Cu interactions within HKUST-1.

6.2.2 Prediction of the diffraction pattern

To determine the feasibility of this project, some initial calculations were performed to see what the theoretical diffraction and PDF pattern would look like. The XRD pattern for the empty and CysamNO loaded CuBTTri structure using a Cu(K_α, λ=1.5406 Å) X-ray anode was done with the General Structure Analysis System (GSAS) [394, 395] and for an Ag(K_α, λ=0.56 Å) X-ray

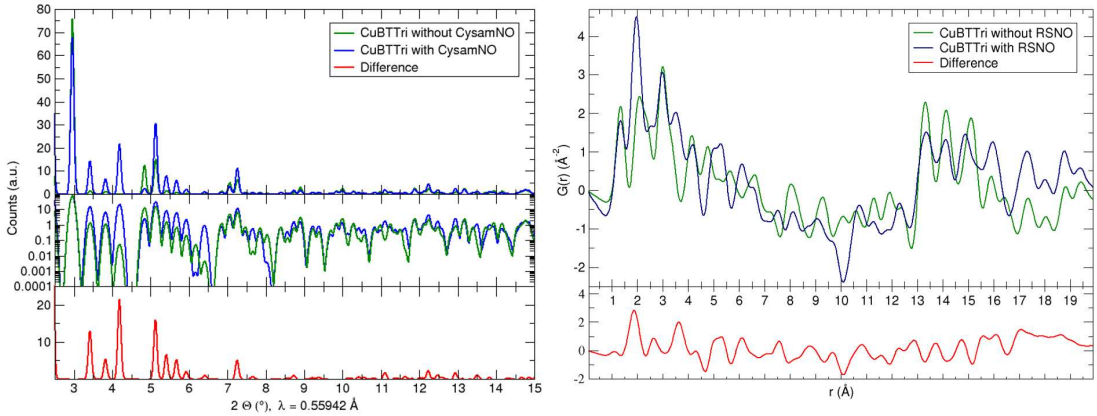

Figure 6.3: The predicted, calculated X-ray total scattering data using an Ag(K_α,λ=0.56 Å) source of the empty CuBTTri and the CuBTTri filled with 24 CysamNO molecules: the XRD pattern (left) and the pair distribution function resulting from it (right).

X-ray anode with CrystalDiffract [396]. These pattern, in addition to the predicted PDF, calculated with the program PDFgui [264] are illustrated in Figure 6.3.

6.2.3 Sample preparation and characterization

MOF: CuBTTri was synthesized following the previously reported procedure. [353] About 200 mg of the 1,3,5-tris(1H-1,2,3-triazol-5-yl)benzene was synthesized based on the published method. This material was dissolved in 30 mL dimethylformamide (DMF) in a 120 mL vial and its pH was adjusted to 4 with diluted hydrochloric acid. $CuCl_2 \cdot 2\ H_2O$ was dissolved in 10 mL DMF and added to the triazole solution. The vial was placed in an oven at 100 °C for 72 h followed by the reaction solution being kept at room temperature for 1 week. The resulting purple powder was centrifuged and washed with DMF three times. Then, the powder was placed in a glass bottle with a screw cap along with deionized water and heated in an oven for 24 h at 100 °C. The supernatant was removed with a pipette and the solvent exchange was repeated once more. The next day, after removing most of the supernatant with a pipette, the remaining water was removed by lyophilisation. Infrared spectroscopy was used to evaluate the level of DMF to water exchange.

RSNO: A fresh stock sollution of CysamNO will be prepared *in situ* prior to the reaction with CuBTTri. A solution of 0.05 mol/L cysteamine hydrochloride will be nitrosated with excess of

t-butyl nitrite. After reacting for 10 min under agitation in an ice bath, the concentration of the red CysamNO solution will be determined by UV-VIS spectroscopy using the characteristic absorption bands for RSNOs at 355 nm (ϵ = 793 L cm^{-1} L^{-1}) and 545 nm (ϵ= 15 L cm^{-1} mol^{-1}).

6.2.4 Total Scattering measurements

Prior to completing the total scattering measurement, the MOF needed to be activated. This was done by drying it for 3 days under vacuum and a temperature of about 80 °C. This is necessary to remove all adsorbed species, particularly water. Removing all molecules form the adsorption sites in the MOF prior to reaction showed to increases the initial NO release rate as seen by Harding *et al.* for HKUST-1. [351] The material was then transferred into a glovebox where it was packed into a quartz capillary with a 1 mm inner diameter (ID). The initial MOF structure was determined via powder X-ray diffraction on a PANanalytical Empyrean with an Ag source (λ=0.56 Å). The sample was measured for 615 min in multiple segments from an angle of 3° to 142° in 2θ. determine the background signal. The same settings to determine the background from measuring the empty capillary. The total scattering structure function, S(Q), and the pair distribution function, G(r), was generated from this data using HighScore Plus. [397] The density (0.7780 g/cm^3) used in this calculation was based on the DFT relaxed, empty CuBTTri structure. To determine the background signal from the bulk solvent, total scattering data for diionized water was also collected under the same conditions. The DFT optimized structure was used as a model for the experimentally generated G(r). Structural refinement was done using PDFgui. [264] Only the scale factor, lattice parameter, delta1 factor, and the isotropic Debye Waller factors for the were allowed to be refined.

6.3 Initial Results and Discussion

Structure Optimization: Given the large size of the unit cells of most MOFs, DFT, out of all quantum chemical methods, is most suitable for routine calculations on the periodic strucutre of MOFs. However, due to large amount of organic moieties, vdW interactions become significant and could not be omitted and the exchange-correlation (XC) functionals needed to be carefully

considered. Hence, the accuracy of the results strongly depends on the choice of the used XC. While there are generally three different classes of XCs to correct for vdW [398], the corrections by Langreth and Ludqvist groups (vdW-DF2) [399] have been very successful. Unfortunately, the vdW-DF2 functional is also know to overestimate bond and lattice distance. Therefore, the rev-vdW-DF2 functional was recently developed by Hamada with the purpose of improving the geometries of vdW-DF2. [392] A comparison between XC functionals and experimental data for adsorption in M_2(dobdc) MOFs was done as well as a comparison to Quantum Monte Carlo (QMC) calculations and indicated that the rev-vdW-DF2 functional shows the best agreement. However, as has often been discussed in the literature, making direct comparison between experimental results and simulations for porous materials is not always straight forward. [398] While this study showed that meta-GGA functionals produced comparable resutls, they required significant more wall time than other functionals. Hence, the rev-vdW-DF2 functional was chosen for our DFT structure optimization.

In addition to finding the most suitable XC functional, other functors need to be considered for optimizing the structure and having an accurate description of the adsorption under biologically relevant conditions. First, what needed to be considered when structures contain metals such as Cu was a standard DFT problem: the self-interaction error (SIE). [400] Not taking this into consideration can lead to many problems such as poorly optimized crystal structures, wrongly assigning states as delocalized, or not finding band gaps and denoting systems as metallic. [401] Generally used solutions to this problem are to either use empirically derived corrections (termed as Hubbard U correction or just +U) or to use hybrid functionals. In a study examining multiple copper compounds, it was found that hybrid functional agree less with the experimentally attained data than standard functionals such as PBEsol+U. [401] There, different U values were derived for compounds containing Cu^{+} which distinct from Cu^{2+}. Not having a Hubbard U correction in MOFs could lead to the incorrect electronic structure which results in binding strengths of the guest molecules to the open-metal sites either being under- or over estimated. [402] Another reason for not using hybrid functionals was shown in a study examining small molecule binding in

MOF-74. [403] There, the use hybrid functionals was prohibitively computationally expensive for large, complex MOFs. In addition to the higher computational cost, using even higher levels of quantum computation, such as cluster models [404], did result in a poor agreement with experimentally attained data for water adsorption in CuBTC. [405] The most sophisticated way to attain the required Hubbard U values is by harnessing *ab initio* calculations as was shown through an established linear response procedure for small molecule adsorption in MOFs. [391]

The binding energy of adsorbate is also influenced by thermal influences with adsorption happening at temperatures above 0 K. This is factored in with the quantum nuclear zero-point-energy (ZPECs) and thermal energy (TECs) corrections needed for an appropriate comparison with experimentally measured isosteric heats of adsorption at room temperature. [402] The final factor to be considered arises from the CysamNO being dissolved in water. Hence, solvent contributions need to be considered and can be treated explicitly, or implicitly. [406] The former provides a full *ab initio* approach and is the most detailed representation of the system. However, this requires averaging over solvent molecular configurations which makes it the more computationally expensive option. A computationally cheaper and more tractable approach is the implicit water model. This is a parameterized approach allowing to replace the solvent molecules with a continuum dielectric. The average over all molecular configurations is embedded in the solvent model parameters. Since this is a simplified approximation, it must be used with care and requires sometimes to still use the first few solvation shells explicitly. [406]

While not used in our initial calculations, it could possibly be addressed by using the models described below. The most commonly used method to model solvation effects is to use a polarizable continuum model. Modeling the solvent as a polarizable continuum makes *ab initio* computation feasible. While a common model in computational chemistry is the "COnductor-like Screening MOdel“ (COSMOS) [407], a newer approch, easily implementable for VASP, is VASPsol. [408] A successful use of the implicit solvation with VASPsol was shown for studying the adsorption of bio-oil model compounds in the zeolite HZSM-5. [409] There, the C1–C4 carboxylic acids adsorption used a non-spin polarized approach with a vdW correction (PBE+D2).

The structure relaxation of the empty, cubic CuBTTri wwas converged after 22 hours resulting in optimized lattice parameters of 18.73938 Å. For finding the ideal adsorption sites within the SOD cage, the ZPECs, TECs, and the implicit solvation model were initially not considered and only vdW corrections and Hubbard U corrections were applied. Even with this limited number of computational parameters, the DFT based optimization could not find an energy minimum within 128 hours. Instead of realigning in the vicinity of the Cu atoms, the CysamNO molecule slowly moved away from these sites towards the center of the SOD cage.

The best explanation for being unable to locate an energy minimum is the high number of degrees of freedom in this system. While all the above mentioned computational factors make the results of a structure optimization more accurate, the amount of the atoms, primarily in the sorbate, increases the internal degrees of freedom and further the computational cost tremendously. For instance, a study using DFT for finding adsorption sites in MOFs used, as the largest molecule studied, propane (C_3H_8). [402] With propane containing only 11 atoms, the potential energy surface is already highly multidimensional and finding a global minimum can be very difficult. This is especially true if the initial structural configuration is sufficiently far from the global minimum. In such a case, the DFT binding geometry can become very easily trapped within a local minima while trying to optimize the structure. Hence, CysamNO containing even more atoms (12) poses and additional challenge for finding a global minimum during our structural relaxation.

Based on our initial results, other approaches need to be considered. A semi-theoretical technique was chosen to find the CO_2 adsorption sites in CuBTT by cooling the system to 10 K, collecting neutron scattering data, followed by the calculation of a Fourier difference map. This served as the starting structure for their DFT structure optimizations. [393] However, to really find the theoretical sites, in order to circumvent our current limitations with DFT, Grand Canonical Monte Carlo (GCMC) simulations with programs such as RASPA might show more success. [410] Another option is to use a combinatorial approach, using DFT for the neat MOF, finding the adsorptions sites with GCMC or molecular dynamics (MD) simulations, and then further optimizing these positions using DFT. However, for either MC and MD, an appropriate force field needs to be

used. While there are easily accessible, commonly used force fields such as UFF [381] or Dreiding [411], these are unable to treat open-Metal sites appropriately. While there are updated force fields specifically designed for MOFs, like UFF4MOF [412, 413] and QuickFF [414, 415], to find a properly suited force fields for CuBTTri, *ab initio* techniques could be used similar to what was done for finding force fields for a series of different MOFs. [416] However, since the reaction of CysamNO splitting is more complicated than just a simple adsorption, other variables must be also considered. For example, the proposed reduction of Cu^{2+} to Cu^{+} during the reaction is currently not covered by a simple DFT structure optimization during an adsorption process in an extended solid. [358] Furthermore, current force fields for MOFs do not allow for bond breaking or reformation which also needs to be taken into consideration during chemical reactions. This could be done by using reactive force fields such as ReaxFF [417, 418] This has already been applied in a number of studies involving MOFs such as the melt-quench process of ZIF-4 [419], the stability of MOFs against water [420–422], and the appending of diamines to the metal-organic framework Mg_2(dobpdc). [423]

Since this is beyond our current capabilities, collaborations need to be sought out for continuing this computational project.

X-ray Total Scattering of neat CuBTTri

It can be seen (Figure 6.4) that the initial fit shows good agreement with the structural model, based on the general peak positions. The intensities match better in the low and high r-ranges but have higher discrepancies in the medium r-range. This could indicate static disorder in the MOF structure. Due to the size and the large number of atoms contained in the structure, further refinement with PDFgui is not feasible. A more sophisticated software package, such as DiffPyCMI [253], or a large box approach with Reverse Monte Carlo (RMC) modeling needs to be used.

6.4 Future Steps

As a future project and a continuation, the local structure of the neat MOF needs to be determined. This is a perfect environment for using the previously developed skills in high-throughput

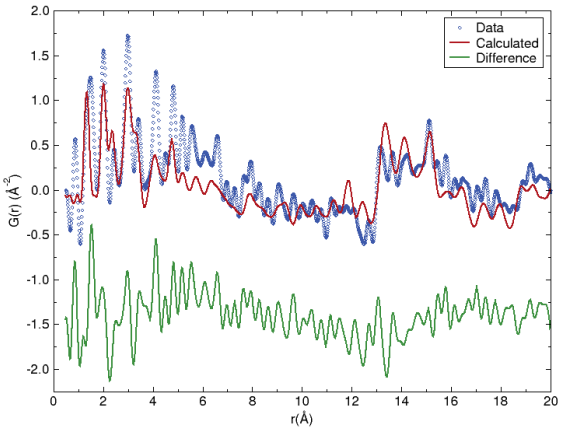

Figure 6.4: Pair Distribution Function (PDF) analysis. The PDF of the empty CuBTTri generated from the in house total scattering experiment (blue) and from the structural refinement (red). Highlighted in green is the difference between these two PDFs.

reverse Monte Carlo modeling to find the disorder within the empty CuBTTri structure. The next step is to synthesize the CysamNO and measure the reaction with the MOF *in operando*. This is proposed to be done in an open capillary to provide a gas outlet for the NO being formed during the reaction (Figure 6.5). To allow powder averaging and mixing of the reagents, the capillary will still have to spin slightly. To determine the influence of the solvent on the MOF, a separate measurement of the bulk solvent and in the MOF needs to be done. Using the program PDFgetX3, the data from the solvent and the capillary will be subtracted before the Fourier transformation of the total scattering data. However, as an initial approach, some Fourier difference maps will be calculated to find average positions of adsorbed molecules. For this, Rietveld refinement method will be used to refine the structure of the CuBTTri. Then, by calculating the Fourier difference map we try to see whether water molecules can be located in close proximity of the copper centers. The structure refinement of the second data set will be used to determine the location of the RSNO. To locate the RSNO in the MOF, Fourier difference will be calculated again. While the adsorption and desorption of the RSNO on the Cu center is a randomized, dynamic process, the coordination on the metal center is supposed to be rather localized. Long measurements and a time averaged signal should make it possible to determine the location and orientation of the RSNO at the metal center. Further structural analysis of the PDFs will follow the initial analysis of the average structure. The

results from theoretical studies, predicting the adsorption sites, will function as a starting structure for the structural refinements. Due to limited intensities and prolonged measurement times, based on the detector setup, the in house instrument can only provide rudimentary results. However, the initial results from this study should enable a proposal seeking an funding and beam time to perform these experiments also at a synchrotron.

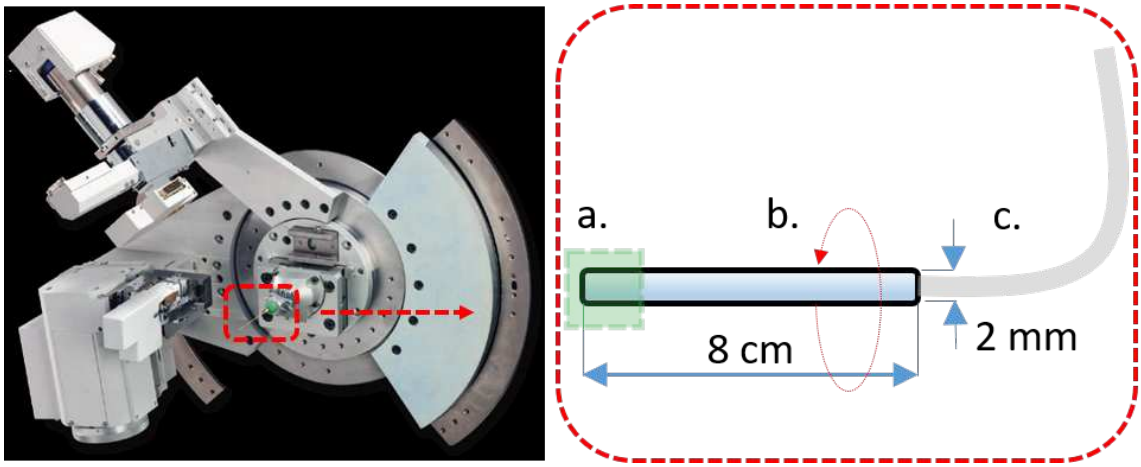

Figure 6.5: Illustration of the proposed experimental setup for the *operando* total scattering measurement. The goniometer setup in the Empyrean diffractometer with the capillary position (left) and a cartoon showing detailed information about a.) the capillary holder, b.) the glass capillary, and c.) the polymer tube for the gas outlet.

Bibliography

[1] U.S. Energy Information Administration. Monthly energy review. Report DOE/EIA-0035(2019/12), U.S. Energy Information Administration, December, 23, 2019 2019.

[2] M. Yaso, T. Takaiwa, Y. Minagi, K. Kubota, S. Morito, T. Ohba, and A. K. Das. Study of microstructures on cross section of japanese sword. *Esomat 2009 - 8th European Symposium on Martensitic Transformations*, 2009.

[3] M. Holler, M. Guizar-Sicairos, E. H. R. Tsai, R. Dinapoli, E. Muller, O. Bunk, J. Raabe, and G. Aeppli. High-resolution non-destructive three-dimensional imaging of integrated circuits. *Nature*, 543(7645):402–+, 2017.

[4] E. Quarez, K. F. Hsu, R. Pcionek, N. Frangis, E. K. Polychroniadis, and M. G. Kanatzidis. Nanostructuring, compositional fluctuations, and atomic ordering in the thermoelectric materials $AgPb_mSbTe_{2+m}$. the myth of solid solutions. *Journal of the American Chemical Society*, 127(25):9177–9190, 2005.

[5] J. D. Figueroa, T. Fout, S. Plasynski, H. McIlvried, and R. D. Srivastava. Advancesn in CO_2 capture technology - the us department of energy's carbon sequestration program. *International Journal of Greenhouse Gas Control*, 2(1):9–20, 2008.

[6] D. Y. C. Leung, G. Caramanna, and M. M. Maroto-Valer. An overview of current status of carbon dioxide capture and storage technologies. *Renewable & Sustainable Energy Reviews*, 39:426–443, 2014.

[7] T. Banaszkiewicz, M. Chorowski, and W. Gizicki. Comparative analysis of cryogenic and ptsa technologies for systems of oxygen production. *Advances in Cryogenic Engineering*, 1573:1373–1378, 2014.

[8] R. R. Vemula, M. V. Kothare, and S. Sircar. Anatomy of a rapid pressure swing adsorption process performance. *Aiche Journal*, 61(6):2008–2014, 2015.

[9] John Meurig Thomas. Summarizing comments on the discussion and a prospectus for urgent future action. *Philosophical Transactions of the Royal Society A: Mathematical, Physical and Engineering Sciences*, 374(2061), 2016.

[10] R. J. Davis, V. V. Guliants, G. Huber, R. F. Lobo, J. T. Miller, M. Neurock, R. Sharma, and L. Thompson. International assessment of research and development in catalysis by nanostructured materials technical report. *WTEC Panel Report*, 2009.

[11] A. G. Slater and A. I. Cooper. Function-led design of new porous materials. *Science*, 348(6238), 2015.

[12] D. Cazorla-Amorós, J. Alcañiz-Monge, M. A. de la Casa-Lillo, and A. Linares-Solano. CO_2 as an adsorptive to characterize carbon molecular sieves and activated carbons. *Langmuir*, 14(16):4589–4596, 1998.

[13] Ch Baerlocher, W. M. Meier, David Olson, and W. M. Meier. *Atlas of zeolite framework types*. Elsevier, Amsterdam ; New York, 5th rev. edition, 2001.

[14] S. R. Batten, N. R. Champness, X. M. Chen, J. Garcia-Martinez, S. Kitagawa, L. Ohrstrom, M. O'Keeffe, M. P. Suh, and J. Reedijk. Terminology of metal-organic frameworks and coordination polymers (iupac recommendations 2013). *Pure and Applied Chemistry*, 85(8):1715–1724, 2013.

[15] K. S. Park, Z. Ni, A. P. Cote, J. Y. Choi, R. D. Huang, F. J. Uribe-Romo, H. K. Chae, M. O'Keeffe, and O. M. Yaghi. Exceptional chemical and thermal stability of zeolitic imidazolate frameworks. *Proceedings of the National Academy of Sciences of the United States of America*, 103(27):10186–10191, 2006.

[16] H. Jeong, D. Kim, K. I. Kim, and I. K. Song. Adsorption characteristics of nitrogen and oxygen onto ion-exchanged X-type zeolite. *Nanocomposites and Nanoporous Materials*, 119:143–+, 2007.

[17] V. N. Choudary, R. V. Jasra, and T. S. G Bhat. Adsorption of nitrogen-oxygen mixture in NaCaA zeolites by elution chromatography. *Ind. Eng. Chem. Res.*, 32:548, 1993.

[18] Guillaume Maurin, Philip L. Llewellyn, Thomas Poyet, and Renaud Denoyel. Nitrogen adsorption on divalent cation substituted x-faujasites: Microcalorimetry and monte carlo simulation. *Adsorption*, 11(1):343–347, 2005.

[19] J. W. Niemantsverdriet. *Spectroscopy in catalysis : an introduction*. Wiley-VCH, Weinheim Chichester, 3rd completely rev. and enl. edition, 2007.

[20] M. El-Roz, P. Bazin, M. Daturi, and F. Thibault-Starzyk. Operando infrared (IR) coupled to steady-state isotopic transient kinetic analysis (SSITKA) for photocatalysis: Reactivity and mechanistic studies. *Acs Catalysis*, 3(12):2790–2798, 2013.

[21] M. Feuerstein and R. F. Lobo. Characterization of li cations in zeolite LiX by solid-state nmr spectroscopy and neutron diffraction. *Chemistry of Materials*, 10(8):2197–2204, 1998.

[22] Paul A. Wright, John M. Thomas, Anthony K. Cheetham, and Andreas K. Nowak. Localizing active sites in zeolitic catalysts: neutron powder profile analysis and computer simulation of deuteropyridine bound to gallozeolite-l. *Nature*, 318(6047):611–614, 1985.

[23] P. A. Wright, J. M. Thomas, S. Ramdas, and A. K Cheetham. Locating the sites of adsorbed species in heterogeneous catalysts: a Rietveld neutron powder profile study of xenon in zeolite-rho. *J. Chem. Soc., Chem. Commun.*, 20:1338, 1984.

[24] A. N. Fitch, H. Jobic, and A. Renouprez. Localization of benzene in sodium-y-zeolite by powder neutron diffraction. *The Journal of Physical Chemistry*, 90(7):1311–1318, 1986.

[25] H. M. Rietveld. A profile refinement method for nuclear and magnetic structures. *Journal of Applied Crystallography*, 2:65–71, 1969.

[26] W. Friedrich, P. Knipping, and M. Laue. Interference appearances in x-rays. *Annalen Der Physik*, 41(10):971–988, 1913.

[27] W. H. Bragg and W. L. Bragg. The reflection of x-rays by crystals. *Proceedings of the Royal Society of London Series a-Containing Papers of a Mathematical and Physical Character*, 88(605):428–438, 1913.

[28] D. D. Rodriguez, C. Grosse, S. Himmel, C. Gonzalez, I. M. de Ilarduya, S. Becker, G. M. Sheldrick, and I. Uson. Crystallographic ab initio protein structure solution below atomic resolution. *Nature Methods*, 6(9):651–U39, 2009.

[29] S. J. L. Billinge and I. Levin. The problem with determining atomic structure at the nanoscale. *Science*, 316(5824):561–565, 2007.

[30] J Il Langford and AJC Wilson. Scherrer after sixty years: a survey and some new results in the determination of crystallite size. *Journal of applied crystallography*, 11(2):102–113, 1978.

[31] Peter Debye. Zerstreuung von röntgenstrahlen. *Annalen der Physik*, 351(6):809–823, 1915.

[32] F Zernike and JA Prins. Die Beugung von Röntgenstrahlen in Flüssigkeiten als Effekt der Molekuelanordnung. *Zeitschrift für Physik*, 41(2-3):184–194, 1927.

[33] P Debye and H Menke. The determination of the inner structure of liquids by x-ray means. *Phys Z*, 31:797–798, 1930.

[34] T Egami. Atomic correlations in non-periodic matter. *Materials Transactions, JIM*, 31(3):163–176, 1990.

[35] B. E. Warren. *X-ray diffraction*. Dover Publications, New York, dover edition, 1990.

[36] Rosalind E Franklin. The interpretation of diffuse x-ray diagrams of carbon. *Acta crystallographica*, 3(2):107–121, 1950.

[37] Rosalind E Franklin. Crystallite growth in graphitizing and non-graphitizing carbons. *Proceedings of the Royal Society of London. Series A. Mathematical and Physical Sciences*, 209(1097):196–218, 1951.

[38] W. H. Zachariasen. The liquid "structure" of methyl alcohol. *Journal of Chemical Physics*, 3(3):158–161, 1935.

[39] W. H. Zachariasen. Note on the scattering of x-rays from fluids containing polyatomic molecules. *Physical Review*, 47(4):277–278, 1935.

[40] D. D. Kofalt, S. Nanao, T. Egami, K. M. Wong, and S. J. Poon. Differential anomalous-x-ray-scattering study of icosahedral and amorphous $\mathrm{pd}_{58.8}\mathrm{u}_{20.6}\mathrm{si}_{20.6}$. *Physical Review Letters*, 57(1):114–117, 1986.

[41] S. Aur, D. Kofalt, Y. Waseda, T. Egami, R. Wang, H. S. Chen, and Teo Boon-Keng. Local structure of amorphous mo50ni50 determined by anomalous x-ray scattering using synchroton radiation. *Solid State Communications*, 48(2):111–115, 1983.

[42] Takeshi Egami and S. J. L. Billinge. *Underneath the Bragg peaks : structural analysis of complex materials*. Pergamon materials series. Elsevier, Amsterdam, second edition edition, 2012.

[43] S. J. L. Billinge and M. G. Kanatzidis. Beyond crystallography: the study of disorder, nanocrystallinity and crystallographically challenged materials with pair distribution functions. *Chemical Communications*, 7:749–760, 2004.

[44] T. Proffen and H. Kim. Advances in total scattering analysis. *Journal of Materials Chemistry*, 19(29):5078–5088, 2009.

[45] S. Bruhne, S. Gottlieb, W. Assmus, E. Alig, and M. U. Schmidt. Atomic structure analysis of nanocrystalline boehmite AlO(OH). *Crystal Growth & Design*, 8(2):489–493, 2008.

[46] M. W. Terban, M. Johnson, M. Di Michiel, and S. J. L. Billinge. Detection and characterization of nanoparticles in suspension at low concentrations using the x-ray total scattering pair distribution function technique. *Nanoscale*, 7(12):5480–5487, 2015.

[47] Anton Gagin, Andrew J Allen, and Igor Levin. Combined fitting of small-and wide-angle x-ray total scattering data from nanoparticles: benefits and issues. *Journal of Applied Crystallography*, 47(2):619–629, 2014.

[48] C. L. Farrow and S. J. L. Billinge. Relationship between the atomic pair distribution function and small-angle scattering: implications for modeling of nanoparticles. *Acta Crystallographica a-Foundation and Advances*, 65:232–239, 2009.

[49] J. L. Billinge Simon. The rise of the x-ray atomic pair distribution function method: a series of fortunate events. *Philosophical Transactions of the Royal Society A: Mathematical, Physical and Engineering Sciences*, 377(2147):20180413, 2019.

[50] S. J. L. Billinge, T. Dykhne, P. Juh, R. Taylor, and J. Florence. Characterisation of amorphous and nanocrystalline molecular materials by total scattering. *CrystEngComm*, 12:1366, 2010.

[51] T. Proffen, S. J. L. Billinge, T. Egami, and D. Louca. Structural analysis of complex materials using the atomic pair distribution function - a practical guide. *Zeitschrift Fur Kristallographie*, 218(2):132–143, 2003.

[52] U.S. DOE Nuclear Energy Research Advisory Committee. A technology roadmap for the generation iv nuclear energy system. Report, U.S. DOE Nuclear Energy Research Advisory Committee and the Generation IV International Forum, 2002.

[53] X. F. Liu, N. Fechler, and M. Antonietti. Salt melt synthesis of ceramics, semiconductors and carbon nanostructures. *Chemical Society Reviews*, 42(21):8237–8265, 2013.

[54] G. Caceres, N. Anrique, A. Girard, J. Degreve, J. Baeyens, and H. L. Zhang. Performance of molten salt solar power towers in chile. *Journal of Renewable and Sustainable Energy*, 5(5), 2013.

[55] H. L. Zhang, J. Baeyens, J. Degreve, and G. Caceres. Concentrated solar power plants: Review and design methodology. *Renewable & Sustainable Energy Reviews*, 22:466–481, 2013.

[56] T. J. Dolan. Introduction. In T. J. Dolan, editor, *Molten salt reactors and thorium energy*, molten salt reactors and thorium energy 1, pages 1–12. Woodhead Publishing, Duxford, UK ; Cambridge, MA, 2017.

[57] H. O. Nam and D. Morgan. Redox condition in molten salts and solute behavior: A first-principles molecular dynamics study. *Journal of Nuclear Materials*, 465:224–235, 2015.

[58] S. Le Roux and P. Jund. Ring statistics analysis of topological networks: New approach and application to amorphous GeS_2 and SiO_2 systems. *Computational Materials Science*, 49(1):70–83, 2010.

[59] N. L. Panwar, S. C. Kaushik, and S. Kothari. Role of renewable energy sources in environmental protection: A review. *Renewable & Sustainable Energy Reviews*, 15(3):1513–1524, 2011.

[60] Robert Everett, Godfrey Boyle, Stephen Peake, and Janet Ramage. *Energy systems and sustainability: Power for a sustainable future*. Oxford Univerity Press, 2012.

[61] W Bludau, A Onton, and W Heinke. Temperature dependence of the band gap of silicon. *Journal of Applied Physics*, 45(4):1846–1848, 1974.

[62] National Renewable Energy Laboratory. Best research-cell efficiencies, 2019.

[63] E. A. Alsema and E. Nieuwlaar. Energy viability of photovoltaic systems. *Energy Policy*, 28(14):999–1010, 2000.

[64] Xiong Li, Dongqin Bi, Chenyi Yi, Jean-David Décoppet, Jingshan Luo, Shaik Mohammed Zakeeruddin, Anders Hagfeldt, and Michael Grätzel. A vacuum flash–assisted solution

process for high-efficiency large-area perovskite solar cells. *Science*, 353(6294):58–62, 2016.

[65] Q. Wang, Y. C. Shao, Q. F. Dong, Z. G. Xiao, Y. B. Yuan, and J. S. Huang. Large fill-factor bilayer iodine perovskite solar cells fabricated by a low-temperature solution-process. *Energy & Environmental Science*, 7(7):2359–2365, 2014.

[66] P. Qin, S. Tanaka, S. Ito, N. Tetreault, K. Manabe, H. Nishino, M. K. Nazeeruddin, and M. Gratzel. Inorganic hole conductor-based lead halide perovskite solar cells with 12.4 *Nature Communications*, 5, 2014.

[67] D. H. Fabini, G. Laurita, J. S. Bechtel, C. C. Stoumpos, H. A. Evans, A. G. Kontos, Y. S. Raptis, P. Falaras, A. Van der Ven, M. G. Kanatzidis, and R. Seshadri. Dynamic stereochemical activity of the sn^{2+} lone pair in perovskite $CsSnBr_3$. *Journal of the American Chemical Society*, 138(36):11820–11832, 2016.

[68] D. H. Fabini, T. A. Siaw, C. C. Stoumpos, G. Laurita, D. Olds, K. Page, J. G. Hu, M. G. Kanatzidis, S. Han, and R. Seshadri. Universal dynamics of molecular reorientation in hybrid lead iodide perovskites. *J Am Chem Soc*, 139(46):16875–16884, 2017.

[69] G. Laurita, D. H. Fabini, C. C. Stoumpos, M. G. Kanatzidis, and R. Seshadri. Chemical tuning of dynamic cation off-centering in the cubic phases of hybrid tin and lead halide perovskites. *Chem Sci*, 8(8):5628–5635, 2017.

[70] Annalise E. Maughan, Alex M. Ganose, Andrew M. Candia, Juliette T. Granger, David O. Scanlon, and James R. Neilson. Anharmonicity and octahedral tilting in hybrid vacancy-ordered double perovskites. *Chemistry of Materials*, 30(2):472–483, 2018.

[71] E. L. Redmond, B. P. Setzler, P. Juhas, S. J. L. Billinge, and T. F. Fuller. In-situ monitoring of particle growth at pemfc cathode under accelerated cycling conditions. *Electrochemical and Solid State Letters*, 15(5):B72–B74, 2012.

[72] Zhijie Kong, Yazan Maswadeh, Jorge A. Vargas, Shiyao Shan, Zhi-Peng Wu, Haval Kareem, Asher C. Leff, Dat T. Tran, Fangfang Chang, Shan Yan, Sanghyun Nam, Xingfang Zhao, Jason M. Lee, Jin Luo, Sarvjit Shastri, Gang Yu, Valeri Petkov, and Chuan-Jian Zhong. Origin of high activity and durability of twisty nanowire alloy catalysts under oxygen reduction and fuel cell operating conditions. *Journal of the American Chemical Society*, 2019.

[73] Vicky V. T. Doan-Nguyen, Kota S. Subrahmanyam, Megan M. Butala, Jeffrey A. Gerbec, Saiful M. Islam, Katherine N. Kanipe, Catrina E. Wilson, Mahalingam Balasubramanian, Kamila M. Wiaderek, Olaf J. Borkiewicz, Karena W. Chapman, Peter J. Chupas, Martin Moskovits, Bruce S. Dunn, Mercouri G. Kanatzidis, and Ram Seshadri. Molybdenum polysulfide chalcogels as high-capacity, anion-redox-driven electrode materials for Li-ion batteries. *Chemistry of Materials*, 28(22):8357–8365, 2016.

[74] Avery E Baumann, Xu Han, Megan M Butala, and V Sara Thoi. Lithium thiophosphate functionalized zirconium mofs for li–s batteries with enhanced rate capabilities. *Journal of the American Chemical Society*, 141(44):17891–17899, 2019.

[75] Dimas G de Oteyza, Patrick Gorman, Yen-Chia Chen, Sebastian Wickenburg, Alexander Riss, Duncan J Mowbray, Grisha Etkin, Zahra Pedramrazi, Hsin-Zon Tsai, Angel Rubio, et al. Direct imaging of covalent bond structure in single-molecule chemical reactions. *Science*, 340(6139):1434–1437, 2013.

[76] Ahmed H Zewail. Four-dimensional electron microscopy. *Science*, 328(5975):187–193, 2010.

[77] Peter J Chupas, Karena W Chapman, and Peter L Lee. Applications of an amorphous silicon-based area detector for high-resolution, high-sensitivity and fast time-resolved pair distribution function measurements. *Journal of Applied Crystallography*, 40(3):463–470, 2007.

[78] Yugang Sun, Yang Ren, Dean R Haeffner, Jonathan D Almer, Lin Wang, Wenge Yang, and Tu T Truong. Nanophase evolution at semiconductor/electrolyte interface in situ probed by time-resolved high-energy synchrotron X-ray diffraction. *Nano letters*, 10(9):3747–3753, 2010.

[79] Haiyan Zhao, Tina M Nenoff, Guy Jennings, Peter J Chupas, and Karena W Chapman. Determining quantitative kinetics and the structural mechanism for particle growth in porous templates. *The Journal of Physical Chemistry Letters*, 2(21):2742–2746, 2011.

[80] Mark A Newton, Karena W Chapman, David Thompsett, and Peter J Chupas. Chasing changing nanoparticles with time-resolved pair distribution function methods. *Journal of the American Chemical Society*, 134(11):5036–5039, 2012.

[81] Kirsten MØ Jensen, Mogens Christensen, Pavol Juhas, Christoffer Tyrsted, Espen D Bøjesen, Nina Lock, Simon JL Billinge, and Bo B Iversen. Revealing the mechanisms behind SnO_2 nanoparticle formation and growth during hydrothermal synthesis: an in situ total scattering study. *Journal of the American Chemical Society*, 134(15):6785–6792, 2012.

[82] Hsiu-Wen Wang, David J Wesolowski, Thomas E Proffen, Lukas Vlcek, Wei Wang, Lawrence F Allard, Alexander I Kolesnikov, Mikhail Feygenson, Lawrence M Anovitz, and Rick L Paul. Structure and stability of SnO2 nanocrystals and surface-bound water species. *Journal of the American Chemical Society*, 135(18):6885–6895, 2013.

[83] Hsiu-Wen Wang, Michael Naguib, Katharine Page, David J Wesolowski, and Yury Gogotsi. Resolving the structure of $Ti_3C_3T_x$ MXenes through multilevel structural modeling of the atomic pair distribution function. *Chemistry of Materials*, 28(1):349–359, 2015.

[84] Katharine Page, Thomas Proffen, Markus Niederberger, and Ram Seshadri. Probing local dipoles and ligand structure in BaTiO3 nanoparticles. *Chemistry of Materials*, 22(15):4386–4391, 2010.

[85] Henry E Fischer, Adrian C Barnes, and Philip S Salmon. Neutron and x-ray diffraction studies of liquids and glasses. *Reports on Progress in Physics*, 69(1):233, 2005.

[86] JE Enderby, DM North, and PA Egelstaff. The partial structure factors of liquid Cu-Sn. *Philosophical Magazine*, 14(131):961–970, 1966.

[87] Anita Zeidler, Philip S Salmon, Henry E Fischer, Jörg C Neuefeind, J Mike Simonson, Hartmut Lemmel, Helmut Rauch, and Thomas E Markland. Oxygen as a site specific probe of the structure of water and oxide materials. *Physical review letters*, 107(14):145501, 2011.

[88] Cristian Ledesma, Jia Yang, De Chen, and Anders Holmen. Recent approaches in mechanistic and kinetic studies of catalytic reactions using SSITKA technique. *ACS Catalysis*, 4(12):4527–4547, 2014.

[89] Jörg Neuefeind, Mikhail Feygenson, John Carruth, Ron Hoffmann, and Kenneth K Chipley. The nanoscale ordered materials diffractometer NOMAD at the spallation neutron source SNS. *Nuclear Instruments and Methods in Physics Research Section B: Beam Interactions with Materials and Atoms*, 287:68–75, 2012.

[90] Przemek Klosowski, Mark Koennecke, JZ Tischler, and Raymond Osborn. NeXus: A common format for the exchange of neutron and synchroton data. *Physica B: Condensed Matter*, 241:151–153, 1997.

[91] Owen Arnold, Jean-Christophe Bilheux, JM Borreguero, Alex Buts, Stuart I Campbell, L Chapon, M Doucet, N Draper, R Ferraz Leal, MA Gigg, et al. Mantid—data analysis and visualization package for neutron scattering and μ sr experiments. *Nuclear Instruments and Methods in Physics Research Section A: Accelerators, Spectrometers, Detectors and Associated Equipment*, 764:156–166, 2014.

[92] Imre-Georges Bajusz, James G Goodwin, Douglas Galloway, and Nanette Greenlay. Effect of Ca^{2+} exchange on adsorption of N_2-O_2 mixtures by NaCaX zeolite. *Langmuir*, 14(10):2876–2883, 1998.

[93] Bilge Yilmaz and Ulrich Müller. Catalytic applications of zeolites in chemical industry. *Topics in Catalysis*, 52(6):888–895, 2009.

[94] J. Wellenbüscher, U. Sauerland, W. Mahdi, G. Ertl, and R. Schlögl. Surface characterization of ruthenium-exchanged y-zeolite used in ammonia synthesis. *Surface and Interface Analysis*, 18(9):650–654, 1992.

[95] R. B. Unde and A. G. Gaikward. Kinetic studies of ammonia formation over Fe and Mo containing HZSM-5 catalysts. *Chemical and Biochemical Engineering Quarterly*, 21(2):139 – 144, 2007.

[96] Stacey E. Siporin, Brian C. McClaine, and Robert J. Davis. Adsorption of N_2 and CO_2 on zeolite X exchanged with potassium, barium, or lanthanum. *Langmuir*, 19(11):4707–4713, 2003.

[97] Thierry Bécue, Robert J. Davis, and Juan M. Garces. Effect of cationic promoters on the kinetics of ammonia synthesis catalyzed by ruthenium supported on zeolite x. *Journal of Catalysis*, 179(1):129 – 137, 1998.

[98] Rodney P Townsend and Eric N Coker. Ion exchange in zeolites. *Studies in surface science and catalysis*, 137:467–524, 2001.

[99] Kenneth J Balkus and Kieu T Ly. The preparation and characterization of an X-type zeolite: An experiment in solid-state chemistry. *J. Chem. Educ*, 68(10):875, 1991.

[100] Bruker. *TOPAS V6.0.* Bruker AXS, Karlsruhe, Germany., 2015.

[101] Stuart R. Miller, Paul A. Wright, Thomas Devic, Christian Serre, Gérard Férey, Philip L. Llewellyn, Renaud Denoyel, Lucia Gaberova, and Yaroslav Filinchuk. Single crystal x-ray diffraction studies of carbon dioxide and fuel-related gases adsorbed on the small pore scandium terephthalate metal organic framework, sc2(o2cc6h4co2)3. *Langmuir*, 25(6):3618–3626, 2009.

[102] J. Getzschmann, I. Senkovska, D. Wallacher, M. Tovar, D. Fairen-Jimenez, T. Duren, J. M. van Baten, R. Krishna, and S Kaskel. Methane storage mechanism in the metal-organic framework $Cu_3(btc)_2$: An in situ neutron diffraction study. *Microporous Mesoporous Mater.*, 136:50, 2010.

[103] Juergen Eckert, Caroline Mellot Draznieks, and Anthony K Cheetham. Direct observation of host- guest hydrogen bonding in the zeolite NaY/chloroform system by neutron scattering. *Journal of the American Chemical Society*, 124(2):170–171, 2002.

[104] Matthew R. Hudson, Wendy L. Queen, Jarad A. Mason, Dustin W. Fickel, Raul F. Lobo, and Craig M. Brown. Unconventional, highly selective CO_2 adsorption in zeolite SSZ-13. *Journal of the American Chemical Society*, 134(4):1970–1973, 2012.

[105] Schohn L Shannon and James G Goodwin Jr. Characterization of catalytic surfaces by isotopic-transient kinetics during steady-state reaction. *Chemical reviews*, 95(3):677–695, 1995.

[106] K. S. Park, Z. Ni, A. P. Cote, J. Y. Choi, R. D. Huang, F. J. Uribe-Romo, H. K. Chae, M. O'Keeffe, and O. M Yaghi. Exceptional chemical and thermal stability of zeolitic imidazolate frameworks. *Proc. Natl. Acad. Sci. U. S. A.*, 103:10186, 2006.

[107] Santi Kulprathipanja. *Zeolites in industrial separation and catalysis*. John Wiley & Sons, 2010.

[108] Jiri Cejka, Avelino Corma, and Stacey Zones. *Zeolites and catalysis: synthesis, reactions and applications*. John Wiley & Sons, 2010.

[109] Ralph T Yang. *Adsorbents: fundamentals and applications*. John Wiley & Sons, 2003.

[110] S. Ivanova and R. Lewis. Producing nitrogen via pressure swing adsorption. *Chem. Eng. Prog.*, 108:38, 2012.

[111] V. N. Choudary, R. V. Jasra, and T. S. G. Bhat. Adsorption of nitrogen-oxygen mixture in nacaa zeolites by elution chromatography. *Ind. Eng. Chem. Res.*, 32:548, 1993.

[112] S. R. Miller, P. A. Wright, T. Devic, C. Serre, G. Ferey, P. L. Llewellyn, R. Denoyel, L. Gaberova, and Y. Filinchuk. Single crystal x-ray diffraction studies of carbon dioxide and fuel-related gases adsorbed on the small pore scandium terephthalate metal organic framework, sc-2(o2cc6h4co2)(3). *Langmuir*, 25:3618, 2009.

[113] C Pichon, H Palancher, JL Hodeau, and JF Bérar. Towards operando characterisation by powder diffraction techniques of molecular sieves. *Oil & Gas Science and Technology*, 60(5):831–848, 2005.

[114] E. J. Carrington, I. J. Vitorica-Yrezabal, and L. Brammer. Crystallographic studies of gas sorption in metal-organic frameworks. *Acta Crystallogr., Sect. B: Struct. Sci., Cryst. Eng. Mater.*, 70:404, 2014.

[115] A. Goguet, F. C. Meunier, D. Tibiletti, J. P. Breen, and R. Burch. Spectrokinetic investigation of reverse water-gas-shift reaction intermediates over a pt/ceo2 catalyst. *J. Phys. Chem. B*, 108:20240, 2004.

[116] J. P. Zhang, A. X. Zhu, and X. M. Chen. Single-crystal x-ray diffraction and raman spectroscopy studies of isobaric n-2 adsorption in sod-type metal-organic zeolites. *Chem. Commun.*, 48:11395, 2012.

[117] A. Hornes, A. B. Hungria, P. Bera, A. L. Camara, M. Fernandez-Garcia, A. Martinez-Arias, L. Barrio, M. Estrella, G. Zhou, J. J. Fonseca, J. C. Hanson, and J. A. Rodriguez. Inverse CeO_2/CuO catalyst as an alternative to classical direct configurations for preferential oxidation of CO in hydrogen-rich stream. *J. Am. Chem. Soc.*, 132:34, 2010.

[118] J. C. Hanson, R. Si, W. Xu, S. D. Senanayake, K. Mudiyanselage, D. Stacchiola, J. A. Rodriguez, H. Zhao, K. A. Beyer, G. Jennings, K. W. Chapman, P. J. Chupas, and A. Martinez-

Arias. Pulsed-reactant in situ studies of ceria/CuO catalysts using simultaneous XRD, PDF and DRIFTS measurements. *Catal. Today*, 229:64, 2014.

[119] B. S. Clausen. Combined (q)exafs/xrd: Technique and applications. *Catal. Today*, 39:293, 1998.

[120] K. W. Chapman, P. J. Chupas, and C. J. Kepert. Selective recovery of dynamic guest structure, in a nanoporous prussian blue through in situ x-ray diffraction: A differential pair distribution function analysis. *J. Am. Chem. Soc.*, 127:11232, 2005.

[121] H. Kim, A. Karkamkar, T. Autrey, P. Chupas, and T. Proffen. Determination of structure and phase transition of light element nanocomposites in mesoporous silica: Case study of nh3bh3 mcm-41. *J. Am. Chem. Soc.*, 131:13749, 2009.

[122] K. W. Chapman, P. J. Chupas, and T. M. Nenoff. Radioactive iodine capture in silver-containing mordenites through nanoscale silver iodide formation. *J. Am. Chem. Soc.*, 132:8897, 2010.

[123] John FC Turner, Chris J Benmore, Carolyn M Barker, Nikolas Kaltsoyannis, John Meurig Thomas, William IF David, and C Richard A Catlow. Probing the nature of acetylene bound to the active site of a nina- zeolite y catalyst by in situ neutron scattering. *The Journal of Physical Chemistry B*, 104(32):7570–7573, 2000.

[124] H. Jobic, H. Schober, and P. Pullumbi. Adsorption and diffusion of n-2 and o-2 in lilsx studied by neutron scattering techniques. *Adsorption*, 11:449, 2005.

[125] H. Wu, J. M. Simmons, Y. Liu, C. M. Brown, X. S. Wang, S. Ma, V. K. Peterson, P. D. Southon, C. J. Kepert, H. C. Zhou, T. Yildirim, and W. Zhou. Metal-organic frameworks with exceptionally high methane uptake: Where and how is methane stored? *Chem. - Eur. J.*, 16:5205, 2010.

[126] Daniel Olds, Keith V. Lawler, Arnold A. Paecklar, Jue Liu, Katharine Page, Peter F. Peterson, Paul M. Forster, and James R. Neilson. Capturing the details of N_2 Adsorption

in Zeolite X using stroboscopic isotope contrasted neutron total scattering. *Chemistry of Materials*, 30(1):296–302, 2018.

[127] D. Olds, K. Page, A. Paecklar, P. F. Peterson, J. Liu, G. Rucker, M. Ruiz-Rodriguez, M. Olsen, M. Pawel, S. H. Overbury, and J. R. Neilson. A high precision gas flow cell for performing in situ neutron studies of local atomic structure in catalytic materials. *Rev. Sci. Instrum.*, 88:034101, 2017.

[128] V. Petříček, M. Dušek, and L. Palatinus. Crystallographic computing system jana2006: General features. *Z. Kristallogr. - Cryst. Mater.*, 229:345, 2014.

[129] K. S. Walton and R. Q. Snurr. Applicability of the bet method for determining surface areas of microporous metal-organic frameworks. *J. Am. Chem. Soc.*, 129:8552, 2007.

[130] J. J. Potoff and J. I. Siepmann. Vapor-liquid equilibria of mixtures containing alkanes, carbon dioxide, and nitrogen. *AIChE J.*, 47:1676, 2001.

[131] K. V. Lawler, A. Sharma, B. Alagappan, and P. M. Forster. Assessing zeolite frameworks for noble gas separations through a joint experimental and computational approach. *Microporous Mesoporous Mater.*, 222:104, 2016.

[132] S. Buttefey, A. Boutin, C. Mellot-Draznieks, and A. H Fuchs. A simple model for predicting the na+ distribution in anhydrous NaY and NaX zeolites. *J. Phys. Chem. B*, 105:9569, 2001.

[133] M. Jeffroy, C. Nieto-Draghi, and A. Boutin. Molecular simulation of zeolite flexibility. *Mol. Simul.*, 40:6, 2014.

[134] R. S. Pillai, G. Sethia, and R. V. Jasra. Sorption of co, ch4, and n-2 in alkali metal ion exchanged zeolite-x: Grand canonical monte carlo simulation and volumetric measurements. *Ind. Eng. Chem. Res.*, 49:5816, 2010.

[135] J. J. Pluth and J. V. Smith. Positions of cations and molecules in zeolites with faujasite-type framework 0.7. dehydrated ca-exchanged x. *Mater. Res. Bull.*, 7:1311, 1972.

[136] T. Frising and P. Leflaive. Extraframework cation distributions in x and y faujasite zeolites: A review. *Microporous Mesoporous Mater.*, 114:27, 2008.

[137] W. Wong-Ng, J. A. Kaduk, Q. Huang, L. Espinal, L. Li, and J. W Burress. Investigation of NaY zeolite with adsorbed CO_2 by neutron powder diffraction. *Microporous Mesoporous Mater.*, 172:95, 2013.

[138] A. N. Fitch, H. Jobic, and A. Renouprez. Localization of benzene in sodium-y-zeolite by powder neutron diffraction. *J. Phys. Chem.*, 90:1311, 1986.

[139] Y. S. Bae and C. H. Lee. Sorption kinetics of eight gases on a carbon molecular sieve at elevated pressure. *Carbon*, 43:95, 2005.

[140] P. Bai, P. Ghosh, J. C. Sung, D. Kohen, J. I. Siepmann, and R. Q. Snurr. A computational study of the adsorption of n-perfluorohexane in zeolite bcr-704. *Fluid Phase Equilib.*, 366:146, 2014.

[141] C. Ledesma, J. Yang, D. Chen, and A Holmen. Recent approaches in mechanistic and kinetic studies of catalytic reactions using ssitka technique. *ACS Catal.*, 4:4527, 2014.

[142] A. Goguet, F. C. Meunier, D. Tibiletti, J. P. Breen, and R Burch. Spectrokinetic investigation of reverse water-gas-shift reaction intermediates over a Pt/CeO_2 catalyst. *J. Phys. Chem. B*, 108:20240, 2004.

[143] J. P. Zhang, A. X. Zhu, and X. M Chen. Single-crystal x-ray diffraction and raman spectroscopy studies of isobaric n-2 adsorption in sod-type metal-organic zeolites. *Chem. Commun.*, 48:11395, 2012.

[144] J. C. Hanson, R. Si, W. Xu, S. D. Senanayake, K. Mudiyanselage, D. Stacchiola, J. A. Rodriguez, H. Zhao, K. A. Beyer, G. Jennings, K. W. Chapman, P. J. Chupas, and A Martinez-Arias. Pulsed-reactant in situ studies of ceria/cuo catalysts using simultaneous xrd, pdf and drifts measurements. *Catal. Today*, 229:64, 2014.

[145] B. S. Clausen. Combined (Q)EXAFS/XRD: Technique and applications. *Catal. Today*, 39:293, 1998.

[146] A. Goursot, V. Vasilyev, and A Arbuznikov. Modeling of adsorption properties of zeolites: Correlation with the structure. *J. Phys. Chem. B*, 101:6420, 1997.

[147] Z. Qin, K. A. Cychosz, G. Melinte, H. El Siblani, J.-P. Gilson, M. Thommes, C. Fernandez, S. Mintova, O. Ersen, and V. Valtchev. Opening the cages of faujasite-type zeolite. *J. Am. Chem. Soc.*, 139:17273, 2017.

[148] F. Salles, G. Maurin, C. Serre, P. L. Llewellyn, C. Knofel, H. J. Choi, Y. Filinchuk, L. Oliviero, A. Vimont, J. R. Long, and G. Ferey. Multistep N_2 breathing in the metal-organic framework Co(1,4-benzenedipyrazolate). *J. Am. Chem. Soc.*, 132:13782, 2010.

[149] A. Zeidler, P. S. Salmon, H. E. Fischer, J. C. Neuefeind, J. M. Simonson, and T. E Markland. Isotope effects in water as investigated by neutron diffraction and path integral molecular dynamics. *J. Phys.: Condens. Matter*, 24:284126, 2012.

[150] E. C. Spencer, J. A. K. Howard, G. J. McIntyre, J. L. C. Rowsell, and O. M Yaghi. Determination of the hydrogen absorption sites in zn4o(1,4-benzenedicarboxylate) by single crystal neutron diffraction. *Chem. Commun.*, 3:278, 2006.

[151] J. S. Dugdale and D. K. C. MacDonald. Lattice thermal conductivity. *Physical Review*, 98(6):1751–1752, 1955.

[152] Thomas M. Brenner, David A. Egger, Andrew M. Rappe, Leeor Kronik, Gary Hodes, and David Cahen. Are mobilities in hybrid organic–inorganic halide perovskites actually "high"? *The Journal of Physical Chemistry Letters*, 6(23):4754–4757, 2015.

[153] Sokseiha Muy, John C. Bachman, Livia Giordano, Hao-Hsun Chang, Douglas L. Abernathy, Dipanshu Bansal, Olivier Delaire, Satoshi Hori, Ryoji Kanno, Filippo Maglia, Saskia Lupart, Peter Lamp, and Yang Shao-Horn. Tuning mobility and stability of lithium ion

conductors based on lattice dynamics. *Energy & Environmental Science*, 11(4):850–859, 2018.

[154] S. L. Chodos, A. M. Black, and C. D. Flint. Vibronic spectra and lattice-dynamics of Cs_2MnF_6 and $a_2{}^1m^{IV}f_6{:}mnf_6{}^{2-}$. *Journal of Chemical Physics*, 65(11):4816–4824, 1976.

[155] V. V. Hizhnyakov, V. G. Plekhanov, V. V. Shepelev, and G. S. Zavt. Hot luminescence of self-trapped excitons in alkali-halide crystals. *Physica Status Solidi B-Basic Research*, 108(2):531–540, 1981.

[156] J. D. Freire and R. S. Katiyar. Lattice-dynamics of crystals with tetragonal $BaTIiO_3$ structure. *Physical Review B*, 37(4):2074–2085, 1988.

[157] D. Khatib, R. Migoni, G. E. Kugel, and L. Godefroy. Lattice-dynamics of $BaTiO_3$ in the cubic phase. *Journal of Physics-Condensed Matter*, 1(49):9811–9822, 1989.

[158] J. Bardeen, L. N. Cooper, and J. R. Schrieffer. Microscopic theory of superconductivity. *Physical Review*, 106(1):162–164, 1957.

[159] Z. H. Dughaish. Lead telluride as a thermoelectric material for thermoelectric power generation. *Physica B-Condensed Matter*, 322(1-2):205–223, 2002.

[160] Boris Sangiorgio, Emil S. Bozin, Christos D. Malliakas, Michael Fechner, Arkadiy Simonov, Mercouri G. Kanatzidis, Simon J. L. Billinge, Nicola A. Spaldin, and Thomas Weber. Correlated local dipoles in pbte. *Physical Review Materials*, 2(8):085402, 2018.

[161] Li-Dong Zhao, Shih-Han Lo, Yongsheng Zhang, Hui Sun, Gangjian Tan, Ctirad Uher, C. Wolverton, Vinayak P. Dravid, and Mercouri G. Kanatzidis. Ultralow thermal conductivity and high thermoelectric figure of merit in SnSe crystals. *Nature*, 508(7496):373–+, 2014.

[162] Xun Shi, Jiong Yang, James R. Salvador, Miaofang Chi, Jung Y. Cho, Hsin Wang, Shengqiang Bai, Jihui Yang, Wenqing Zhang, and Lidong Chen. Multiple-filled skutteru-

dites: High thermoelectric figure of merit through separately optimizing electrical and thermal transports. *Journal of the American Chemical Society*, 133(20):7837–7846, 2011.

[163] R. J. Cava, F. Reidinger, and B. J. Wuensch. Mobile ion distribution and anharmonic thermal motion in fast ion conducting cu2s. *Solid State Ionics*, 5(OCT):501–504, 1981.

[164] A. Yoshiasa, K. Koto, F. Kanamaru, S. Emura, and H. Horiuchi. Anharmonic thermal vibrations in wurtzite-type agi. *Acta Crystallographica Section B-Structural Science*, 43:434–440, 1987.

[165] X. Y. Zhu and V. Podzorov. Charge carriers in hybrid organic-inorganic lead halide perovskites might be protected as large polarons. *J. Phys. Chem. Lett.*, 6:4758, 2015.

[166] Christopher E. Patrick, Karsten W. Jacobsen, and Kristian S. Thygesen. Anharmonic stabilization and band gap renormalization in the perovskite $CsSnI_3$. *Physical Review B*, 92(20), 2015.

[167] O. Yaffe, Y. Guo, L. Z. Tan, D. A. Egger, T. Hull, C. C. Stoumpos, F. Zheng, T. F. Heinz, L. Kronik, M. G. Kanatzidis, J. S. Owen, A. M. Rappe, M. A. Pimenta, and L. E. Brus. Local polar fluctuations in lead halide perovskite crystals. *Phys. Rev. Lett.*, 118:136001, 2017.

[168] R. X. Yang, J. M. Skelton, L. da Silva, J. M. Frost, and A. Walsh. Spontaneous octahedral tilting in the cubic inorganic caesium halide perovskites $CsSnX_3$ and $CsPbX_3$ (X= F, Cl, Br, I). *J. Phys. Chem. Lett.*, 8:4720, 2017.

[169] A. N. Beecher, O. E. Semonin, J. M. Skelton, J. M. Frost, M. W. Terban, H. Zhai, A. Alatas, J. S. Owen, A. Walsh, and S. J. Billinge. Direct observation of dynamic symmetry breaking above room temperature in methylammonium lead iodide perovskite. *ACS Energy Lett.*, 1:880, 2016.

[170] Michael M Lee, Joël Teuscher, Tsutomu Miyasaka, Takurou N Murakami, and Henry J Snaith. Efficient hybrid solar cells based on meso-superstructured organometal halide perovskites. *Science*, 338(6107):643–647, 2012.

[171] S. D. Stranks and H. J. Snaith. Metal-halide perovskites for photovoltaic and light-emitting devices. *Nat. Nanotechnol.*, 10:391, 2015.

[172] Dong Shi, Valerio Adinolfi, Riccardo Comin, Mingjian Yuan, Erkki Alarousu, Andrei Buin, Yin Chen, Sjoerd Hoogland, Alexander Rothenberger, Khabiboulakh Katsiev, Yaroslav Losovyj, Xin Zhang, Peter A. Dowben, Omar F. Mohammed, Edward H. Sargent, and Osman M. Bakr. Low trap-state density and long carrier diffusion in organolead trihalide perovskite single crystals. *Science*, 347(6221):519–522, 2015.

[173] Y. Bi, E. M. Hutter, Y. Fang, Q. Dong, J. Huang, and T. J. Savenije. Charge carrier lifetimes exceeding 15 μ s in methylammonium lead iodide single crystals. *J. Phys. Chem. Lett.*, 7:923, 2016.

[174] H. Zhu, K. Miyata, Y. Fu, J. Wang, P. P. Joshi, D. Niesner, K. W. Williams, S. Jin, and X. Y. Zhu. Screening in crystalline liquids protects energetic carriers in hybrid perovskites. *Science*, 353:1409, 2016.

[175] M. Sendner, P. K. Nayak, D. A. Egger, S. Beck, C. Müller, B. Epding, W. Kowalsky, L. Kronik, H. J. Snaith, A. Pucci, and R. Lovrincic. Optical phonons in methylammonium lead halide perovskites and implications for charge transport. *Mater. Horiz.*, 3:613, 2016.

[176] A. J. Neukirch, W. Nie, J. C. Blancon, K. Appavoo, H. Tsai, M. Y. Sfeir, C. Katan, L. Pedesseau, J. Even, J. J. Crochet, G. Gupta, A. D. Mohite, and S. Tretiak. Polaron stabilization by cooperative lattice distortion and cation rotations in hybrid perovskite materials. *Nano Lett.*, 16:3809, 2016.

[177] Alessandro Pecchia, Desiree Gentilini, Daniele Rossi, Matthias Auf der Maur, and Aldo Di Carlo. Role of ferroelectric nanodomains in the transport properties of perovskite solar cells. *Nano Letters*, 16(2):988–992, 2016.

[178] Mischa Bonn, Kiyoshi Miyata, Euan Hendry, and X. Y. Zhu. Role of dielectric drag in polaron mobility in lead halide perovskites. *ACS Energy Letters*, 2(11):2555–2562, 2017.

[179] Hui Zhu, Qingxiao Wang, Chenxi Zhang, Rafik Addou, Kyeongjae Cho, Robert M. Wallace, and Moon J. Kim. New Mo_6Te_6 sub-nanometer-diameter nanowire phase from 2H-$MoTe_2$. *Advanced Materials*, 29(18), 2017.

[180] C. Katan, A. D. Mohite, and J. Even. Entropy in halide perovskites. *Nature Materials*, 17(5):377–379, 2018.

[181] A. E. Maughan, A. M. Ganose, M. M. Bordelon, E. M. Miller, D. O. Scanlon, and J. R. Neilson. Defect tolerance to intolerance in the vacancy-ordered double perovskite semiconductors Cs_2SnI_6 and Cs_2TeI_6. *Journal of the American Chemical Society*, 138(27):8453–8464, 2016.

[182] P. J. Chupas, X. Qiu, J. C. Hanson, P. L. Lee, C. P. Grey, and S. J. Billinge. Rapid-acquisition pair distribution function (ra-pdf) analysis. *J. Appl. Crystallogr.*, 36:1342, 2003.

[183] P. Juhas, T. Davis, C. L. Farrow, and S. J. L. Billinge. Pdfgetx3: a rapid and highly automatable program for processing powder diffraction data into total scattering pair distribution functions. *Journal of Applied Crystallography*, 46:560–566, 2013.

[184] C. L. Farrow, P. Juhas, J. W. Liu, D. Bryndin, E. S. Bozin, J. Bloch, T. Proffen, and S. J. L. Billinge. Pdffit2 and pdfgui: computer programs for studying nanostructure in crystals. *Journal of Physics-Condensed Matter*, 19(33), 2007.

[185] A. Hammersley, S. Svensson, M. Hanfland, A. Fitch, and D. Hausermann. Two-dimensional detector software: From real detector to idealised image or two-theta scan. *High Pressure Res.*, 14:235, 1996.

[186] J. Neuefeind, M. Feygenson, J. Carruth, R. Hoffmann, and K. K. Chipley. The nanoscale ordered materials diffractometer nomad at the spallation neutron source sns. *Nuclear Instruments & Methods in Physics Research Section B-Beam Interactions with Materials and Atoms*, 287:68–75, 2012.

[187] M. G. Tucker, M. T. Dove, and D. A. Keen. Application of the reverse Monte Carlo method to crystalline materials. *Journal of Applied Crystallography*, 34:630–638, 2001.

[188] Bachir Aoun. Fullrmc, a rigid body reverse monte carlo modeling package enabled with machine learning and artificial intelligence. *Journal of Computational Chemistry*, 37(12):1102–1111, 2016.

[189] K. Momma and F. Izumi. Vesta 3 for three-dimensional visualization of crystal, volumetric and morphology data. *Journal of Applied Crystallography*, 44:1272–1276, 2011.

[190] A. E. Maughan, A. M. Ganose, M. A. Almaker, D. O. Scanlon, and J. R. Neilson. Tolerance factor and cooperative tilting effects in vacancy-ordered double perovskite halides. *Chemistry of Materials*, 30(11):3909–3919, 2018.

[191] A. C. Lawson, J. A. Goldstone, B. Cort, R. I. Sheldon, and E. M. Foltyn. Atomic thermal vibrations of the light actinide elements. *Journal of Alloys and Compounds*, 213:426–428, 1994.

[192] D. J. Safarik, T. Klimczuk, A. Llobet, D. D. Byler, J. C. Lashley, J. R. O'Brien, and N. R. Dilley. Localized anharmonic rattling of al atoms in val10.1. *Physical Review B*, 85(1), 2012.

[193] M. Sakata, J. Harada, M. J. Cooper, and K. D. Rouse. Neutron-diffraction study of anharmonic thermal vibrations in cubic cspbx3. *Acta Crystallographica Section A*, 36(JAN):7–15, 1980.

[194] G. O'Leary and R. Wheeler. Phase transitions and soft librational modes in cubic crystals. *Phys. Rev. B*, 1:4409, 1970.

[195] Douglas F. Cooke and Robin L. Armstrong. Investigation of the rotary lattice mode in R_2PtCl_6 compounds. i. from measurements of the ^{35}cl nuclear quadrupole resonance frequency. *Canadian Journal of Physics*, 49(19):2381–2388, 1971.

[196] R. L. Armstrong and K. R. Jeffrey. Quadrupolar nuclear spin-lattice relaxation in r2mx6 compounds. *Canadian Journal of Physics*, 49(1):49–+, 1971.

[197] H. M. Vandriel, R. L. Armstrong, and M. M. McEnnan. Soft-mode behavior near 111-k displacive phase-transition in k2recl6. *Physical Review B*, 12(1):488–492, 1975.

[198] M. J. Conterio, A. L. Goodwin, M. G. Tucker, D. A. Keen, M. T. Dove, L. Peters, and J. S. O. Evans. Local structure in $Ag_3[Co(CN)_6]$: colossal thermal expansion, rigid unit modes and argentophilic interactions. *Journal of Physics-Condensed Matter*, 20(25), 2008.

[199] Morikazu Toda. One-dimensional dual transformation. *Journal of the Physical Society of Japan*, 20(11):2095A–2095A, 1965.

[200] A. Milchev and G. M. Mazzucchelli. Frenkel-kontorova model with anharmonic interactions. *Physical Review B*, 38(4):2808–2812, 1988.

[201] Jonathon S. Bechtel and Anton Van der Ven. Octahedral tilting instabilities in inorganic halide perovskites. *Physical Review Materials*, 2(2):025401, 2018.

[202] S. Adams. Relationship between bond valence and bond softness of alkali halides and chalcogenides. *Acta Crystallographica Section B-Structural Science*, 57:278–287, 2001.

[203] J. Young and J. M. Rondinelli. Octahedral rotation preferences in perovskite iodides and bromides. *J. Phys. Chem. Lett.*, 7:918, 2016.

[204] Matthew R. Linaburg, Eric T. McClure, Jackson D. Majher, and Patrick M. Woodward. $Cs_{1-x}Rb_xPbCl_3$ and $Cs_{1-x}Rb_xPbBr_3$ solid solutions: Understanding octahedral tilting in lead halide perovskites. *Chemistry of Materials*, 29(8):3507–3514, 2017.

[205] Average U.S. construction costs for solar generation continue to decrease. https://www.eia.gov/todayinenergy/detail.php?id=41153#. Accessed: 2020-02-27.

[206] W. J. Ke and M. G. Kanatzidis. Prospects for low-toxicity lead-free perovskite solar cells. *Nature Communications*, 10, 2019.

[207] Wan-Jian Yin, Tingting Shi, and Yanfa Yan. Unique properties of halide perovskites as possible origins of the superior solar cell performance. *Advanced Materials*, 26(27):4653–4658, 2014.

[208] D. B. Mitzi. Introduction: Perovskites. *Chemical Reviews*, 119(5):3033–3035, 2019.

[209] T. Baikie, Y. N. Fang, J. M. Kadro, M. Schreyer, F. X. Wei, S. G. Mhaisalkar, M. Graetzel, and T. J. White. Synthesis and crystal chemistry of the hybrid perovskite $(CH_3NH_3)PbI_3$ for solid-state sensitised solar cell applications. *Journal of Materials Chemistry A*, 1(18):5628–5641, 2013.

[210] Prashant V. Kamat, Juan Bisquert, and Jillian Buriak. Lead-free perovskite solar cells. *ACS Energy Letters*, 2(4):904–905, 2017.

[211] Sabine Körbel, Miguel A. L. Marques, and Silvana Botti. Stable hybrid organic–inorganic halide perovskites for photovoltaics from ab initio high-throughput calculations. *Journal of Materials Chemistry A*, 6(15):6463–6475, 2018.

[212] Kiyoshi Miyata, Daniele Meggiolaro, M Tuan Trinh, Prakriti P Joshi, Edoardo Mosconi, Skyler C Jones, Filippo De Angelis, and X-Y Zhu. Large polarons in lead halide perovskites. *Science advances*, 3(8):e1701217, 2017.

[213] A. Filippetti and A. Mattoni. Hybrid perovskites for photovoltaics: Insights from first principles. *Physical Review B*, 89(12), 2014.

[214] M. R. Filip, G. E. Eperon, H. J. Snaith, and F. Giustino. Steric engineering of metal-halide perovskites with tunable optical band gaps. *Nature Communications*, 5, 2014.

[215] Y. Yuan, R. Xu, H. T. Xu, F. Hong, F. Xu, and L. J. Wang. Nature of the band gap of halide perovskites ABX_3 (A = CH_3NH_3, Cs; B = Sn, Pb; X = Cl, Br, I): First-principles calculations. *Chinese Physics B*, 24(11), 2015.

[216] R. Prasanna, A. Gold-Parker, T. Leijtens, B. Conings, A. Babayigit, H. G. Boyen, M. F. Toney, and M. D. McGehee. Band gap tuning via lattice contraction and octahedral tilting in perovskite materials for photovoltaics. *Journal of the American Chemical Society*, 139(32):11117–11124, 2017.

[217] Y. Cai, W. Xie, H. Ding, Y. Chen, K. Thirumal, L. H. Wong, N. Mathews, S. G. Mhaisalkar, M. Sherburne, and M. Asta. Computational study of halide perovskite-derived A_2BX_6 inorganic compounds: Chemical trends in electronic structure and structural stability. *Chemistry of Materials*, 29(18):7740–7749, 2017.

[218] Andreas Kaltzoglou, Maria Antoniadou, Athanassios G. Kontos, Constantinos C. Stoumpos, Dorothea Perganti, Eirini Siranidi, Vasilios Raptis, Kalliopi Trohidou, Vassilis Psycharis, Mercouri G. Kanatzidis, and Polycarpos Falaras. Optical-vibrational properties of the Cs_2SnX_6 (X = Cl, Br, I) defect perovskites and hole-transport efficiency in dye-sensitized solar cells. *The Journal of Physical Chemistry C*, 120(22):11777–11785, 2016.

[219] A. E. Maughan, A. M. Ganose, D. O. Scanlon, and J. R. Neilson. Perspectives and design principles of vacancy-ordered double perovskite halide semiconductors. *Chemistry of Materials*, 31(4):1184–1195, 2019.

[220] J. M. Frost, K. T. Butler, F. Brivio, C. H. Hendon, M. van Schilfgaarde, and A. Walsh. Atomistic origins of high-performance in hybrid halide perovskite solar cells. *Nano Letters*, 14(5):2584–2590, 2014.

[221] Shigeru Syoyama, Kenji Osaki, and Shigenori Kusanagi. X-ray study of the crystal structure of K_2TeI_6 and the symmetry of the compounds of this series. *Inorganic and Nuclear Chemistry Letters*, 8(2):181–184, 1972.

[222] W. Abriel. Crystal structure and phase transition of Rb_2TeI_6. *Materials Research Bulletin*, 17(10):1341–1346, 1982.

[223] J.H. Strange and M. Terenzi. Study of ionic motion in salts of the type $(NH_4)_2MX_6$ by nmr relaxation. *Journal of Physics and Chemistry of Solids*, 33(4):923–933, 1972.

[224] R. Blinc and G. Lahajnar. Magnetic resonance study of molecular motion in cubic $(NH_4)_2SiF_6$. *J. Chem. Phys.*, 47:4146, 1967.

[225] Y. Kume, H. Muraoka, T. Matsuo, and H. Suga. Low-temperature heat capacities of ammonium hexachloroselenate and of its deuterated analogue. *J. Chem. Thermodyn.*, 26:211, 1994.

[226] K. Kaasbjerg, K. S. Thygesen, and K. W. Jacobsen. Phonon-limited mobility in n-type single-layer mos2 from first principles. *Physical Review B*, 85(11), 2012.

[227] J. Yan, P. Gorai, B. Ortiz, S. Miller, S. A. Barnett, T. Mason, V. Stevanovic, and E. S. Toberer. Material descriptors for predicting thermoelectric performance. *Energy & Environmental Science*, 8(3):983–994, 2015.

[228] P. A. Mante, C. C. Stoumpos, M. G. Kanatzidis, and A. Yartsev. Electron-acoustic phonon coupling in single crystal ch3nh3pbi3 perovskites revealed by coherent acoustic phonons. *Nature Communications*, 8, 2017.

[229] A. E. Maughan, A. A. Paecklar, and J. R. Neilson. Bond valences and anharmonicity in vacancy-ordered double perovskite halides. *Journal of Materials Chemistry C*, 6(44):12095–12104, 2018.

[230] Y. Kume, R. Ikeda, and D. Nakamura. Phase-transitions in rhombohedral $(CH_3NH_3)_2MCl_6$ crystals as revealed by NQR of chlorine. *Journal of Magnetic Resonance*, 20(2):276–278, 1975.

[231] R. Ikeda, Y. Kume, D. Nakamura, Y. Furukawa, and H. Kiriyama. Motion of methylammonium ions in methylammonium hexachloroplatinate(iv) and hexachlorostannate(iv) as studied by proton magnetic-resonance. *Journal of Magnetic Resonance*, 24(1):9–20, 1976.

[232] Furukawa Yoshihiro, Kiriyama Hideko, and Ikeda Ryuichi. The nuclear quadrupole spin-lattice relaxation of ^{35}Cl in methylammonium hexachlorostannate(iv) and hexachloroplatinate(iv). *Bulletin of the Chemical Society of Japan*, 50(8):1927–1929, 1977.

[233] IP Swainson, RP Hammond, C Soulliere, O Knop, and W Massa. Phase transitions in the perovskite methylammonium lead bromide, $CH_3ND_3PbBr_3$. *Journal of Solid State Chemistry*, 176(1):97–104, 2003.

[234] Mark T Weller, Oliver J Weber, Paul F Henry, Antonietta M Di Pumpo, and Thomas C Hansen. Complete structure and cation orientation in the perovskite photovoltaic methylammonium lead iodide between 100 and 352 K. *Chemical communications*, 51(20):4180–4183, 2015.

[235] C. C. Stoumpos, C. D. Malliakas, and M. G. Kanatzidis. Semiconducting tin and lead iodide perovskites with organic cations: Phase transitions, high mobilities, and near-infrared photoluminescent properties. *Inorganic Chemistry*, 52(15):9019–9038, 2013.

[236] T. Baikie, N. S. Barrow, Y. A. Fang, P. J. Keenan, P. R. Slater, R. O. Piltz, M. Gutmann, S. G. Mhaisalkar, and T. J. White. A combined single crystal neutron/x-ray diffraction and solid-state nuclear magnetic resonance study of the hybrid perovskites $CH_3NH_3PbX_2$ (X = I, Br and Cl). *Journal of Materials Chemistry A*, 3(17):9298–9307, 2015.

[237] A. Poglitsch and D. Weber. Dynamic disorder in methylammoniumtrihalogenoplumbates (ii) observed by millimeter-wave spectroscopy. *J. Chem. Phys.*, 87:6373, 1987.

[238] Roderick E Wasylishen, Osvald Knop, and J Bruce Macdonald. Cation rotation in methylammonium lead halides. *Solid state communications*, 56(7):581–582, 1985.

[239] Noriko Onoda-Yamamuro, Takasuke Matsuo, and Hiroshi Suga. Dielectric study of $CH_3NH_3PbX_3$ (X= Cl, Br, I). *Journal of Physics and Chemistry of Solids*, 53(7):935–939, 1992.

[240] D. H. Fabini, T. Hogan, H. A. Evans, C. C. Stoumpos, M. G. Kanatzidis, and R. Seshadri. Dielectric and thermodynamic signatures of low-temperature glassy dynamics in the hybrid perovskites ch3nh3pbi3 and hc(nh2)2pbi3. *J. Phys. Chem. Lett.*, 7:376, 2016.

[241] J. H. Lee, N. C. Bristowe, P. D. Bristowe, and A. K. Cheetham. Role of hydrogen-bonding and its interplay with octahedral tilting in $CH_3NH_3PbI_3$. *Chemical Communications*, 51(29):6434–6437, 2015.

[242] J. Lahnsteiner, G. Kresse, A. Kumar, D. D. Sarma, C. Franchini, and M. Bokdam. Room-temperature dynamic correlation between methylammonium molecules in lead-iodine based perovskites: An ab initio molecular dynamics perspective. *Physical Review B*, 94(21), 2016.

[243] Marcelo A. Carignano, Ali Kachmar, and Jürg Hutter. Thermal effects on ch3nh3pbi3 perovskite from ab initio molecular dynamics simulations. *The Journal of Physical Chemistry C*, 119(17):8991–8997, 2015.

[244] A. Mattoni, A. Filippetti, M. I. Saba, and P. Delugas. Methylammonium rotational dynamics in lead halide perovskite by classical molecular dynamics: The role of temperature. *The Journal of Physical Chemistry C*, 119(30):17421–17428, 2015.

[245] J. Even, M. Carignano, and C. Katan. Molecular disorder and translation/rotation coupling in the plastic crystal phase of hybrid perovskites. *Nanoscale*, 8(12):6222–6236, 2016.

[246] Edoardo Mosconi, Claudio Quarti, Tanja Ivanovska, Giampiero Ruani, and Filippo De Angelis. Structural and electronic properties of organo-halide lead perovskites: a combined IR-spectroscopy and ab initio molecular dynamics investigation. *Physical Chemistry Chemical Physics*, 16(30):16137–16144, 2014.

[247] Rebecka Lindblad, Dongqin Bi, Byung-wook Park, Johan Oscarsson, Mihaela Gorgoi, Hans Siegbahn, Michael Odelius, Erik MJ Johansson, and Hå kan Rensmo. Electronic structure of $TiO_2/CH_3NH_3PbI_3$ perovskite solar cell interfaces. *The journal of physical chemistry letters*, 5(4):648–653, 2014.

[248] J. Even. Pedestrian guide to symmetry properties of the reference cubic structure of 3d all-inorganic and hybrid perovskites. *Journal of Physical Chemistry Letters*, 6(12):2238–2242, 2015.

[249] M. A. Carignano, Y. Saeed, S. A. Aravindh, I. S. Roqan, J. Even, and C. Katan. A close examination of the structure and dynamics of $HC(NH_2)_2PbI_3$ by md simulations and group theory. *Physical Chemistry Chemical Physics*, 18(39):27109–27118, 2016.

[250] Maksim Grechko, Taisuke Hasegawa, Francesco D'Angelo, Hironobu Ito, Dmitry Turchinovich, Yuki Nagata, and Mischa Bonn. Coupling between intra- and intermolecular motions in liquid water revealed by two-dimensional terahertz-infrared-visible spectroscopy. *Nature communications*, 9(1):885, 2018.

[251] M. Grechko, S. A. Bretschneider, L. Vietze, H. Kim, and M. Bonn. Vibrational coupling between organic and inorganic sublattices of hybrid perovskites. *Angewandte Chemie-International Edition*, 57(41):13657–13661, 2018.

[252] X. Qiu, J. W. Thompson, and S. J. Billinge. Pdfgetx2: a gui-driven program to obtain the pair distribution function from x-ray powder diffraction data. *J. Appl. Crystallogr.*, 37:678, 2004.

[253] P. Juhas, C. L. Farrow, X. H. Yang, K. R. Knox, and S. J. L. Billinge. Complex modeling: a strategy and software program for combining multiple information sources to solve ill posed structure and nanostructure inverse problems. *Acta Crystallographica a-Foundation and Advances*, 71:562–568, 2015.

[254] Koji Yamada, Keiko Mikawa, Tsutomu Okuda, and Kevin S. Knight. Static and dynamic structures of $CD_3ND_3GeCl_3$ studied by tof high resolution neutron powder diffraction and solid state NMR. *Journal of the Chemical Society, Dalton Transactions*, (10):2112–2118, 2002.

[255] Y Kume, Y Miyazaki, T Matsuo, H Suga, WIF David, and RM Ibberson. A strong isotope effect in the low-temperature property of ammonium hexachlorotellurate. *EPL (Europhysics Letters)*, 16(3):265, 1991.

[256] H. Mashiyama, Y. Kawamura, H. Kasano, T. Asahi, Y. Noda, and H. Kimura. Disordered configuration of methylammonium of $CH_3NH_3PbBr_3$ determined by single crystal neutron diffractometry. *Ferroelectrics*, 348(1):182–186, 2007.

[257] Yixin Ren, Iain W. H. Oswald, Xiaoping Wang, Gregory T. McCandless, and Julia Y. Chan. Orientation of organic cations in hybrid inorganic–organic perovskite $CH_3NH_3PbI_3$ from subatomic resolution single crystal neutron diffraction structural studies. *Crystal Growth & Design*, 16(5):2945–2951, 2016.

[258] M. T. Weller, P. F. Henry, V. P. Ting, and C. C. Wilson. Crystallography of hydrogen-containing compounds: realizing the potential of neutron powder diffraction. *Chemical Communications*, (21):2973–2989, 2009.

[259] Chick C Wilson, Paul F Henry, Marc Schmidtmann, Valeska P Ting, Edward Williams, and Mark T Weller. Neutron powder diffraction–new opportunities in hydrogen location in molecular and materials structure. *Crystallography Reviews*, 20(3):162–206, 2014.

[260] K. Page, C. E. White, E. G. Estell, R. B. Neder, A. Llobet, and T. Proffen. Treatment of hydrogen background in bulk and nanocrystalline neutron total scattering experiments. *Journal of Applied Crystallography*, 44:532–539, 2011.

[261] O. Tange. Gnu parallel - the command-line power tool. *The USENIX Magazine*, 36(1):42–47, Feb 2011.

[262] Jonathon Anderson, Patrick J Burns, Daniel Milroy, Peter Ruprecht, Thomas Hauser, and Howard Jay Siegel. Deploying rmacc summit: an hpc resource for the rocky mountain region. In *Proceedings of the Practice and Experience in Advanced Research Computing 2017 on Sustainability, Success and Impact*, page 8, New York, NY, USA, 2017. ACM.

[263] A. B. Yoo, M. A. Jette, and M. Grondona. Slurm: Simple linux utility for resource management. *Job Scheduling Strategies for Parallel Processing*, 2862:44–60, 2003.

[264] CL Farrow, P Juhas, JW Liu, D Bryndin, ES Božin, J Bloch, Th Proffen, and SJL Billinge. PDFfit2 and PDFgui: computer programs for studying nanostructure in crystals. *Journal of Physics: Condensed Matter*, 19(33):335219, 2007.

[265] R. J. Worhatch, H. Kim, I. P. Swainson, A. L. Yonkeu, and S. J. Billinge. Study of local structure in selected organic-inorganic perovskites in the Pm$\bar{3}$m phase. *Chem. Mater.*, 20:1272, 2008.

[266] R. L. McGreevy and L. Pusztai. Reverse monte carlo simulation: A new technique for the determination of disordered structures. *Molecular Simulation*, 1(6):359–367, 1988.

[267] R. L. McGreevy. Reverse Monte Carlo modelling. *Journal of Physics-Condensed Matter*, 13(46):R877–R913, 2001.

[268] R. L. McGreevy and P. Zetterstrom. To RMC or not to RMC? the use of reverse Monte Carlo modelling. *Current Opinion in Solid State & Materials Science*, 7(1):41–47, 2003.

[269] Helen Y Playford, Lewis R Owen, Igor Levin, and Matt G Tucker. New insights into complex materials using reverse monte carlo modeling. *Annual Review of Materials Research*, 44:429–449, 2014.

[270] M. G. Tucker, D. A. Keen, M. T. Dove, A. L. Goodwin, and Q. Hui. RMCProfile: reverse Monte Carlo for polycrystalline materials. *Journal of Physics-Condensed Matter*, 19(33), 2007.

[271] G. Evrard and L. Pusztai. Reverse Monte Carlo modelling of the structure of disordered materials with RMC++: a new implementation of the algorithm in C++. *Journal of Physics-Condensed Matter*, 17(5):S1–S13, 2005.

[272] G. Opletal, T. C. Petersen, I. K. Snook, and S. P. Russo. HRMC_2.0: Hybrid Reverse Monte Carlo method with silicon, carbon and germanium potentials. *Computer Physics Communications*, 184(8):1946–1957, 2013.

[273] L. Karlsson and R. L. McGreevy. Rmc modelling of rotational disorder in molecular crystals: Kcn. *Physica B*, 234:100–101, 1997.

[274] S. Rycroft, A. Chahid, and R. L. McGreevy. Neutron diffraction and RMC study of CN^{-} orientations in $Na(CN)_x\ Br_{1-x}$. *Physica B*, 276:284–285, 2000.

[275] A. L. Goodwin, S. A. T. Redfern, M. T. Dove, D. A. Keen, and M. G. Tucker. Ferroelectric nanoscale domains and the 905 k phase transition in srsno(3): A neutron total-scattering study. *Physical Review B*, 76(17), 2007.

[276] N. Kitamura, S. C. Vogel, and Y. Idemoto. Local structure analysis on (La,Ba)(Ga,Mg)O_3-delta by the pair distribution function method using a neutron source and density functional theory calculations. *Solid State Communications*, 163:46–49, 2013.

[277] N. Kitamura. Atomic-configuration modeling of ion-conducting crystalline oxide by diffraction technique and theoretical calculation. *Journal of the Ceramic Society of Japan*, 123(1440):637–642, 2015.

[278] J. R. Neilson and T. M. McQueen. Representational analysis of extended disorder in atomistic ensembles derived from total scattering data. *Journal of Applied Crystallography*, 48:1560–1572, 2015.

[279] M. S. Senn, D. A. Keen, T. C. A. Lucas, J. A. Hriljac, and A. L. Goodwin. Emergence of long-range order in $BaTiO_3$ from local symmetry-breaking distortions. *Physical Review Letters*, 116(20), 2016.

[280] J. X. Liu, A. E. Phillips, D. A. Keen, and M. T. Dove. Thermal disorder and bond anharmonicity in cesium lead iodide studied by neutron total scattering and the Reverse Monte Carlo method. *Journal of Physical Chemistry C*, 123(24):14934–14940, 2019.

[281] N. Kitamura, N. Hayashi, N. Ishida, and Y. Idemoto. Local structure in a-site-deficient perovskite na0.5bi0.5tio3 and its effect on electrical conduction. *Chemistry Letters*, 48(11):1398–1401, 2019.

[282] D. C. Palmer. Visualization and analysis of crystal structures using crystalmaker software. *Zeitschrift Fur Kristallographie-Crystalline Materials*, 230(9-10):559–572, 2015.

[283] The code for the computational analysis of MA_2SnI_6 can be found in the following github repository. https://github.com/aapaecklar/MA2SnI6.

[284] J. Ma and L. W. Wang. Nanoscale charge localization induced by random orientations of organic molecules in hybrid perovskite $CH_3NH_3PbI_3$. *Nano Letters*, 15(1):248–253, 2015.

[285] A. M. A. Leguy, J. M. Frost, A. P. McMahon, V. G. Sakai, W. Kockelmann, C. H. Law, X. E. Li, F. Foglia, A. Walsh, B. C. O'Regan, J. Nelson, J. T. Cabral, and P. R. F. Barnes. The dynamics of methylammonium ions in hybrid organic-inorganic perovskite solar cells. *Nature Communications*, 6, 2015.

[286] S. D. Stranks, G. E. Eperon, G. Grancini, C. Menelaou, M. J. P. Alcocer, T. Leijtens, L. M. Herz, A. Petrozza, and H. J. Snaith. Electron-hole diffusion lengths exceeding 1 micrometer in an organometal trihalide perovskite absorber. *Science*, 342(6156):341–344, 2013.

[287] Y Kawamura and H Mashiyama. Modulated structure in phase ii of $CH_3NH_3PbCl_3$. *JOURNAL-KOREAN PHYSICAL SOCIETY*, 35:S1437–S1440, 1999.

[288] AM Glazer. The classification of tilted octahedra in perovskites. *Acta Crystallographica Section B: Structural Crystallography and Crystal Chemistry*, 28(11):3384–3392, 1972.

[289] A. Walsh, D. J. Payne, R. G. Egdell, and G. W. Watson. Stereochemistry of post-transition metal oxides: revision of the classical lone pair model. *Chemical Society Reviews*, 40(9):4455–4463, 2011.

[290] R. Ramesh and N. A. Spaldin. Multiferroics: progress and prospects in thin films. *Nature Materials*, 6(1):21–29, 2007.

[291] M. Fontecave and J. L. Pierre. The basic chemistry of nitric-oxide and its possible biological reactions. *Bulletin De La Societe Chimique De France*, 131(6):620–631, 1994.

[292] E. G. Rozantsev. *Free nitroxyl radicals*. Plenum Press, New York,, 1970.

[293] Daniel B Menzel. The role of free radicals in the toxicity of air pollutants (nitrogen oxides and ozone). In *Free radicals in biology*, volume 2, pages 181–202. Academic Press, New York, 1976.

[294] Louis J Ignarro. Introduction and overview. In Louis J Ignarro, editor, *Nitric oxide: biology and pathobiology*, pages 3–19. Academic press, San Diego, 1st edition, 2000.

[295] J. Garthwaite, S. L. Charles, and R. Chesswilliams. Endothelium-derived relaxing factor release on activation of nmda receptors suggests role as intercellular messenger in the brain. *Nature*, 336(6197):385–388, 1988.

[296] L. J. Ignarro, G. M. Buga, K. S. Wood, R. E. Byrns, and G. Chaudhuri. Endothelium-derived relaxing factor produced and released from artery and vein is nitric-oxide. *Proceedings of the National Academy of Sciences of the United States of America*, 84(24):9265–9269, 1987.

[297] MA Marletta, MA Tayeh, and JM Hevel. Unraveling the biological significance of nitric oxide. *BioFactors (Oxford, England)*, 2(4):219–225, 1990.

[298] Ruth SoRelle. Nobel prize awarded to scientists for nitric oxide discoveries. *Circulation*, 98(22):2365–2366, 1998.

[299] R. Iyengar, D. J. Stuehr, and M. A. Marletta. Macrophage synthesis of nitrite, nitrate, and n-nitrosamines - precursors and role of the respiratory burst. *Proceedings of the National Academy of Sciences of the United States of America*, 84(18):6369–6373, 1987.

[300] R. M. J. Palmer, A. G. Ferrige, and S. Moncada. Nitric-oxide release accounts for the biological-activity of endothelium-derived relaxing factor. *Nature*, 327(6122):524–526, 1987.

[301] L. Li, A. Hsu, and P. K. Moore. Actions and interactions of nitric oxide, carbon monoxide and hydrogen sulphide in the cardiovascular system and in inflammation - a tale of three gases! *Pharmacology & Therapeutics*, 123(3):386–400, 2009.

[302] A. W. Carpenter and M. H. Schoenfisch. Nitric oxide release: Part ii. therapeutic applications. *Chemical Society Reviews*, 41(10):3742–3752, 2012.

[303] A. B. Seabra, A. Fitzpatrick, J. Paul, M. G. De Oliveira, and R. Weller. Topically applied S-nitrosothiol-containing hydrogels as experimental and pharmacological nitric oxide donors in human skin. *British Journal of Dermatology*, 151(5):977–983, 2004.

[304] M. Mowbray, X. J. Tan, P. S. Wheatley, R. E. Morris, and R. B. Weller. Topically applied nitric oxide induces t-lymphocyte infiltration in human skin, but minimal inflammation. *Journal of Investigative Dermatology*, 128(2):352–360, 2008.

[305] H. C. Champion, T. J. Bivalacqua, R. Wang, P. J. Kadowitz, L. K. Keefer, J. E. Saavedra, J. A. Hrabie, P. C. Doherty, and W. J. G. Hellstrom. Induction of penile erection by intracavernosal and transurethral administration of novel nitric oxide donors in the cat. *Journal of Urology*, 161(6):2013–2019, 1999.

[306] Louis J. Ignarro. *Nitric oxide : biology and pathobiology*. Academic Press, London, 2nd edition, 2010.

[307] H. F. Zhu, B. Ka, and F. Murad. Nitric oxide accelerates the recovery from burn wounds. *World Journal of Surgery*, 31(4):624–631, 2007.

[308] J. Gao, W. T. Zheng, J. M. Zhang, D. Guan, Z. M. Yang, D. L. Kong, and Q. Zhao. Enzyme-controllable delivery of nitric oxide from a molecular hydrogel. *Chemical Communications*, 49(80):9173–9175, 2013.

[309] K. S. B. Masters, S. J. Leibovich, P. Belem, J. L. West, and L. A. Poole-Warren. Effects of nitric oxide releasing poly(vinyl alcohol) hydrogel dressings on dermal wound healing in diabetic mice. *Wound Repair and Regeneration*, 10(5):286–294, 2002.

[310] T. P. Amadeu, A. B. Seabra, M. G. de Oliveira, and A. M. A. Costa. S-nitrosoglutathione-containing hydrogel accelerates rat cutaneous wound repair. *Journal of the European Academy of Dermatology and Venereology*, 21(5):629–637, 2007.

[311] M. B. Witte, T. Kiyama, and A. Barbul. Nitric oxide enhances experimental wound healing in diabetes. *British Journal of Surgery*, 89(12):1594–1601, 2002.

[312] J. R. Lancaster. The physical properties of nitric oxide: Determinants of the dynamics of no in tissue. In Louis J Ignarro, editor, *Nitric oxide: biology and pathobiology*, pages 209–224. Academic press, San Diego, 1st edition, 2000.

[313] K. A. Mowery, M. H. Schoenfisch, J. E. Saavedra, L. K. Keefer, and M. E. Meyerhoff. Preparation and characterization of hydrophobic polymeric films that are thromboresistant via nitric oxide release. *Biomaterials*, 21(1):9–21, 2000.

[314] J. H. Shin, S. K. Metzger, and M. H. Schoenfisch. Synthesis of nitric oxide-releasing silica nanoparticles. *Journal of the American Chemical Society*, 129(15):4612–4619, 2007.

[315] P. S. Wheatley, A. R. Butler, M. S. Crane, S. Fox, B. Xiao, A. G. Rossi, I. L. Megson, and R. E. Morris. No-releasing zeolites and their antithrombotic properties. *Journal of the American Chemical Society*, 128(2):502–509, 2006.

[316] D. A. Riccio and M. H. Schoenfisch. Nitric oxide release: Part i. macromolecular scaffolds. *Chemical Society Reviews*, 41(10):3731–3741, 2012.

[317] B. Xiao, P. S. Wheatley, X. B. Zhao, A. J. Fletcher, S. Fox, A. G. Rossi, I. L. Megson, S. Bordiga, L. Regli, K. M. Thomas, and R. E. Morris. High-capacity hydrogen and nitric oxide adsorption and storage in a metal-organic framework. *Journal of the American Chemical Society*, 129(5):1203–1209, 2007.

[318] P. Horcajada, R. Gref, T. Baati, P. K. Allan, G. Maurin, P. Couvreur, G. Ferey, R. E. Morris, and C. Serre. Metal-organic frameworks in biomedicine. *Chemical Reviews*, 112(2):1232–1268, 2012.

[319] J. E. Saavedra and L. K. Keefer. Nitrogen-based diazeniumdiolates: Versatile nitric oxide-releasing compounds in biomedical research and potential clinical applications. *Journal of Chemical Education*, 79(12):1427–1434, 2002.

[320] Wilmarie Thomas, Douglas D. Flores-Santana, David A. Switzer, Christopher H. Wink, and Lisa A. Ridnour. Determinants of nitric oxide chemistry: impact of cell signaling processes. In Louis J. Ignarro, editor, *Nitric oxide : biology and pathobiology*, pages 3–25. Academic Press, London, 2nd edition, 2010.

[321] M. J. Ingleson, R. Heck, J. A. Gould, and M. J. Rosseinsky. Nitric oxide chemisorption in a postsynthetically modified metal-organic framework. *Inorganic Chemistry*, 48(21):9986–9988, 2009.

[322] J. G. Nguyen, K. K. Tanabe, and S. M. Cohen. Postsynthetic diazeniumdiolate formation and no release from mofs. *Crystengcomm*, 12(8):2335–2338, 2010.

[323] A. Lowe, P. Chittajallu, Q. H. Gong, J. Li, and K. J. Balkus. Storage and delivery of nitric oxide via diazeniumdiolated metal organic framework. *Microporous and Mesoporous Materials*, 181:17–22, 2013.

[324] S. Bordiga, L. Regli, F. Bonino, E. Groppo, C. Lamberti, B. Xiao, P. S. Wheatley, R. E. Morris, and A. Zecchina. Adsorption properties of hkust-1 toward hydrogen and other small molecules monitored by ir. *Physical Chemistry Chemical Physics*, 9(21):2676–2685, 2007.

[325] A. C. McKinlay, J. F. Eubank, S. Wuttke, B. Xiao, P. S. Wheadey, P. Bazin, J. C. Lavalley, M. Daturi, A. Vimont, G. De Weireld, P. Horcajada, C. Serre, and R. E. Morris. Nitric oxide adsorption and delivery in flexible MIL-88(Fe) metal-organic frameworks. *Chemistry of Materials*, 25(9):1592–1599, 2013.

[326] C. Prestipino, G. Berlier, F. X. L. I. Xamena, G. Spoto, S. Bordiga, A. Zecchina, G. T. Palomino, T. Yamamoto, and C. Lamberti. An in situ temperature dependent ir, epr and high resolution XANES study on the NO/Cu^1-ZSM-5 interaction. *Chemical Physics Letters*, 363(3-4):389–396, 2002.

[327] F. Bonino, S. Chavan, J. G. Vitillo, E. Groppo, G. Agostini, C. Lamberti, P. D. C. Dietzel, C. Prestipino, and S. Bordiga. Local structure of CPO-27-Ni metallorganic framework upon dehydration and coordination of NO. *Chemistry of Materials*, 20(15):4957–4968, 2008.

[328] A. H. Khan, K. Peikert, M. Froba, and M. Bertmer. No adsorption in amino-modified $Cu_3(btc)_2$-type mofs studied by solid-state nmr. *Microporous and Mesoporous Materials*, 216:111–117, 2015.

[329] Arafat Hossain Khan, Benjamin Barth, Martin Hartmann, Jürgen Haase, and Marko Bertmer. Nitric oxide adsorption in MIL-100 (Al) mof studied by solid-state nmr. *The Journal of Physical Chemistry C*, 122(24):12723–12730, 2018.

[330] B. Barth, M. Mendt, A. Poppl, and M. Hartmann. Adsorption of nitric oxide in metal-organic frameworks: Low temperature IR and EPR spectroscopic evaluation of the role of open metal sites. *Microporous and Mesoporous Materials*, 216:97–110, 2015.

[331] Matthias Mendt, Benjamin Barth, Martin Hartmann, and Andreas P öppl. Low-temperature binding of NO adsorbed on MIL-100 (Al)—A case study for the application of high resolution pulsed EPR methods and DFT calculations. *The Journal of chemical physics*, 147(22):224701, 2017.

[332] Matthias Mendt, Felix Gutt, Negar Kavoosi, Volodymyr Bon, Irena Senkovska, Stefan Kaskel, and Andreas Pöppl. Epr insights into switchable and rigid derivatives of the metal–organic framework dut-8 (ni) by no adsorption. *The Journal of Physical Chemistry C*, 120(26):14246–14259, 2016.

[333] E. D. Bloch, W. L. Queen, S. Chavan, P. S. Wheatley, J. M. Zadrozny, R. Morris, C. M. Brown, C. Lamberti, S. Bordiga, and J. R. Long. Gradual release of strongly bound nitric oxide from $Fe_2(NO)_2$(dobdc). *Journal of the American Chemical Society*, 137(10):3466–3469, 2015.

[334] A. C. McKinlay, B. Xiao, D. S. Wragg, P. S. Wheatley, I. L. Megson, and R. E. Morris. Exceptional behavior over the whole adsorption-storage-delivery cycle for no in porous metal organic frameworks. *Journal of the American Chemical Society*, 130(31):10440–10444, 2008.

[335] Christof Von Eiff and Georg Peters. Pathogenesis and detection of biofilm formation on medical implants. In Jana Jass, Susanne Surman, and James Walker, editors, *Medical biofilms : detection, prevention, and control*, pages 51–72. John Wiley & Sons, Ltd, Chichester, West Susssex ; Hoboken, NJ, 2003.

[336] C.G. Douglas, J.L. Cobbs. Prosthetic valve endocarditis. In D. Kaye, editor, *Infective Endocarditis*, pages 375–396. Raven Press, New York, 2 edition, 1992.

[337] Peter Gilbert, Andrew J. McBain, Alexander H. Rickard, and Sarah R. Schooling. Control of biofilms associated with implanted medical devices. In *Medical biofilms : detection, prevention, and control*, pages 73–96. John Wiley & Sons, Ltd, Chichester, West Susssex ; Hoboken, NJ, 2003.

[338] A. Vertes, V. Hitchins, and K. S. Phillips. Analytical challenges of microbial biofilms on medical devices. *Analytical Chemistry*, 84(9):3858–3866, 2012.

[339] J. W. Costerton, P. S. Stewart, and E. P. Greenberg. Bacterial biofilms: A common cause of persistent infections. *Science*, 284(5418):1318–1322, 1999.

[340] D.R. Steckelberg, J.M. Osmon. Prosthetic joint infections. In Alan L. Bisno and Francis A. Waldvogel, editors, *Infections associated with indwelling medical devices*, pages 259–290. ASM Press, Washington, D.C., 2nd edition, 1994.

[341] Rodney M. Donlan. Problems of biofilms associated with medical devices and implants. In Jana Jass, Susanne Surman, and James Walker, editors, *Medical biofilms : detection, prevention, and control*, pages 31–49. John Wiley & Sons, Ltd, Chichester, West Susssex ; Hoboken, NJ, 2003.

[342] D. G. Allison and P. McBain, A. J. Gilbert. Biofilms: problems of control. In D. G. Allison, P. Gilbert, H. M. Lappin-Scott, and M. Wilson, editors, *Community structure and co-operation in biofilms*, pages 309–327. Cambridge University Press, Cambridge, UK, 2000.

[343] C. EspadasTorre, V. Oklejas, K. Mowery, and M. E. Meyerhoff. Thromboresistant chemical sensors using combined nitric oxide release ion sensing polymeric films. *Journal of the American Chemical Society*, 119(9):2321–2322, 1997.

[344] D. Lyn H. Williams. The chemistry of S-Nitrosothiols. *Accounts of Chemical Research*, 32(10):869–876, 1999.

[345] A. R. Butler and P. Rhodes. Chemistry, analysis, and biological roles of S-nitrosothiols. *Analytical Biochemistry*, 249(1):1–9, 1997.

[346] D. J. Sexton, A. Muruganandam, D. J. Mckenney, and B. Mutus. Visible-light photochemical release of nitric-oxide from S-nitrosoglutathione - potential photochemotherapeutic applications. *Photochemistry and Photobiology*, 59(4):463–467, 1994.

[347] S. C. Askew, D. J. Barnett, J. Mcaninly, and D. L. H. Williams. Catalysis by Cu^{2+} of nitric-oxide release from S-nitrosothiols (rsno). *Journal of the Chemical Society-Perkin Transactions 2*, (4):741–745, 1995.

[348] S. C. Puiu, Z. R. Zhou, C. C. White, L. J. Neubauer, Z. F. Zhang, L. E. Lange, J. A. Mansfield, M. E. Meyerhoff, and M. M. Reynolds. Metal ion-mediated nitric oxide generation from polyurethanes via covalently linked copper(ii)-cyclen moieties. *Journal of Biomedical Materials Research Part B-Applied Biomaterials*, 91b(1):203–212, 2009.

[349] B. K. Oh and M. E. Meyerhoff. Catalytic generation of nitric oxide from nitrite at the interface of polymeric films doped with lipophilic Cu(il)-complex: a potential route to the preparation of thromboresistant coatings. *Biomaterials*, 25(2):283–293, 2004.

[350] S. Hwang and M. E. Meyerhoff. Polyurethane with tethered copper(ii)-cyclen complex: Preparation, characterization and catalytic generation of nitric oxide from S-nitrosothiols. *Biomaterials*, 29(16):2443–2452, 2008.

[351] J. L. Harding and M. M. Reynolds. Metal organic frameworks as nitric oxide catalysts. *Journal of the American Chemical Society*, 134(7):3330–3333, 2012.

[352] Stephen S.-Y. Chui, Samuel M.-F. Lo, Jonathan P. H. Charmant, A. Guy Orpen, and Ian D. Williams. A chemically functionalizable nanoporous material [cu3(tma)2(h2o)3]n. *Science*, 283(5405):1148–1150, 1999.

[353] J. L. Harding, J. M. Metz, and M. M. Reynolds. A tunable, stable, and bioactive mof catalyst for generating a localized therapeutic from endogenous sources. *Advanced Functional Materials*, 24(47):7503–7509, 2014.

[354] A. Demessence, D. M. D'Alessandro, M. L. Foo, and J. R. Long. Strong CO_2 binding in a water-stable, triazolate-bridged metal-organic framework functionalized with ethylenediamine. *Journal of the American Chemical Society*, 131(25):8784–+, 2009.

[355] M. J. Neufeld, B. R. Ware, A. Lutzke, S. R. Khetani, and M. M. Reynolds. Water-stable metal-organic framework/polymer composites compatible with human hepatocytes. *Acs Applied Materials & Interfaces*, 8(30):19343–19352, 2016.

[356] Megan J. Neufeld, Alec Lutzke, Jesus B. Tapia, and Melissa M. Reynolds. Metal–organic framework/chitosan hybrid materials promote nitric oxide release from S-nitrosoglutathione in aqueous solution. *ACS Applied Materials & Interfaces*, 9(6):5139–5148, 2017.

[357] Mofgen ltd. http://www.mofgen.com/, 2017. Accessed: 08.09.2017.

[358] T. P. Li, K. Taylor-Edinbyrd, and R. Kumar. A computational study of the effect of the metal organic framework environment on the release of chemically stored nitric oxide. *Physical Chemistry Chemical Physics*, 17(36):23403–23412, 2015.

[359] K. Taylor-Edinbyrd, T. P. Li, and R. Kumar. Effect of chemical structure of S-nitrosothiols on nitric oxide release mediated by the copper sites of a metal organic framework based environment. *Physical Chemistry Chemical Physics*, 19(19):11947–11959, 2017.

[360] P. K. Allan, P. S. Wheatley, D. Aldous, M. I. Mohideen, C. Tang, J. A. Hriljac, I. L. Megson, K. W. Chapman, G. De Weireld, S. Vaesen, and R. E. Morris. Metal-organic frameworks for the storage and delivery of biologically active hydrogen sulfide. *Dalton Transactions*, 41(14):4060–4066, 2012.

[361] H. Kim, A. Karkamkar, T. Autrey, P. Chupas, and T. Proffen. Determination of structure and phase transition of light element nanocomposites in mesoporous silica: Case study of NH_3BH_3 MCM-41. *Journal of the American Chemical Society*, 131(38):13749–13755, 2009.

[362] C. A. Young and A. L. Goodwin. Applications of pair distribution function methods to contemporary problems in materials chemistry. *Journal of Materials Chemistry*, 21(18):6464–6476, 2011.

[363] I. E. Collings, M. G. Tucker, D. A. Keen, and A. L. Goodwin. Static disorder and local structure in zinc(ii) isonicotinate, a quartzlike metal-organic framework. *Zeitschrift Fur Kristallographie-Crystalline Materials*, 227(5):313–320, 2012.

[364] T. D. Bennett, A. L. Goodwin, M. T. Dove, D. A. Keen, M. G. Tucker, E. R. Barney, A. K. Soper, E. G. Bithell, J. C. Tan, and A. K. Cheetham. Structure and properties of an amorphous metal-organic framework. *Physical Review Letters*, 104(11), 2010.

[365] Thomas D. Bennett and Anthony K. Cheetham. Amorphous metal–organic frameworks. *Accounts of Chemical Research*, 47(5):1555–1562, 2014.

[366] T. D. Bennett, T. K. Todorova, E. F. Baxter, D. G. Reid, C. Gervais, B. Bueken, B. Van de Voorde, D. De Vos, D. A. Keen, and C. Mellot-Draznieks. Connecting defects and amorphization in uio-66 and mil-140 metal-organic frameworks: a combined experimental and computational study. *Physical Chemistry Chemical Physics*, 18(3):2192–2201, 2016.

[367] D. Prill, P. Juhas, S. J. L. Billinge, and M. U. Schmidt. Towards solution and refinement of organic crystal structures by fitting to the atomic pair distribution function. *Acta Crystallographica a-Foundation and Advances*, 72:62–72, 2016.

[368] N. Rademacher, L. L. Daemen, E. L. Chronister, and T. Proffen. Pair distribution function analysis of molecular compounds: significance and modeling approach discussed using the example of p-terphenyl. *Journal of Applied Crystallography*, 45:482–488, 2012.

[369] T. Dykhne, R. Taylor, A. Florence, and S. J. L. Billinge. Data requirements for the reliable use of atomic pair distribution functions in amorphous pharmaceutical fingerprinting. *Pharmaceutical Research*, 28(5):1041–1048, 2011.

[370] D. Prill, P. Juhas, M. U. Schmidt, and S. J. L. Billinge. Modelling pair distribution functions (pdfs) of organic compounds: describing both intra- and intermolecular correlation functions in calculated pdfs. *Journal of Applied Crystallography*, 48:171–178, 2015.

[371] S. J. L. Billinge. Atomic pair distribution function: a revolution in the characterization of nanostructured pharmaceuticals. *Nanomedicine*, 10(16):2473–2475, 2015.

[372] S. Thakral, M. W. Terban, N. K. Thakral, and R. Suryanarayanan. Recent advances in the characterization of amorphous pharmaceuticals by x-ray diffractometry. *Advanced Drug Delivery Reviews*, 100:183–193, 2016.

[373] D. Hasa, C. Giacobbe, B. Perissutti, D. Voinovich, M. Grassi, A. Cervellino, N. Masciocchi, and A. Guagliardi. Nanostructured drugs embedded into a polymeric matrix: Vinpocetine/pvp hybrids investigated by debye function analysis. *Molecular Pharmaceutics*, 13(9):3034–3042, 2016.

[374] Marzena Rams-Baron, Renata Jachowicz, Elena Boldyreva, Deliang Zhou, Witold Jamroz, and Marian Paluch. Order vs. disorder in the solid state. In *Amorphous Drugs: Benefits and Challenges*, pages 9–39. Springer International Publishing, Cham, 2018.

[375] K. M. O. Jensen, C. Tyrsted, M. Bremholm, and B. B. Iversen. In situ studies of solvothermal synthesis of energy materials. *Chemsuschem*, 7(6):1594–1611, 2014.

[376] V. Petkov, Y. Peng, G. Williams, B. H. Huang, D. Tomalia, and Y. Ren. Structure of gold nanoparticles suspended in water studied by x-ray diffraction and computer simulations. *Physical Review B*, 72(19), 2005.

[377] M. Zobel, R. B. Neder, and S. A. J. Kimber. Universal solvent restructuring induced by colloidal nanoparticles. *Science*, 347(6219):292–294, 2015.

[378] J. L. Mi, K. M. O. Jensen, C. Tyrsted, M. Bremholm, and B. B. Iversen. In situ total x-ray scattering study of the formation mechanism and structural defects in anatase TiO_2 nanoparticles under hydrothermal conditions. *Crystengcomm*, 17(36):6868–6877, 2015.

[379] J. Becker, M. Bremholm, C. Tyrsted, B. Pauw, K. M. O. Jensen, J. Eltzholt, M. Christensen, and B. B. Iversen. Experimental setup for in situ x-ray saxs/waxs/pdf studies of the formation and growth of nanoparticles in near- and supercritical fluids. *Journal of Applied Crystallography*, 43:729–736, 2010.

[380] D. Saha, E. D. Bojesen, A. H. Mamakhel, M. Bremholm, and B. B. Iversen. In situ pdf study of the nucleation and growth of intermetallic ptpb nanocrystals. *Chemnanomat*, 3(7):472–478, 2017.

[381] A. K. Rappe, C. J. Casewit, K. S. Colwell, W. A. Goddard, and W. M. Skiff. UFF, a full periodic table force field for molecular mechanics and molecular dynamics simulations. *Journal of the American Chemical Society*, 114(25):10024–10035, 1992.

[382] M. D. Hanwell, D. E. Curtis, D. C. Lonie, T. Vandermeersch, E. Zurek, and G. R. Hutchison. Avogadro: an advanced semantic chemical editor, visualization, and analysis platform. *Journal of Cheminformatics*, 4, 2012.

[383] M. Dinca, W. S. Han, Y. Liu, A. Dailly, C. M. Brown, and J. R. Long. Observation of Cu^{2+}-H_2 interactions in a fully desolvated sodalite-type metal-organic framework. *Angewandte Chemie-International Edition*, 46(9):1419–1422, 2007.

[384] B. J. Campbell, H. T. Stokes, D. E. Tanner, and D. M. Hatch. Isodisplace: a web-based tool for exploring structural distortions. *Journal of Applied Crystallography*, 39:607–614, 2006.

[385] G. Kresse and J. Hafner. Ab initio molecular dynamics for liquid metals. *Phys. Rev. B: Condens. Matter Mater. Phys.*, 47:558, 1993.

[386] G. Kresse and J. Hafner. Ab-initio molecular-dynamics simulation of the liquid-metal amorphous-semiconductor transition in germanium. *Physical Review B*, 49(20):14251–14269, 1994.

[387] G. Kresse and J. Furthmuller. Efficiency of ab-initio total energy calculations for metals and semiconductors using a plane-wave basis set. *Computational Materials Science*, 6(1):15–50, 1996.

[388] G. Kresse and D. Joubert. From ultrasoft pseudopotentials to the projector augmented-wave method. *Physical Review B*, 59(3):1758–1775, 1999.

[389] P. E. Blochl. Projector augmented-wave method. *Physical Review B*, 50(24):17953–17979, 1994.

[390] John P. Perdew, Kieron Burke, and Matthias Ernzerhof. Generalized gradient approximation made simple. *Physical Review Letters*, 77(18):3865–3868, 1996.

[391] G. W. Mann, K. Lee, M. Cococcioni, B. Smit, and J. B. Neaton. First-principles hubbard u approach for small molecule binding in metal-organic frameworks. *Journal of Chemical Physics*, 144(17), 2016.

[392] I. Hamada. van der waals density functional made accurate. *Physical Review B*, 89(12), 2014.

[393] Mehrdad Asgari, Sudi Jawahery, Eric D. Bloch, Matthew R. Hudson, Roxana Flacau, Bess Vlaisavljevich, Jeffrey R. Long, Craig M. Brown, and Wendy L. Queen. An experimental and computational study of co_2 adsorption in the sodalite-type M-BTT (M = Cr, Mn, Fe, Cu) metal-organic frameworks featuring open metal sites. *Chemical Science*, 2018.

[394] B. H. Toby. EXPGUI, a graphical user interface for gsas. *Journal of Applied Crystallography*, 34:210–213, 2001.

[395] A. C. Larson and R. B. Von Dreele. General structure analysis system (GSAS). Report LAUR 86-748, Los Alamos National Laboratory Report, 2000.

[396] DC Palmer. Crystaldiffract 6.7.3. *CrystalMaker Software, Yarnton, UK*, 2019.

[397] T. Degen, M. Sadki, E. Bron, U. Konig, and G. Nenert. The highscore suite. *Powder Diffraction*, 29:S13–S18, 2014.

[398] Bess Vlaisavljevich, Johanna Huck, Zeric Hulvey, Kyuho Lee, Jarad A. Mason, Jeffrey B. Neaton, Jeffrey R. Long, Craig M. Brown, Dario Alfè, Angelos Michaelides, and Berend Smit. Performance of van der waals corrected functionals for guest adsorp-

tion in the M_2(dobdc) metal–organic frameworks. *The Journal of Physical Chemistry A*, 121(21):4139–4151, 2017.

[399] K. Lee, E. D. Murray, L. Z. Kong, B. I. Lundqvist, and D. C. Langreth. Higher-accuracy van der waals density functional. *Physical Review B*, 82(8), 2010.

[400] J. Grafenstein and D. Cremer. The self-interaction error and the description of non-dynamic electron correlation in density functional theory. *Theoretical Chemistry Accounts*, 123(3-4):171–182, 2009.

[401] A. B. Kehoe, D. O. Scanlon, and G. W. Watson. Modelling potential photovoltaic absorbers Cu_3MCh_4 (M = V, Nb, Ta; Ch = S, Se, Te) using density functional theory. *Journal of Physics-Condensed Matter*, 28(17), 2016.

[402] Kyuho Lee, Joshua D. Howe, Li-Chiang Lin, Berend Smit, and Jeffrey B. Neaton. Small-molecule adsorption in open-site metal–organic frameworks: A systematic density functional theory study for rational design. *Chemistry of Materials*, 27(3):668–678, 2015.

[403] Samuel O. Odoh, Christopher J. Cramer, Donald G. Truhlar, and Laura Gagliardi. Quantum-chemical characterization of the properties and reactivities of metal–organic frameworks. *Chemical Reviews*, 115(12):6051–6111, 2015.

[404] Ira N. Levine. *Quantum chemistry*. Pearson, Boston, seventh edition. edition, 2014.

[405] L. Grajciar, O. Bludsky, and P. Nachtigall. Water adsorption on coordinatively unsaturated sites in cubtc mof. *Journal of Physical Chemistry Letters*, 1(23):3354–3359, 2010.

[406] Neerav Kharche. Tutorial 7: Vasp calculations with model solvation. URL: https://fdocuments.in/document/tutorial-7-vasp-calculations-with-model-solvation.html, 11 2014.

[407] A. Klamt and G. Schuurmann. Cosmo - a new approach to dielectric screening in solvents with explicit expressions for the screening energy and its gradient. *Journal of the Chemical Society-Perkin Transactions 2*, (5):799–805, 1993.

[408] K. Mathew, R. Sundararaman, K. Letchworth-Weaver, T. A. Arias, and R. G. Hennig. Implicit solvation model for density-functional study of nanocrystal surfaces and reaction pathways. *Journal of Chemical Physics*, 140(8), 2014.

[409] X. B. Li, Y. Zhao, S. R. Wang, Y. Y. Zhu, and G. H. Yang. DFT-D2 study of the adsorption of bio-oil model compounds in HZSM-5: C-1-C-4 carboxylic acids. *Catalysis Letters*, 146(10):2015–2024, 2016.

[410] D. Dubbeldam, S. Calero, D. E. Ellis, and R. Q. Snurr. Raspa: molecular simulation software for adsorption and diffusion in flexible nanoporous materials. *Molecular Simulation*, 42(2):81–101, 2016.

[411] S. L. Mayo, B. D. Olafson, and W. A. Goddard. Dreiding - a generic force-field for molecular simulations. *Journal of Physical Chemistry*, 94(26):8897–8909, 1990.

[412] M. A. Addicoat, N. Vankova, I. F. Akter, and T. Heine. Extension of the universal force field to metal-organic frameworks. *Journal of Chemical Theory and Computation*, 10(2):880–891, 2014.

[413] D. E. Coupry, M. A. Addicoat, and T. Heine. Extension of the universal force field for metal-organic frameworks. *Journal of Chemical Theory and Computation*, 12(10):5215–5225, 2016.

[414] L. Vanduyfhuys, S. Vandenbrande, T. Verstraelen, R. Schmid, M. Waroquier, and V. Van Speybroeck. Quickff: A program for a quick and easy derivation of force fields for metal-organic frameworks from ab initio input. *Journal of Computational Chemistry*, 36(13):1015–1027, 2015.

[415] L. Vanduyfhuys, S. Vandenbrande, J. Wieme, M. Waroquier, T. Verstraelen, and V. Van Speybroeck. Extension of the quickff force field protocol for an improved accuracy of structural, vibrational, mechanical and thermal properties of metal-organic frameworks. *Journal of Computational Chemistry*, 39(16):999–1011, 2018.

[416] L. C. Lin, K. Lee, L. Gagliardi, J. B. Neaton, and B. Smit. Force-field development from electronic structure calculations with periodic boundary conditions: Applications to gaseous adsorption and transport in metal-organic frameworks. *Journal of Chemical Theory and Computation*, 10(4):1477–1488, 2014.

[417] A. C. T. van Duin, S. Dasgupta, F. Lorant, and W. A. Goddard. Reaxff: A reactive force field for hydrocarbons. *Journal of Physical Chemistry A*, 105(41):9396–9409, 2001.

[418] T. P. Senftle, S. Hong, M. M. Islam, S. B. Kylasa, Y. X. Zheng, Y. K. Shin, C. Junkermeier, R. Engel-Herbert, M. J. Janik, H. M. Aktulga, T. Verstraelen, A. Grama, and A. C. T. van Duin. The ReaxFF reactive force-field: development, applications and future directions. *Npj Computational Materials*, 2, 2016.

[419] Y. J. Yang, Y. K. Shin, S. C. Li, T. D. Bennett, A. C. T. van Duin, and J. C. Mauro. Enabling computational design of ZIFs using ReaxFF. *Journal of Physical Chemistry B*, 122(41):9616–9624, 2018.

[420] J. A. Greathouse and M. D. Allendorf. The interaction of water with MOF-5 simulated by molecular dynamics. *Journal of the American Chemical Society*, 128(33):10678–10679, 2006.

[421] Sang Soo Han, Seung-Hoon Choi, and Adri CT Van Duin. Molecular dynamics simulations of stability of metal–organic frameworks against H_2O using the ReaxFF reactive force field. *Chemical communications*, 46(31):5713–5715, 2010.

[422] X. Y. Liu, S. J. Pai, and S. S. Han. Reaxff molecular dynamics simulations of water stability of interpenetrated metal-organic frameworks. *Journal of Physical Chemistry C*, 121(13):7312–7318, 2017.

[423] Jun Xu, Yifei Michelle Liu, Andrew S. Lipton, Jinxing Ye, Gina L. Hoatson, Phillip J. Milner, Thomas M. McDonald, Rebecca L. Siegelman, Alexander C. Forse, Berend Smit, Jeffrey R. Long, and Jeffrey A. Reimer. Amine dynamics in diamine-appended Mg_2(dobpdc)

metal–organic frameworks. *The Journal of Physical Chemistry Letters*, 10(22):7044–7049, 2019.

[424] K. S. Walton and R. Q Snurr. Applicability of the bet method for determining surface areas of microporous metal-organic frameworks. *J. Am. Chem. Soc.*, 129:8552, 2007.

[425] Amit Gupta, Shaji Chempath, Martin J Sanborn, Louis A Clark, and Randall Q Snurr. Object-oriented programming paradigms for molecular modeling. *Molecular Simulation*, 29(1):29–46, 2003.

[426] Ding-Yu Peng and Donald B Robinson. A new two-constant equation of state. *Industrial & Engineering Chemistry Fundamentals*, 15(1):59–64, 1976.

[427] Caroline Mellot-Draznieks, Severine Buttefey, Anne Boutin, and Alain H Fuchs. Placement of cations in NaX faujasite-type zeolite using (N, V, T) Monte Carlo simulations. *Chemical Communications*, (21):2200–2201, 2001.

[428] Marie Jeffroy, Elena Borissenko, Anne Boutin, Angela Di Lella, Florence Porcher, Mohamed Souhassou, Claude Lecomte, and Alain H Fuchs. Evidence of a framework induced cation redistribution upon water adsorption in cobalt exchanged x faujasite zeolite: A joint experimental and simulation study. *Microporous and Mesoporous Materials*, 138(1-3):45–50, 2011.

[429] Marie Jeffroy, Anne Boutin, and Alain H Fuchs. Understanding the equilibrium ion exchange properties in faujasite zeolite from Monte Carlo simulations. *The Journal of Physical Chemistry B*, 115(50):15059–15066, 2011.

[430] Orhan Talu and Alan L Myers. Reference potentials for adsorption of helium, argon, methane, and krypton in high-silica zeolites. *Colloids and Surfaces A: Physicochemical and Engineering Aspects*, 187:83–93, 2001.

[431] D Wolf, P Keblinski, SR Phillpot, and J Eggebrecht. Exact method for the simulation of coulombic systems by spherically truncated, pairwise r- 1 summation. *The Journal of chemical physics*, 110(17):8254–8282, 1999.

[432] Lieve Uytterhoeven, Dirk Dompas, and Wilfried J Mortier. Theoretical investigations on the interaction of benzene with faujasite. *Journal of the Chemical Society, Faraday Transactions*, 88(18):2753–2760, 1992.

[433] Eugenio Jaramillo and Scott M Auerbach. New force field for Na cations in faujasite-type zeolites. *The Journal of Physical Chemistry B*, 103(44):9589–9594, 1999.

[434] Pierre Pascual, Philippe Ungerer, Bernard Tavitian, Pascal Pernot, and Anne Boutin. Development of a transferable guest–host force field for adsorption of hydrocarbons in zeolites i. reinvestigation of alkane adsorption in silicalite by grand canonical monte carlo simulation. *Physical Chemistry Chemical Physics*, 5(17):3684–3693, 2003.

[435] Koichi Momma and Fujio Izumi. VESTA: a three-dimensional visualization system for electronic and structural analysis. *Journal of Applied Crystallography*, 41(3):653–658, 2008.

[436] Katharine Page, Claire E White, Eben G Estell, Reinhard B Neder, Anna Llobet, and Th Proffen. Treatment of hydrogen background in bulk and nanocrystalline neutron total scattering experiments. *Journal of Applied Crystallography*, 44(3):532–539, 2011.

[437] O. Arnold, J. C. Bilheux, J. M. Borreguero, A. Buts, S. I. Campbell, L. Chapon, M. Doucet, N. Draper, R. F. Leal, M. A. Gigg, V. E. Lynch, A. Markvardsen, D. J. Mikkelson, R. L. Mikkelson, R. Miller, K. Palmen, P. Parker, G. Passos, T. G. Perring, P. F. Peterson, S. Ren, M. A. Reuter, A. T. Savici, J. W. Taylor, R. J. Taylor, R. Tolchenov, W. Zhou, and J Zikovsky. Mantid-data analysis and visualization package for neutron scattering and mu sr experiments. *Nucl. Instrum. Methods Phys. Res., Sect. A*, 764:156, 2014.

Part 2

The Influence of self-regulated learning interventions in general chemistry courses at Colorado State University

Chapter 1

Introduction

1.1 Problem

During their elementary and secondary education, students have a strong level of guidance provided primarily by teachers and parents. However, once students reach post-secondary education, they are, for the most part, on their own and are required to be in control of their learning, their motivation, their planning of goals, and managing their resources [Bembenutty, 2011a]. These qualities are part of what is defined as self-regulation of learning or self-regulated learning (SRL) defined as "processes whereby learners personally activate and sustain cognitions, affects, and behaviors that are systematically oriented towards the attainment of personal goals" [Zimmerman, 2011, p. 1]. This transition from one educational environment to the next is especially difficult for many students because they lack the skills needed for such a self-regulatory environment. Additionally, many students are not aware of good study strategies [Hartwig et al., 2012, Kornell and Bjork, 2007, McCabe, 2011, Morehead et al., 2016]. This deficiency in knowledge about effective study strategies can be attributed, at least partly, to the lack of necessary training and information about self-regulation and motivation provided to teachers and school psychologists [Cleary, 2011]. Not having the appropriate environment for learning can lead to students being, despite their interest in the subject, disengaged during the instructions they receive in the classroom. Furthermore, students' interest in engaging in interventions, intended to increase their level of self-reflections, is decreased. Additionally, the interaction with the learners and the classroom climate generated by educators also has a strong influence on self-regulation [Bembenutty, 2011b]. These are reasons for educators, researchers and policy makers to pay more attention to self-regulated learning in higher education and its implications on student success.

1.2 Self-monitoring

It was proposed that self-regulated learning is a cyclic process which occurs in three phases [Zimmerman, 2000]: the forethought, performance control, and self-reflection phase. The forethought phase, occurring before the actual learning process, is where learners generate goals and do strategic planning. The performance phase refers to the actual learning task including attention focusing, self-instruction and self-monitoring. The self-reflection phase is considered the final phase after the completion of the learning activity. This includes self-evaluation of the performance leading to adaptation of performance based on their success or failure and subsequent finding of explanations and adaptations for future tasks. This signals the starting point for the next forethought phase for reinitiating the SRL process.

A self-monitoring process, during the learning process in the performance phase, could be defined as one in which the effectiveness of learning strategies are assessed and the very first step for making self-learning even possible [Pressley and Ghatala, 1990]. Furthermore, it must reflect a learner's "deliberate attention to some aspect of one's behavior" [Schunk, 2012, p. 102]. Hence, the execution of this process must be intended and not arbitrarily or mindlessly done. Several examples in the literature show positive effects of monitoring on student success such as a study done on fifth and sixth graders on a computerized problem-solving task asking them questions at multiple stages during the process [Delclos and Harrington, 1991]. They reported, that students in the control group solved fewer complex problems and took longer to solve problems than students in the self-monitoring group. An example for continuous monitoring, also used in higher education, are learning diaries [Dörrenbächer and Perels, 2016, Fabriz et al., 2014]. A self-monitoring intervention resulted in increased levels of SRL strategy use and also better performing students compared to the control group even in a graduate level statistics course [Lan, 1996].

Self-evaluation, as part of the third phase of Zimmerman's SRL framework, includes comparing outcomes with the set goals. This can be done by, for instance, evaluating the results of exams commonly seen as the final step after completion of a learning activity. However, when multiple exams occur within a course and also only the final exam grade is considered as a goal-

measure, individual exams could be interpreted as part of the learning process and a measure of self-monitoring. Being tested by others was also identified by students as a self-monitoring strategy [Lan, 2005]. Students using this strategy seemed to realize the inaccuracy in evaluating their own learning. Another category of student responses identified by Lan (2005), highly related to being tested, was reviewing previous performance.

This process of reviewing or reflecting previous performance is also a good example for monitoring. Similar to previous approaches [Nelson and Narens, 1994], monitoring was viewed as 'a data-driven dimension of metacognition functions to inform control processes' [p.160, Nietfeld, Cao, & Osborne, 2006] which reflects the process of making changes to study habits based on previous data representing performance on exams. This process could be augmented with intentional and systematic interventions. It was claimed that these interventions are a suitable approach to SRL components such as monitoring [Schunk and Zimmerman, 2003]. Positive effects of such interventions have been shown in the literature. For example, improved monitoring was indicated in a psychology and educational psychology course to lead to improved self-regulation and improved performance [Thiede et al., 2003]. Similarly, feedback, given after an exam and classes, led to a higher level of calibration and performance in an educational psychology course [Nietfeld et al., 2006]. Also in a mathematics course, self-assessment of academic quiz outcomes led to higher performance [Glenn, 2010, Zimmerman et al., 2011]. Based on these examples from the literature, it is predicted that additional feedback gathered over time, either through external sources or though self-monitoring, would lead to better understanding of students' strength and weaknesses but also help them regulate and adjust their learning and learning strategies.

A similar approach was taken in introductory general chemistry courses at Colorado State University (CSU) with several different learning-to-learn activities intended to improve the students' level of self-monitoring and foster SRL. One of the interventions used was the Post-Exam Self-Assessments (further denoted as PESA) intervention. This approach provides additional opportunities to monitor and evaluate their learning progress and understanding of the material. This type of intervention has not only been used at CSU in chemistry, but also in other departments such as

biology or microbiology, immunology and pathology. It is also an example of one of the interventions used in the chemistry department, based on [Nilson, 2013], to decrease the high DFW-rates. PESAs at CSU have been used with different approaches, for example, one course used post exam assignments only after the first exam versus being part of the entire course. However, this type of intervention has not been analyzed on its effectiveness to help students perform better in these courses which was addressed in this study.

1.3 Post-exam Self-Assessment

A Post-Exam Self-Assessment intervention is considered to increase the level of self-monitoring in an academic environment. It was suggested that possible interventions in chemistry courses could be through communicating the role of effort and strategies as well as the facilitation of strategy use [Zusho et al., 2003]. The latter means that the instructor could model specific strategies of thinking for learning chemistry in the course. One way this can be done is through post-test analyses [Achacoso, 2004] which are also known as "Post-exam wrappers" [Ambrose et al., 2010, Kaplan et al., 2013, Lovett, 2010]. The post-exam self-assessment is based on a student's reflection on a past event which is not a generally well established practice. For example, 86% of students reported not reviewing course material after a course had ended [Kornell and Bjork, 2007]. It was also observed that there is generally a low level of self-reported self-monitoring at different levels of education ranging from elementary school to graduate school [Lan, 2005]. Across all education levels, only 22% of the students reported to use some self-monitoring strategy after class. Once higher stakes are involved, such as a quiz or a final exam, 36% and 31% of the students reported self-monitoring strategies respectively. The self-monitoring strategies reported by students were categorized in six groups (self-testing, being tested by others, overt presentation, elaboration, systematic rehearsal, and reviewing previous performance). It was also observed that older students reported higher levels of self-monitoring compared to younger ones. The identified self-monitoring categories of reviewing previous performance (e.g. exam or assignments) was used by only about 2% of the sampled students and marked the least used strategy. This confirms

a similar trend from a previously published study on 10th-graders who reported their level of reviewing tests when interviewed about their use of self-regulation strategies [Zimmerman and Pons, 1986]. Even at the graduate level, students have not optimized self-monitoring and self-regulated learning strategies yet [Lan, 1996]. This supports a general belief that students do not usually judge their learning after an exam in actual courses and usually, once an exam is graded and returned, students often quickly forget the details about the exam performance or how they prepared for the exam. This prevents them from discovering how their learning process and their study strategies went wrong. Traditionally, exams have marked the end of a learning process before a new learning begins for the next exam. Hence, an exam is not considered being an integrative part of the learning process itself. However, testing should be part of the learning process. The procedure of testing can entail for students to actually reflect on, for instance, what they had done wrong on that exam, what type of mistakes they made and what study strategies they used. This has been done in a similar manner by course instructors which reflect on how students performed, compare that to the learning objectives and further adjust their teaching or syllabus for the next semester when they teach the same course again. Since instructors are already more aware of these processes, they could help students overcome the difficulties of self-monitoring caused sometimes by not having a familiar self-monitoring system in place. Such an approach could address the motivational obstacles hindering students from self-monitoring [Zimmerman, 1998] which are on the one hand students being un- or misinformed about the effectiveness of self-monitoring and on the other hand the lack of self-efficacy on using self-monitoring strategies. A systematic self-monitoring system could be a Post-Exam Self-Assessment implementation in subject courses.

Marsha Lovett introduced the concept of PESA as part of a study which looked at four courses including introductory mathematics, and science courses (biology, chemistry and physics) at Carnegie Mellon University [Lovett, 2010]. The courses had different assignments and activities, but all their exams were fairly similar. The goal of her study was to determine the practical viability of these post-exam wrappers across several different courses as well as to get an initial formative assessment. The data that was used to evaluate the effectiveness were the students' responses pro-

vided on the wrapper, the answers provided on the survey at the end of the semester which inquired about their learning experience and the student ratings of different learning strategies which came from questionnaire responses at the beginning and at the end of the semester. Students were asked three kinds of questions in the initial design of her exam wrappers: a. how they prepared for the exam b. what kind of errors they made on the exam and c. what they might do differently to prepare for the next exam. The main purpose of this approach was not to get detailed answers from the students per se, but rather induce reflection and self-monitoring. Students are enabled to answer for themselves whether they studied enough or sufficiently in advance. Furthermore, by asking them about the study strategies that they used they consider that there are many option that they could have harnessed. One of the outcomes from Lovett's study was, that more than half of the students claimed to have changed in how they learn the material and study for exams. From this proportion of participants, 90% of them reported to have adopted a new learning strategy in chemistry. Another finding was, as predicted, students showed a higher increase in metacognitive ability the more courses they took that used exam wrappers. Furthermore, the more the students were exposed to the courses using exam wrappers, the more effective study strategies they used and the more accurately they rated study strategies on their level of effectiveness. Unfortunately, this research did not include a control group. This method should help to promote a different view of exams so students see them not only as a mere evaluation tool, but more of a valuable piece that is part of the learning cycle. For example, it has been shown that repeated retrieval, representative for testing, can enhance long-term learning [Brame and Biel, 2015]. This can also be seen to be an incubator for self-regulated learning which would profit in particular the students who are transitioning to college. The more instructors in other subject courses use these wrappers, the more students can learn about metacognitive skills in different contexts which increases the possibility that students might use these skills in new situations.

Post-exam wrappers can easily be implemented into a course. Generally speaking, any intervention should be easily adaptable to different disciplinary contents or formats of the course (whether it is a small or large student population). Additionally, instructors should not have to

design a distinct instrument for every course. The post-exam wrappers fulfill these requirements which makes them a tool that is repeatable but flexible enough to accommodate variations in format. These exam wrappers can be done as an in-class activity, as part of a homework that the students can turn in the next time they come to class or that can be done on an online learning management system. One more advanced way to administer post-exam self-assessments is to proceed with the interaction after students have turned the post exam assignments in. This can be done by returning them to the students at a later point during the semester when they are supposed to start studying for the next exam. This helps to remind students of what they have learned when doing the last exam wrappers. Then, students can ask some questions about it which can also be accompanied by an in-class group discussion on what effective study strategies are. Discussion items can tackle issues such as how many hours a student studied or when they started to study for the last exam. This process could lead students to think, for example, that they should work through more practice problems in order to better understand how to set up certain equations. This intervention was designed to increase metacognitive skills, however, reflections on exams can also increase motivational factors as a study in a college mathematics course showed [Zimmerman, 2011]. There, students who received self-reflection training and who used it to self-assess academic quiz outcomes, outperformed students in the control group. These students also showed better self-efficacy beliefs. Hence, such an intervention creates higher levels of motivation and might be useful as an intervention in a chemistry course.

1.4 Help-Seeking

Help-seeking is considered to be an important self-regulated learning strategy [Zimmerman, 2008]. This might sound contrary to self-regulated learning since searching for social assistance is contrary to the self-regulation process, which is by definition, nonsocial [Zimmerman and Pons, 1986]. A nonsocial approach is also reflected in societal norms focusing more on an individualistic nature than a collective, social environment [Karabenick and Berger, 2013]. This is also buttressed by John Garner, former Secretary of Health, Education and Welfare of the United States who said:

"The ultimate goal of the educational system is to shift to the individual the burden of pursuing his own education." [Lan, 2005] Therefore, it might not be surprising that, despite having been acknowledged as, for more than three decades, a self-regulated learning strategy [Karabenick and Gonida, 2018], many college students still do not seek the help that is needed for their academic success. While embarrassment is one of the reasons, there are a multitude of others ranging from showing weakness, over feeling hopeless to not being aware of needing help. Preventing students from asking the instructor questions can be based on their feeling of instructors judgment or their feeling of instructors not being receptive [Karabenick and Sharma, 1994]. In other instances, students realize that they have problems but do not ask for help because they lack the ability to identify what exactly they have not mastered yet. Not asking for help could also mean that there is a lack of understanding but students are unable to formulate a reasonable question preventing them from asking [Renkl, 2002].

However, there is evidence that successful students using other learning strategies are more likely to pursue looking for help when needed [Karabenick and Knapp, 1991]. Also Zimmerman and Pons (1986) identified seeking social assistance as a self-regulated learning strategy and showed that seeking assistance was a strong differentiator between the two achievement groups. 50% of the high achieving students reported asking for assistance from peers while only 23% of the low achieving students did. High achieving students also reported to seek help 27% more frequently from adults than the low achieving students. This result suggests that students relied more heavily on social sources of assistance to succeed in academic endeavors following similar findings on social learning which demonstrated that inhibition and self-controlling processes can be acquired and modified through observation of a model [Bandura et al., 1967]. This way using help-seeking as a self-regulated learning strategy helps to increase understanding enabling the student to act on future problems independently.

Help seeking is part of all three phases in the cyclic self-regulation model as a social strategy for gaining needed assistance [Usher and Schunk, 2018]. While originally only thought of occurring in the performance phase as a social strategy for acquiring needed assistance [Zimmerman and

Moylan, 2009], it may occur, according to Karabenick and Gonida (2018), as error identification and self-observation in the performance phase, task analysis during the forethought phase, and also self-evaluation in the self-reflection phase. Despite there being differences in the various models for the help-seeking process, they can generally be divided into eight steps [Karabenick and Berger, 2013, Karabenick and Newman, 2009, Nelson-Le Gall, 1981]. Although the order of the steps can change, usually the first two steps are task analysis, which embraces determining whether there is a problem, and determining whether help is needed [Karabenick and Berger, 2013]. Based on that, the ideal adaptive help seeker was described as one who asks questions regarding whether help is necessary, the content of the request, and the target, but also possesses interpersonal skills as well as self-system resources permitting him or her to persevere in situations and environments inhibiting or undermining help seeking [Newman, 2008]. In order to identify a problem, cognition or metacognition competencies need to be present which are also related to understanding that help is needed and how to seek help. While this represents a major competency for adaptive help seeking, emotional and social competencies are important at each stage of the help-seeking process. For example, with help-seeking being one out of the only two social self-regulatory strategies, learners need to have proper social skills for interacting with teachers or peers who could provide the needed help [Makara and Karabenick, 2013].

Learners not being aware of situational shortcoming requiring them to seek help are, therefore, attributed to metacognitive deficiencies in the self-regulated learning process [Efklides, 2011]. Hence, cultivating adaptive help seeking would require also improving cognitive competencies [Karabenick and Berger, 2013]. The challenge is to find effective intervention programs addressing specifically students with weak cognitive, metacognitive and motivational competencies. Suggestions have been published for instructors to create environments in school classrooms that can be considered help-seeking-friendly [Karabenick and Berger, 2013]. The environment in the classroom plays an important role, such as whether students perceive mastery goal or performance goal orientation within a classroom [Karabenick and Gonida, 2018]. Furthermore, it was claimed that teacher instructional support and emotional support are predictors for academic help

seeking in adolescents. For example, students' adaptive help seeking level was found to be higher in middle and high school classes in which students perceived higher levels of support [Zusho et al., 2007]. Therefore, it was suggested that instructors should clearly outline rules and procedures for the students on how to acquire help and what resources they have available [Newman, 2008]. Unfortunately, some teachers themselves are unaware of correctly contextualizing help seeking for themselves and their students [Butler, 2007b]. Occasionally, this leads them to make students believe that they should constantly work alone and not ask for help or that students should only get praised for independent work [Butler, 2007a, Karabenick and Gonida, 2018, Karabenick and Sharma, 1994, Strati et al., 2017]. In addition, the adjustments that can be made for preparing a help-seeking-friendly environment as well as the level of instructor support are limited in a classroom for larger introductory college courses. Therefore, other approaches need to be taken and help-seeking interventions need to be designed to adapt to different groups and environments. While there is a list of possible interventions to competencies in help seeking, most of them have not been studied in relation to help seeking behaviors. The question also remains whether a specialized training on self-regulated learning as part of a stand-alone course or distinct interventions implemented in a subject specific course would benefit students more.

1.5 Measuring Self-Regulated Learning

Since it is important to "understand cognition in the context of natural purposeful activity" [Neisser, 1976, p. 7], a classroom is the most appropriate setting for determining student qualities related to SRL. A typical methodology to determine these values in psychological or educational experiments is to perform experiments in a laboratory setting. There, several different experiments can be done to observe values such as reaction time or think-aloud protocols to measure strategy use or actual experimental manipulations to induce certain types of motivational goals [Ericsson and Simon, 1993, Graham and Golan, 1991]. However, laboratory experiments are not always the most appropriate setting. For example, they often sacrifice external validity and generalizability to the classroom setting. This is due to students' self-efficacy beliefs for most academic tasks based

on their familiarity with comparable tasks in a classroom setting. In comparison to their familiar classroom, the laboratory tasks could be relatively unfamiliar to them. The personal interest level and values for tasks performed in an academic classroom setting are also different for students. This means, that most laboratory tasks probably have low value for the typical student since their exposure to certain tasks, which may appear to be artificial, make the students rate the activity as unimportant or not meaningful to real life. Other examples for differences between laboratory and classrooms are more complex forms of learning, longer periods of learning, greater motivation, and longer delays between learning and testing. Laboratory settings, on the other hand, have the advantage that certain experiments can be performed, such as reaction time and think-aloud protocols, which are difficult in a classroom. Other advantages of experiments performed in a laboratory are the possibility to precisely specify and control of variables and relationships that are difficult to achieve in the field. Therefore, experiments performed in these different environments can yield different or sometimes even opposing results. For example, this was observed for the 'Memory of Past Test' effect. While a laboratory setting [Finn and Metcalfe, 2008] indicated the presence of this effect, the actual classroom setting could not find evidence for this effect [Foster et al., 2017]. However, there were more variations in the design of the study which makes it difficult to claim that the different outcomes are solely based on the this variable. To summarize, laboratory findings are considered to not be readily generalizable to classroom contexts [Lundeberg and Fox, 1991, McCormick, 2003]. Hence, based on the desired "close to reality"-situation in a classroom compared to a laboratory, the best way to collect data is actually in a classroom setting.

Some of the instruments that can be used in a classroom are observations, stimulated recall, interviews, and questionnaires. Let us review each of these methods briefly and determine its usability for measuring abilities related to self-regulated learning. A reason for using observations as an instrument is because many indicators of motivation are behavioral in nature such as choice of task level or effort on task and persistence at task. However, simply observing these characteristics is not sufficient to determine student motivation since it is important to also collect data on students' perceptions and beliefs about the task. This is based on the goal theory [Ames, 1992]

which distinguishes between a student's tendency toward mastery-orientation and performance orientation. One way a student's orientation could be determined with just behavioral observation is through speech recording. However, this approach usually entails too much effort to be a viable option for covering the student's orientation and, therefore, is not feasible in a classroom setting.

A method to obtain the same type of data, generated by observational methods as well as measures of students' beliefs and perceptions of their behavior, is called stimulated recall. [Bloom, 1953, Siegel et al., 1963, McConnell, 1985] The way this method works is to have students respond to a videotaped replay of their behavior from an earlier classroom session. The recording provides cues stimulating students to reflect on the shown class. This approach helps them to remember what their in-class thought process was. Hence, stimulated recall allows researcher to understand students' motivation and cognition in an actual classroom. While this method is meant to deliver the best data in the context of reliability and validity, it is expensive, time consuming, and not adequate when researchers lack the required equipment.

Contrary to stimulated recall, other self-reported instruments such as interviews and questionnaires are easy to use in classroom settings. Questionnaires are especially well suited for large groups of participants. For example, if the questionnaire items are closed-ended, it requires little time for preparing and scoring them. Questionnaires can also be used to obtain information on strategy use. This can be achieved by asking concrete questions about actual behavior that the students could engage in instead of abstract cognitive operations. Therefore, the items on a questionnaire can target actual behavior that the students might perform when studying the course material. However, some of these items may be difficult to be understood by younger participants as, for example, children [Garcia and Pintrich, 1996]. Based on these findings, questionnaires seem to be the most appropriate tool for determining qualities and abilities for becoming self-regulated learners in a college setting. While earlier there were questionnaire based tools to assess college student learning, they were considered to not be based on theoretical frameworks. In the literature these questionnaires are sometimes also defined as inventories. Some problems with inventories were, for instance, that there was no coherent definition of study skills, some inventories contained

subscales that had a very low reliability, the inventories were not validated as a diagnostic instrument, many of the inventories can quickly be deciphered by the students which makes it easy for them to give their desired image of themselves or most inventories look at only one part of effective study (consistent and regular study). Newer inventory based research on self-regulated learning in chemistry courses has focused more on particular areas of self-regulated learning such as evaluating metacognitive skills. For example, students in these courses have been evaluated on their learning with the Metacognitive Activities Inventory [Cooper et al., 2008,Cooper and Sandi-Urena, 2009, Sandi-Urena et al., 2011b]. However, with this inventory other very important components of self-regulated learning, such as motivation, have not been addressed.

A tool that examines both the student's motivation and learning strategies, which includes metacognition, is the Motivated Strategies for Learning Questionnaire (MSLQ). A review by Duncan and McKeachie (Duncan & McKeachie, 2005) illustrates the background of the MSLQ as well as the areas where it has been applied. Despite its wide usage and success in different levels of education ranging from 4th-grader [Andreou, 2004] to graduate students [Hamman et al., 2000], newer inventories are slowly replacing the MSLQ. The more recent achievement goal literature uses the Patterns of Adaptive Learning Scales (PALS) [Ross et al., 2005, Hackel et al., 2016] and the Revised Achievement Goal Questionnaire (AGQ-R) [Elliot and Murayama, 2008], with the latter being most appropriate for college students.

Measuring help seeking can be done with the MSLQ, but one critique is that it's help seeking scale does not distinguish between different sources of help. A more thorough scale was developed by Stuart Karabenick (2004) at the University of Michigan.

1.6 Summary of the Chemistry Education Part of the Dissertation

The second part of this dissertation aims to highlight that other factors besides just the actual chemistry content are important when studying this subject matter. We must ensure that knowledge gets understood and transferred effectively by fostering the appropriate "soft-skills" enabling

students to be more self-aware and become self-driven learners. The lack thereof has lead to high failure rates in science courses following a large number of students leaving this field. Similar trends were seen at Colorado State University with high drop- and withdraw-rates as well as a large number of D and F grades in introductory chemistry courses. This led to the introduction of SRL interventions in these courses. While the initial subjective evaluations were promising, a more in depth evaluation had to be conducted to further understand the influence on SRL qualities, motivation, but also on overall course grades.

Chapter two focuses on the chemistry course CHEM 111 with multiple types of interventions such as reading assignments, pre-exam knowledge surveys, and post-exam self-assessment. Their impact on motivational aspects (intrinsic goal orientation, extrinsic goal orientation, task value, control of learning beliefs, and self-efficacy) as well as a learning strategies aspect (help seeking) was evaluated with a paper-based survey using questions from the Motivated Strategies for Learning Questionnaire [Duncan and McKeachie, 2005]. While our experimental design was unable to detect statistically significant impact, broader implications are discussed. The final chapter evaluates the influence of only one intervention, the post-exam self assessment, and its influence on different aspects of help seeking (general intention to seek needed help, general intention to avoid needed help, perceived cost of help-seeking, instrumental help-seeking goal, expedient help-seeking goal, seeking help from formal sources, and seeking help from informal sources) and the influence on student grades. This was the only intervention introduced in a separate course, CHEM 107, and evaluated during two consecutive semesters allowing for an exploratory and confirmatory study. Similarly to the first study, students reported help-seeking information on in-class, paper-based surveys following the design of Karabenick (2004). Even eliminating influential factors such other interventions or different courses as comparative measures, did not yield a measurable statistically, significant effect in our experimental setup.

The appendices for this part of the dissertation contain examples of the surveys used for each study as well as additional figures from the two chemistry education chapters.

Chapter 2

Metacognitive reflection and self-regulated learning qualities in general chemistry college courses

2.1 Introduction

Introductory undergraduate science and engineering courses often have high failure rates, leading to a large number of students leaving the Science, Technology, Engineering, and Mathematics (STEM) field [Freeman et al., 2011]. Presaging these trends, declines in motivation and engagement in high school are greater in science courses than in other subjects [Gottfried et al., 2001,Shumow and Schmidt, 2013]. Accordingly, it is paramount to better understand such declines in motivation/engagement and to identify methods of enhancing academic achievement and retention in STEM fields.

One possible explanation is that success in STEM fields requires a broad understanding of learning so as to master complex, math-intensive concepts. However, survey data suggest that undergraduates may possess incomplete or erroneous knowledge of effective learning strategies [Hartwig and Dunlosky, 2012, Kornell and Bjork, 2007, McCabe, 2011, Morehead et al., 2016]. Further, students may underestimate their role in learning [Ruohoniemi and Lindblom-Ylänne, 2009] and fail to implement effective strategies even if they have adequate knowledge of those strategies [Foerst et al., 2017]. Thus, in conjunction with a variety of other factors that might undermine learning outcomes [Kirschner and van Merriënboer, 2013,Nilson, 2013,Singleton-Jackson et al., 2010], the literature suggests potentially important deficits in knowledge and production of optimal learning strategies [Rhodes et al., 2020].

Accordingly, it is imperative that students engage in effective self-regulation, "... self-generated thoughts, feelings, and actions that are planned and cyclically adapted to the attainment of personal goals" [Zimmerman, 2000, p. 14]. This may be especially important at the college

level, where most learning occurs outside of a structured environment and without instructor guidance. Students, therefore, frequently engage in self-regulated learning (SRL). This includes monitoring and control of cognition (metacognition; [Dunlosky J., 2008, Flavell, 1979, Rhodes, 2019]) as well as monitoring and control of one's emotion, motivation, behavior, and learning environment. Indeed, students are increasingly expected to be self-regulated learners [Kirschner et al., 2006, Wirth and Leutner, 2008] , with some curricular frameworks establishing effective SRL as a primary goal [European Commission, 2008]. Deficits in SRL may manifest in shortfalls in strategic knowledge (e.g., algorithms need to solve problems), deficient knowledge of cognitive tasks (e.g., assessing the difficulty of a task), and/or poor self-knowledge (e.g., awareness of one's strengths and weaknesses), among other possibilities [Pintrich, 2002].

In the current study, we explored an approach to remediating shortfalls in students' SRL skills. Prior research has considered generalized approaches via courses on how to learn [Bail et al., 2008,Hofer and Yu, 2003,Schmitz, 2001]. Although highly promising, it may also be advantageous to situate training in SRL skills within a content course rather than extracurricular training [Hattie and Marsh, 1996, Paris and Paris, 2001, Pressley et al., 1992, Tricot and Sweller, 2014]. Accordingly, we tested a focused SRL intervention within a large, multi-section introductory chemistry course. Broadly, the interventions consisted of reflections elicited during readings and knowledge assessments before and after exams (see the Methods section for details).

Of key interest were changes in SRL skills over the course of a semester. Prior work suggests that, absent an intervention, some elements of SRL may decline over time. For instance, Zusho, Pintrich, and Coppola (2003) measured self-regulated learning among students in a general chemistry course and reported that motivation and metacognition declined over a single semester [Zusho et al., 2003, Eccles J. S., 1998, Pintrich and Schunk, 2002]. Zusho et al. also reported that self-efficacy [Bandura, 1997], "students' judgments of their capabilities to perform a task, as well as their beliefs about their agency in the course" (p. 1083, Zusho et al., 2003), was the best predictor of course performance. These data comport with a meta-analysis reported by Robbins et al. (2004) showing that self-efficacy, along with achievement motivation, had a strong, positive relationship

with college GPA [Robbins et al., 2004] . A much more extensive synthesis of meta-analyses of 105 variables linked to achievement in higher education [Schneider and Preckel, 2017] further showed that self-efficacy robustly predicted academic performance. Other factors, such as goal orientation or intrinsic academic motivation, had smaller relationships with performance.

Prior work also suggests that an intervention implemented within a chemistry class may positively influence SRL. For instance, Olakanmi and Gumbo (2017) implemented in-class instruction for students on how to self-regulate their learning and set learning goals in each of the selected six lessons of a secondary school chemistry course. Students were prompted to ask questions about content during each lesson and reflected on their learning, revisiting their learing goals at the end of each lesson. A control group was exposed to the same course content but without instructions on how to self-regulate learning. Those students exposed to the intervention gained higher meta-cognitive self-regulation as well as slightly greater improvements in the knowledge of the covered topic (reaction rates).[4] However, what remains to be addressed is whether a targeted intervention can enhance SRL specifically in an introductory, college STEM course such as general chemistry. Further, prior research has not addressed whether the interventions implemented in this study would positively influence students' metacognitive abilities or their level of motivation in a large, introductory general chemistry course.

Accordingly, in the current study, we compared SRL skills in an introductory chemistry course with targeted interventions to an introductory chemistry course without any intervention. SRL skills were operationalized by measuring six different categories related to SRL (intrinsic goal orientation, extrinsic goal orientation, task value, control of learning beliefs, self-efficacy for learning and performance, and help seeking). Participants provided self-report survey data on each of these measures prior to the intervention and at two time points during the semester. Based on this design, we tested the following hypotheses:

[4]The results and methods used in the Olakanmi and Gumbo (2017) study were not taken into consideration for our study since the study was published after data collection for the present study had already taken place.

Hypothesis 1. Relative to a course not receiving the targeted intervention, participants in a course with the SRL intervention should exhibit higher levels of self-reported SRL abilities (motivation, self-efficacy, and metacognition).

Hypothesis 2. Exposing students to the interventions should positively influence their level of metacognition, cognition, and motivation over time. Hence, the level of self-reported SRL abilities should either increase or remain stable compared from the beginning to the end of the semester. In contrast, the control group should replicate findings reported by Zusho et al. (2003), indicating a decrease in students' self-reported metacognitive abilities as well as a decrease in motivational aspects from the beginning to the end of one semester.

2.2 Methods

Note on author contributions: This chapter was submitted for publication in Journal of Chemistry Education by Arnold A. Paecklar, Matthew G. Rhodes, Melissa M. Reynolds. AAP performed the experiments, wrote the initial draft, and collected and analyzed the data. MGR supported the data analysis efforts as well as edited the manuscript. MMR contributed to editing and finalization of the manuscript.

Participants:

Participants in this study were students enrolled in the introductory, on-campus chemistry courses CHEM 111 and CHEM 107 at Colorado State University. Participants in the four sections of CHEM 111 were assigned to receive the SRL intervention described in the following section. A companion introductory chemistry course, CHEM 107, served as the control group and did not receive any intervention. CHEM 107 is taught by different instructors, requires less use of mathematics than CHEM 111 and also covers some of the material covered in a follow-up course for CHEM 111. Nevertheless, the CHEM 107 course is closest in its content and curriculum to the CHEM 111 course compared to other introductory chemistry courses.

Demographic information for the students enrolled in both courses is reported in Table 2.1. A total of 921 individuals were enrolled across the six sections studied. Although 665 participants

completed the first survey, only students participating in all three surveys and answering all questions were included in the data reported. The final number of participants decreased to 70 (50 females, 18 males reported; age: M = 19.61 years, SD= 2.70) and 157 (107 females, 49 males reported; age: M = 19.23 years, SD= 2.30) students for CHEM 107 and CHEM 111 respectively.[5] A sensitivity analysis for the test of the simple main effect, assuming an $\alpha = .05$ and power ($1 - \beta$ = .80), indicated that the smallest effect size we could detect was d = .304. Likewise, a sensitivity analysis using the same parameters indicated that a relatively small interaction (d = .17) could be detected via this design. Taken together, our post hoc sensitivity analyses indicated that we had sufficient power to test the central hypotheses.

Table 2.1: Demographic information describing the participants in the CHEM 107 and CHEM 111 course

Category	CHEM 107	CHEM 111
Ethnicity		
Caucasian	78.3%	75.0%
Hispanic	8.7%	9.0%
Asian-American	4.3%	3.8%
African-American	-	2.6%
Mixed/Other	8.7%	9.6%
Class level		
Freshman	65.2%	79.5%
Sophomore	17.4%	12.2%
Junior	10.1%	7.1%
Senior	7.2%	1.3%
Most common majors		1.3%
Psychology	13.6%	
HDFS	7.6%	
HES	7.6%	11.6%
Animal science		9.7%
Biology		12.3%
Explanation of abbreviations: HDFS...Human Development and Family Studies, HES...Health and Exercise Science		

[5]We address the ramifications of this level of attrition in the General Discussion.

2.3 Materials and Procedure

Materials:

Interventions

The interventions, based on examples provided in the literature [Nilson, 2013], were implemented in the large, multi-section introductory course (CHEM 111) and were managed through the online learning management tool (Canvas) associated with that course. In addition to the actual intervention during the semester, two knowledge surveys, one at the beginning of the semester and one at the end of the semester, were implemented. These surveys were identical and asked students questions pertaining to each learning goal covered during the semester. Students indicated whether they felt able to answer the question without actually providing the answer to the question. Two types of interventions were implemented in the CHEM 111 course during the semester:

Reading Assignments:

Reading assignments comprised four questions on readings assigned prior to each lecture as a preparatory exercise. The questions that students were asked to reflect on were: 'What is the assigned reading from the text?', 'What is the main point of the reading?', 'What was surprising in the reading?', and 'What was confusing in the reading and why?'. Selected answers to these questions were discussed in class.

Interventions before and after the exams:

Pre-exam knowledge surveys: A subset of questions from the Beginning-of-Semester Knowledge Survey, addressing only the topics covered on each individual exam, were used for the Pre-exam knowledge survey and given to the students about a week prior to the exam. This consisted of 25 to 41 learning goals for each exam. Students rated their level of confidence about their ability to answer a question related to each learning goal. The students had six answer options reflecting different confidence levels ranging from 'I do not understand the question or task' to 'I know that I can answer the question well enough for grading now' (see Appendix D.1 for an example). The goal was for students to consider the concepts to be addressed on the exam, potentially encouraging them to differentiate and focus on topics that required additional study.

Post-exam self-assessment: These assignments were given after each exam had been graded and encouraged students to consider their test preparation. Several different questions prompted students to reflect on the difference between their actual and the predicted/desired outcome of the exam, how students prepared for the exam, errors that were made and how they would prepare for the subsequent exam (see Appendix D.2 for questions). This assignment was done independently, but some instructors occasionally led an in-class discussion on what students learned from the post-exam assessment.

SRL Inventory

SRL was measured via responses to the Motivated Strategies for Learning Questionnaire (MSLQ). While other scales have been successfully used in previous studies addressing college chemistry courses [Cooper and Sandi-Urena, 2009, Cooper et al., 2008, Sandi-Urena et al., 2011a, Sandi-Urena et al., 2011b], the MSLQ [Duncan and McKeachie, 2005] addresses not only metacognition but also other aspects of SRL, including motivation. For the current study, students provided responses to six subscales (see Appendix D.3 for the questions used):

Intrinsic goal orientation: Includes questions intended to indicate a student's goals in a learning task, as curiosity or mastery.

Extrinsic goal orientation: This is complementary to intrinsic goal orientation and describes a student's reason for participation in a course. Some example extrinsic reasons are grades, rewards, comparison to others, or evaluation by others.

Task value: Evaluates a student's perception of how interesting, how important, or how useful the material is that is being used in the course to achieve the goal.

Control of learning beliefs: This notion reflects a student's belief of how dependent positive outcomes are on internal factors such as his or her own efforts to learn.

Self-efficacy for learning and performance: This scale describes one's confidence in the skills needed for mastering a task but also the judgement of successfully accomplish the task.

Help seeking: In the academic environment managing support of others is very important. This scale addresses this issue and particularly discriminates between help being accessible from peers or instructors.

Procedure:

Students in CHEM 111 had the opportunity to gain extra credit for participating in Thinking about Learning activities (interventions). Participation in these activities was independent of participation in this study. Details on what activity was done as well as when and how each activity was graded are listed in Table 2.2. These activities were introduced to the students in the course syllabus as a set of tools to help them improve learning. The exams were always given on Thursday evenings and occurred during the 4th, 7th, 10th and the 13th week of classes. The final exam was on the Tuesday during the finals week.

Table 2.2: Occurrence and Grading Scheme for the Thinking about Learning activity

Activity	Due Date
Beginning-of-Semester Knowledge Survey	One week after class started
Writing on Assigned Readings	Monday, Wednesday, Friday
Pre-Exam Knowledge Survey	Wednesday before each exam
Post-exam self-assessment	Fridays, 8 days after the exam
End-of-Semester Knowledge Survey	The end of the last week of classes

Activity	Points	Frequency
Beginning-of-Semester Knowledge Survey	3	1
Writing on Assigned Readings	0.5 each	39
Pre-Exam Knowledge Survey	2 each	4
Post-exam self-assessment	4 each	4
End-of-Semester Knowledge Survey	3	1

Students in the intervention group (CHEM 111), completed the MSLQ three times during the semester, before the first (time 1), third (time 2), and fifth/final (time 3) exam in class. Each survey

also contained a consent form and a demographic information sheet. The control group (CHEM 107 course), without any Thinking about Learning activities, followed the same procedure. The study was introduced a week before the first data collection in class by the first author. The students were also given a short verbal reminder about the details of the study in class right before the second and third data collection. This study was done with the permission from all faculty in the involved courses and was approved by the Institutional Review Board (IRB).

Analytic Approach: Average values were calculated for each sub-scale, with some items on the help-seeking scale reverse-coded. Each sub-scale was analyzed via a 2 (Course: intervention, no intervention) x 3 (Time: 1, 2, 3) mixed-factor analysis of variance (ANOVA). An alpha level of .05 was used for all subsequent statistical tests. Partial eta values of .0099, .0588, and .1379, are considered to be benchmarks for small, medium, and large effect sizes respectively (Richardson, 2011).

2.4 Results

Intrinsic goal orientation: Mauchly's test indicated that the assumption of sphericity had been violated, $\chi^2(2)= 6.033$, p = .049; therefore the degrees of freedom were corrected using Huynh-Feldt estimates of sphericity (ϵ=.987). Overall, the rating of intrinsic goal orientation (see $Figure\ 2.1a$) differed across time, F(1.974, 444.092) = 16.072, p < .001, η_p^2= .067. The pairwise comparison for the main effect of time, corrected using a Bonferroni adjustment, indicated that the significant main effect reflects a significant difference (p < .001) between time 1 and time 2 and time 1 and time 3 but not between time 2 and time 3 (p = .587). In addition, students in CHEM 111 reported higher overall levels of goal orientation than students in CHEM 107, F(1, 225) = 3.96, p = .048, η_p^2= .017. There was no course x time interaction, F(1.974, 444.092) = .803, p = .447, η_p^2 =.004.

Extrinsic goal orientation: Mauchly's test indicated that the assumption of sphericity had been violated, $\chi^2(2)= 18.333$, p< .001; therefore degrees of freedom were corrected using Huynh-Feldt estimates of sphericity (ϵ=.939). Overall, the rating of extrinsic goal orientation (see $Figure\ 2.1b$) differed across time, F(1.877, 422.403)= 11.323, p < .001, η_p^2 = .048. The pairwise comparison for

the main effect of time, corrected using a Bonferroni adjustment, indicated that the significant main effect reflected a significant difference between time 1 and time 2 (p = .017) and time 1 and time 3 (p < .001) but not between time 2 and time 3 (p = .067). There was no difference between the ratings of extrinsic goal orientation between the students in CHEM 111 and the students in CHEM 107, F(1, 225) = .000, p = .985, η_p^2 < .000. In addition, there was no course x time interaction, F(1.877, 422.403) = 1.363, p = .257, η_p^2 = .006.

Task value: Mauchly's test indicated that the assumption of sphericity had been violated, $\chi^2(2)$= 23.849, p < .001; therefore degrees of freedom were corrected using Huynh-Feldt Estimates of sphericity (ϵ=.919). Overall, the rating of task value (see $Figure\ 2.1c$) differed across time, F(1.839, 413.694) = 47.958, p < .001, η_p^2= .176. The pairwise comparison for the main effect of time corrected using a Bonferroni adjustment indicated that the significnat main effect reflects a significant difference (p < .001) between time 1 and 2 and time 1 and time 3 but not between time 2 and time 3 (p=.051). In addition, students in CHEM 111 reported higher levels of task value than student sin CHEM 107, F(1, 225) = 6.169, p = .014, η_p^2= .027. There was no course x time interaction, F(1.839, 414.694) = .074, p = .915, η_p^2 < .001.

Control of learning beliefs: Mauchly's test indicated that the assumption of sphericity had been violated, $\chi^2(2)$= 7.419, p = .024; therefore degrees of freedom were corrected using Huynh-Feldt Estimates of sphericity (ϵ=.981). Overall, the rating of control of learning beliefs (see $Figure\ 2.1d$) differed across time, F(1.962, 441.476) = 5.79, p = .003, η_p^2 = .025. The pairwise comparison for the main effect of time, corrected using a Bonferroni adjustment, indicated that the significant main effect reflects a significant difference between time 1 and time 2 (p = .005) but not between time 1 and time 2 (p = .172) and time 2 and time 3 (p = .361). However, there was no difference between the ratings of extrinsic goal orientation between the students in CHEM 111 and the students in CHEM 107, F(1,225) = .894, p = .345, η_p^2 = .004. Course did not interact with time, F(1.962, 441.476) = .316, p = .725, η_p^2= .001.

Self-efficacy for learning and performance: Mauchly's test indicated that the assumption of sphericity had been violated, $\chi^2(2)$= 40.324, p < .001; therefore degrees of freedom were cor-

rected using Huynh-Feldt Estimates of sphericity (ϵ=.868). Overall, the rating of self-efficacy (see $Figure\ 2.1e$) for learning and performance did not differ across time, F(1.737, 390.767) = 2.904, p = .064, η_p^2= .013. In addition, students in CHEM 107 reported higher levels of self-efficacy for learning and performance than students in CHEM 111, F(1,225) = 7.778, p = .006, η_p^2= .033. There was no course x time interaction, F(1.737, 390.767) = .430, p = .622, η_p^2= .002.

Help seeking: Mauchly's test indicated that the assumption of sphericity had been violated, $\chi^2(2)$= 33.373, p < .001; therefore degrees of freedom were corrected using Huynh-Feldt Estimates of sphericity (ϵ=.889). Overall, the rating of help seeking (see $Figure\ 2.1f$) did not differ across time, F(1.777, 399.922) = .281, p = .729, η_p^2= .001. Furthermore, there was no difference between self-reported help seeking between the students in CHEM 111 and the students in CHEM 107, F(1, 225) = .001, p = .971, η_2 < .001 and no course x time interaction, F(1.777, 399.922) = .023, p = .968, η_p^2 < .001.

2.5 Discussion

Based on studies in secondary as well as tertiary education showing positive effects of SRL interventions [Bail et al., 2008, Leidinger and Perels, 2012, Schmitz and Perels, 2011, Stegers-Jager et al., 2012], we examined whether similar positive effects would be obtained for a SRL intervention in a general chemistry course. Taken as a whole, our results provide little evidence for the impact of the SRL intervention implemented. For instance, students in the control group reported higher levels of self-efficacy at all measurement points relative to students in the intervention group. Furthermore, no difference was evident in self-reported extrinsic motivation, control over learning, or help seeking. Intervention students did, overall, report higher levels of intrinsic orientation and task value, but these patterns must be qualified. In particular, the key prediction was that a time x group interaction would be evident for measures of SRL, such that students exposed to the intervention would be more likely to remain stable or show increases in measures of SRL across measurement time points than control students. No such pattern was evident for any measure.

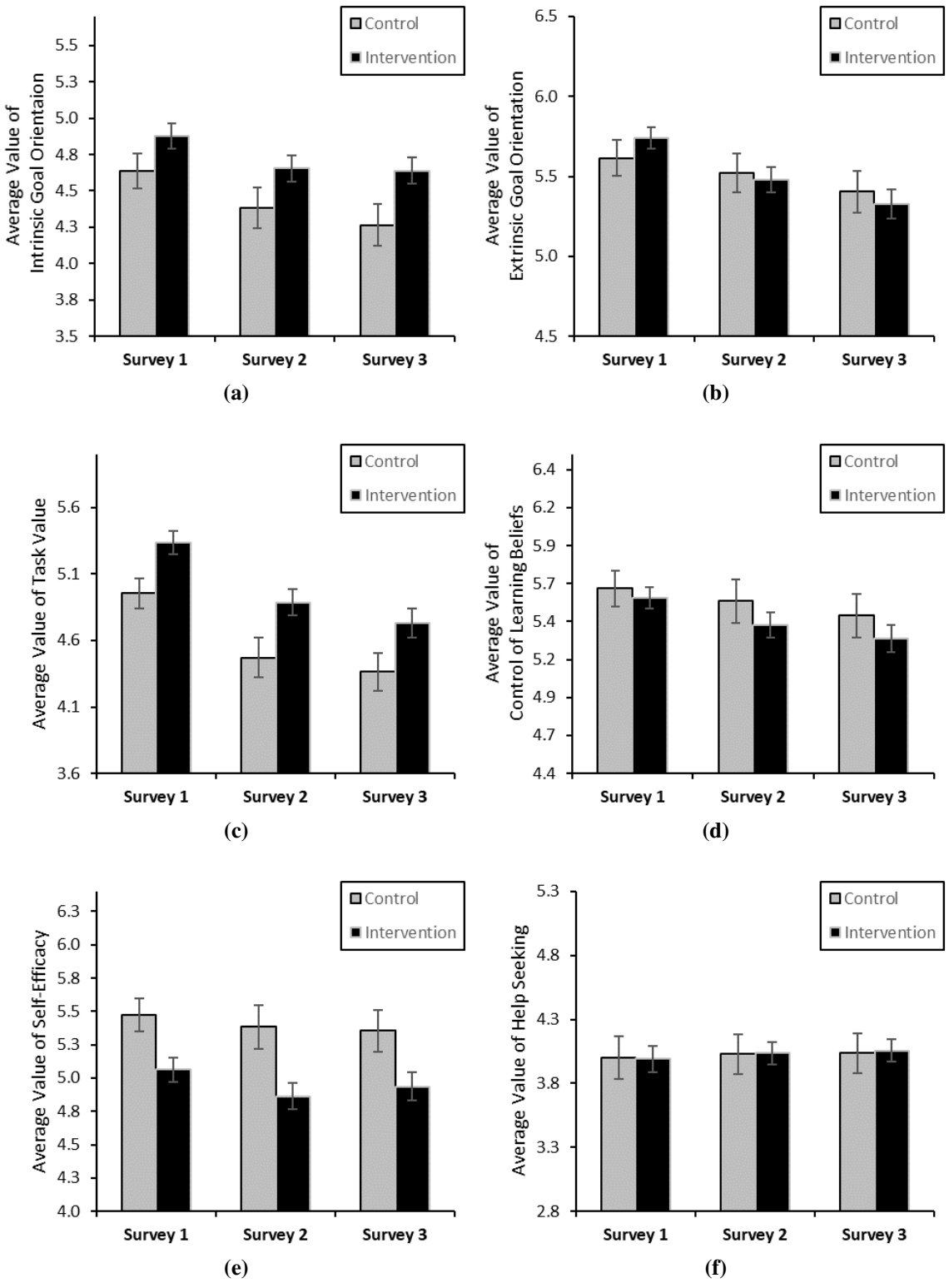

Figure 2.1: Average value of the of the MSLQ subscale measuring: (a) Intrinsic Goal Orientation, (b) Extrinsic Goal Orientation, (c) Task Value, (d) Control of Learning Beliefs, (e) Self-Efficacy, and (f) Help Seeking. Standard errors are represented in the figure by the error bars attached to each column.

In contrast to several prior studies [Olakanmi and Gumbo, 2017, Stegers-Jager et al., 2012, Zusho et al., 2003], our SRL intervention did not affect self-reported learning behaviors. Although necessarily speculative, several explanations may account for the failure to detect differences between the intervention and control groups. For instance, traits such as self-efficacy may be relatively stable and less subject to change [Bandura, 1997, Pajares, 1996]. As illustrative, Nietfield and colleagues [Nietfeld et al., 2006] provided an educational psychology course with short monitoring exercises during class. Students were asked to rate their understanding of the day's content, identify concepts they found difficult to understand, report what they would do to improve their understanding of these concepts, and answer three multiple choice review questions of the day's material paired with a confidence judgement for each question. The review items were answered, discussed and reflected on before the end of the class, with students in the treatment group feedback on the accuracy of monitoring their judgment of the test performance after each test. However, relative to a comparison class, neither group showed changes in self-efficacy.

In a related vein, the quality, amount, and frequency of the intervention employed in the current study may be insufficient to produce any meaningful change in SRL. For example, Schmitz and Perels (2011) showed that students prompted to engage in self-monitoring over 49 days indicated increased levels of self-regulation, self-efficacy and improved math test scores compared to baseline measures taken before the SRL intervention period. By comparison, the interventions used in the current study were far less frequent and thus may reflect a much lower "dose" of the intervention. Thus, future work might employ a similar intervention implemented with greater frequency and intensity than reported in this study. Additionally, we note that the level of attrition among participants (see the Methods section) may have introduced non-random sources of variability that might have diminished the likelihood of a successful intervention. For example, students who regularly attend class and participate in the interventions may have less need for remediating SRL. By extension, students who might have been most likely to benefit from the interventions may have been excluded from the study due to infrequent class attendance that excluded them from data collection opportunities.

Further, although our study compared two different chemistry courses based on similar course content and student demographics, other differences may have been present between the two courses that we did not control. For example, this study did not control or test for classroom goal structures [Urdan, 2010] that may have exerted direct and indirect influences on students' performance. As illustrative, the influence of three variables (lecture engagement, evaluation focus, and harsh evaluation) on undergraduates' perception of their chemistry classroom environment was examined as well as the influence on course performance and intrinsic motivation [Church et al., 2001]. Lecture engagement was positively related to a mastery goal orientation whereas harsh evaluation negatively predicted a mastery orientation. However, Church et al. did not detect any relationship with course performance. Although these variables are controlled by the instructor, goal structures might also reflect the values of students enrolled in the course. Prior work suggests that variability in goal orientation is frequently greater within a course rather than between courses [Miller and Murdock, 2007,Urdan, 2010]. Accordingly, we believe our results are unlikely to reflect differences in goals among students enrolled in these similar courses.

Educational Implications

A clear implication for educators is that not all implementations of interventions have a directly measureable positive effect on students' level of SRL qualities. This could mean that certain interventions work differently depending on the course subject but also depend on the way they are introduced or administered. Although immediate effects are not always indicated by some interventions, a positive effect leading to changes in students' long-term SRL cannot be excluded or predicted. Furthermore, it remains unclear whether the intervention might exert effects on students' grades and suggests an avenue for future research.

Indeed, even if differences were detected between students subjected to an intervention and a control group, the intervention should be sufficiently robust so as to produce appreciable benefits to student learning [Hattie, 2008]. Hattie also noted that many instructional strategies may enhance learning, leading instructors to the conclusion that their chosen method enhances learning [Hattie,

2015]. A more beneficial strategy is to identify those strategies that have greater or lesser impacts on learning. For instance, methods that have greater effects on learning include, but are not limited to, teachers being adept at cognitive task analysis, reciprocal teaching, spaced learning, and peer teaching (see [Hattie et al., 2015], for details on successful implementation). [Schneider and Preckel, 2017] Schneider and Preckel (2017) have extended this approach to focus on post-secondary education. Their meta-synthesis of best practices in learning suggest that learning benefits when instructors incorporate practices such as student peer-assessment, ensuring that presentations of abstract concepts are clear and understandable, encouraging of questions and discussions, making course objectives and requirements clear, academic skill training, and mastery learning. This also suggests that, based on the vast diversity of teaching methods and interventions for enhancing student learning, faculty training is also important at the university level in order to become an effective teacher. Similar to self-regulated learning, all of the attributes and approaches towards effectiveness can be taught leading to enhanced university teaching.

Limitations: We should always be cautious about how the results of self-reported measures of motivation and learning strategies are interpreted. The validity of self-reported data has been a problem due to factors such as social desirability bias. However, when Duncan and McKeachie have included so called measures of social desirability (e.g. the Crown-Marlowe social desirability scale) they could show that these measures of response bias did not account for any significant amount of variance and it also did not change the final result. Further, there was no random assignment of participants to the intervention groups which would be desirable, but very difficult to realize in university contexts.

Chapter 3

The influence of Post-Exam Self-Assessment Interventions on student performance and help seeking in a college level general chemistry course

3.1 Introduction

Students are required to be in control of their own learning [Bembenutty, 2011a but often struggle to achieve this since they are not aware of good study strategies [Hartwig et al., 2012, Kornell and Bjork, 2007, McCabe, 2011, Morehead et al., 2016]. The lack of these qualities hinders self-regulated learning (further abbreviated as SRL) and very often leads to overwhelmed students getting too often letter grades D and F, or drop out of courses despite exerted learning efforts. To excel in SRL, students need to be able to understand where they are in their learning process, what they have already mastered and what still needs to be learned. This involves a cyclic process and often referred to as self-monitoring [Zimmerman, 2000]. How monitoring can have positive effects on student learning, such as higher performance, was shown in the literature [Delclos and Harrington, 1991, Lan, 1996]. Self-monitoring can be done in multiple ways, but effective techniques correctly identified by students themselves are, for example, being tested by others or reviewing previous performance [Lan, 2005]. This can function as a direct input for making changes to study habits [Nietfeld et al., 2006] which was shown to result in higher performances on quizzes in a mathematics course [Glenn, 2010, Zimmerman et al., 2011]. Based on this example from the literature, it is predicted that additional feedback from, for example, self-monitoring can lead to better understanding of what the students' strengths and weaknesses are but also help them to regulate and adjust their learning. One method, considered to increase the level of self-monitoring in an academic environment, is in post-exam self-assessments. This can be done by post-test analyses [Achacoso, 2004] which are also known as "Post-exam wrappers" [Ambrose et al., 2010, Ka-

plan et al., 2013, Lovett, 2010]. While self-monitoring or self-reflection is still not a wide spread practice [Kornell and Bjork, 2007, Lan, 2005], it could be easily enforced by implementing post-exam self-assessments (further denoted as PESA) into subject courses such as general chemistry. PESA has already been used in mathematics as well as biology, chemistry and physics courses at other institutions, leading to more than half of the surveyed students claiming that they have changed how they learn the material and study for exams [Lovett, 2010]. Furthermore, 90% of them reported to have adopted a new learning strategy in chemistry. Self-reflection and self-assessment have shown to also increase motivational factors such as self-efficacy [Zimmerman, 2011]. However, the question still remains how other self-regulated learning strategies, such as help-seeking, might be influenced by such self-monitoring interventions. While help-seeking is considered to be an important self-regulated learning strategy [Zimmerman, 2008], many college students still do not seek out the needed help [Karabenick and Gonida, 2018]. However, in a college organic chemistry course it could be shown that students with a higher tendency to seek help were higher achieving than the group with lower help-seeking tendencies [Szu et al., 2011]. Furthermore, not only the level of help-seeking but also time time when it is done during the semester is important. For example, Szu et al (2011) showed that while the overall frequency and study time did not differ between the lower and higher achieving group, the higher achieving students showed higher levels of seeking instructor assistance at the beginning of the semester. Similar trends were seen in other STEM courses such as mathematics [Treisman, 1992]. This is a good example of how students apply SRL strategies by seeking information early on allowing them insight that they need to master the semester.

A distinct intervention to foster help seeking through improved metacognitive competencies in a subject specific course could be PESA. It was proposed that learners would seek help more frequently if they were more aware of what they did not know and how to get help [Karabenick and Dembo, 2011]. Self-monitoring, self-evaluation as well as planning for exams and assignments are metacognitive strategies. It was shown that higher levels of self-monitoring resulted in more specific help seeking [Tobias, 2006]. As specified earlier, PESA indicate improved monitoring

in academic courses, which is part of metacognition, and, therefore, an important factor in help seeking. Hence, SRL could also be enhanced by strengthening an important learning strategy such as help seeking [Zimmerman, 2008]. Help seeking in a college level chemistry course was already studied previously and particularly put in the context of achievement goal theory [Karabenick, 2004]. The results for three introductory chemistry courses and three organic chemistry course were similar as for the group of introductory psychology students. It was shown that instrumental help seeking led to preferentially using their teachers over others as their source of help. Another important finding was that students' performance in these courses was positively related to help-seeking approach which was also found in an organic chemistry course [Horowitz et al., 2013]. Students following this trend had a higher likelihood to seek help in order to gain higher levels of autonomy. Contrarily, students endorsing performance goals were concerned about outperforming others as well as being perceived as less able leading them to avoiding help seeking and would only seek help to avoid work. However, this study gives only a static picture of help seeking in a chemistry course and also does not take the influence of possible interventions on the level of help seeking into considerations.

Hypothesis

Based on the previous literature and the presented example of PESA as a possible intervention to increase monitoring and help seeking as a self-regulated learning strategy, specific hypotheses were developed that were to be tested in our study.

A. The implementation of a post-exam self-assessment in an introductory, general chemistry course improves students' monitoring skills and further leads to higher course grades compared to the control group.

B. The use of a post-exam self-assessment intervention improves students' metacognitive abilities, leading to better understanding on when and how students need to seek out help which increases the level of self-reported help seeking in an introductory, general chemistry course during the course of the semester.

An introductory chemistry course at Colorado State University was used to test these hypothesis during the academic year 2017/2018. During the Fall Semester 2017 an exploratory study was done where only the influence of the post-exam self-assessment intervention on students' performance was determined. During the Spring Semester 2018 a confirmatory analysis was conducted with the extension of also looking at the intervention's influence on students' level of help seeking. At the beginning of the Spring Semester the confirmatory study was preregistered with the Open Science Framework (https://osf.io/qnk3s/register/565fb3678c5e4a66b5582f67).

3.2 Methods

Participants:

Exploratory study:

The exploratory study during the Fall semester 2017 was sampling CSU students from the two sections of the introductory, general chemistry course CHEM 107. Students were sampled from the population of all students at this university. To enroll in the general chemistry CHEM 107 course being studied, students must meet a mathematics prerequisite required by the university. One of the sections was assigned to the control group whereas the other section functioned as the intervention group. All students in each section were eligible to participate. The course instructor informed students that they would have the chance to participate in a study over the course of the semester and I was invited to the class to introduce the study, describe the procedures for consent, and answer any questions. As part of this recruitment, it was made very clear to students that the study was entirely voluntary and that nobody was required to participate.

The overall participation in the intervention group for all surveys (1 - 3 times) was 189 students (110 females, 77 males reported; age: M = 20.84 years, SD= 4.72). Regarding ethnicity in CHEM 107, 78.3% identified as Caucasian, 10.1% as Hispanic, 5.3% Asian-American, 1.6% African-American and the rest identified as mixed or other ethnicity. Regarding their class level, 20.8% stated to be Freshman, 44.8% Sophomore, 26.8% Junior, and 7.7% declared to be Senior. While there was a wide variety of majors from all different colleges, the three top most common

majors were psychology (17.5%), Health and Exercise Science (9.0%), and equine science equally as computer science (8.5%). However, the students who only participated in all three surveys was only 55 (41 females, 12 males reported; age: M = 21.35 years, SD= 4.77). The number of students who participated in the intervention, the post-exam self-assessment, once, twice and three times were 21, 24, and 38 respectively. Only the 38 students (28 females, 9 males reported; age: M = 21.26 years, SD= 5.84) who participated in all three interventions were considered for this study. Participation in the study also meant allowing us to have their course grades shared by the instructor. Students who volunteered to participate in the study were eligible to earn 6 points of extra credit towards their course grade for each survey and post-exam self-assessment; those who participate during all three times got a 7-point bonus which means they got 25 points instead of 18. There was no partial credit possible. Individuals who did not consent to participate in the study also had the opportunity to earn the equivalent amount of extra points through reading activities (of equal duration) offered by the instructor.

The number of students in the control group who only participated in reading assignment (1 - 3 times) were 104. However, only 103 participants gave consent to use their grades. Students in the control group had the opportunity to earn 6 points of extra credit towards their course grade through reading activities (of equal duration) offered by the instructor; those who participated during all three times got a 7-point bonus which meant they got 25 points instead of 18.

For both groups, only data from participants who signed the informed consent form were included in the research study. In addition to the incentive of a payment with points towards the course grade, the faculty and the researcher highlighted its importance when introducing it to the students in the class room. The more of a benefit the students see for themselves and future students in the potential outcomes of the study the more they are inclined to participate. This was pointed out in previous literature [Scharff et al., 2011] claiming that participation is also influenced by how the instructor presents the value of the task. This study was done with the permission from all faculty in the involved courses and was approved by the Institutional Review Board (IRB).

Confirmatory Study:

The confirmatory study was done during the Spring semester 2018 and sampled CSU students in a similar way to the exploratory study from the two sections of the introductory, general chemistry course CHEM 107. For this study, students were sampled in the two sections of the general chemistry CHEM 107 course. One section was randomly designated to receive the intervention and the other section received no intervention (but provided survey data). All students in each section were eligible to participate. The overall participation in the intervention group for all surveys (1 - 3 times) was 235 (129 females, 104 males reported; age: M = 19.71 years, SD= 2.56). Regarding ethnicity in the intervention group in CHEM 107, 80.7% identified as Caucasian, 12.9% as Hispanic, 2.6% Asian-American, 0.9% African-American, and the rest identified as mixed or other ethnicity. Regarding their class level, 25.3% stated to be Freshman, 47.1% Sophomore, 20.7% Junior, and 6.9% declared to be Senior. While there was a wide variety of majors from all different colleges, the three top most common majors were psychology (15.3%), Health and Exercise Science (10.2%), and Fish, Wildlife and Conservation Biology (8.5%). The number of participants in all three surveys 142. Students who participated in the post-exam self-assessment once, twice and three times were 30, 25, and 85 respectively. However, the number of students relevant for this study, participation in all surveys and also all three interventions, was only 82 (51 females, 30 males reported; age: M = 19.94 years, SD= 3.55). Students who volunteered to participate in the study were eligible to earn extra credit towards their course grade (2 points for participation in each survey and 4 points for each post-exam self-assessment; those who participate during all three times get a 7-point bonus which means they get 25 points instead of 18). Individuals who did not consent to participate in the study also had the opportunity to earn the equivalent amount of extra points through reading activities (of equal duration) offered by the instructor. Only data from students who completely fill out the assignment were awarded the extra credit. There was no partial credit possible.

The overall participation in the control group for all surveys (1 - 3 times) was 88 (53 females, 35 males reported; age: M = 20.83 years, SD= 3.92). Regarding ethnicity in the control group in CHEM 107, 80.5% identified as Caucasian, 9.2% as Hispanic, 5.7% Asian-American, 2.3%

Native-American, 1.1% African-American, and the rest identified as mixed or other ethnicity. Regarding their class level, 25.3% stated to be Freshman, 47.1% Sophomore, 20.7% Junior, and 6.9% declared to be Senior. While there was a wide variety of majors from all different colleges, the three top most common majors were psychology (18.2%), health and exercise science (10.2%), and Human Development and Family Studies equally as Natural Resources Management (7.6%). The number of relevant students who participated in all surveys was only 54 (36 females, 18 males reported; age: M = 20.57 years, SD= 4.48). Out of all participants in the control group, 88 students gave consent to have their grades used for this study. Students who volunteered to participate in the study (fill out the help-seeking survey) could earn extra credit towards their course grade (2 points for participation in the survey; those who participated during all three times got a 2-point bonus which means they get 8 points instead of 6). In addition, there was an opportunity to earn 17 points of extra credit which was not connected to the research at all. Students were given the opportunity to do a reading assignment which was worth 4 points. If participating students did all three assignments, they could get a bonus of 5 points. Hence, instead of 12 points they could get 17 points. Only data from students who completely filled out the assignment were awarded the extra credit. There is no partial credit possible.

3.3 Materials and Procedure

Help Seeking:

To measure the level of helps seeking, questions from a previous study probing help seeking [Karabenick, 2004] referring to 7 categories (General Intention to Seek Needed Help, General Intention to Avoid Needed Help, Perceived Costs of Help-Seeking (threat), Instrumental (Autonomous) Help-Seeking Goal, Expedient (Executive), Help-Seeking Goal, Seeking Help from Formal Source (teachers), Seeking Help from Informal Source (other students)) were combined with the help-seeking subscale of the Motivated Strategies for Learning Questionnaire (MSLQ) [Pintrich P. R., 1991]. The help-seeking data for all questions was provided on a 7-point scale. The individual help seeking questions are illustrated in the Appendix E.1.

Post-Exam Self-Assessment:

The post-exam self-assessment was used as the metacognitive intervention in this study. The assignment was created by the general chemistry coordinator at CSU based on Nilson (2013) and was slightly modified by the researcher before introducing it to the students in the course. The entire assignment can be found in the Appendix D.2. Students could access the assignment though the online learning platform supporting the course.

Procedure:

Exploratory Study:

The study occurred over the course of one semester. The intervention group was given the first survey in the week before the second exam. All the subsequent surveys were administered one week before exam 3 and 4. In the exploratory study, the control group was not asked to fill out a survey. After Exam 2, 3 and 4 students, the intervention group engaged in a metacognitive reflection, the post-exam self-assessment, and turned in the assignment regarding this reflection no later than a week after the individual exam. Students in both groups took also a final exam but no group filled out a survey prior to that exam nor did they do any metacognitive reflection afterwards. The alternative assignments for the control group, the reading assignments, also had to be turned in no later than a week after the exam (same day as the intervention group).

The manipulated variable that differentiates the control from the intervention group was the exposure to a metacognitive intervention, the post-exam self-assessment, but also the exposure to help-seeking surveys. Thus, there was a single variable (Metacognitive Intervention) with 2 levels (exposed to intervention, not exposed to intervention). Two different types of data were measured during the exploratory study: 1. The questions on the help-seeking survey correspond to 8 different subcategories. 2. All individual exam scores and the final course grade were delivered from the course instructor. The first and second exam score was averaged and used as a covariate for subsequent ANCOVAS. Due to the lack of help-seeking data from the control group the influence of the intervention could not be determined. Therefore, this data was not further analyzed for the exploratory study.

Confirmatory study:

Similarly, to the exploratory study, the confirmatory study occurred over the course of one semester. The study was introduced to the students by the first author approximately two weeks prior to their second exam. The first survey was administered in the intervention in the week before the second exam. All students also took a survey 1 week prior to Exam 3 and Exam 4. After Exam 2, students in the intervention group engaged in a metacognitive reflection and turned in the assignment regarding this reflection no later than a week after their exam. This same procedure was followed for the subsequent Exam 3 and 4. Students in both groups took also a final exam but no group filled out a survey prior to that exam nor was there any metacognitive reflection. The same regulations applied to the control group where students were exposed to the same survey the same day as the intervention group. Their reading assignments also had to be turned in no later than a week after the exam (same day as the intervention group).

The manipulated variable that differentiates the control from the intervention group during the confirmatory study was the exposure to a metacognitive intervention, the post-exam self-assessment. Thus, there was a single variable (Metacognitive Intervention) with 2 levels (exposed to intervention, not exposed to intervention). Two different types of data were measured: 1. The questions on the help-seeking survey correspond to 8 different subcategories which were averaged accordingly and reported as a single score for each category. 2. All individual exam scores and the final course grade will be delivered from the course instructor. The first and second exam score will be averaged and used as a covariate for subsequent ANCOVAS.

3.4 Results

Exploratory study

Student Performance: A one-way analysis of variance (ANOVA) (Figure 3.1) was conducted to compare the effect of the number of participation in the PESA (IV) on the average final exam score (DV). The number of participation contained four groups of participation 0 times (control group), 1 time, 2 times and 3 times. No significant effect of the number of participation in the

PESA on the average final exam score was observed, F(3, 182)= .609, p = .610, η_p^2= .010 (Power = .175). Additionally, to account for the notion that "Better Students are more likely to participate", a one-way analysis of covariance (ANCOVA) (Figure 3.2) was conducted to determine a statistically significant difference between number of exposures to PESA on final exam grade controlling for the average score of exam one and two. The ANCOVA did not detect a significant effect of the number of exposures to PESA controlling for the average score on exam one and two, F(3, 181)= 1.060, p =.368, η_p^2=. 017 (Power = .284). Hence, the post-exam self-assessment intervention, regardless of the number of participation, did not show any effect on the average grade of the final exam.

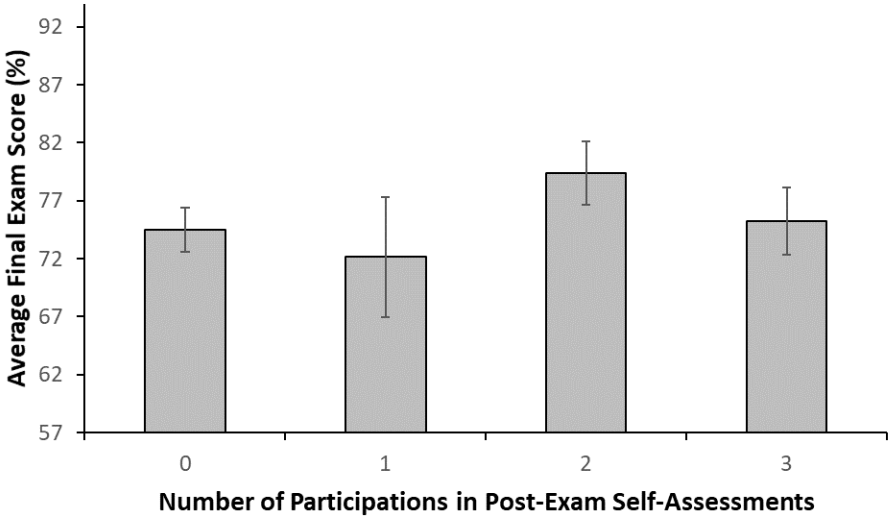

Figure 3.1: ANOVA Results - Average Final Exam Scores for the exploratory study during the Fall Semester 2017.

Confirmatory study

Student Performance: A one-way ANOVA (Figure 3.3) was conducted to compare the effect of the number of participation in the PESA (IV) on the average final exam score (DV). The number of participation contained four groups of participation 0 times (control group), 1 time, 2 times and 3 times. No significant effect of the number of participation in the PESA on the average final exam score was observed, F(3, 223)= .677, p = .567, η_p^2= .009 (Power = .192). Additionally, to

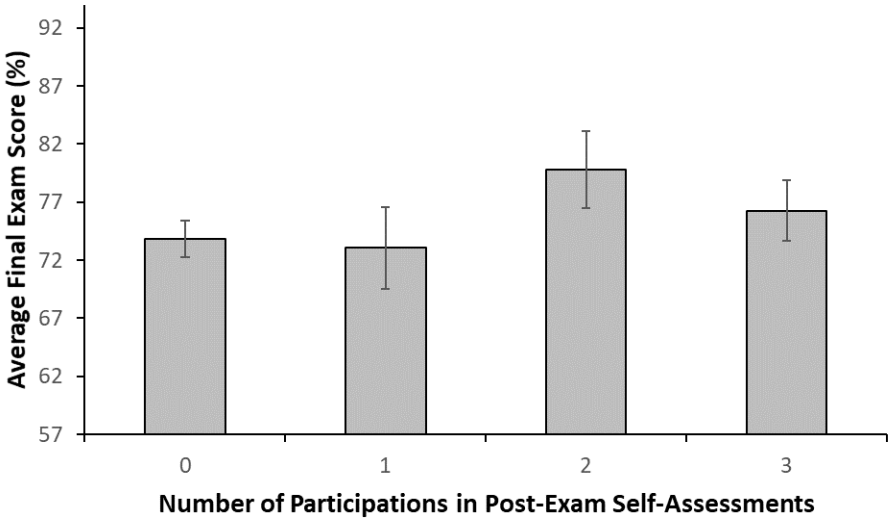

Figure 3.2: ANCOVA Results - Average Final Exam Scores for the exploratory study during the Fall Semester 2017.

account for the notion that "Better Students are more likely to participate", a one-way ANCOVA (Figure 3.4) was conducted to determine a statistically significant difference between number of exposures to PESA on final exam grade controlling for the average score of exam one and two. The ANCOVA did not detect a significant effect of the number of exposures to PESA controlling for the average score on exam one and two, F(3, 222)= .224, p =.880, η_p^2=.003 (Power = .092). Hence, the post-exam self-assessment intervention, regardless of the number of participation, did not show any effect on the average grade of the final exam.

Help Seeking: An index for each of the 8 different help seeking subcategories was generated for each data collection time. Each sub-scale was analyzed via a 2 (Group: intervention, no intervention) x 3 (Time: 1, 2, 3) mixed-factor analysis of variance (ANOVA). This was done to determine any changes of the level of help seeking over the course of the study within a group but also between the two groups. An alpha level of .05 was used for all subsequent statistical tests. Partial eta values of .0099, .0588, and .1379, are considered to be benchmarks for small, medium, and large effect sizes respectively (Richardson, 2011).

The average value, for each help-seeking category, was calculated by summing the scores from all questions in that category and dividing by the number of questions in that category. The last help

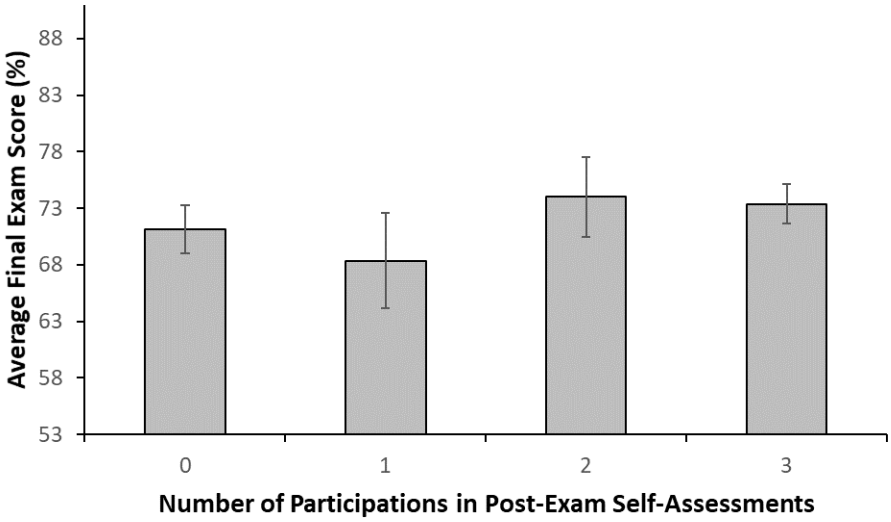

Figure 3.3: ANOVA Results - Average Final Exam Scores for the confirmatory study during the Spring Semester 2018.

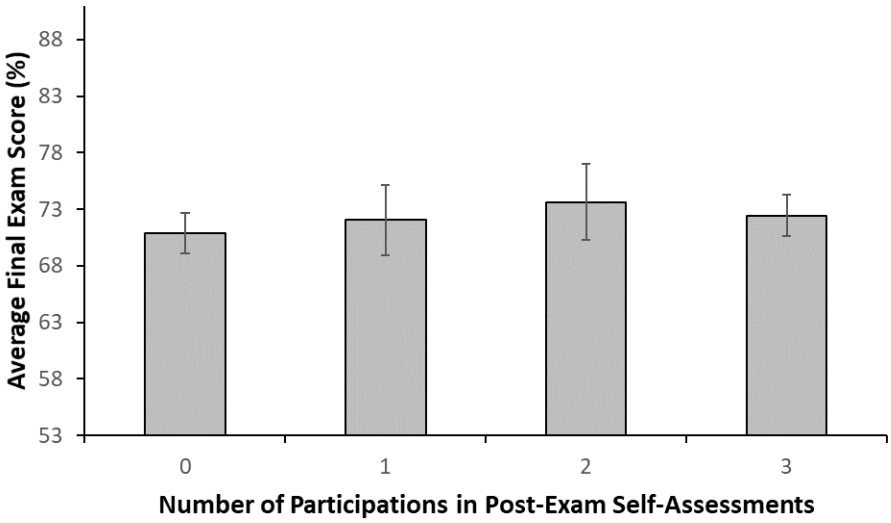

Figure 3.4: ANCOVA Results - Average Final Exam Scores the confirmatory study during the Spring Semester 2018.

seeking category (4 questions form the MSLQ) contained a question that first needed to be reverse coded before its score could be averaged. It could be shown that the intervention does neither significantly change the level of help-seeking over the course of the semester, nor significantly increase the level of help-seeking compared to control group.

General Intention to Seek Needed Help Mauchly's test indicated that the assumption of sphericity had been violated, $\chi^2(2)= 21.694$, $p < .001$; therefore the degrees of freedom were corrected using Huynh-Feldt estimates of sphericity (ϵ=.886). Overall, the rating of the general intention to seek needed help (Figure E.1) did not differ across time, F(1.772, 239.942) = .168, p = .820, η_p^2= .001. In addition, there was no difference in students' reported ratings of the general intention to seek needed help between the control and intervention group, F(1, 134) = .094, p = .760, η_p^2= .001. Furthermore, here was no group x time interaction, F(1.772, 239.942) = .334, p = .690, η_p^2 =.002.

General Intention to Avoid Needed Help Mauchly's test indicated that the assumption of sphericity had not been violated, $\chi^2(2)= 0.912$, p = .634; therefore no correction for the degrees of freedom was needed. Overall, the general intention to avoid needed help (Figure E.2) did not differ across time, F(2, 268) = .396, p = .674, η_p^2= .003. In addition, there was no difference in students' reported ratings of the general intention to avoid needed help between the control and intervention group, F(1, 134) = 3.103, p = .080, η_p^2= .023. Furthermore, there was no group x time interaction, F(2, 268) = .171, p = .843, η_p^2 =.001.

Perceived Costs of Help-Seeking (threat) Mauchly's test indicated that the assumption of sphericity had been violated, $\chi^2(2)= 19.010$, $p < .001$; therefore the degrees of freedom were corrected using Huynh-Feldt estimates of sphericity (ϵ=.900). Overall, the rating of the perceived cost of help-seeking (Figure E.3) did not differ across time, F(1.800, 236.501) = .365, p = .672, η_p^2= .003. In addition, there was no difference in students' reported ratings of the perceived cost of help-seeking between the control and intervention group, F(1, 134) = 1.562, p = .214, η_p^2= .012. Furthermore, there was no group x time interaction, F(1.800, 236.501) = 2.393, p = .100, η_p^2 =.018.

Instrumental (Autonomous) Help-Seeking Goal Mauchly's test indicated that the assumption of sphericity had been violated, $\chi^2(2)= 9.190$, p = .010; therefore the degrees of freedom were corrected using Huynh-Feldt estimates of sphericity (ϵ=.957). Overall, the rating of the instrumental help-seeking goal (Figure E.4) did not differ across time, F(1.915, 256.566) = 1.419, p = .244, η_p^2= .010. In addition, there was no difference in students' reported ratings of the instrumental help-seeking goal between the control and intervention group, F(1, 134) = .941, p = .334, η_p^2= .007. Furthermore, there was no group x time interaction, F(1.915, 256.566) = .077, p = .919, η_p^2 =.001.

Expedient (Executive) Help-Seeking Goal Mauchly's test indicated that the assumption of sphericity had been violated, $\chi^2(2)= 10.951$, p = .004; therefore the degrees of freedom were corrected using Huynh-Feldt estimates of sphericity (ϵ=.946). Overall, the rating of the expedient help-seeking goal (Figure E.5) did not differ across time, F(1.892, 248.368) = 1.822, p = .166, η_p^2= .013. In addition, there was no difference in students' reported ratings of the expedient help-seeking goal between the control and intervention group, F(1, 134) = .232, p = .631, η_p^2= .002. Furthermore, there was no group x time interaction, F(1.892, 248.368) = 1.442, p = .239, η_p^2 =.011.

Seeking Help from Formal Source (teachers) Mauchly's test indicated that the assumption of sphericity had not been violated, $\chi^2(2)= .702$, p = .704; therefore no correction for the degrees of freedom was needed. Overall, the rating of seeking help from formal sources (Figure E.6) did not differ across time, F(2, 268) = .858, p = .425, η_p^2= .006. In addition, there was no difference in students' reported ratings of seeking help from formal sources between the control and intervention group, F(1, 134) = .376, p = .541, η_p^2< .003. Furthermore, there was no group x time interaction, F(2, 268) = 1.347, p = .262, η_p^2 =.010.

Seeking Help from Informal Source (other students) Mauchly's test indicated that the assumption of sphericity had been violated, $\chi^2(2)= 8.505$, p = .014; therefore the degrees of freedom were corrected using Huynh-Feldt estimates of sphericity (ϵ=.962). Overall, the rating of seeking help from informal sources (Figure E.7) differed across time, F(1.924, 257.757) = 3.185, p = .045, η_p^2= .023. However, the pairwise comparison for the main effect of time, corrected using a

Bonferroni adjustment, indicated that the significant main effect does neither reflects a significant difference (p = .082) between time 1 and time 3, nor between time 1 and time 2 (p = 1.000) nor between time 2 and time 3 (p = .160). In addition, there was no difference in students' reported ratings of seeking help from informal sources between the control and intervention group, F(1, 134) = 2.834, p = .095, η_p^2= .021. Furthermore, there was no group x time interaction, F(1.924, 257.757) = .651, p = .517, η_p^2 =.005.

Help Seeking Scale from MSLQ Mauchly's test indicated that the assumption of sphericity had not been violated, $\chi^2(2)$= 4.336, p = .114; therefore no correction for the degrees of freedom was needed. Overall, the rating on the general help seeking scale from the MSLQ (Figure E.8) differed across time, F(2, 268) = 11.144, p < .001, η_p^2= .077. The pairwise comparison for the main effect of time, corrected using a Bonferroni adjustment, indicated that the significant main effect reflects a significant difference (p = .001) between time 1 and time 2 and time 1 and time 3 (p < .001) but not between time 2 and time 3 (p = 1.000). However, there was no difference between the ratings on the general help seeking scale from the MSLQ betweeen the students in the intervention and the control group, F(1, 134) = 0.015, p = .903, η_p^2< .000. In addition, there was a group x time interaction, F(2, 268) = 3.805, p = .023, η_p^2 =.028.

3.5 Discussions

Based on previous findings from tertiary education showing positive effects of SRL interventions specifically focusing on self-monitoring and reflection [Lan, 2005, Lovett, 2010, Glenn, 2010, Zimmerman et al., 2011], we examined whether similar positive effects could be obtained for a post-exam self-assessment intervention in a general chemistry course. We were particularly interested in the possible influence of the level of help-seeking and students' performance. However, taken as a whole, our results provide little evidence for the impact of the PESA intervention on these two factors. There are two main perspectives that could be used to explain the lack of influence of the intervention. On the one hand, it could be hypothesized that a PESA intervention by itself does not have a large effect on students' metacognitive abilities, motivation, and their

course grades. This idea could be supported by previous results from a study investigating the influence of reflection and incentives on the level of student calibration [Hacker et al., 2008]. Hacker et al. (2008) collected students' calibration data prior to testing and immediately after the exam about the predicted number of correct items. Overall, subsequent reflections on the differences between pre- and postdiction did not change the students' accuracy for future calibration. Interestingly, different results were seen for the various performance groups within the course. Similar results for different abilities groups were also observed previously [Kruger and Dunning, 1999]. The high-performing students were already highly calibrated and, provided their constrained standard deviations, their accuracy approached a ceiling. The results for the lower-performing students are mixed. The students who received extrinsic incentives gained postdiction accuracy. However, contrary to expectations, students who were asked to reflect on their performance lost postdiction accuracy. Hacker et al. (2008) attributes these findings to the effect of their reflection intervention being too weak to induce changes in calibration. Similarly, it could be that our intervention has a rather small impact making it hard to determine any effects with our sample size. Consequently, a much larger sample size would be needed to make clear indication on whether or not an intervention is useful in a specific environment. Hacker et al. (2008) also pointed out that, due to the small number of students in their intervention groups, their results need to be approached with caution. They further suggests, that the students' judgments of performance could be primarily impacted by stable and persistent beliefs about their performance. This phenomena could be based on judgments of calibration not being based on directly accessing activated memory, but rather on inferences on the activated memories [Koriat, 1993]. A pattern shown during studying pictures comparing the learning style of massing and spaced. Students performed better in the spaced learning condition, but when asked immediately after exams in a laboratory study, they still exhibit false judgments of effective learning by favoring massed learning [Kornell and Bjork, 2008].

Additionally, compared to previous examples in the literature [Nietfeld et al., 2006], our intervention could be less effective since students do not engage to the same level. The PESA intervention puts all the weight on students and does not provide additional instructor feedback or practice

as was shown in other studies to be part of a successful intervention [Zimmerman et al., 2011]. It could also be argued that metacognitive skills are needed in the first place for students to realize what kind of effort they have to put into the interventions. This leads us to the question whether we just need to change the extent to which we engage students in interventions.

Based on this notion, interventions in the current form might not be useful or might not make the best use of students' and instructors' time. Other interventions could be more effective and better suited for the studied chemistry courses. For example, a recent review paper highlighted a plethora of factors influencing achievement in higher education [Schneider and Preckel, 2017]. Their results were based on 38 meta analyses covering 1.9 million participants. 105 variables in 11 categories could be identified as influential factors, with different degrees of influencing students. Based on their results, other approaches could be tested. While not only the type of intervention is important, also the timing is crucial. For example, regularity and proximity are key for effective self-monitoring [Bandura, 1986].

Another possible explanation cannot be excluded: our intervention actually increased students' level of help seeking but we were unable to detected it since we measured the wrong characteristics. Our help-seeking scales were based on seeking help through more traditional approaches such as teachers and peers. However, nowadays students are prone to focus more on harnessing newer technologies, such as google or YouTube, as their primary source for help. This explains the necessity of modifying the survey.

Additional variables that are very often neglected in the equation are the social and cultural background of students. The group of lower performing students is very often still comprised of minorities as well as students with migration backgrounds. Different cultural influences could have an extra effect on how help seeking is approached and what intervention might work best. [Volet and Järvelä, 2001]

To further improve our experimental design and evaluate the influence of the PESA, a future study needs to increase the frequency of the interventions and the survey times. For example, a future design should include at least a 4th survey at the end of the semester. This is necessary to

capture the influence of the third post-exam self-assessment, currently not captured by only three surveys. Varying the level of self-reflection that students are engaged in, but also the level of feedback the students receive, poses another important modification. The experimental design of this study was purely quantitative and did not analyze students' responses to the surveys. Hence, additional insight on possible changes of students' learning strategies might be gained by a qualitative research where students answers on the post-exam self-assessment are analyzed.

Nevertheless, despite not having detected changes, our results cannot predict how a repeated exposure to self-reflection interventions over multiple semesters changes students' SRL. Neither can we answer how often students need to be prompted to engage in self-reflection exercises before they keep using them independently. Other questions needing to be addressed are to what extent students can transfer SRL skills, acquired in e.g. general chemistry, to other STEM courses.

Educational Implications

Most classrooms are complex environments with a multitude of variables influencing learning. Carefully controlling all variable within this setting, leave alone factors influencing learning outside the classroom, is very difficult and designing targeted interventions must be first based on actual scientific findings, but also on the specific learning environment. When considering implementing an intervention for a college course, not only the type of an intervention, but also the timing [Szu et al., 2011] are important factors that need to be considered. For example as was recently pointed out for flipped classroom approaches in chemistry [Jarvis, 2020], when poorly implemented they can fail to raise student scores or even put some students in disadvantaged position. Specific interventions fostering a good help seeking culture should specifically target the beginning of the semester. While often students determine that they struggle after a few weeks into the semester, seeking out help is often too late at this point. Then, it is difficult for students to catch up and they often end up compensating by utilizing wrong or inefficient learning strategies. Since self-regulated learning can be learned, it is not surprising that help-seeking was defined to be a developmental skill [Nelson-Le Gall, 1981]. Therefore, when trying to foster a good help seeking culture, a developmental approach must be taken by creating not only an environment

inviting students to ask questions, but also providing manifold opportunities for deep reflection and self-monitoring.

Limitations: There should always be caution about how the results of self-reported measures as help-seeking are interpreted. While observations would be a better measure to determine the level of help seeking, it is totally impractical in a college context, especially in introductory courses with hundreds of students. Besides, observations will not give an accurate picture since college students seek most of their help outside of classrooms. However, when conditions are well specified, it can be assumed that self-reported data and the actual behavior are highly correlated for intentions related to help-seeking [Ajzen, 1980]. Another limitation was that no real randomization of assigning participants to the intervention and control groups occurred, which would be desirable, but very difficult to realize in university contexts.

Bibliography

[Achacoso, 2004] Achacoso, M. V. (2004). Post-test analysis: A tool for developing students' metacognitive awareness and self-regulation. *New directions for teaching and learning*, 2004(100):115–119.

[Ajzen, 1980] Ajzen, I. (1980). *Understanding attitudes and predicting social behavior.* Englewood Cliffs, N.J. : Prentice-Hall.

[Ambrose et al., 2010] Ambrose, S. A., Bridges, M. W., DiPietro, M., Lovett, M. C., and Norman, M. K. (2010). *How learning works: Seven research-based principles for smart teaching*. John Wiley & Sons.

[Ames, 1992] Ames, C. (1992). Classrooms - goals, structures, and student motivation. *Journal of Educational Psychology*, 84(3):261–271.

[Andreou, 2004] Andreou, E. (2004). Bully/victim problems and their association with machiavellianism and self-efficacy in greek primary school children. *British Journal of Educational Psychology*, 74:297–309.

[Bail et al., 2008] Bail, F. T., Zhang, S., and Tachiyama, G. T. (2008). Effects of a self-regulated learning course on the academic performance and graduation rate of college students in an academic support program. *Journal of college reading and learning*, 39(1):54–73.

[Bandura, 1986] Bandura, A. (1986). *Social foundations of thought and action: a social cognitive theory.* Englewood Cliffs, N.J.: Prentice-Hall.

[Bandura, 1997] Bandura, A. (1997). *Self-efficacy: The exercise of control*. Macmillan.

[Bandura et al., 1967] Bandura, A., Grusec, J. E., and Menlove, F. L. (1967). Some social determinants of self-monitoring reinforcement systems. *Journal of personality and social psychology*, 5(4):449.

[Bembenutty, 2011a] Bembenutty, H. (2011a). Introduction: Self-regulation of learning in post-secondary education. *New directions for teaching and learning*, 2011(126):3–8.

[Bembenutty, 2011b] Bembenutty, H. (2011b). New directions for self-regulation of learning in postsecondary education. *New Directions for teaching and Learning*, 2011(126):117–124.

[Bloom, 1953] Bloom, B. S. (1953). Thought-processes in lectures and discussions. *The Journal of General Education*, 7(3):160–169.

[Brame and Biel, 2015] Brame, C. J. and Biel, R. (2015). Test-enhanced learning: the potential for testing to promote greater learning in undergraduate science courses. *CBE—Life Sciences Education*, 14(2):es4.

[Butler, 2007a] Butler, R. (2007a). An achievement goal perspective on student help seeking and teacher help giving in the classroom: Theory, research, and educational implications. In Karabenick, S. A. and Newman, R. S., editors, *Help seeking in academic setting: Goals, groups, and contexts.*, pages 15–44. Lawrence Erlbaum Associates Publishers, Mahwah, NJ, US, 1 edition.

[Butler, 2007b] Butler, R. (2007b). Teachers' achievement goal orientations and associations with teachers' help seeking: Examination of a novel approach to teacher motivation. *Journal of educational psychology*, 99(2):241.

[Church et al., 2001] Church, M. A., Elliot, A. J., and Gable, S. L. (2001). Perceptions of classroom environment, achievement goals, and achievement outcomes. *Journal of educational psychology*, 93(1):43.

[Cleary, 2011] Cleary, T. J. (2011). Professional development needs and practices among educators and school psychologists. *New Directions for Teaching and Learning*, 2011(126):77–87.

[Cooper and Sandi-Urena, 2009] Cooper, M. M. and Sandi-Urena, S. (2009). Design and validation of an instrument to assess metacognitive skillfulness in chemistry problem solving. *Journal of Chemical Education*, 86(2):240.

[Cooper et al., 2008] Cooper, M. M., Sandi-Urena, S., and Stevens, R. (2008). Reliable multi method assessment of metacognition use in chemistry problem solving. *Chemistry Education Research and Practice*, 9(1):18–24.

[Delclos and Harrington, 1991] Delclos, V. R. and Harrington, C. (1991). Effects of strategy monitoring and proactive instruction on children's problem-solving performance. *Journal of Educational Psychology*, 83(1):35.

[Dörrenbächer and Perels, 2016] Dörrenbächer, L. and Perels, F. (2016). More is more? evaluation of interventions to foster self-regulated learning in college. *International journal of educational research*, 78:50–65.

[Duncan and McKeachie, 2005] Duncan, T. G. and McKeachie, W. J. (2005). The making of the motivated strategies for learning questionnaire. *Educational psychologist*, 40(2):117–128.

[Dunlosky J., 2008] Dunlosky J., M. J. (2008). *Metacognition*, volume 1. Thousand Oaks, CA: SAGE Publications, Inc.

[Eccles J. S., 1998] Eccles J. S., Wigfield A., . S. U. (1998). Motivation to succeed. In Damon, W., Lerner, R. M., and Eisenberg, N., editors, *Handbook of child psychology, social, emotional, and personality development*, volume 3, chapter 10. John Wiley & Sons, New York, 3 edition.

[Efklides, 2011] Efklides, A. (2011). Interactions of metacognition with motivation and affect in self-regulated learning: The masrl model. *Educational psychologist*, 46(1):6–25.

[Elliot and Murayama, 2008] Elliot, A. J. and Murayama, K. (2008). On the measurement of achievement goals: Critique, illustration, and application. *Journal of Educational Psychology*, 100(3):613–628.

[Ericsson and Simon, 1993] Ericsson, K. A. and Simon, H. A. (1993). *Protocol analysis : verbal reports as data*. MIT Press, Cambridge, Mass., rev. edition.

[European Commission, 2008] European Commission (2008). The european qualifications framework for lifelong learning (eqf).

[Fabriz et al., 2014] Fabriz, S., Dignath-van Ewijk, C., Poarch, G., and Büttner, G. (2014). Fostering self-monitoring of university students by means of a standardized learning journal—a longitudinal study with process analyses. *European Journal of Psychology of Education*, 29(2):239–255.

[Finn and Metcalfe, 2008] Finn, B. and Metcalfe, J. (2008). Judgments of learning are influenced by memory for past test. *Journal of Memory and Language*, 58(1):19–34.

[Flavell, 1979] Flavell, J. H. (1979). Metacognition and cognitive monitoring: A new area of cognitive–developmental inquiry. *American psychologist*, 34(10):906.

[Foerst et al., 2017] Foerst, N. M., Klug, J., Jöstl, G., Spiel, C., and Schober, B. (2017). Knowledge vs. action: discrepancies in university students' knowledge about and self-reported use of self-regulated learning strategies. *Frontiers in psychology*, 8:1288.

[Foster et al., 2017] Foster, N. L., Was, C. A., Dunlosky, J., and Isaacson, R. M. (2017). Even after thirteen class exams, students are still overconfident: the role of memory for past exam performance in student predictions. *Metacognition and Learning*, 12(1):1–19.

[Freeman et al., 2011] Freeman, S., Haak, D., and Wenderoth, M. P. (2011). Increased course structure improves performance in introductory biology. *CBE—Life Sciences Education*, 10(2):175–186.

[Garcia and Pintrich, 1996] Garcia, T. and Pintrich, P. R. (1996). Assessing students' motivation and learning strategies in the classroom context: The motivated strategies for learning questionnaire. In Birenbaum, M. and Dochy, F. J. R. C., editors, *Alternatives in assessment of achievements, learning processes, and prior knowledge*. Kluwer Academic Publishers, Norwell, MA.

[Glenn, 2010] Glenn, D. (2010). How students can improve by studying themselves. https://www.chronicle.com/article/struggling-students-can/64004.

[Gottfried et al., 2001] Gottfried, A. E., Fleming, J. S., and Gottfried, A. W. (2001). Continuity of academic intrinsic motivation from childhood through late adolescence: A longitudinal study. *Journal of educational psychology*, 93(1):3.

[Graham and Golan, 1991] Graham, S. and Golan, S. (1991). Motivational influences on cognition - task involvement, ego involvement, and depth of information-processing. *Journal of Educational Psychology*, 83(2):187–194.

[Hackel et al., 2016] Hackel, T. S., Jones, M. H., Carbonneau, K. J., and Mueller, C. E. (2016). Re-examining achievement goal instrumentation: Convergent validity of agq and pals. *Contemporary Educational Psychology*, 46:73–80.

[Hacker et al., 2008] Hacker, D. J., Bol, L., and Bahbahani, K. (2008). Explaining calibration accuracy in classroom contexts: The effects of incentives, reflection, and explanatory style. *Metacognition and Learning*, 3(2):101–121.

[Hamman et al., 2000] Hamman, D., Berthelot, J., Saia, J., and Crowley, E. (2000). Teachers' coaching of learning and its relation to students' strategic learning. *Journal of Educational Psychology*, 92(2):342–348.

[Hartwig and Dunlosky, 2012] Hartwig, M. K. and Dunlosky, J. (2012). Study strategies of college students: Are self-testing and scheduling related to achievement? *Psychonomic Bulletin & Review*, 19(1):126–134.

[Hartwig et al., 2012] Hartwig, M. K., Was, C. A., Isaacson, R. M., and Dunlosky, J. (2012). General knowledge monitoring as a predictor of in-class exam performance. *British Journal of Educational Psychology*, 82(3):456–468.

[Hattie, 2008] Hattie, J. (2008). *Visible learning: A synthesis of over 800 meta-analyses relating to achievement*. routledge.

[Hattie, 2015] Hattie, J. (2015). The applicability of visible learning to higher education. *Scholarship of Teaching and Learning in Psychology*, 1(1):79.

[Hattie and Marsh, 1996] Hattie, J. and Marsh, H. W. (1996). The relationship between research and teaching: A meta-analysis. *Review of educational research*, 66(4):507–542.

[Hattie et al., 2015] Hattie, J., Masters, D., and Birch, K. (2015). *Visible learning into action: International case studies of impact*. Routledge.

[Hofer and Yu, 2003] Hofer, B. K. and Yu, S. L. (2003). Teaching self-regulated learning through a" learning to learn" course. *Teaching of Psychology*, 30(1):30–33.

[Horowitz et al., 2013] Horowitz, G., Rabin, L. A., and Brodale, D. L. (2013). Improving student performance in organic chemistry: Help seeking behaviors and prior chemistry aptitude. *Journal of the Scholarship of Teaching and Learning*, pages 120–133.

[Jarvis, 2020] Jarvis, C. L. (2020). The flip side of flipped classrooms. *Chemical & Engineering News*, 98(3):23–25.

[Kaplan et al., 2013] Kaplan, M., Sliver, N., LaVaque-Manty, D., and Meizlish, D. (2013). *Using reflection and metacognition to improve student learning: Across the disciplines, across the academy*. Sterling, Virginia: Stylus Publishing, LLC., 1 edition.

[Karabenick and Gonida, 2018] Karabenick, S. and Gonida, E. N. (2018). Academic help seeking as a self-regulated learning strategy: Current issues, future directions. In Greene, D. H. S. . J. A., editor, *Handbook of self-regulation of learning and performance*. Routledge, New York, 2 edition.

[Karabenick and Newman, 2009] Karabenick, S. and Newman, R. (2009). Seeking help: Generalizable self-regulatory process and social-cultural barometer. *Contemporary motivation research: From global to local perspectives*, pages 25–48.

[Karabenick, 2004] Karabenick, S. A. (2004). Perceived achievement goal structure and college student help seeking. *Journal of educational psychology*, 96(3):569.

[Karabenick and Berger, 2013] Karabenick, S. A. and Berger, J.-L. (2013). Help seeking as a self-regulated learning strategy.

[Karabenick and Dembo, 2011] Karabenick, S. A. and Dembo, M. H. (2011). Understanding and facilitating self-regulated help seeking. *New directions for teaching and learning*, 2011(126):33–43.

[Karabenick and Knapp, 1991] Karabenick, S. A. and Knapp, J. R. (1991). Relationship of academic help seeking to the use of learning strategies and other instrumental achievement behavior in college students. *Journal of educational psychology*, 83(2):221.

[Karabenick and Sharma, 1994] Karabenick, S. A. and Sharma, R. (1994). Perceived teacher support of student questioning in the college classroom: Its relation to student characteristics and role in the classroom questioning process. *Journal of Educational Psychology*, 86(1):90.

[Kirschner et al., 2006] Kirschner, P. A., Sweller, J., and Clark, R. E. (2006). Why minimal guidance during instruction does not work: An analysis of the failure of constructivist, discovery, problem-based, experiential, and inquiry-based teaching. *Educational psychologist*, 41(2):75–86.

[Kirschner and van Merriënboer, 2013] Kirschner, P. A. and van Merriënboer, J. J. (2013). Do learners really know best? urban legends in education. *Educational psychologist*, 48(3):169–183.

[Koriat, 1993] Koriat, A. (1993). How do we know that we know? the accessibility model of the feeling of knowing. *Psychological review*, 100(4):609.

[Kornell and Bjork, 2007] Kornell, N. and Bjork, R. A. (2007). The promise and perils of self-regulated study. *Psychonomic Bulletin & Review*, 14(2):219–224.

[Kornell and Bjork, 2008] Kornell, N. and Bjork, R. A. (2008). Learning concepts and categories: Is spacing the "enemy of induction"? *Psychological Science*, 19(6):585–592.

[Kruger and Dunning, 1999] Kruger, J. and Dunning, D. (1999). Unskilled and unaware of it: How difficulties in recognizing one's own incompetence lead to inflated self-assessments. *Journal of Personality and Social Psychology*, 77(6):1121–1134.

[Lan, 2005] Lan, W. (2005). Self-monitoring and its relationship with educational level and task importance. *Educational Psychology*, 25(1):109–127.

[Lan, 1996] Lan, W. Y. (1996). The effects of self-monitoring on students' course performance, use of learning strategies, attitude, self-judgment ability, and knowledge representation. *The Journal of Experimental Education*, 64(2):101–115.

[Leidinger and Perels, 2012] Leidinger, M. and Perels, F. (2012). Training self-regulated learning in the classroom: Development and evaluation of learning materials to train self-regulated learning during regular mathematics lessons at primary school. *Education Research International*, 2012.

[Lovett, 2010] Lovett, M. C. (2010). Using reflection and metacognition to improve student learning: Make exams worth more than the grade - using exam wrappers to promote metacognition. In Ambrose, S. A., editor, *How learning works : seven research-based principles for smart teaching*. Jossey-Bass, San Francisco, CA, 1 edition.

[Lundeberg and Fox, 1991] Lundeberg, M. A. and Fox, P. W. (1991). Do laboratory findings on test expectancy generalize to classroom outcomes? *Review of Educational Research*, 61(1):94–106.

[Makara and Karabenick, 2013] Makara, K. A. and Karabenick, S. A. (2013). Characterizing sources of academic help in the age of expanding educational technology: A new conceptual framework. *Advances in help seeking research and applications: The role of information and communication technologies*, pages 37–72.

[McCabe, 2011] McCabe, J. (2011). Metacognitive awareness of learning strategies in undergraduates. *Memory & Cognition*, 39(3):462–476.

[McConnell, 1985] McConnell, D. (1985). Learning from audiovisual media: assessing students' thoughts by stimulated recall. *Journal of Educational Television*, 11(3):177–187.

[McCormick, 2003] McCormick, C. B. (2003). Metacognition and learning. In *Handbook of psychology: Educational psychology*, volume 7, pages 79–102. John Wiley & Sons Inc, Hoboken, NJ, US.

[Miller and Murdock, 2007] Miller, A. D. and Murdock, T. B. (2007). Modeling latent true scores to determine the utility of aggregate student perceptions as classroom indicators in hlm: The case of classroom goal structures. *Contemporary Educational Psychology*, 32(1):83–104.

[Morehead et al., 2016] Morehead, K., Rhodes, M. G., and DeLozier, S. (2016). Instructor and student knowledge of study strategies. *Memory*, 24(2):257–271.

[Neisser, 1976] Neisser, U. (1976). *Cognition and reality : principles and implications of cognitive psychology*. W. H. Freeman, San Francisco.

[Nelson and Narens, 1994] Nelson, T. O. and Narens, L. (1994). Why investigate metacognition? In Shimamura, J. M. . A. P., editor, *Metacognition : knowing about knowing*, pages 1–25. MIT Press, Cambridge, Mass.

[Nelson-Le Gall, 1981] Nelson-Le Gall, S. (1981). Help-seeking: An understudied problem-solving skill in children. *Developmental Review*, 1(3):224–246.

[Newman, 2008] Newman, R. S. (2008). The motivational role of adaptive help seeking in self-regulated learning. *Motivation and self-regulated learning: Theory, research, and applications*, pages 315–337.

[Nietfeld et al., 2006] Nietfeld, J. L., Cao, L., and Osborne, J. W. (2006). The effect of distributed monitoring exercises and feedback on performance, monitoring accuracy, and self-efficacy. *Metacognition and learning*, 1(2):159.

[Nilson, 2013] Nilson, L. (2013). *Creating self-regulated learners: Strategies to strengthen students? self-awareness and learning skills*. Stylus Publishing, LLC.

[Olakanmi and Gumbo, 2017] Olakanmi, E. E. and Gumbo, M. T. (2017). The effects of self-regulated learning training on students' metacognition and achievement in chemistry. *International Journal of Innovation in Science and Mathematics Education (formerly CAL-laborate International)*, 25(2).

[Pajares, 1996] Pajares, F. (1996). Self-efficacy beliefs in academic settings. *Review of educational research*, 66(4):543–578.

[Paris and Paris, 2001] Paris, S. G. and Paris, A. H. (2001). Classroom applications of research on self-regulated learning. *Educational psychologist*, 36(2):89–101.

[Pintrich, 2002] Pintrich, P. R. (2002). The role of metacognitive knowledge in learning, teaching, and assessing. *Theory into practice*, 41(4):219–225.

[Pintrich and Schunk, 2002] Pintrich, P. R. and Schunk, D. H. (2002). *Motivation in education : theory, research, and applications*. Upper Saddle River, N.J.: Merrill, 2 edition.

[Pintrich P. R., 1991] Pintrich P. R., Smith A. D. & McKeachie, W. J. (1991). A manual for the use of the motivated strategies for learning questionnaire (mslq). http://soe.umich.edu/files/mslq/2013-MSLQ-Manual.pdf.

[Pressley and Ghatala, 1990] Pressley, M. and Ghatala, E. S. (1990). Self-regulated learning: Monitoring learning from text. *Educational psychologist*, 25(1):19–33.

[Pressley et al., 1992] Pressley, M., Harris, K. R., and Marks, M. B. (1992). But good strategy instructors are constructivists! *Educational Psychology Review*, 4(1):3–31.

[Renkl, 2002] Renkl, A. (2002). Worked-out examples: Instructional explanations support learning by self-explanations. *Learning and instruction*, 12(5):529–556.

[Rhodes, 2019] Rhodes, M. G. (2019). Metacognition. *Teaching of Psychology*, 46(2):168–175.

[Rhodes et al., 2020] Rhodes, M. G., Cleary, A. M., and DeLosh, E. L. (2020). *A guide to effective studying and learning: Practical strategies from the science of learning*. Oxford University Press.

[Robbins et al., 2004] Robbins, S. B., Lauver, K., Le, H., Davis, D., Langley, R., and Carlstrom, A. (2004). Do psychosocial and study skill factors predict college outcomes? a meta-analysis. *Psychological bulletin*, 130(2):261.

[Ross et al., 2005] Ross, M. E., Blackburn, M., and Forbes, S. (2005). Reliability generalization of the patterns of adaptive learning survey goal orientation scales. *Educational and Psychological Measurement*, 65(3):451–464.

[Ruohoniemi and Lindblom-Ylänne, 2009] Ruohoniemi, M. and Lindblom-Ylänne, S. (2009). Students' experiences concerning course workload and factors enhancing and impeding their learning–a useful resource for quality enhancement in teaching and curriculum planning. *International Journal for Academic Development*, 14(1):69–81.

[Sandi-Urena et al., 2011a] Sandi-Urena, S., Cooper, M. M., Gatlin, T. A., and Bhattacharyya, G. (2011a). Students' experience in a general chemistry cooperative problem based laboratory. *Chemistry Education Research and Practice*, 12(4):434–442.

[Sandi-Urena et al., 2011b] Sandi-Urena, S., Cooper, M. M., and Stevens, R. H. (2011b). Enhancement of metacognition use and awareness by means of a collaborative intervention. *International journal of science education*, 33(3):323–340.

[Scharff et al., 2011] Scharff, L., Rolf, J., Novotny, S., and Lee, R. L. (2011). Factors impacting completion of pre-class assignments (jitt) in physics, math, and behavioural sciences. In Rust, C., editor, *ISL18 Global Theories and Local Practices: Institutional, Disciplinary and Cultural Variations.* Oxford Brookes University, Oxford, UK.

[Schmitz, 2001] Schmitz, B. (2001). Self-monitoring zur unterstützung des transfers einer schulung in selbstregulation für studierende. eine prozessanalytische untersuchung. *Zeitschrift für Pädagogische Psychologie/German Journal of Educational Psychology*.

[Schmitz and Perels, 2011] Schmitz, B. and Perels, F. (2011). Self-monitoring of self-regulation during math homework behaviour using standardized diaries. *Metacognition and Learning*, 6(3):255–273.

[Schneider and Preckel, 2017] Schneider, M. and Preckel, F. (2017). Variables associated with achievement in higher education: A systematic review of meta-analyses. *Psychological bulletin*, 143(6):565.

[Schunk, 2012] Schunk, D. H. (2012). *Learning theories an educational perspective sixth edition*. Pearson.

[Schunk and Zimmerman, 2003] Schunk, D. H. and Zimmerman, B. J. (2003). Self-regulation and learning. *Handbook of psychology*, pages 59–78.

[Shumow and Schmidt, 2013] Shumow, L. and Schmidt, J. A. (2013). *Enhancing adolescents' motivation for science*. Corwin Press.

[Siegel et al., 1963] Siegel, L., Siegel, L. C., Capretta, P. J., Jones, R. L., and Berkowitz, H. (1963). Students thoughts during class: A criterion for educational research. *Journal of Educational Psychology*, 54(1):45.

[Singleton-Jackson et al., 2010] Singleton-Jackson, J. A., Jackson, D. L., and Reinhardt, J. (2010). Students as consumers of knowledge: Are they buying what we're selling? *Innovative Higher Education*, 35(5):343–358.

[Stegers-Jager et al., 2012] Stegers-Jager, K. M., Cohen-Schotanus, J., and Themmen, A. P. (2012). Motivation, learning strategies, participation and medical school performance. *Medical education*, 46(7):678–688.

[Strati et al., 2017] Strati, A. D., Schmidt, J. A., and Maier, K. S. (2017). Perceived challenge, teacher support, and teacher obstruction as predictors of student engagement. *Journal of Educational Psychology*, 109(1):131.

[Szu et al., 2011] Szu, E., Nandagopal, K., Shavelson, R. J., Lopez, E. J., Penn, J. H., Scharberg, M., and Hill, G. W. (2011). Understanding academic performance in organic chemistry. *Journal of Chemical Education*, 88(9):1238–1242.

[Thiede et al., 2003] Thiede, K. W., Anderson, M., and Therriault, D. (2003). Accuracy of metacognitive monitoring affects learning of texts. *Journal of educational psychology*, 95(1):66.

[Tobias, 2006] Tobias, S. (2006). The importance of motivation, metacognition, and help seeking in web-based learning. *Web-based learning: Theory, research and practice*, pages 203–220.

[Treisman, 1992] Treisman, U. (1992). Studying students studying calculus: A look at the lives of minority mathematics students in college. *The College Mathematics Journal*, 23(5):362–372.

[Tricot and Sweller, 2014] Tricot, A. and Sweller, J. (2014). Domain-specific knowledge and why teaching generic skills does not work. *Educational psychology review*, 26(2):265–283.

[Urdan, 2010] Urdan, T. (2010). The challenges and promise of research on classroom goal structures. In *Handbook of research on schools, schooling and human development*, pages 110–126. Routledge.

[Usher and Schunk, 2018] Usher, E. L. and Schunk, D. H. (2018). Social cognitive theoretical perspective of self-regulation. In *Handbook of self-regulation of learning and performance, 2nd ed.*, Educational psychology handbook series., pages 19–35. Routledge/Taylor & Francis Group, New York, NY, US.

[Volet and Järvelä, 2001] Volet, S. and Järvelä, S. (2001). *Motivation in learning contexts theoretical and methodological implications*. Amsterdam: Emerald Group Publishing Limited, 1 edition.

[Wirth and Leutner, 2008] Wirth, J. and Leutner, D. (2008). Self-regulated learning as a competence: Implications of theoretical models for assessment methods. *Zeitschrift für Psychologie/Journal of Psychology*, 216(2):102–110.

[Zimmerman, 1998] Zimmerman, B. J. (1998). Developing self-fulfilling cycles of academic regulation: An analysis of exemplary instructional models. In Zimmerman, D. H. S. . B. J., editor, *Self-regulated learning: From teaching to self-reflective practice*, pages 1–19. uilford Publications, New York, NY, US.

[Zimmerman, 2000] Zimmerman, B. J. (2000). Attaining self-regulation: A social cognitive perspective. In *Handbook of self-regulation*, pages 13–39. Elsevier.

[Zimmerman, 2008] Zimmerman, B. J. (2008). Investigating self-regulation and motivation: Historical background, methodological developments, and future prospects. *American educational research journal*, 45(1):166–183.

[Zimmerman, 2011] Zimmerman, B. J. (2011). Motivational sources and outcomes of self-regulated learning and performance: Graduate center of city university of new york. In *Handbook of self-regulation of learning and performance*, pages 63–78. Routledge.

[Zimmerman et al., 2011] Zimmerman, B. J., Moylan, A., Hudesman, J., White, N., and Flugman, B. (2011). Enhancing self-reflection and mathematics achievement of at-risk urban technical college students. *Psychological Test and Assessment Modeling*, 53(1):141–160.

[Zimmerman and Moylan, 2009] Zimmerman, B. J. and Moylan, A. R. (2009). Self-regulation: Where metacognition and motivation intersect. In *Handbook of metacognition in education*, pages 311–328. Routledge.

[Zimmerman and Pons, 1986] Zimmerman, B. J. and Pons, M. M. (1986). Development of a structured interview for assessing student use of self-regulated learning strategies. *American educational research journal*, 23(4):614–628.

[Zusho et al., 2007] Zusho, A., Karabenick, S. A., Bonney, C. R., and Sims, B. C. (2007). Contextual determinants of motivation and help seeking in the college classroom. In Smart, R. P. P. . J. C., editor, *The Scholarship of Teaching and Learning in Higher Education: An Evidence-Based Perspective*, pages 611–659. Springer Netherlands, Dordrecht.

[Zusho et al., 2003] Zusho, A., Pintrich, P. R., and Coppola, B. (2003). Skill and will: The role of motivation and cognition in the learning of college chemistry. *International journal of science education*, 25(9):1081–1094.

Appendix A

Supplemental Information for "Capturing the details of N_2 adsorption in zeolite X using stroboscopic isotope contrasted neutron total scattering"

Gas Adsorption Measurements - Experimental Details

100 mg of the pressed Ca exchanged zeolite X sample was activated under dynamic vacuum at 400°C for 24 hours followed by a N_2 surface area measurement at 77 K. Adsorption isotherms were measured using a Micromeritics ASAP 2020 adsorption analyzer fitted with a He cryostat with a stability of 0.01 K. All the isotherms were collected with at least five initial 0.5 cm^3/g incremental doses of gas followed by further 5 cm^3/g incremental doses up to 1 atm with sufficiently long equilibration times for each dose. The measured N_2 adsorption isotherms are all type 1. Desorption measurements were taken at the end of each isotherms to monitor that no hysteresis occurred. Prior to each measurement, the sample was reactivated at 200°C under dynamic vacuum for an hour followed by an hour of equilibration in the cryostat at the target temperature. N_2 isotherms were measured at 77 K and then every 10 K from 140 K to 300 K. The BET surface area was evaluated over the nanoporous regime, $0.01 \leq P/P_0 \leq 0.10$, of the 77 K N_2 adsorption isotherm following the recommendation of Walton and Snurr. [424] Isosteric heats of adsorption (HOA) were calculated by using the Clausius-Clapeyron relation between at least three measured isotherms. No hysteresis and sufficiently long equilibration times ensure that thermodynamic equilibration has been achieved, which is necessary to determine accurate heats of adsorption determined by the Clausius-Clapeyron relation. As little to no hysteresis was observed in the experimental isotherms and there was no uptick at the tail end of the HOA characteristic of increased fluid-fluid interactions, it can be determined that the physisorbed N2 did not undergo significant capillary condensation or multilayer formation under the thermal conditions measured. Results are shown in Figure A.2.

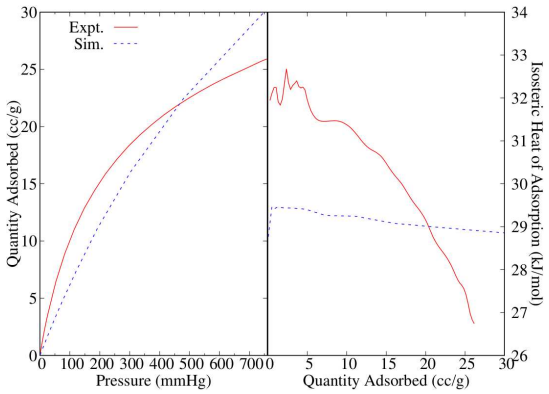

Figure A.1: Experimental Heats of Adsorption for N_2 adsorption into CaX. The three temperatures indicate which three isotherms were used for the Clausius-Clapeyron relation.

Comparison of Measured Heats of Adsorption at Several Temperatures

GCMC Simulation Details Gas adsorption was simulated with Monte Carlo in the grand canonical ensemble (GCMC) with our own in-house modified version of the MuSiC package. [425] The Peng-Robinson equation of state was used to determine the fugacity of N_2 for each temperature/pressure examined. [426] Each simulation employed 5,000 initialization, 500,000 equilibration, and 500,000 production cycles. A cycle consisted of N moves, where N is the number of adsorbed particles and cations rounded up to the nearest multiple of 10. The value for N started at $N_{cations}$+20 and could fluctuate (never decreasing) during the initialization cycles to match the system, and it was held constant throughout the equilibration and production cycles. The cations could fluctuate through random translations and re-insertions (jumps), and the adsorbed N_2 particles could fluctuate with random translations, rotations, re-insertions, insertions, and deletions. Each move was weighted equally. The experimentally determined crystal structure was used to represent the zeolite framework, which was held as rigid during the simulations. $Ca_{43}Si_{106}Al_{86}O_{384}$ was the stoichiometry used for the zeolite corresponding to ideal 86X with 100% Ca exchange. Owing to its previous success in describing cation positions and ion exchange in FAU-type zeolites, a simplified T-atom description that doesn't distinguish between Al and Si was used to describe the framework. [132, 427–429] A brief NVT simulation of a single unit cell with only framework and cations present was used to refine the cation positions in the activated sample. The final snapshot

was then expanded into the 2×2×2 super cell and used as the initial guess for cation positons in all the GCMC simulations. The volumes in the zeolite framework inaccessible to N_2 were blocked using our recently developed energy based pore mapping program. The accessible pore volume was mapped using similarly sized Ar as the probe molecule: ϵ=120 K, σ=3.4 Å, [131, 430] The simulated adsorption isotherms were excess corrected using the calculated accessible pore volume. Simulated heats of adsorption were obtained with fluctuation theory. Radial distribution functions and density maps were produced from the snapshots of the system collected at the end of each production cycle. The guest (cation and adsorbate)-framework Coulomb interactions were computed using Ewald sums with a damping parameter, α, of 0.31601 $Å^{-1}$ ($\sim$2.5 π/L). The on-the-fly guest-guest Coulomb interaction were computed using the damped, shifted potential method of Wolf with a cutoff of 12 Å. [431] The damping parameter, α, for the on-the-fly Coulomb calculations was set to 0.07 $Å^{-1}$ as it best reproduced the cation configuration of the brief NVT simulation done with much slower on-the-fly Ewald summations. The partial charges and van der Waals interaction parameters for the simulation are found in Table A.1. The partial charges for the framework atoms were found via an interpolation of the electronegativity equalization method (EEM) charges determined by Mortier *et al.* for FAU-type zeolites according to the Si/Al ratio. [132, 432] Following the model of Jeffroy *et al.*, the fully ionic charge for Ca was employed, and a Buckingham (exp-6: $Ae^{-b/r} - Cr^{-6}$) potential was used to describe the interaction between the Ca and framework oxygen: A= 61.1·10^6 K, b= 4.05 Å, C=7.552·10^5 K$Å^6$. [133, 433] The atomistic LJ parameters for N_2 were taken from the all atom TraPPe-small force field, which employs a charged ghost "Gh" atom at the molecular center of mass to replicate N_2's quadrupole moment. [130] The remaining van der Waals interactions for the framework oxygen-N_2, Ca-N_2, N_2-N_2 and Ca-Ca were computed with 12-6 Lennard-Jones (LJ) potentials cutoff at 12 Å; Lorentz-Berthelot mixing rules were used to obtain the pair-wise LJ parameters from the atomistic parameters listed in Table A.1.

We provide the details of the final snapshot of the GCMC simulation to demonstrate the dominant interaction governing adsorption in this simulation is the Coulombic interaction between the Ca and N_2:

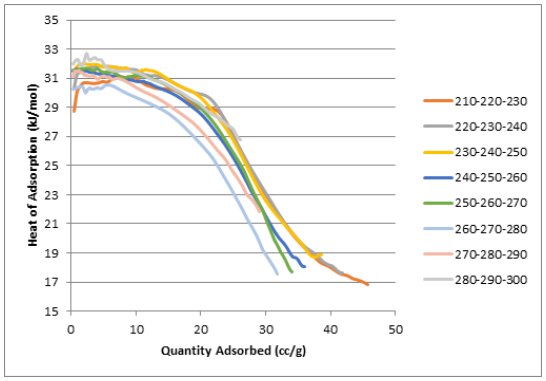

Figure A.2: Simulated (blue) and Experimental (red) isotherms (left) and heat of adsorption (right) for N_2 adsorption into CaX at 300 K.

- The net electrostatic interaction between the N_2 and the Ca is attractive: -3333.15 kJ/mol

- The net VDW interaction between the N_2 and the Ca is repulsive: 204.739 kJ/mol

- The interaction with the framework is 887.987 kJ/mol (electrostatic) and -810.044 kJ/mol (VDW) which combine to give a small net repulsive interaction with the adsorbed N_2.

When the electrostatic interactions between the framework and Ca with the N_2 are turned off, the GCMC predicted adsorption drops to 0.64 molecules/unit cell, which is effectively the same as for a siliceous (no cations present) FAU framework: 0.66 molecules/unit cell. If only the electrostatic interactions with the cations are turned off, the adsorption drops even further to 0.18 molecules/unit cell confirming the repulsive interaction indicated in the snapshot energetics. This clearly indicates that the electrostatic interaction between the Ca and the N_2 is by far the dominant interaction governing adsorption.

Table A.1: Atomistic Force Field Parameters: '-' indicates not used in potentials.

	σ(Å)	ϵ(K)	q(e)	Ref.
T	-	-	1.23735	[132,432,434]
O	3.000	93.53	-0.84263	[132,432,434]
Ca	2.586	50.27	2.00000	[133]
N	3.310	36.00	-0.48200	[130]
Gh	-	-	0.96400	[130]

Comparison of Experimental and Simulated Adsorption

Rietveld refinement and Fourier difference map of static dosed data for zeolite X

Rietveld refinement of crystal structures were carried out in TOPAS academic version 6. A second order polynomial (TOF = DIFC·d + DIFA·d^2 + ZERO) was used to convert the time-of-flight (TOF) to d-spacing, DIFC and ZERO were determined from a NIST Si-64d standard sample while DIFA was allowed to refine to account for the sample position variation. The diffraction peak shape was primarily modeled using a Pseudo-Voigt function, with an additional convolution of an exponential function (or a type-3 GSAS back-to-back function in JANA 2006) to model the extended peak tails for TOF diffraction data. Charge balance was used to constrain the Ca occupancies on the three different Ca sites (16·occCa1 + 32·occCa2 + 32·occCa3 = 43) with an additional split site occupancy constraint for the Ca1 and Ca2 sites (occCa1 + occCa2 $\leq$ 1). A Fourier difference map was used to identify the potential N_2 positions in the structure of the static loaded sample. The pristine structure (without N_2) was used as the starting model for the Refinement in JANA2006. [128] Only the atomic positions and Ca occupancies are allowed to vary during the refinement. After converging, the Fourier difference map was calculated and plotted in VESTA software [435] with a positive residual threshold value of 0.3 fm/Å^3. It was found while modeling the nitrogen atomic position for the dosed data set, that the occupancy and atomic displacement parameters are correlated. An initial fit with the occupancy fixed to the value derived from SSITKA analysis found the refined value of the B_{iso} to be 5.3(1.1) Å^2. In subsequent refinements, the atomic displacement parameter of nitrogen was this refined value. Table A.2 and Figure A.3 display results of the pristine structure refined against the 154° bank NOMAD data.

This pristine structure results in the presented positions in Figure 3.1, and was used to generate the presented Fourier difference maps (when compared to the dosed data) in Figure 3.2. Table A.3 and Figure A.4 display results of the dosed structure refinement against the 154° bank NOMAD data.

Table A.4 displays the results of the dosed structure refinement, completed without modeling the N position, against the 154° bank NOMAD data.

Stroboscopic and data-informed reduction procedure

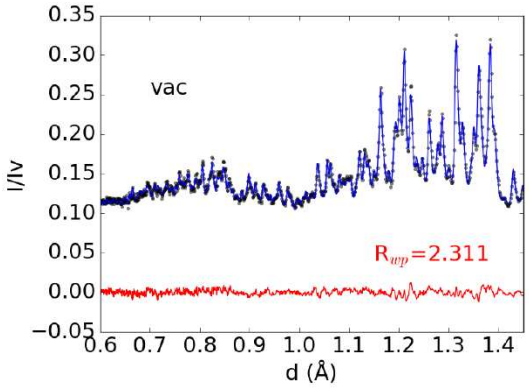

Figure A.3: Results of fit in TOPAS to pristine structure refinement with data in black, fit in blue, and residual in red. Resultant parameters from this refinement are shown in Table A.2.

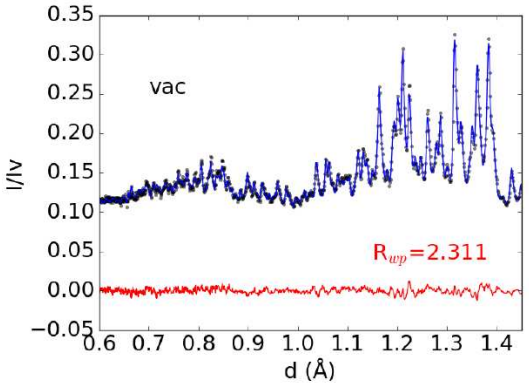

Figure A.4: Results of fit to dosed structure refinement with data in black, fit in blue, and residual in red. Resultant parameters from this refinement are shown in Table A.3.

Table A.2: The fixed and refined values used to fit the pristine diffraction data. Note the refined parameters include associated error, while the fixed values do not.

Space group = $Fd\bar{3}$, a = a = 25.0419(22) Å, $R_{wp} = 2.359$					
Atom	x	y	z	Occ.	$b_{iso}(Å^2)$
Si(1)	-0.0524(4)	0.1243(4)	0.0356(5)	1.0	0.23(15)
Si(2)	-0.0586(4)	0.0336(5)	0.1206(5)	0.11	0.23(15)
Al(1)	-0.0586(4)	0.0336(5)	0.1206(5)	0.89	0.23(15)
O(1)	-0.1116(3)	0.0021(6)	0.1068(3)	1.0	1.46(14)
O(2)	-0.0042(4)	-0.0037(4)	0.1411(2)	1.0	1.46(14)
O(3)	-0.0348(2)	0.0642(5)	0.0655(5)	1.0	1.46(14)
O(4)	-0.0616(2)	0.0758(4)	0.1730(5)	1.0	1.46(14)
Ca(1)	0.0	0.0	0	0.727(59)	0.58
Ca(2)	0.0622(6)	0.0622(6)	0.0622(6)	0.250(23)	0.58
Ca(3)	0.2227(2)	0.2237(3)	0.2227(3)	0.730(18)	0.58

During this study it was found that an unexpected and significant uptake of water into the sample occurred, which greatly complicated the standard PDF data reduction procedures. We present our advanced data-informed reduction procedure to mitigate the artifacts introduced by the uptake of water, and thus isolate the scattering signal due to the adsorption of nitrogen during steady-state flow conditions in the zeolite sample.

Stroboscopic gas flow measurement considerations

Three characteristic times are associated with stroboscopic gas-flow measurements, the switching period of the dosing gasses, the initial delay between the flow of a gas species at the switch and its' arrival at the sample, and the exhaust delay between the gas reaching the sample and being detected downstream at the RGA. While the first of these is known a priori (based on the prescribed switch rate), the remaining two must be determined experimentally for each sample. To determine the total travel time of gas from switch to RGA (which encompasses all plumbing and flow-related timing as well as any mechanical delay of the gas through the column of sample), a small quantity of inert tracer gas (in this case, Ar) in one of the dosing isotopes is employed. When the flow is switched to the gas containing the tracer, this total travel time can be quantified by detecting the inert gas signature on the RGA. Note that any delay of the dosing gas (^{14}N) separate from the tracer gas upon switching can thus be attributed directly due to the catalytic reaction, and associ-

Table A.3: The fixed and refined values used to fit the nitrogen-dosed diffraction data. Note the refined parameters include associated error, while the fixed values do not.

Space group = $Fd\bar{3}$, a = 24.9846(18) Å, $R_{wp} = 2.311$					
Atom	x	y	z	occ.	$b_{iso}(Å^2)$
Si(1)	-0.0524(4)	0.1240(4)	0.0363(4)	1.0	0.22(14)
Si(2)	-0.0585(4)	0.0336(4)	0.1201(4)	0.11	0.22(14)
Al(1)	-0.0585(4)	0.0336(4)	0.1201(4)	0.89	0.22(14)
O(1)	-0.1115(4)	0.0017(6)	0.1073(4)	1.0	1.55(13)
O(2)	-0.0038(5)	-0.0039(5)	0.1410(2)	1.0	1.55(13)
O(3)	-0.0348(2)	0.0641(5)	0.0653(5)	1.0	1.55(13)
O(4)	-0.0618(2)	0.0761(5)	0.1732(5)	1.0	1.55(13)
Ca(1)	0.0	0.0	0	0.690(56)	0.58
Ca(2)	0.0615(6)	0.0615(6)	0.0615(6)	0.267(22)	0.58
Ca(3)	0.2237(2)	0.2237(2)	0.2237(2)	0.732(18)	0.58
N	0.2761(13)	0.2761(13)	0.2761(13)	0.195(37)	5.30

ated residency time, of the sample with the gas. The details of calculating such residency times from SSITKA-studies are covered elsewhere [127]. As the delay in travel time of gas from switch to sample is identical for both the inert tracer and the dosant gas, total travel time is sufficient to extract residency time characteristics. However, determination of the delay from switch-to-sample is necessary to accurately reduce measured diffraction data stroboscopically. To this end, the measured diffraction data itself can be used as a tool to self-determine the delay of switch-to-sample at beam. Because we are using two isotopes of gas with significantly different scattering power (9.37 barn for ^{14}N compared to 6.44 barn for ^{15}N), we employ instantaneous integrated-intensity as a reliable metric of relative isotope presence in the sample, with the assumption that lower integrated scatter intensity indicates a greater presence of $^{15}N_2$, and vice-versa. The details of the time-delay extrapolation are covered in the next section.

Data-informed water mitigation and PDF reduction procedures

The relative populations of measured exhaust gas on the RGA are shown, for $^{14}N_2$, $^{15}N_2$, and Ar, in Figure A.5a, in which we observe the expected and prescribed isotope switching behavior, as well as the slight offset of the inert tracer gas from the $^{14}N_2$ signal.

Inspection of the measured total scattering structure factor, S(Q), as a function of time, as shown in Figure A.5(b), reveals the dominant change in the sample over time to be a steady rise

Table A.4: The refined structural parameters from Jana.

Space group = Fd$\bar{3}$, a = 25.0919(32) Å, $R_{wp} = 2.632$					
Atom	x	y	z	occ.	b_{iso}(Å^2)
Si(1)	-0.0524	0.1243	0.0356	1.0	0.23(15)
Si(2)	-0.0586	0.0336	0.1206	0.11	0.23(15)
Al(1)	-0.0586	0.0336	0.1206	0.89	0.23(15)
O(1)	-0.1121(4)	0.0020(7)	0.1061(4)	1.0	1.46(14)
O(2)	-0.0038(6)	-0.0043(6)	0.1419(2)	1.0	1.46(14)
O(3)	-0.0351(2)	0.0638(6)	0.0649(5)	1.0	1.46(14)
O(4)	-0.0622(3)	0.0770(6)	0.1738(6)	1.0	1.46(14)
Ca(1)	0.0	0.0	0	0.701(65)	0.58
Ca(2)	0.0637(8)	0.0637(8)	0.0637(8)	0.238(32)	0.58
Ca(3)	0.2223(4)	0.2223(4)	0.2223(4)	0.733(25)	0.58

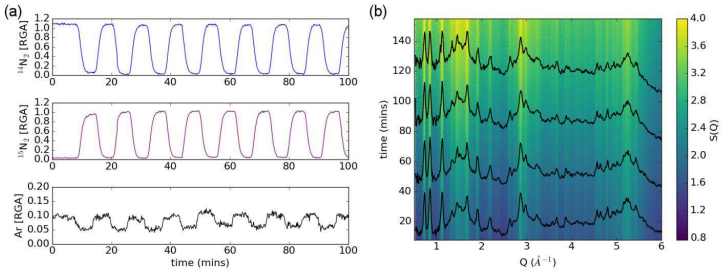

Figure A.5: (a.) Measured exhaust gas readout from RGA, indicating relative fraction of gas species. (b.) Measured total scattering structure factor from Zeolite-X sample under oscillating gas flow as a function of time, with four 100-second averages along this evolution plotted concurrently.

in diffuse scattered intensity, which we attribute to an unexpected uptake of water into the sample. Consider that the total measured scatter at any given time will be due to the steady-state zeolite structure (which is constant), the contributions of water (which are increasing with time), and the small oscillatory contributions due to the changing nitrogen isotope. In order to isolate the gas-dependent signal, we must first mitigate the effects of this water-feature. We do this by developing a time-dependent water-scatter model, described below. To begin, we average the first 430 seconds of data, wherein the flow of gas was fixed to ^{14}N/Ar mixture. We subtract this constant 'dry' zeolite model from all datasets, resulting in a signal which contains scatter due to the presence of water, nitrogen, isotope differences, and any changes in the host-structure over time (which should be minimal). We refer to this as the animated scattering signal, $S_A(Q)$. To generate a 'fully saturated' water model, we average the last 70 seconds of data in $S_A(Q)$, and fit this using a

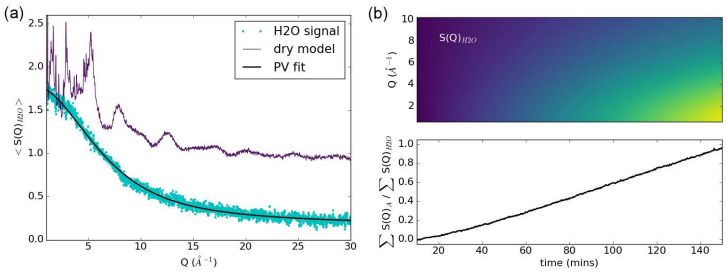

Figure A.6: (a) Average scatter from final 70 seconds of measurement, when data is fully saturated with water, and overlaid Psuedo-Voigt (PV) fit. For comparison, the dry-model zeolite scatter is also overlaid. (b-top) The water model, plotted as a function of time. (b-bottom) The integrated intensity of the observed data normalized by the as-fit water model.

Psuedo-Voigt function [436], which is shown in Fig. A.6a. The total integrated intensity of each dataset in $S_A(Q)$ is compared to the integrated intensity of this full-water model, resulting in a time-dependent metric of relative water saturation, $S_A(Q)/S_{H_2O}(Q)$. Thus, a time-dependent water-scatter model can be generated by scaling the full-water model by this saturation metric, which is shown in Fig. A.6(b).

The time-dependent water model, $S_{H_2O}(Q)$, can now be subtracted from $S_A(Q)$, resulting in the isolated scattering signal due to the gas-signal and any small structural changes in the host, referred to here as the $S_{gas}(Q)$. The integrated intensity of this gas-only scatter reveals the expected oscillatory signal. This isolated gas-signature, as well as the integrated intensity metric, are shown in Figure A.7a. The signal is further isolated by examining the residual of the integrated time-dependent water model to the integrated animated signal, which clearly highlights the expected sinusoidal behavior. A sine-wave is fit to this residual, shown in Figure A.7(b), which is ultimately used to stroboscopically bin the data. The observed sinusoidal uptake of nitrogen is found to be offset from the switching time of the dosing gas by approximately 50 seconds, allowing us to quantify the previously unknown source-to-sample delay.

With the associated gas-transport times now fully characterized, accurate stroboscopic rebinning of the measured scattering data is now possible. This was carried out using the Mantid data reduction framework. [437] The diffraction data from the 154° NOMAD detector bank of data was fit using TOPAS refinement package [100]. The refined atomic structure from the static-dosed

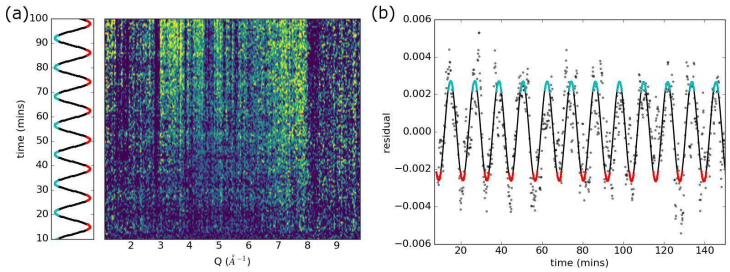

Figure A.7: (a) Time-dependent views of the gas-only scatter signal, $S_{gas}(Q)$, with the as-fit sine wave to the integrated intensity, color-coded to the stroboscopic binning scheme used with the $^{14}N_2$ associated data in red, and the $^{15}N_2$ associated data in cyan. (b) The residual and associated fit used to derive the sine-curve used in the stroboscopic rebinning.

zeolite data, found in Table A.3, was used for both the stroboscopically binned ^{14}N- and ^{15}N-data, with only the nitrogen occupancy allowed to vary. This resulted in a refined occupancy value of 0.672(52) for the ^{14}N-data and 0.465(66) for the ^{15}N-data, which produces a ratio of 1.45(24). This result is very consistent with the anticipated scattering power difference of the two isotopes of nitrogen, being 9.37 barn for ^{14}N, and 6.44 barns for ^{15}N, the ratio of which is $\sim$1.46. We find that this trends hold even when all parameters in the refinement are allowed to vary. The difference in refined nitrogen occupancy of the static- vs.-stroboscopically dosed data could be due to either the adsorption of water (inadvertently being fit as nitrogen occupancy in the stroboscopic data) or that the static dosed case was not fully saturated with N_2.

Appendix B

Supplemental Information for "Bond Valences and Anharmonicity in Vacancy-Ordered Double Perovskite Halides"

Prior to the RMC simulations presented in this work, we attempted to model the Cs–I/I–I pair correlations in the pair distribution function with a linear combination of three Gaussian functions to approximate the individual Cs–I, I–Iintra, and I–Iinter contributions to the peak shape and determine the origin of the peak asymmetry. However, while modeling with three Gaussian features easily reproduces the XPDF data, we found that the trends in peak height, position, and full width at half maximum were inconclusive, likely due to the large degree of overlap of these pair correlations. In this light, we found that unconstrained modeling of this feature was inappropriate, and instead turned to the more rigorous modeling routines employed in Reverse Monte Carlo simulations.

Traditional free-motion Reverse Monte Carlo (RMC) simulations were performed to ensure consistency with our rigid-body RMC approach. The optimized supercells are shown in Figure B.1 and the fits to the XPDF and S(Q)-1 are shown in Figure B.2.

The partial radial distribution functions for the I–Iintra, I–Iinter, and Cs–I pair correlations extracted from the free-motion RMC simulations of Cs_2SnI_6 and Cs_2TeI_6 are shown in Figure

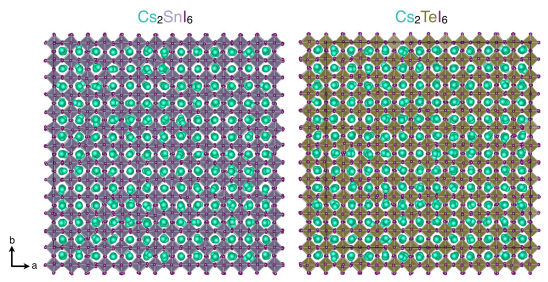

Figure B.1: Supercells of Cs_2SnI_6 and Cs_2TeI_6 optimized from free-motion RMC simulations.

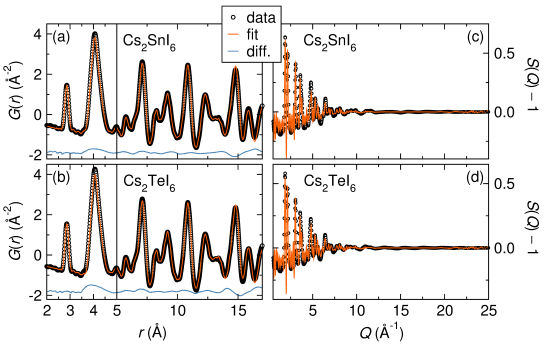

Figure B.2: Calculated G(r) and S(Q)-1 from free-motion RMC-optimized supercells of Cs_2SnI_6 and Cs_2TeI_6 compared against the experimental G(r) and S(Q)-1 from X-ray total scattering data. Experimental data are shown as open circles, the fits from the RMC optimizations are shown as orange lines, and the difference curves are shown as blue lines. The x-axes in (a) and (b) are split to highlight the low-r pair correlations.

B.3. The peaks are modeled by Gaussian functions to reveal asymmetry in the peak shape. In both Cs_2SnI_6 and Cs_2TeI_6, the Cs–I pair correlation is quite asymmetric, consistent with the pseudorigid-body RMC simulations shown in the main article. We have calculated the bond valence sum of cesium from the RMC-optimized supercells of Cs_2SnI_6 and Cs_2TeI_6, as shown in Figure B.4. The distributions were fit to Gaussian functions, and the centroid of the peak was taken as the bond valence sum. The results of the fitting are presented in Table B.1.

Table B.1: Bond valence sum analysis for Cs^+ from the RMC-optimized supercells of Cs_2SnI_6 and Cs_2TeI_6.

	free-motion RMC	pseudo-rigid-body RMC
Cs_2SnI_6	1.21 ± 0.13	1.21 ± 0.11
Cs_2TeI_6	1.19 ± 0.09	1.19 ± 0.10

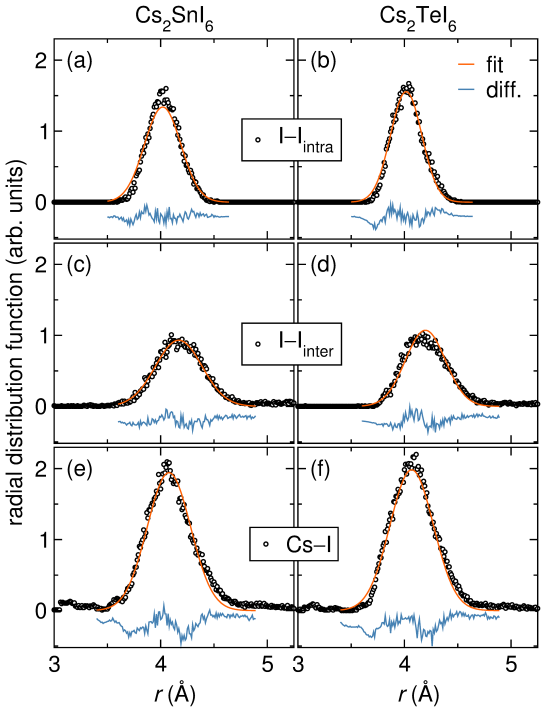

Figure B.3: Partial radial distribution functions for I–Iintra (a,b), I–Iinter (c,d), and Cs–I (e,f) pair correlations in Cs_2SnI_6 and Cs_2TeI_6 obtained from free-motion Reverse Monte Carlo simulations (circles). The distributions are fit with Gaussian functions, shown by the orange line. The difference curves are shown in blue and reveal asymmetries in the I–Iinter and Cs–I RDFs.

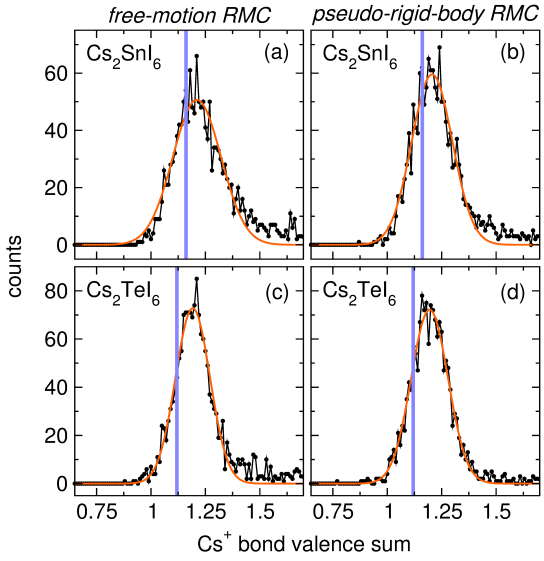

Figure B.4: Bond valence sum distributions for cesium in the $6 \times 6 \times 6$ supercells of Cs_2SnI_6 and Cs_2TeI_6 optimized within the (a,c) free-motion RMC approach and (b,d) the pseudo-rigid-body RMC approach. The distributions were fit to Gaussian functions and the centroid of the peak was taken as the bond valence sum. The blue vertical lines denote the bond valence sum of Cs^+ calculated from the cubic structures of Cs_2SnI_6 and Cs_2SnI_6 refined against the XPDF data.

Appendix C

Supplemental Information for "Finding Order within the disordeered methylammonium tin iodide"

As a reference, the orientations of the methylammonium cations in the starting structure for the RMC modeling was plotted (Figure C.1).

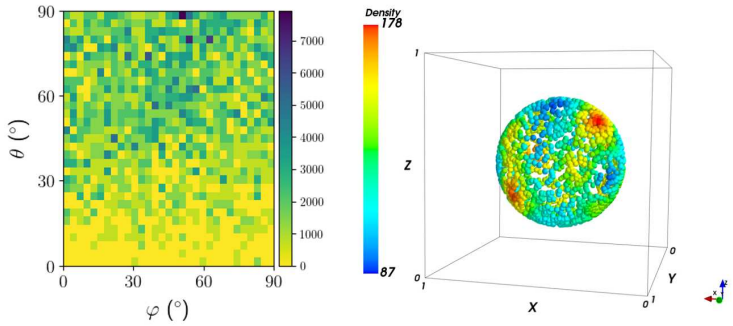

Figure C.1: Histogram illustrating orientations of the methylammonium cations in spherical coordinates, ϕ and θ, folded to 0 - 90° (left) as well as a kernel density estimate plot in Cartesian coordinates.

Additional histograms for reference structures not shown in Chapter 5 are illustrated in Figure C.2. A different mixing of reference structures was generated and shown.

To see whether the methylammonium cations in $(MA)_2SnI_6$ have any influence on the off-centering of the Sn atoms in the $[SnI_6]$ octahedra, a 2D histogram of the distribution of the $\vec{r}_{CSn}$=($\vec{r}_{Centroid\ of\ octahedra}$ - $\vec{r}_{Sn}$) was generated (Figure C.3).

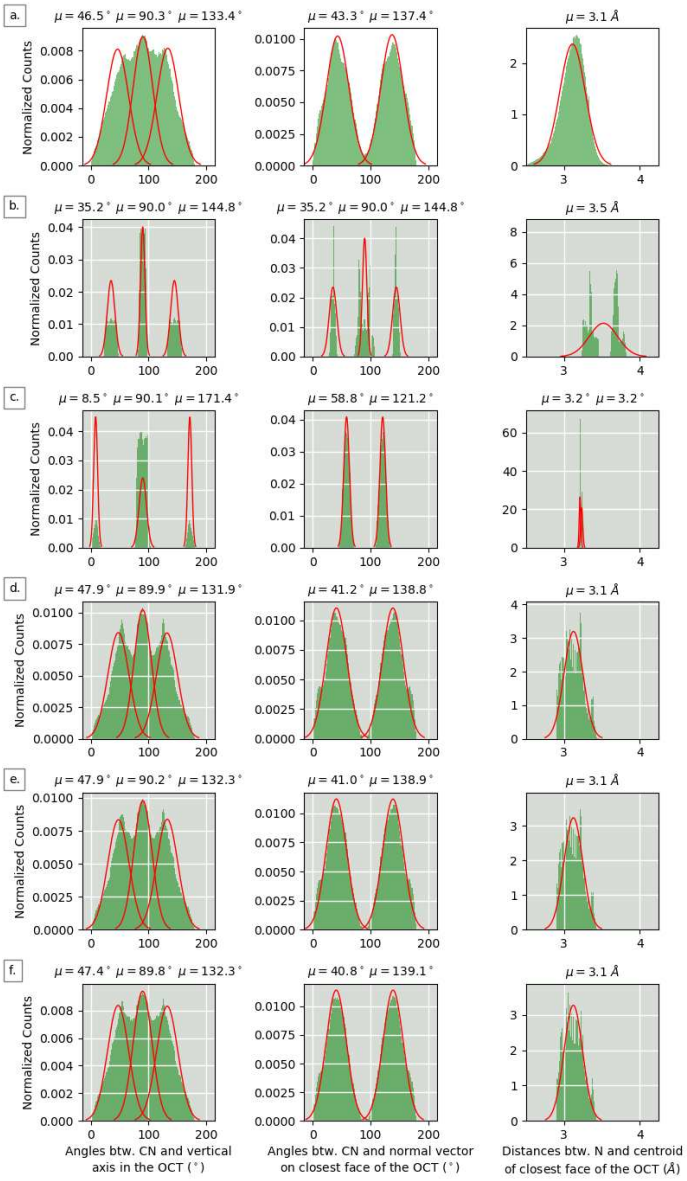

Figure C.2: Histograms illustrating the distances between N and centroid on the faces of the octahedra (left), angles between the C-N vector and the normal vector on the faces of the octahedra (middle), and the vertical axis of the octahedra (right). Gaussian fits are overlaid to the extracted data (red). Data for a.) Data from the 720 RMC simulations, b.) MA oriented about $\langle 111 \rangle$ with octahedra randomly tilted up to 11° towards $\langle 111 \rangle$, c.) MA oriented about $\langle 100 \rangle$ with octahedra randomly tilted up to 11° in any direction, d.) to f.) contain mixtures of MA randomly oriented with octahedra randomly tilted up to 11° in any direction, MA oriented about $\langle 111 \rangle$ with octahedra randomly tilted up to 11° in any direction, c.), and MA oriented about $\langle 110 \rangle$ with octahedra randomly tilted up to 11° in any direction, with 79.2%/8.3%/4.2%/8.3%, 83.3%/6.9%/2.8%/6.9%, and 87.5%/5.6%/1.4%/5.6%, respectively.

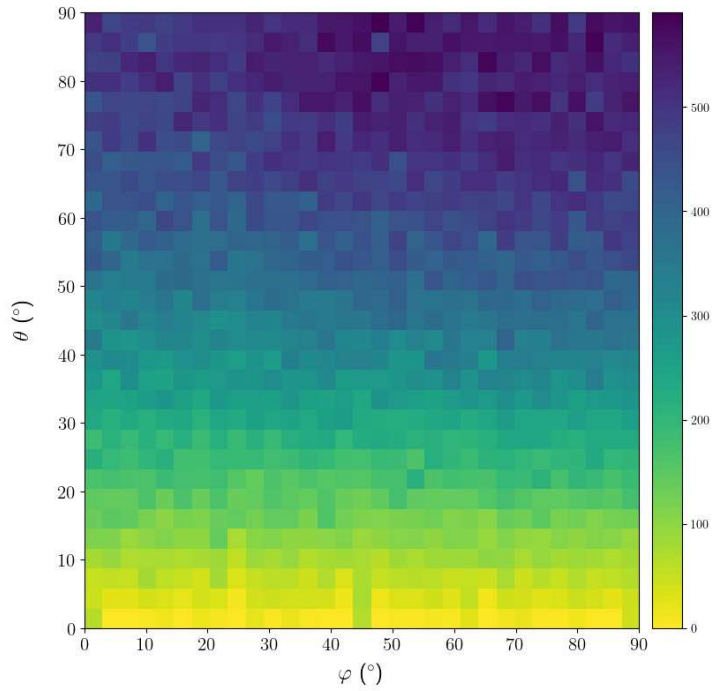

Figure C.3: Histogram illustrating orientations of the tin off-centering in the octahedra in spherical coordinates, ϕ and θ, folded to 0 - 90°.

Appendix D

Suppelemental information for "Metacognitive reflection and self-regulated learning qualities in general chemistry college courses"

D.1 Example from Pre-exam knowledge survey

Explain the role and the characteristics of the three types of subatomic particles in the volume and density of the atom and its nucleus

- I do not understand the question or task
- I do not understand the technical terms
- I do not think I can give a correct answer
- I think I understand the question and I think I can answer at least half of it correctly
- I think I understand the question and I know exactly where to find the information I need to give a correct answer in 20 minutes or less
- I know that I can answer the question well enough for grading now

D.2 Example from Post-exam self-assessment

Chem 111 Post-Exam Self-Assessment

See the instructions in Canvas for more details about how this assignment will be scored.

1. Fill in these blanks: Exam Number _____ Your Predicted Exam Score _____% Actual Exam Score _____%

2. How did your actual score on this exam compare to the score you expected? How do you explain the difference, if any?

3. How do you feel about your exam grade? Are you surprised, relieved, disappointed, or what?

4. Write about you spent your time preparing for the exam. That is, what study techniques did you use? Address at least 4 of these examples, and feel free to add your own:

    - Did you take notes on the readings?
    - Did you do SmartWork review or end-of-chapter problems?
    - Did you rebuild your pie after the ALEKS Knowledge Check?
    - Did you talk about the course material with other students?
    - Did you go to office hours?
    - Did you use the sample exam?
    - Did you test yourself in some other way?
    - Did you complete the Exam 1 Knowledge Survey (in Canvas)?
    - Was your study time focused, or did you multitask while studying?

5. How many hours did you study for the exam? Was this enough time to get the grade you wanted, or should you have spent more time preparing? Should you have spent your study time differently?

6. Fill out the table below for every question you missed on the exam. (If you need more rows, put your cursor in the last box of the last row and press tab.)

    Your exam version: ____

Question number	Knowledge Survey Item for this question	Type of question	Careless Mistake	Unfamiliar Material	Misinterpreted Question	Could Not Solve	Did Not Complete	Other Reason
		List all that apply from the list below.	Mark an X if this reason applies					Explain

Types of questions may include:

true/false, calculation, equation, interpret a graph, interpret a picture, draw Lewis structure. (You can also suggest other types.)

7. Examine the questions that you answered incorrectly on the exam. To what extent did these items come from a specific set of class materials (readings, lectures, recitations, ALEKS, end-of-chapter problems)? To what extent did they focus on certain topics? Did you tend to misread the questions? Were you careless? Did you run out of time?

8. Set a goal to get a certain percentage correct on the next exam. Consider what you found to be effective from your study for this exam. What study strategies and schedule will enable you to earn that score? (Be specific – it is not sufficient to say, "I'll keep doing what I have been.")

D.3 MSLQ – Scales and questions used on the surveys

Intrinsic Motivation

- In a class like this, I prefer course material that really challenges me so I can learn new things.
- In a class like this, I prefer course material that arouses my curiosity, even if it is difficult to learn.
- The most satisfying thing for me in this course is trying to understand the content as thoroughly as possible.
- When I have the opportunity in this class, I choose course assignment that I can learn from even if they don't guarantee a good grade.

Extrinsic Motivation

- Getting a good grade in this class is the most satisfying thing for me right now.
- The most important thing for me right now is improving my overall grade point average, so my main concern in this class is getting a good grade.
- If I can, I want to get better grades in this class than most of the other students.
- I want to do well in this class because it is important to show my ability to my family, friends, employer, or others.

Task Value

- I think I will be able to use what I learn in this course in other courses.
- It is important for me to learn the course material in this class.
- I am very interested in the content area of this course.
- I think the course material in this class is useful for me to learn.

- I like the subject matter of this course.
- Understanding the subject matter of this course is very important to me.

Control of Learning Beliefs

- If I study in appropriate ways, then I will be able to learn the material in this course.
- It is my own fault if I don't learn the material in this course.
- If I try hard enough, then I will understand the course material.
- If I don't understand the course material, it is because I didn't try hard enough.

Self-Efficacy for Learning and Performance

- I believe I will receive an excellent grade in this class.
- I'm certain I can understand the most difficult material presented in the reading for this course.
- I'm confident I can understand the most complex material presented by the instructor in this course.
- Considering the difficulty of this course, the teacher, and my skills, I think I will do well in this class.
- I'm certain I can master the skills being taught in this class.
- I expect to do well in this class.
- I'm confident I can learn the basic concepts taught in this course.
- I'm confident I can do an excellent job on the assignment and test in this course.

Help Seeking

- Even if I have trouble learning the material in this class, I try to do the work on my own, without help from anyone (REVERSED)
- I ask the instructor to clarify concepts I don't understand well.
- When I can't understand the material in this course, I ask another student in this class for help.
- I try to identify students in this class whom I can ask for help if necessary.

Appendix E

Suppelemental information for "The influence of Post-Exam Self-Assessment Interventions on Student performance and help seeking in a college level general chemistry course"

E.1 Help-Seeking Questionnaire

General Intention to Seek Needed Help

- If I needed help in this class I would ask someone for assistance.
- If I needed help understanding the lectures in this class I would ask for help.
- If I needed help with the readings in this class I would ask for help.

General Intention to Avoid Needed Help

- If I didn't understand something in this class I would guess rather than ask someone for assistance.
- I would rather do worse on an assignment I couldn't finish than ask for help.
- Even if the work was too hard to do on my own, I wouldn't ask for help with this class.

Perceived Costs of Help-Seeking (threat)

- Getting help in this class would be an admission that I am just not smart enough to do the work on my own.
- I would not want anyone to find out that I needed help in this class.

- Asking for help would mean I am not as smart as other students in the class.
- Others would think I was dumb if I asked for help in this class.

Instrumental (Autonomous) Help-Seeking Goal

- I would get help in this class to learn to solve problems and find answers by myself.
- If I were to get help in this class it would be to better understand the general ideas or principles.
- Getting help in this class would be a way for me to learn more about basic principles that I could use to solve problems or understand the material.

Expedient (Executive) Help-Seeking Goal

- The purpose of asking somebody for help in this class would be to succeed without having to work as hard.
- If I were to ask for help in this class it would be to quickly get the answers I needed.
- Getting help in this class would be a way of avoiding doing some of the work.

Seeking Help from Formal Source (teachers)

- If I were to seek help in this class it would be from the teacher.
- If I were to seek help in this class I would ask the teacher.

Seeking Help from Informal Source (other students)

- If I were to seek help in this class it would be from another student.
- If I were to seek help in this class I would ask another student

Help Seeking Scale from MSLQ

- Even if I have trouble learning the material in this class, I try to do the work on my own, without help from anyone (REVERSED)
- I ask the instructor to clarify concepts I don't understand well.
- When I can't understand the material in this course, I ask another student in this class for help.
- I try to identify students in this class whom I can ask for help if necessary.

E.2 Individual Help Seeking Scale Plots

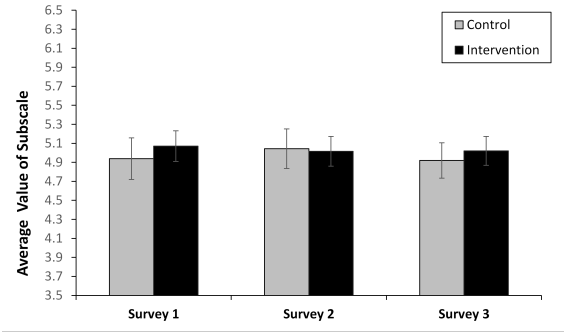

Figure E.1: Results from the help Seeking Survey Subscale: General Intention to Seek Needed Help.

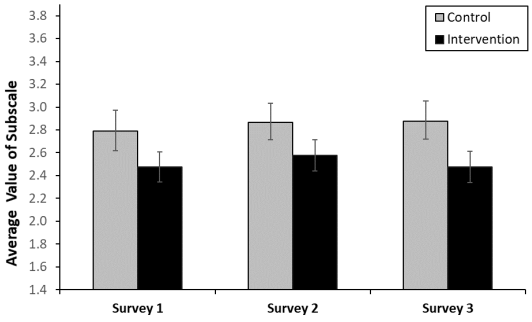

Figure E.2: Results from the help Seeking Survey Subscale: General Intention to Avoid Needed Help.

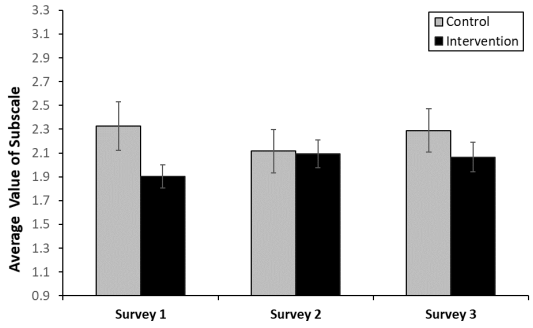

Figure E.3: Results from the help Seeking Survey Subscale: Perceived Costs of Help-Seeking (threat).

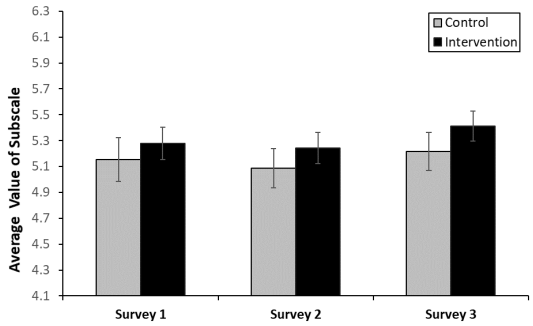

Figure E.4: Results from the help Seeking Survey Subscale: Instrumental (Autonomous) Help-Seeking Goal.

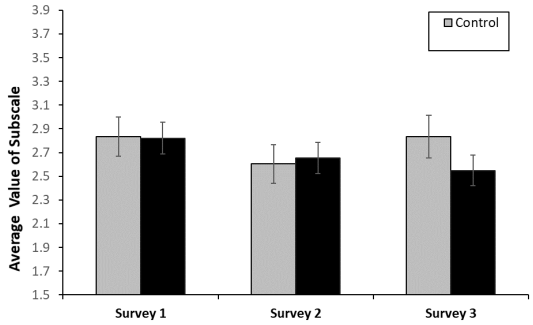

Figure E.5: Results from the help Seeking Survey Subscale: Expedient (Executive) Help-Seeking Goal.

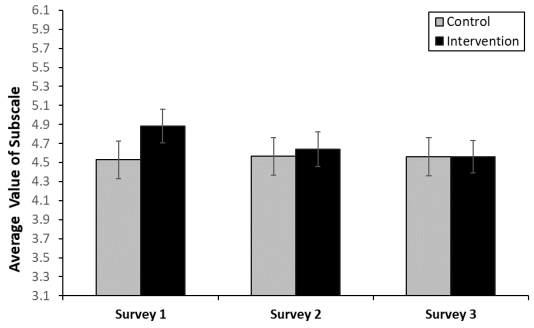

Figure E.6: Results from the help Seeking Survey Subscale: Seeking Help from Formal Source (teachers).

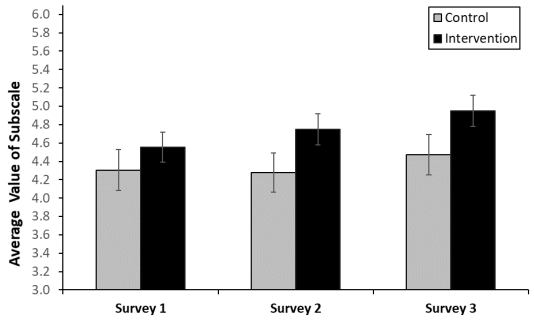

Figure E.7: Results from the help Seeking Survey Subscale: Seeking Help from Informal Source (other students).

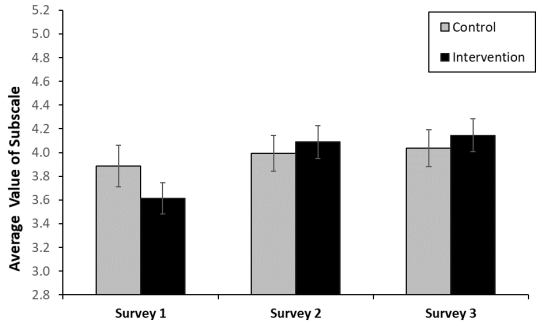

Figure E.8: Results from the help Seeking Survey Subscale of the MSLQ.